

THE UNIVERSITY OF HULL

TECHNO-ECONOMIC ANALYSIS OF HYBRID ADIABATIC COMPRESSED-AIR AND
BIOMASS GASIFICATION ENERGY STORAGE SYSTEMS FOR POWER GENERATION
THROUGH MODELLING AND SIMULATION

being a Thesis submitted for the Degree of Doctor of Philosophy (PhD)

in the University of Hull

by

Chidiebere Diyoke (B-Eng, MSc)

September 2018

Abstract

Energy storage has gained an increasing attention as a technology to smoothen out the variations associated with renewable energy power sources and adapt them into a dispatchable product to meet variable demand loads. An energy storage system can be a hybrid or stand alone. There is a rising interest for hybrid energy storage systems cited close to local consumers which is able to exploit the amount of local renewable sources on site, to provide demand side flexibility and also help to decarbonize the heating sector.

The thesis is based on modelling and simulation of overall thermodynamic performance and economic analysis of an integrated hybrid energy storage system consisting of adiabatic compressed air energy storage (A-CAES), biomass gasification system with a wood dryer coupled to a syngas-diesel fuelled electric generator for the dual production of electricity and low temperature hot water for domestic use.

The first part of the research work involves the modelling of the latent heat (LH) thermal energy storage (TES) for the A-CAES component. Implicit finite difference technique was applied to discretize the energy equations of the heat transfer fluid and phase change material and the resulting equations solved using a developed Matlab computer code. The developed model of the LH TES was validated using experiment measurement from literature and its performance assessed using charging rate, energy efficiency and exergy efficiency.

The second part consists of modelling of biomass gasification through a developed Matlab computer code. Kinetic free stoichiometric equilibrium modelling approach was adopted. The developed model showed good agreement with two different experimental measurements. Predictions that can be done with the model include syngas yield, temperature profiles of the pyrolysis, oxidation and reduction zones respectively including syngas yield, carbon conversion efficiency and lower calorific value of the syngas.

In the third part, thermodynamic modelling of the overall novel integrated system is developed. It combines the models of different components of the integrated system earlier developed. The system designed for a maximum capacity of 1.3 MW is to utilize

the high syngas temperature from the biomass gasifier and the relatively hot dual fuel engine (DFE) exhaust temperature to heat up the compressed air from the A-CAES component during the charging and discharging modes, respectively. Also, the heat contained in the DFE jacket water is recovered to produce low temperature hot water for domestic hot water use. Key output parameters to assess the performance of the hybrid systems are total system efficiency (TSE), round trip efficiency (RTE) of the A-CAES, electrical efficiency, effective electrical efficiency, and exergy efficiency for the system. Furthermore, exergy destruction modelling is done to ascertain and quantify the main sources of exergy destruction in the systems components.

Finally, an economic feasibility of the overall system is presented using the electricity and heat demand data of Hull Humber region as a case study.

The results of this study reveals that it is technically possible to deploy the proposed system in a distributed generation to generate dispatchable wind power and hot water for domestic use. The total energy and exergy efficiency of the system is about 37.12% and 28.54%, respectively. The electrical and effective electrical efficiency are 29.3 and 32.7 %, respectively. In addition, the round trip efficiency of the A-CAES component of the system is found to be about 88.6% which is higher than that of a standalone A-CAES system, thus demonstrating the advantage of the system to recover more stored wind electricity than in conventional A-CAES system. However, the TSE of the system is less than that of a conventional A-CAES system but comparable to similar hybrid configurations. The exergy destruction of the hybrid system components is highest in the biomass gasifier followed by the DFE and the least exergy destruction occurs in the HAD. Furthermore, economic analysis results show that the system is not profitable for commercial power generation unless a 70% of the total investment cost is waived in the form of subsidy. Expectedly, the cost of electricity (COE) of £0.19 per kWh is more than the range of the mean electricity tariff for a medium user home in the UK including taxes which is £0.15 per kWh. With a subsidy of 70%, the system becomes profitable with a positive NPV value of £137,387.2 and COE of £0.10 per kWh at the baseline real discount rate of 10%.

The main contribution of the thesis is that it provides an intergraded realistic tool that can simulate the future performance (thermodynamic and economic) of a hybrid

energy storage system, which can aid a potential investor to make informed decision on the profitability and financial outlays for the investment

Key words: Energy Storage, Renewable Energy, Gasifier, Net Present value, Cost of electricity, Hybrid Power System.

List of Publications from the thesis

Journal papers

1. Diyoke, C., Aneke, M., Wang, M. & Wu, C. (2018) Techno-economic analysis of wind power integrated with both compressed air energy storage (CAES) and biomass gasification energy storage (BGES) for power generation. *Royal Society of Chemistry Advances*, 8 22004-22022.
2. Diyoke, C., Gao, N., Aneke, M., Wang, M. & Wu, C. (2018) Modelling of down-draft gasification of biomass – An integrated pyrolysis, combustion and reduction process. *Applied Thermal Engineering*, 142 444-456.

Conference presentation

1. **Diyoke, C. & Wu, C.** (2017) Numerical studies of two charging modes of thermal energy storage (TES) for wind power: UK-China International Particle Technology Forum VI 201. Yangzhou China, 8-11 September 2017.

Dedication

This work is dedicated to God, the giver of knowledge and to my wife Ngozi and Children (Chiamaka Vannessa, and Ifechukwu Max)

Acknowledgments

I acknowledge the immense support I received from my Supervisor Dr. Chunfei Wu throughout the period of his supervision. With his motivation, encouragement, guidance and above all humane approach to issues, I was able to complete this thesis as well as publish some papers in scholarly academic journals of good repute. I look forward to future opportunities working with him.

I would also like to acknowledge the initial support I received from Prof Meihong Wang who was my supervisor until he left for the University of Sheffield at the beginning of my second year. I would also like to place on record the motivation and guidance of Dr Mathew Aneke throughout the duration of my PhD study.

The PhD study would not have been successful without the overall support, love and loyalty of my adorable wife (Ngozi Diyoke). She braved all the odds to make sure she took proper care of the family throughout the period of this PhD research. With her unflinching sacrifice and support, I was able to focus all my energy on the research work.

My daughter and son Chiamaka and Ifechukwu deserve special mention for the understanding they showed about my busy PhD lifestyle especially the weekends that I was supposed to be home to play with them but ended up spending in the school. Also, I want to acknowledge the total moral and financial support from my brother Engr. Innocent Diyoke. I owe all I am now to him

Lastly, I offer my thanks and blessings to my sponsors; the management and staff of Enugu State University of Science and Technology (ESUT), all the staff of the University of Hull including my PhD colleagues, and friends who in one way or the other has contributed towards the success of this PhD journey. May God richly bless you all

Table of Contents

Dedication	iv
Acknowledgments.....	v
List of Tables	xv
List of Figures	xvii
Abbreviations	xxi
Nomenclature	xxiii
Chapter 1 Need for renewable energy based distributed generation	1
1.1 Introduction.....	1
1.2 Energy storage technologies	5
1.2.1 Mechanical energy storage	5
1.2.1.1 Flywheel energy storage (FES).....	6
1.2.1.2 Compressed Air Energy Storage (CAES).....	6
1.2.1.3 Pumped hydroelectric storage (PHS).....	7
1.2.2 Electrical energy storage (EES).....	8
1.2.2.1 Capacitor	8
1.2.2.2 Super-capacitor energy storage (SCES).....	8
1.2.2.3 Superconducting magnetic energy storage (SMES)	8
1.2.3 Chemical energy storage (CES).....	9
1.2.3.1 Hydrogen energy storage (HES).....	9
1.2.3.2 Batteries energy storage (BESS).....	9

1.2.4 Thermal Energy Storage	10
1.2.4.1 TES storage media	11
1.2.4.2 Sensible heat storage (SHS).....	11
1.2.4.3 Latent heat storage (LHS).....	13
1.2.5. Thermochemical heat storage	14
1.3 Comparison of sensible, latent and thermal energy storage	15
1.4. Applications and selection of energy storage technologies	15
1.5 Motivation and innovation of the study	19
1.5.1 Motivation of the study	19
1.5.2 Operating principle of the proposed novel system	21
1.5.3 Innovation of the research.....	24
1.6 Research objectives.....	25
1.7 Thesis Structure	26
Chapter 2 Literature review on Compressed Air Energy Storage (CAES)	30
2.1 Introduction.....	30
2.2 Overview of compressed air energy storage.....	31
2.3 Classification of A-CAES.....	36
2.4 Review of previous work on CAES.....	38
2.4.1 CAES Configurations	38
2.4.2 Analysis methods	38
2.4.3 Different TES configuration/storage media.....	40
2.4.4 CAES hybrid configurations.....	41
2.5 Phase change thermal energy storage	44

2.5.1 Introduction.....	44
2.5.2 Materials	45
2.5.3 Classification of PCMs	45
2.5.4 Latent heat TES systems/modelling.....	49
2.6 Mathematical modelling of LH-TES systems.....	50
2.6.1 Single Phase model (SPM)	51
2.6.2 Two phase model (TPM)	51
2.6.2.1 Continuous solid phase models (CSFM)	51
2.6.2 .2 Schumann's model	52
2.6.2 3 The Concentric Dispersion model (CDM).....	53
2.7 Summary	58
Chapter 3 Modelling of PCM based thermal energy storage for A-CAES.....	59
3.1 Introduction.....	59
3.2 Two charging modes of A-CAES	60
3.2.1 Mode1	60
3.2.2 Mode2	61
3.3 Description of the PCM based TES tank unit.....	62
3.4 The thermal capacity of the TEST	64
3.5 Selected phase change materials.....	65
3.6 Previous models on LH TES based on CAES	66
3.7 Mathematical formulation.....	68
3.7.1 Assumptions.....	69
3.7.2 Governing mathematical equations for HTF and PCM.....	69

3.7.3 Boundary and initial conditions	72
3.8 Solution Method.....	74
3.8.1 Implicit difference equation formulation for the HTF.....	74
3.8.2 Discretizing the PCM equation	75
3.8.3 State judgment system (SJS).....	78
3.9 Estimation of model parameters	81
3.9.1 Density and thermal conductivity	81
3.9.2 The pressure drop along the bed	82
3.9.3 The overall heat loss coefficient (U).....	82
3.10 Performance metrics	84
3.11 Parametric analysis	86
3.12 Results and discussion	86
3.12.1 Grid independent study	86
3.12.2 Validation.....	88
3.12.3 Charging mode general charging behaviour	89
3.10.12.1 Temperature histories of the PCM and HTF.....	91
3.12.3.2 Stored and accumulated energy	94
3.12.4 Discharging mode general discharging behaviour.....	96
3.12.5 Energy and exergy efficiency	100
3.12.6 Parametric analysis results	104
3.12.6.1 Influence of packing height	104
3.12.6.2 Effects of number of multiple PCM.....	106
3.13 Conclusions.....	109

Chapter 4 Modelling of biomass gasification	111
4.1 Introduction.....	111
4.2 Overview of gasification.....	111
4.3 Classification of gasification reactors.....	112
4.3.1 Gasification agent	112
4.3.2 Heat source.....	113
4.3.3 Operating pressure	113
4.3.4 Reactor type	113
4.4 Fixed bed reactors.....	114
4.4.1 Updraft gasifier	114
4.4.2 Downdraft gasifier	115
4.4.3 The cross-draft gasifier	116
4.5 Fluidised bed gasifiers	117
4.5.1 Bubbling fluidised bed gasifier (BFBG).....	118
4.5.2 Circulating fluidised bed gasifier (CFBG).....	118
4.6 Entrained flow gasifier (EFG)	119
4.7 Review of biomass gasification simulation models.....	119
4.7.1 Thermodynamic equilibrium models.....	119
4.7.1.1 Stoichiometric equilibrium models.....	120
4.7.1.2 Non-stoichiometric equilibrium models	121
4.7.2 Kinetic rate models	122
4.8 Review on models on downdraft biomass gasification.....	124
4.9 Model development	126

4.9.1. Drying zone.....	128
4.9.2. Pyrolysis zone	129
4.9.2.1 Estimation of pyrolysis yields.....	130
4.9.3. Oxidation zone	132
4.9.4 Energy Balance	134
4.9.4.1. Energy balance of the pyrolysis zone	134
4.9.4.2 Energy balance of the oxidation zone.....	136
4.9.5 Reduction zone.....	138
4.9.5.1 Mass and energy balance equations.....	141
4.10 Performance parameters.....	143
4.11 Model validation	144
4.12. Results and Discussion	149
4.12.1. Temperature profile of the downdraft gasifier.....	149
4.12.2. Gas concentration profile.....	150
4.12.3. Influence of process parameters.....	153
4.12.3.1. Influence of air preheating.....	153
4.12.3.2. Effect of moisture content.....	155
4.12.3.3. Effect of equivalence ratio.....	158
4.13 Conclusions.....	161
Chapter 5 Thermodynamic analysis of integrated A-CAES and BMGES system	163
5.1 Introduction.....	163
5.2. Thermodynamic analysis	165
5.2.1 Energy modelling of system components	167

5.2.1.1 Dual fuel engine	167
5.2.1.2 Biomass Gasifier (BMG)	169
5.2.1.3 Hot Air Dryer (HAD) system	170
5.2.1.4 A-CAES sub system	172
5.2.2 Exergy analysis	178
5.2.2.1 Air Compressor (AC).....	179
5.2.2.2 Hot Air Dryer (HAD).....	179
5.2.2.3 Biomass Gasifier (BMG)	180
5.2.2.4 Dual Fuel Engine (DFE).....	182
5.2.2.5 Turbine/Air expander (AE).....	183
5.2.2.6 Heat exchangers (HXs).....	183
5.2.2.7 Throttle Valve	183
5.3 System performance metrics.....	183
5.3.1 Energy_efficiency	183
5.3.2 Exergy_efficiency_and_exergy_destruction.....	185
5.4. Results and discussion	186
5.4.1 Overall performance results	186
5.4.2 Sensitivity analysis results	194
5.4.2.1. Impact of TES round trip efficiency of the A-CAES	194
5.4.2.2. Impact of syngas temperature	195
5.4.2.3. Influence of the dual fuel engine exhaust temperature ...	196
5.4.2.4. Influence of heat exchangers' effectiveness	197
5.4.2.5. Influence of DFE syngas fraction	198

5.4.2.6. Impact of minimum operating pressure of the air store ..	199
5.4.2.7: Impact of reference temperature	200
5.5 Conclusions	203
Chapter 6 Economic Analysis of the Integrated System	205
6.1 Introduction.....	205
6.2 Economic modelling	205
6.2.1 Component cost estimation.....	206
6.2.2 Economic evaluation methodology.....	209
6.2.3 Electricity/heat buy and sell tariffs	214
6.3 Demand profiles.....	214
6.4 Results.....	215
6.5 Sensitivity analysis.....	217
6.5.1. Impact of cost factors.....	217
6.5.2 Impact of technical factors.....	220
6.5.2.1 Syngas fraction of the dual fuel engine.....	220
6.5.2.2 Capacity factor	221
6.5.2.3 Round trip efficiency	222
6.5.2.4 DFE exhaust gas temperature	223
6.5.2.5 Biomass gasifier syngas temperature.....	224
6.5.2.6 Number of households	224
6.6 Limitations of the study	226
6.7 Conclusions and recommendations.....	226
Chapter 7 Conclusions and further research	229

7.1 Main findings	232
7.2 Further research	237
7.2.1 Downdraft biomass gasifier model	237
7.2.2 Thermal energy storage model.....	238
7.2.3 Overall system model	238
7.2.4 Economic model	239
7.3 Outlook	239
Appendix 1. Correlations used in estimating fluid properties	241
1.1 Water vapour saturation pressure.....	241
1.2 Enthalpy of water	241
1.3 Constant pressure specific heat for water	242
1.4 Entropy of water	242
1.5 Constant specific heat for air	242
1.6 Enthalpy of air.....	242
Appendix 2. Detailed components investment cost	243
References.....	244

List of Tables

Table 1.1 Characteristics of various energy storage technologies (Aneke & Wang, 2016; World Energy Council, 2016).....	18
Table 1.2 Fluid/material making up the stream numbers of Figure 1.7.....	23
Table 2.1 Thermo physical properties of PCMs investigated for different applications (Agyenim et al., 2010)	48
Table 2.2 Desirable characteristics of PCM for TES application (Zalba et al., 2003)	49
Table 2.3 Comparison of Schumann's model, Continuous solid phase models and concentric dispersion model	57
Table 3.1 Operating characteristics of the two modes	64
Table 3.2 Selected PCM properties	66
Table 3.3 Computational decision of the SJS	80
Table 3.4 PCM arrangement (Ar) options for parametric analysis.....	86
Table 3.5 Stored energy at different computational grid.	87
Table 3.6 Thermo physical proprieties of the paraffin wax. (Benmansour et al., 2006) ..	88
Table 4.1 Characteristics of fixed bed gasifiers (Basu, 2010)	117
Table 4.2 Advantages and limitations of biomass gasification simulation models	125
Table 4.3 Ultimate and proximate analysis of rubber wood (Jayah et al., 2003)	144
Table 4.4 Comparison of predicted results with the experimental data (Jayah et al., 2003)	145

Table 4.5 The comparison of results from modified model with experimental data (Jayah et al., 2003)	146
Table 4.6 Comparison of results from modified model with experimental data (Altafini et al., 2003)	148
Table 5.1 Input design parameters for the system.	175
Table 5.2 Thermo physical properties of the PCMs (Pereira da Cunha & Eames, 2016).	177
Table 5.3 Biomass gasifier operating parameters and syngas composition.....	181
Table 5.4 Constant pressure specific heat of various gases (Borgnakke & Sonntag, 2009)	182
Table 5.5 Standard chemical exergy of different syngas gas components (Cengel & Boles, 2006)	182
Table 5.6 Energy and exergy efficiency of each component in the cycle	184
Table 5.7 Properties of each stream in the system.....	187
Table 5.8 Technical performance results for the integrated system	189
Table 5.9 Thermodynamic performance results for the components of the system	193
Table 6.1 Reference costs of equipment with their maximum size	209
Table 6.2 Main cost parameters of the integrated system.....	214
Table 6.3 Economic performance results for the integrated system.....	216
Table A1.1 Constants for entropy of water calculation	242
Table A2.1 Cost of major component of the integrated system	243

List of Figures

Figure 1.1 Classification of ES technologies (Morris & Cleveland, 2013; Luo et al., 2015)	6
Figure 1.2 Pumped hydro storage (Luo et al., 2015)	7
Figure 1.3 The three cycles in TES system.....	10
Figure 1.4 Methods of thermal energy storage (a) Sensible heat, (b) latent heat, (c) thermochemical reaction (de Gracia & Cabeza, 2015).....	11
Figure 1.5 Multiple PCMs in shell and tube LH TES unit	13
Figure 1.6 Real life applications and technology marching (Aneke & Wang, 2016).....	17
Figure 1.7 Integrated A-CAES and biomass gasification system (Diyoke et al., 2018a)..	22
Figure 1.8 Proposed integrated design model.....	27
Figure 2.1 Classification of CAES (Daniel, 2011)	31
Figure 2.2 Conventional CAES plant	32
Figure 2.3 Layout of adiabatic compressed air energy storage (Luo et al., 2016).....	34
Figure 2.4 Solar assisted CAES	36
Figure 2.5 Classification of PCM	46
Figure 2.6 Classification of commonly used PCM containers in terms of the geometry and configuration	50
Figure 3.1 Schematic of TEST showing two charging modes.....	60
Figure 3.2 Finite difference grid for the TEST	72
Figure 3.3 Grid points in the PCM.....	75

Figure 3.4 Node temperature vs. enthalpy for the SJS	79
Figure 3.5 Flow chart of solution method.....	81
Figure 3.6 Temperature histories of the HTF at different computational grids.....	87
Figure 3.7 Experimental vs. Model predicted temperature histories of the PCM	89
Figure 3.8 PCM surface temperature profile ($x=H/45$, $r=0$) VS charging time in the TEST.....	90
Figure 3.9 PCM outlet temperature at four locations of the TEST (a) top section , (b) middle section, (c) bottom section.....	91
Figure 3.10 Temperature distribution of the HTF along the TEST during charging.....	93
Figure 3.11 Stored and accumulated energy VS time.....	95
Figure 3.12 Heat loss during charging and discharging mode.....	96
Figure 3.13 Outlet temperature of PCM during discharge mode (a) Top section (T_s), $x=1$ (b) Middle section, $x=0.25L_s$ (Ms) (c) Bottom section (Bs), $x=0.5L_s$	98
Figure 3.14 Temperature map of HTF during discharging mode.....	99
Figure 3.15 Energy and exergy efficiency of charging mode.....	102
Figure 3.16 Energy and exergy efficiency of discharging mode	102
Figure 3.17 Overall energy and exergy efficiency.....	103
Figure 3.18 Temperature profile of PCM at height of $2L_s/3$	104
Figure 3.19 Energy and Exergy efficiency for various arrangements	105
Figure 3.20 Accumulated stored energy of 3PCM vs. 2PCM	106
Figure 3.21 Energy efficiency and Exergy efficiency of 3PCM vs. 2PCM	107
Figure 4.1 Updraft (a) and downdraft (b) biomass gasifier	114
Figure 4.2 Three zone downdraft gasifier(Diyoke et al., 2018b).....	127

Figure 4.3 Energy input/output for a pyrolysis process	134
Figure 4.4 Cross-section of the oxidation zone showing species input/output.....	137
Figure 4.5 Measured and predicted temperatures along RZ (Jayah et al., 2003)	147
Figure 4.6 Temperature profile of the zones of pyrolysis, oxidation and reduction of the reactor using biomass with different moisture contents (5, 10 and 20 wt.%).....	149
Figure 4.7 Gas concentration profile along RZ height	151
Figure 4.8 LHV profile along RZ height	152
Figure 4.9 Efficiency profile along RZ height at different temperatures	152
Figure 4.10 Influence of inlet air temperature on the concentration of product gas.....	154
Figure 4.11 Influence of temperature of inlet air on yield, CGE, LHV.....	155
Figure 4.12 Influence of moisture content on gas composition.....	156
Figure 4.13 Influence of moisture content on performance indicators	157
Figure 4.14 Influence of ER on the concentration of syngas.....	159
Figure 4.15 Influence of ER on CGE, Yield and CCE.....	161
Figure 5.1 Control volume of DFE showing energy and fluid flows	167
Figure 5.2 Hot air dryer system(Diyoke et al., 2018a)	170
Figure 5.3 A diagrammatic representation of the TEST (1-3).....	176
Figure 5.4 Impact of change in RTE on system performance	195
Figure 5.5 Impact of gasifier syngas temperature on the system performance	196
Figure 5.6 Impact of DFE exhaust temperature (Tex, DFE) on the system performance	197
Figure 5.7 Impact of heat exchanger effectiveness on the system performance	198
Figure 5.8 Impact of DFE syngas fraction on the system performance.....	199

Figure 5.9 Impact of air store minimum pressure on the system performance.....	200
Figure 5.10 Impact of reference temperature on Exergy destruction and exergy efficiency.....	202
Figure 6.1 Daily hourly electrical and thermal demand profiles for North Humberside (Diyoke et al., 2018a).....	215
Figure 6.2 Impact of economic factors on COE	218
Figure 6.3 Impact of economic factors on TLCC	219
Figure 6.4 Impact of variation of sf and CF on COE and TLCC.....	221
Figure 6.5 Impact of RTE of A-CAEs TEST on COE	222
Figure 6.6 Impact of EGT on COE and TLCC	223
Figure 6.7 Impact of syngas temperature on COE.....	224
Figure 6.8 Impact of NOHs on COE and NPV	225
Figure 6.9 Variation of NPV with sensitivity cost parameters	226

Abbreviations

A-CAES	Adiabatic compressed air energy storage
AC	Air compressor
AE	Air expander
A/F	Air fuel ratio
A-CAES+BMGES	Adiabatic compressed air and biomass gasification energy storage
AS	Air store
BMG	Biomass gasification/gasifier
BOP	Balance of plant
BY	Base year
CAES	Compressed air energy storage
CDM	Concentric dispersion model
CF	Capacity factor
CGE	Cold gas efficiency
CHP	combined heating and power
COE	Cost of electricity
CV	Calorific value
CY	Currency year
df	Diesel fraction
DFE	Dual fuel engine
ER	Equivalent ratio
Ff	Frequency factor
HAD	Hot air dryer
HHV	Higher heating value
HTF	Heat Transfer fluid
HX	Heat exchanger
HV	Heating value
LHV	Lower heating value

LMTD	Logarithmic mean temperature difference
MC	Moisture content
Mm	Molar mass or weight
NPV	Net present value
OZ	Oxidation zone
PCM	Phase change material
PESR	primary energy saving ratio
PZ	Pyrolysis zone
RTE	Round trip efficiency
RZ	Reduction zone
sf	Syngas fraction
SGS	Syngas store
TES	Thermal energy storage
TEST	Thermal energy storage tank
TET	Turbine or air expander exit temperature
TIC	Total investment cost
TIT	Turbine or air expander inlet temperature
TLCC	Total life cycle cost
TSE	Total system efficiency

Nomenclature

Symbols

a	specific heat constant ($\text{Jmol}^{-1}\text{K}^{-1}$)	N_f	mass fraction of nitrogen in fuel
adb	Air dry basis	Nu	Nusselt number
A	Area (m^2)	O	Mass fraction of oxygen in fuel
b	specific heat constant ($\text{Jmol}^{-1}\text{K}^{-1}$)	P	Power (kW)
Bi	Biot number	P	pressure (Pa)
C_w	circumference of TEST wall (m)	P_C	power output by A-CAES (kW)
C_p	Constant pressure specific heat ($\text{J kg}^{-1} \text{K}^{-1}$)	$P_{e,DFE}$	Rated electrical output of DFE (kW)
C	Mass fraction of carbon in fuel (%)	Pe	Peclet number
D	Diameter of capsule (m)	Pr	Prandtl number
D	Diameter of TEST (m)	Q_{air}	Flow rate of air (m^3/s),
\dot{D}_{ex}	Depletion number (%)	Q_{dry}	Heat to dry away moisture (Jmol^{-1})
E	Activation energy (kJkmol^{-1})	$Q_{l,p}$	Heat loss in pyrolysis zone (Jmol^{-1})
En	Energy (W)	$Q_{l,ox}$	Heat loss in oxidation zone (Jmol^{-1})
Ex	Exergy of stream (W)	R	Gas constant($\text{Jmol}^{-1}\text{K}^{-1}$)
Eff	Efficiency (%)	$r_{R,i}$	Rate of reaction ($\text{molm}^{-3}\text{s}^{-1}$) for i^{th} reaction
f_{uf}	storage material utilisation coefficient	Rt	Rate of production ($\text{molm}^{-3}\text{s}^{-1}$)
G	superficial mass velocity ($\text{kg s}^{-1} \text{m}^{-2}$)	V	Gas velocity (m/s)
Ff	Frequency factor for reaction(s^{-1})	W	Amount of moisture (mol^{-1} of wood)
h^\cdot	Molar specific enthalpy ($\text{Jmol}^{-1}\text{K}^{-1}$)	P	Partial pressure (Pa)
$\dot{h}_{f,B}$	Heat of formation of biomass ($\text{Jmol}^{-1}\text{K}^{-1}$)	q_i	Power input (W)
H	Weight percent of hydrogen in fuel (%)	q_e	Power output (W)
H	Height (m)	$q_{l,p}$	Pump Power (W)
HV	Heating value (MJkg^{-1})	Q_l	Heat loss (W)
H	Enthalpy (kJkg^{-1})	q_s	Power stored (W)
$\Delta\dot{h}_f$	Enthalpy of formation (Jmol^{-1})	Q_{Th}	Thermal power (W)
$\Delta\dot{h}_v$	Heat of vaporization of moisture (Jmol^{-1})	r_p	PCM radius m (m)

h_c	heat transfer coefficient between fluid / particle ($W m^{-2} K^{-1}$)	R_{conv}	Convective thermal resistance ($W^{-1} m^2 K^1$)
h_p	heat transfer coefficient between fluid / particle ($W m^{-2} K^{-1}$)	R_{cond}	Conductive thermal resistance ($W^{-1} m^2 K^1$)
h_{ef}	Effective heat transfer coefficient between fluid / particle ($W m^{-2} K^{-1}$)	Re	Reynolds number
$h_{ef,m}$	effective heat transfer coefficient ($W m^{-2} K^{-1}$)	R	universal gas constant ($kJmol^{-1}K^{-1}$)
h_w	heat transfer coefficient between fluid / ($W m^{-2} K^{-1}$)	RH	relative humidity (%)
h_v	Volumetric heat transfer coefficient ($W m^{-3} K^{-1}$)	S	entropy (kJ)
H	Enthalpy, (Jkg^{-1})	S	mass fraction of sulphur in fuel
k_{ef}	effective thermal conductivity ($W m^{-1} K^{-1}$)	T	temperature of the liquid phase °C
K	thermal conductivity of the solid ($W m^{-1} K^{-1}$)	U_w	overall wall heat transfer coefficient ($W m^{-2} K^{-1}$)
L	Latent heat (Jkg^{-1})	V	Volume (m^3)
L	Length/Height (m)	v_a	interstitial fluid velocity (ms^{-1})
L_s	Length/Height of section (m)	\dot{W}	Power (W)
LHV	lower heating value ($kJkg^{-1}$)	x_p	PCM thickness (m)
LHV _{sg}	Syngas lower heating value ($MJ(Nm^3)^{-1}$)	X	axial coordinate (m)
\dot{m}	mass flow rate ($kg s^{-1}$)	\dot{X}	Exergy destruction (kW)
m_{PCM}	Mass of PCM (kg)	\dot{X}_{dp}	exergy destruction proportion
M_m	molar mass ($kgmol^{-1}$)	Z	axial coordinate (m)
MC	Fuel moisture content (wt.%)		
n	No of moles or molar flow rate		
N	No of moles/Engine speed (RPM)		
n_k	is the molar fraction of the k-th specie		

Subscripts

A	Air/HTF	N	year
AC	Air compressor	O	Out/outlet/overall
AE	Air expander	O&M	Operation and maintenance
Amb	ambient	O	restricted dead state
Ave	average	0	Overall
B	Biomass	Ph	physical
C	cold	P	Capsule/PCM

Ch	Chemical/charge	R	Real
cr	convection and radiation	Recup	Recuperation
cv	Control volume	Ref	Reference
Dch	discharge	RH	Percentage relative humidity (%)
Db	Dry basis	S	Sensible/solid
Df	Diesel fuel	Sf	Syngas fraction
Dch	discharge	Sg	Syngas/product gas
E	Electrical/electricity/ Exit/outgoing	S	stored
Ex	exhaust	T	Time (sec)
Ev	evaporation	T	total
HA	Hot air	Th	thermal
HX	Heat exchanger	V	volumetric
I	Initial/entering/Input/inlet/in	W	Water/moisture
Isen	isentropic	Wb	Wet basis
Insu	Insulation	WT	Wind turbine
L	liquid	\dot{W}	Work rate or electricity (kW)
M	Mechanical/melting	W_w	mass fraction of moisture in the biomass,
Min	minimum	X	Reaction number
Max	maximum	Vol	Volumetric
Mc	No of atoms of carbon	W	Wet/moisture
Mh	No of atoms of hydrogen	Wb	Wet basis
Mo	No of atoms of oxygen	Wv	Water vapour
Greek letters			
β	stage pressure ratio	η	efficiency
ϵ	Porosity/void fraction	η_T	Total system efficiency
E	effectiveness	η_E	Efficiency of production of electricity only
θ	temperature of the PCM ($^{\circ}\text{C}$)	η_{ee}	Effective electrical efficiency
γ	Ratio of specific heats	η_{ex}	Total exergy efficiency
ρ	density (kgm^{-3})	η_H	Efficiency of production of heat only
η	efficiency	η_{rE}	the reference efficiency value for electricity
η_m	Mechanical efficiency	η_{rH}	reference efficiency value for heat production
α	Thermal diffusivity (m^2s^{-1})	$\eta_{O,DF}$	Overall efficiency in dual fuel mode
μ	Viscosity of air ($\text{kgm}^{-1}\text{s}^{-1}$)	B	Biomass exergy coefficient
$\eta_{O,DF}$	Overall efficiency in dual fuel mode	Ψ	Specific exergy (kJkg^{-1})
φ	moisture ratio in kg per kg dry air	Ψ	specific fan power ($\text{kWm}^{-3}\text{s}^{-1}$)

Chapter 1

Need for renewable energy based distributed generation

This chapter introduces the research background. Section 1.1 updated current status of Energy storage. Section 1.2 highlights the motivations and innovation of this study. Section 1.3 summarises the aim and objectives and Section 1.4 outlines what is covered in each chapter.

1.1 Introduction

Availability and affordability of energy is one of the precursors for development. The demand for this vital resource continues to increase yearly across the globe because of rapid population and economic growth. However the economic growth is not inclusive, as many people from developing countries especially those from the rural areas still suffer from daunting energy and economic poverty due to a complete lack of access or a prohibitively high cost of energy as the case may be. In sub-Saharan Africa, electricity costs are as high as 0.2-0.55\$/kWh against a global average of about 0.1\$/kWh (Indrawati, 2015). Countries with even high access to electricity frequently have extremely unreliable service. An all-encompassing economic growth is the single most effective panacea for reducing poverty and boosting prosperity. Yet most economic activity is impossible without sufficient, dependable and competitively priced modern energy.

Decentralized energy generation through distributed generation (DG) has been identified as a promising way to electrify the rural areas and make electricity affordable to the rural dwellers. In some situations, DG can serve as a standby power for emergency utilization like in hospitals and data centres (Zhang et al., 2017). The approach involves the deployment of small scale electricity generation technologies to generate electricity close to the area of power demand thus avoiding the problems of losses and cost of a complex electricity distribution and transmission grid infrastructure. Other attractive potential benefits include; lower-cost of electricity, higher reliability and security with

fewer environmental consequences compared to the traditional power generators (Corfee et al., 2014). The capacity of DG technologies ranges from small kilowatt (kW) to about 100 megawatts (MW). Some examples of DG technologies include modular generators (Reciprocating Engines, Fuel cells, Gas turbines, coal plants) and renewable energy systems (wind turbine, solar hydro Power, and Biomass) (Corfee et al., 2014; Zhang et al., 2017).

Apart from the rural areas and isolated communities of developing countries, DG has also been proposed to play a key role globally. In the UK, DG is seen to hold the key towards the development of the low carbon energy technologies (ETI, 2012). The DTI Centre for Distributed Generation and Sustainable Electrical Energy in their report titled “Integration of Distributed Generation into the UK Power System” opined that “*a sustainable power system of the future is likely to comprise of a varied collection of generation technologies including both DG and conventional generation, quite unlike the present system, and that this will require substantial alteration in system arrangements*” (Strbac et al., 2007).

Previously, the commonly employed DG technology is the reciprocating engines, generating electricity in the range of kW to several MW (Diyoke et al., 2014). However, generation of energy using fossil fuels has been implicated as a chief source of the global emission of carbon dioxide (CO₂), a major anthropogenic greenhouse gas (GHG) that causes global warming. To reduce these greenhouse gases means to reduce the rates of the production from their sources. Three distinct options for this are (Leung et al., 2014):

- Improvement in energy efficiency and promotion of energy conservation.
- Increase in use of low carbon fuels, including natural gas, hydrogen or nuclear power.
- Deployment of renewable energy (solar, wind, hydropower and biomass) and CO₂ capture and storage (CCS).

Wind power has a huge role to play among the renewables due to its established technology, wide availability, good scalability and relatively low cost with estimated levelized cost of electricity (LCOE) below \$34 per MWh for onshore wind compared to \$54 per MWh for large, ground-mounted PV in the United States at 3% discount factor

(IEA, 2015). Many wind energy system have been installed worldwide. At the end of 2017, 52GW of wind power was installed across the globe bringing the cumulative global installed capacities of wind turbine to 539 GW (GWEC) with the highest installations of 19.7 GW of new capacities taking place in China (GWEC, 2018).

Despite the growing global status of wind as one of the most reliable renewable energy source, there are some barriers that have to be overcome in order for wind to become more competitive and assume its potential dominant role in the energy mix. One of the existing barriers is the intermittency of wind as an energy source making it difficult to properly size a wind energy system to be able to match demand with supply. In addition, in comparison to conventional energy sources, wind and other renewable energy (RE) sources are less competitive due to their dependence on weather, and high initial cost (Baños et al., 2011). In order to overcome this barrier and to provide an economic, reliable, and sustained supply of electricity, energy storage (ES) has been identified as a key solution (Eyer & Corey, 2010; Luo et al., 2015); helping to time shift supply from time of excess wind electricity generation to time of insufficient electricity supply or excess demand, increase the robustness and reliability of power systems, reduce the instability in energy markets and optimize the use of current and future assets (Mendoza, 2014).

Among many energy storage technologies, adiabatic compressed air energy storage technology (A-CAES) has been recognized as a viable option. Up until recently, most of the research papers relating to the wind-energy storage system have focused on the standalone energy storage systems.

A possible technological alternative for increasing the versatility and performance of a wind electricity powered adiabatic compressed air energy storage (A-CAES) system is to design a DG systems with different types of sources, whose generation features must complement each other (Loh et al., 2013). Although there is no assurance that a non-variable stream of energy will continually be produced if the sources are commonly uncontrollable like RE sources. For a better control, energy storage seem to be inevitable, although their capacity can be reduced if there are multiple source types in the systems (Loh et al., 2013). The energy storage installed need not be of similar type. Instead, they could be designed with a variety.

Biomass gasification energy storage system is an attractive technology for combination with A-CAES. This is because biomass gasification is a renewable energy power source with waste heat that can benefit a wind A-CAES system and also provide heat energy for providing domestic hot water as well as low temperature heating needs.

The technology of biomass gasification is gaining popularity lately due to the increasing exploitation and utilization of renewable energy sources for power generation. Besides, the product gas from gasification consisting of mainly a mixture of hydrogen and carbon monoxide, is one of the most attractive substitutes for natural gas for use in distributed combined heat and power (CHP) and tri-generation system for meeting combined cooling, heating and power (CCHP) (Ahrenfeldt et al., 2013). Downdraft gasifiers are fit for small to medium-sized applications. This technology has a fairly efficient biomass to gaseous fuel conversion and produces syngas with relatively low amounts of tar that is suitable for direct use in internal combustion engines (Reed & Das, 1988). Hence, a fixed bed downdraft biomass gasifier is considered to be the most suitable in this case.

A wind A-CAES system integrated with downdraft biomass gasification energy storage system is an important trend since it alleviates the dependence on fossil fuels and can produce two useful streams of energy (electricity and heat). In fact, it has the potential to eliminate some of the obstacles to biomass and wind based electricity generation, including wind intermittency, the high cost of fuel transport and remote location of high wind and low-cost biomass resources. Before now, large scale A-CAES has been the focus of researchers. The combined effects of high transportation costs of biomass, low population in the local communities and the intermittent nature of wind are expected to limit the size of hybrid energy system consisting of A-CAES and BMGES system.

Hence, a small integrated adiabatic compressed air energy storage and biomass gasification energy storage (A-CAES+BMGES) system for DG can offer higher reliability to maintain continuous stable power output even in the situation of large load fluctuation and it could make the DG generation units more flexible to be used just like as fossil powered plants on a dispatchable basis, allowing generation to match demand.

1.2 Energy storage technologies

Energy storage (ES) involves storing electricity when it is in excess or not needed for use when it is needed usually during peak periods. Energy storage (ES) is seen as an essential tool for smart, future electricity grids and in fact, it has the potential to provide tremendous benefits across the energy delivery value chain—from generation to transmission and distribution. It has been tipped to play a key role in ensuring renewable generation integration to the grid (Eyer & Corey, 2010).

So many benefits are derivable with the deployment of wind electricity storage technologies; increased electrical energy availability/capacity in high demand periods, greenhouse gas (GHG) emissions reduction, increased power quality, availability and reliability improvement, system stability, cost reduction for wind generated electricity, increase of annual capacity factor, more even distribution of electricity production, full load operation of the thermodynamic cycle at high efficiency etc. (Luo et al., 2015)

A good number of electrical energy storage technologies exist. They can be classified in various ways such as: in terms of their functions, form of energy stored, response times, and suitable storage durations (Luo et al., 2015). Classification based on form of energy stored in the system is the most widely used method. Based on this, ES can be classified into mechanical, electrochemical, electrical, thermochemical (solar fuels), chemical and thermal energy storage as in Figure 1.1 (Chen et al., 2009; ULB, 2010; Evans et al., 2012; Morris & Cleveland, 2013; Indrawati, 2015; Luo et al., 2015; Aneke & Wang, 2016 and Zhang et al., 2017). A brief discussion of each type of ES technology will follow in the following section. Detailed information of ES technologies can be found in the literatures (Morris & Cleveland, 2013; Luo et al., 2015).

1.2.1 Mechanical energy storage

Mechanical energy storage involves a change in the potential or kinetic energy state of matter. Mechanical storage options include but are not limited to compressed air energy storage (CAES), pumped hydro storage (PHS) and flywheel energy storage (FES). These devices deliver a great amount of power. Some mechanical energy storage methods have a high storage capacity and low power capability that are more suited in load levelling

applications in electric utilities. CAES is an example of one such technology (Copeland, 1983).

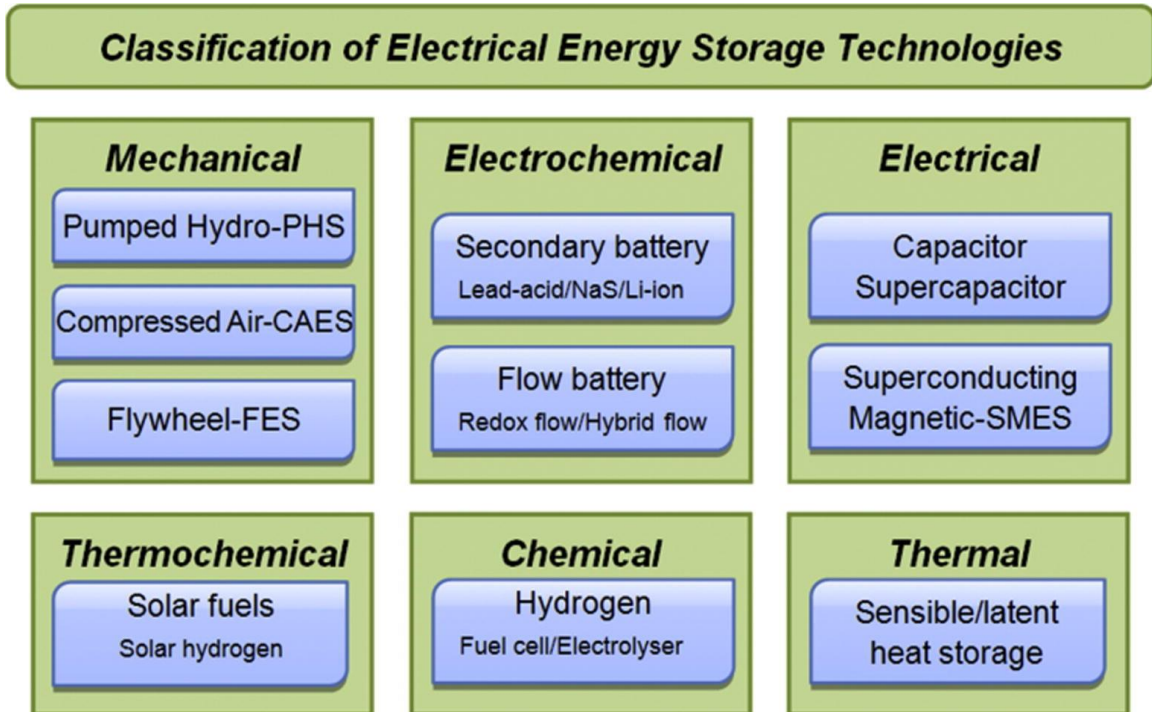


Figure 1.1 Classification of ES technologies (Morris & Cleveland, 2013; Luo et al., 2015)

1.2.1.1 Flywheel energy storage (FES)

FES store electrical energy as kinetic energy in rotating discs or cylinders suspended on magnetic bearings. They are suitable for applications that require high power for short periods and require slight maintenance, in comparison to other ES technologies. FES accelerates and decelerates when it is charging and discharging, respectively. The quantity of stored energy depends on the rotating speed of flywheel and its inertia. They can be categorized into two sets: (1) low speed FES systems typically used for short-term and medium/high power applications and (2) high speed FES systems applied mainly in high power quality and ride-through power service in traction and the aerospace industry (Luo et al., 2015).

1.2.1.2 Compressed Air Energy Storage (CAES)

CAES systems deploy excess or off-peak electricity to power a compressor to compress air, storing it in above ground tanks or underground caverns/salt domes or

aquifers. The stored high pressure compressed air is later released to an air expander where it expands to generate the electricity during peak/ periods of demand. Its operation is based on the operation of a conventional gas turbine generator. Detailed description of this technology will be found in chapter two on literature review.

1.2.1.3 Pumped hydroelectric storage (PHS)

PHS is one of the commercialised ES technology that can be used in MW scales. It accounts for more than 99% of global bulk storage capacity and contributes to about 3% of global generation (Luo et al., 2015). It comprises of two water reservoirs separated vertically; the upper reservoir is higher than the lower one as in Figure 1.2. During charging mode, the water is pumped from the lower reservoir to the upper reservoir and it is stored in form of potential energy. During discharging mode, water flows down into the lower level reservoir. In the process, the kinetic energy of the water powers turbine units coupled to a generator to generate electricity. The magnitude of stored energy is dependent on the change in height between the two reservoirs and the total volume of water stored. Pumped hydro (PHS) have a benefit of higher degree of reversibility but disadvantages include non-negligible energy losses and substantially large space requirements for grid scale storage.

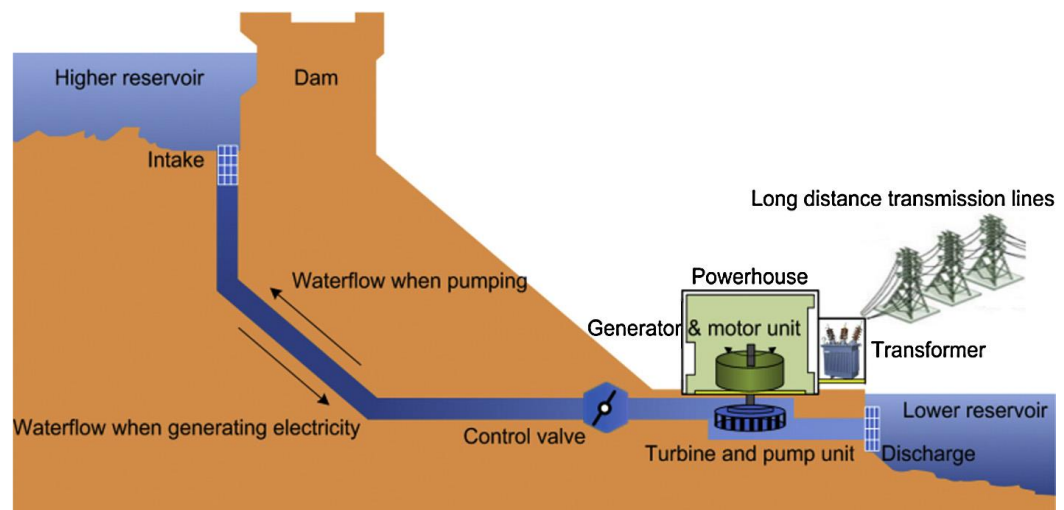


Figure 1.2 Pumped hydro storage (Luo et al., 2015)

1.2.2 Electrical energy storage (EES)

EES store excess or off-peak electricity either in an electric or magnetic field; later it can give the stored energy back. The key technologies are capacitors, super capacitors energy storage (SCES) and superconducting magnetic energy storage (SMES)

1.2.2.1 Capacitor

Capacitor is made of two close conductors (usually plates) that are separated by a dielectric material. During charging, the plates accumulate electric charge when connected to power source. One plate accumulates positive charge and the other plate accumulates negative charge. The maximum operating voltage of capacitors depends on the dielectric material breakdown features. Capacitors are suitable for storing small amounts of electrical energy. They have a higher power to weight ratio and smaller charging time in comparison to conventional batteries (Luo et al., 2015). However, they suffer from relatively low energy density, limited capacity, and high energy dissipation as a result of the high self-discharge losses

1.2.2.2 Super-capacitor energy storage (SCES)

SCES systems are also referred to as ultra-capacitors or double-layer capacitors. It works in the same way as traditional capacitors. It contains two conductor electrodes, an electrolyte and a porous membrane separator. Though, it is made up of electrochemical cells like in a battery, but no chemical reaction takes place within it. Instead, the cells form a double capacitor, more powerful than a traditional one. Owing to their structures, SCES can possess both the features of traditional capacitors and electrochemical batteries (Luo et al., 2015). The electricity is stored in the form of static charge on the surfaces between the electrolyte and the two conductor electrodes (Luo et al., 2015).

1.2.2.3 Superconducting magnetic energy storage (SMES)

SMES stores off peak electricity in a magnetic field formed by a direct current (DC) in the superconducting coil that has been cooled cryogenically to a temperature below its superconducting critical temperature (Luo et al., 2015). It consists of three main elements; (1) a superconducting coil unit, (2) a power conditioning subsystem, and (3) a refrigeration and vacuum subsystem. During discharging, the SMES system releases the stored electrical energy back to the Alternating Current (AC) system, by a connected power converter

module. The magnitude of stored energy is dependent on the current flowing through coil and its self-inductance.

1.2.3 Chemical energy storage (CES)

Chemical energy storage (CES) stores electrical energy in chemicals by means of chemical reactions; electricity is either produced from storage or the storage is charged by electricity (Copeland, 1983). CES technologies include batteries, fuel cells and chemicals (e.g., hydrogen energy storage) produced from electricity but used to produce heat or another form of energy.

1.2.3.1 Hydrogen energy storage (HES)

HES systems use two separate method for storing energy and producing electricity namely: through natural gas and by electrolysis of water. The method of electrolysis of water is a common way to produce hydrogen. The produced hydrogen is stored (in big quantities unlike electricity) in high pressurised containers and/or transported by pipelines for future use in fuel cells, where the chemical energy of the stored hydrogen is converted back to electricity

1.2.3.2 Batteries energy storage (BESS)

BESS system operates based on a chemical reaction that takes place in a cell powered by two electrodes (cathode and anode) and plunged into an electrolyte. There are numerous battery technologies, each with distinct chemical reaction that determines its mode of operation. Moreover Batteries can be broadly used in diverse applications, such as power quality, energy management, ride through power and transportation systems (Luo et al., 2015). Some of the best-known technologies are Sodium–sulphur (NaS) batteries, Lithium-Ion, Lead-Acid, Nickel-Cadmium, among others. A resurgence of research in battery technology has been taking place lately due to the increasing interest in ES. Batteries can possibly store huge amounts of energy per unit weight. Batteries and capacitors have the advantage of directly storing the final usable form of energy i.e. electrical energy, but have disadvantages of high costs (Edwards et al., 2016).

1.2.4 Thermal Energy Storage

Thermal energy storage (TES) involves using the heat capacity of a solid, liquid, or phase-change medium to store electrical energy in the form of thermal energy through cooling or heating a storage medium in order that the stored energy can be utilised at a later time either for power generation, cooling or heating applications (IRENA, 2013). TES devices mainly employ relatively inexpensive media, but containment and heat exchangers are expensive (Copeland, 1983). Thus, the current research on TES focus on those areas. TES has the capability to reduce the demand of fossil fuel energy sources for two reasons: First, they help to avoid the disparity in electricity supply and the power demand when generating electricity from RE sources. Secondly, use of waste heat generated from industrial processes by TES decreases the final energy consumption

TES systems can be classified as active or passive types (Kuravi et al., 2013). In active systems, the heat storage medium is a fluid and flows between the storage tanks. If the storage medium serves also as the heat transfer fluid (HTF), the system is referred to as direct-active system (Kuravi et al., 2013). The two tank system and thermocline systems are active TES systems. In indirect active storage, the heat storage fluid and HTF are different and a heat exchanger is required. In passive TES system, the storage medium is a solid and the HTF passes through the storage material only for charging and discharging (Kuravi et al., 2013). The packed bed is an example of passive TES system.

Three steps make up a complete TES process (Dincer & Rosen, 2011): charging, storing and discharging as illustrated in Figure 1.3

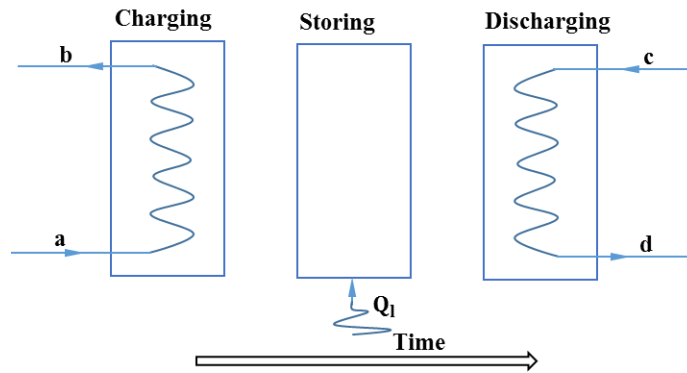


Figure 1.3 The three cycles in TES system

In the illustration, the three steps are shown distinct but in practical systems, the steps may overlap and each step may occur more than once in each storage cycle (Dincer, 2002). To charge the store, the electrical energy is added in the form of heat (Q_i) from a high temperature heat source (a-b) which leads to a temperature rise in the TES media store. To discharge the TES media, high heat source stored in the store is released to a lower temperature (c-d) heat transfer fluid which is then converted to electricity using a heat engine. TES is applied in diverse fields including power generation, space heating/ cooling, industrial process heat as well as the management of vehicles thermal energy processes.

1.2.4.1 TES storage media

Any material used to store thermal energy is called a TES media. The process can be classified as: (a) sensible heat storage (SHS) (b) latent heat storage (LHS) and (c) thermocline heat storage (THS) system as in Figure 1.4

1.2.4.2 Sensible heat storage (SHS)

Sensible heat storage (SHS) (Figure 1.4a) involves storing the electrical energy as thermal energy by heating or cooling a liquid or solid storage medium like water, oils, stone, sand, concrete, packed bed of alumina, molten salts, rocks etc.(IRENA, 2013). The most critical parameters for this kind of storage are density and specific heat; nevertheless other vital factors are operational temperatures, thermal conductivity and diffusivity.

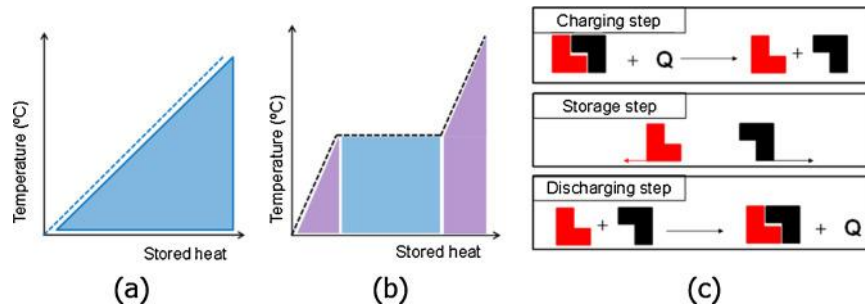


Figure 1.4 Methods of thermal energy storage (a) Sensible heat, (b) latent heat, (c) thermochemical reaction (de Gracia & Cabeza, 2015)

The quantity of energy (Q) stored during charging process in a SHS can be calculated as follows (Ferruzza, 2015):

$$Q = \int_{T_i}^{T_e} V\rho C_p(T)dT \quad (1.1)$$

Where T, V, ρ, C_p denote temperature (K), volume (m^3), density (kgm^{-3}) and constant pressure specific heat ($kJkg^{-1}K^{-1}$) respectively and subscripts i and e denote initial and final state of the storage media.

During this form of energy storage, the material used for storage does not undergo any form of phase change within the temperature range of application (Aneke & Wang, 2016). Thus the main focus during the design of SHS TES (STES) is on the selection of appropriate storage materials and their characteristics in satisfying desired requirements. Typically STES media are sub-divided into two main groups, solid storage media (concrete stone, steel, cast ceramics etc) and liquid storage media (water, molten salts, mineral and synthetic oils etc). Solid media are mostly favoured for building applications and likewise in some specific cases of high temperature solar applications (Ferruzza, 2015). The core benefits of such systems are: They are cheap and viable at very high temperatures, without the risks inherent in the use of toxic materials. Moreover, the storage media in SHS is contained in containers as bulk material, thus easing the system design. The foremost disadvantage of SHS systems is its low energy density thus making it require a very high volume of storage vessel to store a given amount of energy (de Gracia & Cabeza, 2015).

Water is the sensible heat storage (SHS) of choice for low to medium temperature applications (Hasnain, 1998). This is because it has one of the highest specific heat contents of any liquid at ambient temperatures. Though, its specific heat is not as high as that of many solids, it has the advantage of being a liquid, allowing heat to be pumped around. It also allows good heat transfer rates. Oils are suitable for medium to high temperature applications while solids are deployed for both low and higher temperature applications and have the advantage of taking up a smaller storage space because of their higher specific heat capacities (Hasnain, 1998). Gaseous media are not considered for heat storage purposes because of their very low volumetric heat capacity at ambient pressure (Daniel, 2011). However, Liquid and solid states offer clear advantages of higher volumetric heat capacities (Dincer, 2002; Daniel, 2011).

1.2.4.3 Latent heat storage (LHS)

Latent heat TES (LHS) involves storing latent heat which occurs as a result of phase change in the storage media. The process occurs at constant temperature and can comprise the latent heat of phase change during fusion (solid-liquid transition) and latent heat of vaporization (liquid-vapour transition). The storage media that is applied to store energy during LHS are called Phase change materials (PCM). Storage of heat through LHS can provide improved heat transfer and storage capability compared to SHS. Its main advantage is a higher storage density due to the high latent heat associated with the phase change (Ferruzza, 2015). For energy storage modelling application, the phase transition temperature (usually from solid to liquid) is made to match with the temperature of the heat source (T_{HS}). The stored heat in a LHS process is mainly dependent on the mass, the latent heat and sensible heat of each material as follows:

$$Q = \int_{T_i}^{T_m} V\rho C_p(T)dT + V\rho L + \int_{T_m}^{T_e} V\rho C_p(T)dT \quad (1.2)$$

Where L is the latent heat of melting or solidification of the PCM in (kJkg^{-1}) and subscripts m denote melting.

LHS system can be classified as single PCM system or cascaded systems wherein multiple PCMs are employed. When employing multiple PCMs, it is vital to select the appropriate PCMs and relative proportions of the PCMs (Kenisarin, 2010). The multiple PCMs should be arranged in the containing vessel in the decreasing order of their melting points such that the PCM with the highest melting temperature lie first in the HTF flow direction and the melting temperature decreases in the charging process and increases in the discharging process (Kenisarin, 2010) as illustrated in Figure 1.5

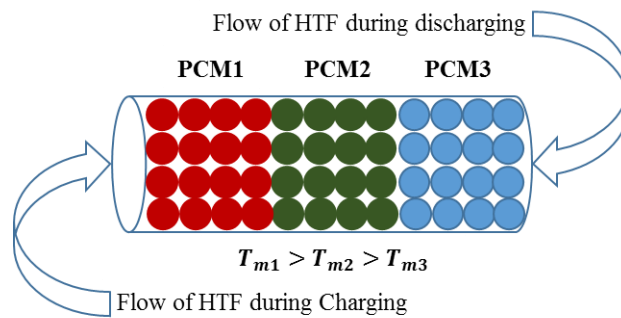


Figure 1.5 Multiple PCMs in shell and tube LH TES unit

Published research from numerous scholars (Gong & Mujumdar, 1996; Gong & Mujumdar, 1997b; Chiu & Martin, 2013; and Aldoss & Rahman, 2014) converged that cascade PCMs are better than single PCMs for heat storage applications. This is because the charging rate in the TES unit is primarily dependent on the difference in temperature between the PCM and the HTF. For a single PCM design, the temperature difference drops in the direction of flow of the HTF, which leads to a decrease in heat transfer rate and hence poor performance. For a cascade design, as shown in Figure 1.5, the temperature difference can be kept at an approximate constant value since for the charging and discharging processes, both the temperature of the HTF and PCM are decreasing and increasing respectively in the direction of the HTF flow. Consequently, the heat flux from the PCM to the HTF is approximately constant.

A good number of work has been published on studies related to employing multiple PCMs in different configurations of LH TES units (Farid & Kanzawa, 1989; Gong & Mujumdar, 1996; Gong & Mujumdar, 1997b; Chiu & Martin, 2013 and Aldoss & Rahman, 2014). The authors (Farid & Kanzawa, 1989) used three PCMs of different melting points packed in cylindrical capsules with air as the HTF. They reported a 10% increase in heat transfer rate during both charging and discharging with three PCMs since the onset of melting/solidification was simultaneous in all three PCMs units, whereas in single PCM design, the onset of the phase change was not simultaneous but started at different times

1.2.5. Thermochemical heat storage

Thermo-chemical storage (TCS) involves storing and releasing the thermal energy by means of reversible chemical reactions as represented by Eq.1.3 (Hasnain, 1998; IRENA, 2013; Edwards et al., 2016) in which heat is stored during the endothermic reaction step and released during the exothermic step. Owing to the possibility of storing the compounds separately without the loss of energy, TCS is appropriate for thermal energy storage over large period of times. This concept is still in the early stage of development and thus it has high costs (Ferruzza, 2015). Nevertheless this technology is actually attractive and promising owing to the fact that it has much higher density compared to SH

TES and LH TES. Additionally, with future development the cost can significantly come down.



In the reversible forward exothermic reaction above, A is the thermochemical material. With heat supply, A dissociates into components C and D, which can be at any phase and stored separately. During discharge, a reverse endothermic reaction between C and D takes place, giving back the stored heat.

1.3 Comparison of sensible, latent and thermal energy storage

Thermal energy storage has a low thermal to electrical energy efficiency of conversion but can be improved with heat recovery from waste heat sources like nuclear power plants, coal power plants and parabolic trough (Edwards et al., 2016). In general, PCMs used in LHS have poor thermal conductivities and therefore need special heat exchangers to increase the rate of heat transfer between the heat transfer fluid and PCMs and this leads to increase in the whole system cost. Sensible heat storage is moderately cheaper than LHS and TCS systems. However, its low energy density (three and five times lower than that of PCM and TCS systems, respectively) means more storage volume is required per kWh compared to PCM and TCS systems respectively (IRENA, 2013). In addition, LHS has the following advantages against SHS

- Large energy density i.e. low weight per unit storage capacity
- Adaptable to conventional structural mass while SHS requires a larger mass to store the same amount of energy;
- Storage of energy within a narrow temperature change, hence big temperature variation is circumvented;
- More efficient energy management

1.4. Applications and selection of energy storage technologies

The critical factors that should be considered before selecting any of the ES technologies for any applications areas are: round trip efficiency (ratio of energy charge in (MWh) to energy retrieved from storage (MWh)), durability, environmental impact, cost,

energy capacity, depth of discharge (DOD), discharge time, power rating, self- discharge, energy and power densities (Kousksou et al., 2014). Comparison has been made of the various ES technologies using these parameters as yardstick. Figure 1.6 matches real life applications with efficiency, discharge time and power requirement of application for different ES technologies. As can be observed, ES systems can be used to provide the following services; maintain power quality by adjusting supply to changing demand, time shift production to match demand by storing surplus electricity in ES system and using it when necessary. Other services include ancillary services, intermittent balancing, operating reserve, power fleet optimization, energy arbitrage, generation capacity deferral, ramping, electric transportation, renewable integration, and end-user applications. Within each of these application area, different timescales from seconds to hours apply. The selection of which energy storage technologies are best suited for a given application depends on the purpose of the storage and the timescale of response required as in Figure 1.6. As can be observed from the figure, small capacity ES systems with short discharge times can be used for fast-response applications like dealing with momentary outages, voltage spikes/sags and other transient events. ES Systems having high discharge times can help to time shift demand from high cost peak hours to low cost off-peak hours. Today, PHS and CAES has the capability to discharge electricity for tens of hours, with capacities that can attain 1,000 MW. Researchers are working to extend other ES technologies to reach comparable capacities in the future. The perfect ES system should meet the following requirements (Denholm, 2006; Mendoza, 2014)

- Long cycle life
- High energy density (Wh/m^3) and specific energy (Wh/kg)
- High round trip efficiency
- Operable in a wide range of environmental conditions
- Reliable in operation
- Maintenance-free
- Cheap and environmentally friendly
- Made of materials that will enable efficient reclamation of materials at end of service-life

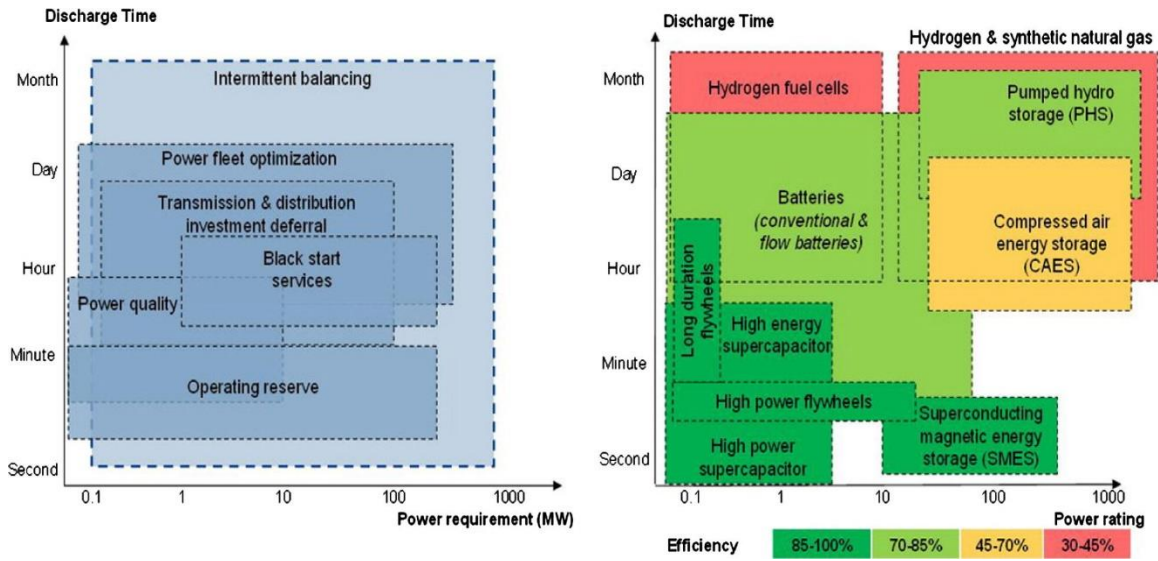


Figure 1.6 Real life applications and technology marching (Aneke & Wang, 2016)

Among these various energy storage technologies, CAES and PHS are the most viable ones for large scale storage applications (Yang et al., 2014). Compared to PHS, CAES has a lower capital and maintenance cost per kW and less geographic limitations, which makes it more attractive.(Yang et al., 2014). The features of these ES technologies are shown in Table 1.1.

Table 1.1 Characteristics of various energy storage technologies (Aneke & Wang, 2016; World Energy Council, 2016)

Technology	Energy density Whkg ⁻¹ (WhL ⁻¹)	Power density W/kg(W/L)	Power rating (MW)	Discharge time	Suitable storage duration	Life time (years)	Cycle life (cycles)	Capital Cost (\$kW ⁻¹)	Round trip efficiency (%)
Flywheel	10–30 (20–80)	400–1500 (1000–2000)	0–0.25	ms–15 min	s–min	~15	20,000+	250–350	85–95
PHES	0.5–1.5 (0.5–1.5)		0.1–5.0	1–24 h+	h–months	40–60		600–2000	65–87
CAES	30–60(3–6)		0.005–0.3	1–24 h+	h–months	20–60		400–800	50–89
Super-capacitor	2.5–15	500–5000	0–0.3	ms–60 min	s–h			100–300	90–95
NaS	150–240 (150–250)	150–230	0.05–8.	s–h	s–h	10–15	2500	1000–3000	80–90
NaNiCl	100–120 (150–180)	150–200 (220–300)	0–0.3	s–h	s–h	10–14	2500+	150–300	85–90
ZnBr	30–50 (30–60)		0.05–2	s–10 h	h–months	5–10	2000+	700–2500	70–80
Li-ion	75–200 (200–500)	500–2000	0–0.1	min–h	min–days			1200–4000	85–90
SMES	0.5–5 (0.2–2.5)	500–2000 (1000–4000)	0.1–10	m–8 s	min–h	20+	100,000+	200–300	95–98

1.5 Motivation and innovation of the study

1.5.1 Motivation of the study

In an adiabatic compressed air energy storage (A-CAES) process, the excess electricity is used to compress and store air. Thermal energy is then recovered from the generated compression heat and stored in a thermal energy storage media. Later on, the stored thermal energy is recovered and made to expand through an air turbine to generate the electricity back. So many options are available for storing the thermal energy in the reservoir including sensible heating of liquids and solids, latent heat storage in phase change materials etc. (Nithyanandam et al., 2012).

The effectiveness of the conversion of the wind electrical energy to thermal energy and back to electrical energy in the A-CAES process is governed by laws of thermodynamics. According to these laws, it is impossible to convert all the electricity to heat and reconvert all the stored heat back to power. These limitations can be quantified by considering the power output of a theoretical cycle generating electricity from heat supplied at a constant (high) temperature ($T_{HTF,in}$) and rejected at a constant (low) temperature ($T_{b,in}$), given as (Quaak et al., 1999)

$$\text{Power}_{\text{output}} = \left(1 - (T_{HTF,in}/T_{b,in})\right) \times \text{Power}_{\text{input}} \quad (1.4)$$

From the above formula, it is evident that the higher the temperature of the HTF, the more the heat supplied to the thermal energy storage medium at high temperature level and the higher the overall performance.

In an A-CAES process, this high temperature ($T_{HTF,in}$) is limited to the maximum possible exit temperature of state-of-the art compressor technology, which is approx. 400-450 °C (Daniel, 2011). In air expander this temperature is limited to the maximum turbine inlet temperature of about 900 °C without blade cooling and up to 1400 °C with blade cooling (Daniel, 2011)

To attain an entrance temperature to the thermal energy store that is more than the exit temperature from the compressor, downdraft biomass gasification (DBMG) electrical system is a potential subsystem that can be integrated into the A-CAES electrical system

(ES) so that the high temperature waste heat from the syngas and other sources from the biomass gasifier electrical system can be used to further pre heat the air post compression from the air compressor before entering the TES tank. This will improve the thermal energy delivered to the thermal energy store and hence the overall efficiency of the A-CAES process. However, this comes with a penalty of increased cost of the whole system. The degree of improvement of the performance of the system vis-a-vis the increased cost is sensitive to the performance of each unit in the integrated system and the approach of integrating the units of the plant.

Although, the downdraft biomass gasification (DBMG) is a much known technology, using (DBMG) coupled to A-CAES is one of the possible configurations that have not received much attention by the researchers. Consequently, this study will offer the research community and industry a significant knowledge on the performance of such a combined hybrid renewable energy system. In addition, there are several technical and economic questions which should be answered before the full deployment of the proposed (A-CAES+BBMGES) systems. These questions include:

- What is the energy and exergy efficiency of the system and how much power can it produce?
- What is the actual cost, value and profitability of A-CAES+BMGES system for distributed generation applications?
- What is the effect of the community size on the performance and the economic benefit of A-CAES+BMGES?
- How are the economic performance affected by the key parameters of the different components of the A-CAES+BMGES system?

The literature review discussed in the next chapter shows that there has been no such a holistic techno-economic studies that considered a hybrid adiabatic compressed air energy storage (A-CAES) and biomass gasification energy storage (BMGES) power system for distributed generation in the literature. Previous focus was on a specific A-CAES technologies and/or its hybrids with solar PV, flywheel, concentrated solar as detailed in the literature review section. In particular, there is a work by the authors (Denholm, 2006), on a base load diabatic CAES system that combines wind energy,

compressed air energy storage, and biomass gasification. Biomass derived fuel is used in the combustor and storage system instead of air and natural gas respectively. In addition, the syngas produced by the biomass gasifier is used to substitute air used in the compressors and turbines. Different from their work, the A-CAES+BMGES system analysed in this research is a small scale adiabatic system for distributed generation. The syngas produced in the system is used in a dual fuel internal combustion engine (ICE) and thermal energy storage using PCM has been considered. Therefore, there is a research gap in studying the technical and economic performance of a hybrid small A-CAES and BMGES system for distributed generation and the impact of the size of the community and the system size on the performance and business case

The present study, aims to cover this gap. This research provides a comprehensive thermodynamic modelling and techno-economic analysis of a hybrid adiabatic compressed air energy storage system coupled with biomass gasification energy storage system (A-CAES+BMGES) as shown in Figure 1.7.

To the best of knowledge of the author, there is no study that has considered the techno economic analysis of an integrated A-CAES+BMGES system. Therefore, this type of study is considered novel, which will offer researchers and other people involved in the design of energy storage systems (ESS) substantial knowledge when they need to advise the decision makers and also to develop an optimum design.

1.5.2 Operating principle of the proposed novel system

The proposed system as in Figure 1.7 consists of four main parts: (i) a hot air dryer (HAD) system (ii) an air biomass gasification and cleaning subsystem, consisting of a downdraft biomass gasifier (BMG), a product gas cooler (HX2, HX3), a cleaning system consisting of filter and scrubber and a syngas store (SgS) (iii) an A-CAES generation subsystem, consisting of air compressors (ACs), air expanders (AEs), thermal energy storage (TES), heat exchangers (HX1, HX4, HX5, HX6) and air store (AS) and (iv) an internal combustion engine (ICE) subsystem, consisting of a dual fuel engine (DFE) and a hot water heat exchanger (HX7). The numbers (1-46) in the figure (Figure 1.7) represents stream numbers. Table 1.8 lists the fluid type that makeup of each stream number.

Table 1.2 Fluid/material making up the stream numbers of Figure 1.7

No	Fluid type	No	Fluid type
1	Ambient air	24	Diesel fuel
2	Compressed air exiting AC1	25	Ambient air
3	Cool compressed air entering AC2	26	Cool compressed air exiting AS
4	Compressed air exiting AC2	27	Cool compressed air heated up by TES ₃
5	Cool compressed air entering AC3	28	Compressed air heated further by HX4
6	Compressed air exiting AC3	29	Air exiting AE1
7	Cool compressed air entering AC4	30	Air from AE1 heated up by TES ₂
8	Compressed air exiting AC4	31	Air from TES ₂ heated further by HX5
9	Heated compressed air	32	Air exiting AE2
10	Cool compressed air entering AS	33	Air from AE2 heated up by TES ₁
11	Ambient air	34	Air from TES ₁ heated further by HX6
12	Ambient air heated by HX1	35	Air exiting AE3
13	Ambient air	36	Hot DFE exhaust gas entering HX6
14	Ambient air heated by syngas HX3	37	Cool DFE exhaust gas exiting HX6
15	Heated ambient air to HAD	38	Hot DFE exhaust gas entering HX5
16	Wet biomass feed	39	Cool DFE exhaust gas exiting HX6
17	Moist air exiting HAD	40	Hot DFE exhaust gas entering HX4
18	Dry biomass entering gasifier	41	Cool DFE exhaust gas exiting HX6
19	High temperature syngas	42	Cool DFE exhaust gas
20	Medium temperature Syngas	43	Cold water in
21	Low temperature syngas	44	Warm water out
22	Cleaned syngas to storage	45	Hot DFE cooling water
23	Syngas to DFE	46	Cooled DFE cooling water

The high temperature product gas (19) produced from the gasifier is passed through the first product gas cooler heat exchanger (HX2). The heat recovered by HX2 is utilised to further heat the temperature of the compressed air (CA) from AC4 (8) to higher temperature (9) before it is made to pass through the TES3 where the energy it contains is absorbed and stored by phase change material (PCM). The CA is then stored in the air store (AS). Because, the temperature of the CA at point 8 is high, after releasing heat in HX2, the outlet syngas (20) still has a high temperature. The remaining heat is used to raise hot air at a temperature of about 80 °C by means of the second syngas cooler heat exchanger (HX3). The recovered heat (14) is channelled to the HAD for biomass drying. Then the cooled syngas (21) is passed through a cleaning system to remove impurities and thereafter stored in the insulated syngas store (SgS). The syngas from downdraft gasifier contains

low impurities and thus can be used directly in ICE (Reed & Das, 1988). However, various gas clean-up methods/stages available like cyclones, candle filters, wet electrostatic precipitators and wet scrubber can be used. Some methods have the capacity to remove several contaminants in a single process such as wet scrubbing, whilst others focus on the removal of only one contaminant.

During the discharge mode, the stored purified syngas gas (23) and diesel fuel (24) are fed into the DFE for generating electricity. Simultaneously, the stored CA in the AS is throttled down to the minimum pressure of the AE (40 bar) and made to pass through the thermal energy storage tank (TES3). As the CA passes the TEST, the PCMs releases their stored energy to it and the temperature of the CA increases. The temperature of the CA is further raised by means of the exhaust temperature of the DFE using heat exchangers, HX4, HX5 and HX6 respectively for AE1, AE2 and AE3. The heat contained in jacket water (45) from the DFE is used to provide low temperature space heating/domestic hot water (44) at temperature of in/out of 35/55 °C for users by means of the heat exchanger (HX7). The system gives out two products: electricity and low temperature heat for space heating/domestic hot water (Dw) applications.

A specific net power value of $0.3 MW_e$ is set for the dual fuel engine and system design parameters that can achieve that target power value are calculated. A wind turbine excess electricity input of $1 MW_e$ is assumed. The system is scaled to more than cover the peak electricity demand and any excess electricity generated is sold to the grid. The sources of revenue of the power plant under consideration are electricity sales to the customers/national grid and heat sale to the customers.

1.5.3 Innovation of the research

The benefits derivable from the proposed A-CAES+BMGES in this research work include but not limited to the following:

- A comprehensive model through which the thermodynamic and economic performance evaluation of A-CAES+BMGES can be carried out.
- Supports the more diffusion of renewable distributed generation technologies especially wind and biomass generation technologies at the local community level.

- Enables communities/customers to use their own RE generation by shifting excess generation to meet their demand load later
- Empowers utility/private investors to create new business models, with cost effective energy prices that is in sync with customers' expectations and preferences

1.6 Research objectives

The general objective of the thesis is to provide a better understanding of the performance of the integrated A-CAES and downdraft biomass gasification energy storage system (A-CAES+BMES) proposed, including their energy and exergy efficiencies, fuel consumption, and cost per unit of electrical power produced using techno-economic analysis.

In light of the above background, the specific objectives of the work described in this thesis are as follows:

- To propose a novel integrated adiabatic compressed air energy storage and biomass gasification energy storage systems (ACAES+BMGES);
- to develop a detailed mathematical model suitable for analyzing the thermal performance of the TES unit as a separate component and as an fundamental part of the A-CAES system
- To develop a model of downdraft biomass gasifier as a stand-alone component and as an integral part of the integrated system.
- To carry out a thermal performance analysis of the TES unit and downdraft biomass gasification as separate units and as vital parts of the overall system
- To develop a thermodynamic model of the integrated A-CAES+BMGES system
- To conduct energy and exergy analyses of the integrated A-CAES+BMGES system proposed to evaluate its performance;
- To develop thermo economic models to assess the thermo-economic performance of the A-CAES+BMGES considered. In this models, the electricity and heat demand data for Hull Humberside, UK is used.

In order to accomplish the above objectives, the proposed research will include the following specific work on each of the sub components of the A-CAES+BMGES.

A-CAES

- To propose two charging modes of adiabatic compressed air energy storage using phase change material thermal energy storage (PCM-TES);
- Development of numerical model with capability to analyse the thermal characteristics and thermal performance of the two charging modes of A-CAES.

Downdraft biomass gasification

- To develop a model of the hot air biomass dryer
- To develop a model of downdraft biomass gasifier
- To carry out a performance analysis of the downdraft biomass gasification as separate units and as vital parts of the overall system

The integrated system

- To develop a thermodynamic model of the integrated A-CAES+BMGES system
- To conduct energy and exergy analyses of the integrated A-CAES+BMGES system considered to evaluate its performance;
- To develop techno economic models to assess the techno-economic performance of the A-CAES+BMGES system considered. In this models, the electricity and heat demand data for Hull Humberside, UK is used.

1.7 Thesis Structure

To address the research aim and objectives, this research starts with a comprehensive literature review on the subject matter to explore the state-of-the-art knowledge in the area, and identify the knowledge gaps. After identifying the knowledge gaps, the system is modelled. This is done by separately modelling each of the main components of the A-CAES+BMGES system such as A-CAES (compressors, turbines and thermal energy storage tank) and down draft biomass gasification electrical system (BMGES) (consisting of a biomass gasifier (BMG) with a hot air fuel dryer and a dual fuelled internal combustion engine (ICE)) as shown pictorially in Figure 1.8.

A validation of the A-CAES TEST and gasification sub model is presented using published experimental data. Then each of the sub models is integrated into a single unit called the integrated A-CAES+BMGES.

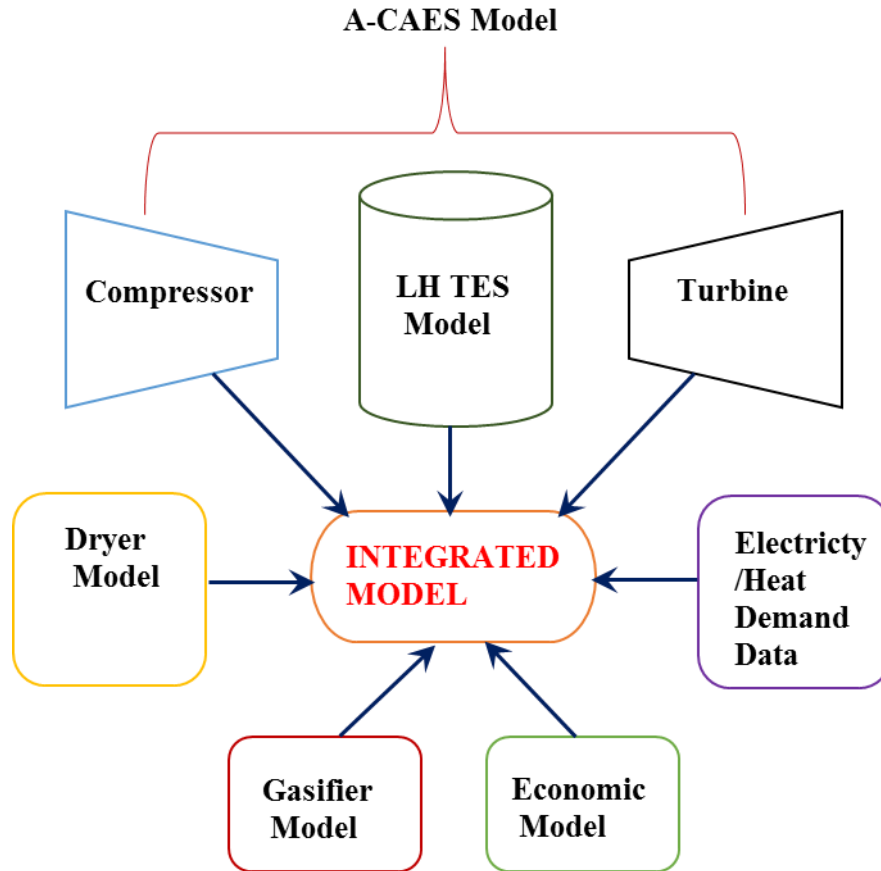


Figure 1.8 Proposed integrated design model

The thesis comprises of seven chapters and is organised as follows:

Chapter 1 – The need for renewable energy storage based distributed power generation

This chapter sets the scene for the context in which the work is to be completed, and explains why the research is valuable.

Chapter 2 – Literature review

In this chapter, following the introduction of the work presented in Chapter 1, an overview of literatures on the current and previous research on A-CAES and thermal energy storage is presented.

Chapter 3 – Numerical modelling of A-CAES PCM thermal energy storage

The Numerical model of the PCM TES for use in the A-CAES process is presented in this chapter. Earlier TES models related to the current research are revised. Following the review. Applicable initial and boundary conditions for a one-dimensional dispersion concentric model (DCM) for spherical balls packed in a cylindrical vessel is developed. Adjustment of the external node of the discretized equations of the PCM is carried out to suit the geometry considered. A matrix inversion technique algorithm for solving for the temperatures of the HTF and PCM at each node is developed. Several thermodynamic relations required for analysis of LH TES bed are identified and formulated. Two and Three multiple PCMs having different melting points are used as the potential TES media. Their thermal performance are analysed and compared.

Chapter 4 – Modelling of downdraft biomass gasification

A thorough literature review is conducted to describe the principle of operation of biomass gasification (BMG). Existing Biomass gasification modelling is reviewed, and a new downdraft biomass gasification model is created to predict the syngas concentration and temperature distribution within the gasifier. In this chapter, the modelling of the biomass gasifier was based on multi step stoichiometric, equilibrium approach. Sensitivity analysis of the key parameters that affect the performance of the system is contained herein. In addition, the model of the hot air biomass drier is contained in this section, including its energy requirements.

Chapter 5 – Thermodynamic modelling of integrated A-CAES+BMGES

In this chapter, using the sub models of the different components of the integrated system developed in previous chapters, an integrated model for the whole system capable of performing thermodynamic analysis is developed. The Chapter also contains a sensitivity analysis results of the impact of some sensitive technical parameters on the thermodynamic performance of the integrated system

Chapter 6 – Economic analysis of the integrated A-CAES+BMGES

In this chapter, using the results of the thermodynamic analysis, an economic model for the whole system capable of performing economic analysis is developed. In addition, costing of the various components of the sub models of the system is developed in this chapter. The Hull Humberside is used as a case study for the model and performance results is reported. The Chapter also contains a sensitivity analysis results of the impact of technical and economic factors on the economic performance of the integrated system

Chapter 7 – Conclusions

Key findings relating precisely to the aims of the thesis are clearly laid out and some recommendations are presented in this chapter. In addition, recommendations for future research works are suggested

Chapter 2

Literature review on Compressed Air Energy Storage (CAES)

2.1 Introduction

The review of CAES plants can be classified based on compressors, turbines, thermal energy storage system deployed, configuration, application type, or analysis type. However, since compressors and turbines are off the shelf equipment with negligible room for performance improvements, what mainly distinguishes one research on CAES plant from another is the configuration of the plant in itself; whether it is hybrid or stand alone, and the thermal energy storage type and configuration used. Therefore, the literature review reported in in this section focuses on the configuration, analysis method, thermal energy storage method deployed and type of TES models used.

First a general overview of CAES is done, followed by a review of the studies involving different analysis that have been conducted (thermodynamic, energy and exergy, thermo-economic etc.) for CAES. This is followed by review on different thermal energy storage method, configuration or media applied. Thermal energy storage (TES) is central to the operation and performance of the CAES plant. Since LH TES is chosen for use in the A-CAES component, a review on PCM, types, characteristics and most importantly mathematical models and earlier modelling approaches for PCM based TES vessel is contained in this section. This literature review was done so as to select the most suitable type of TES system to be used for energy storage in the A-CAES component of the integrated system and also to select the best suited mathematical model for describing the process.

The selected mathematical model called the Concentric Dispersion model (CDM) is explained in more detail in section 2.4.5. Furthermore, a critical review of the modelling work on only A-CAES using LH TES technologies including the storage media selected for use in the selected energy storage system and the modelling approach is presented in Chapter 3.

2.2 Overview of compressed air energy storage

CAES is a commercialised energy storage (ES) technology which can provide power output of over 100 MW with a single unit. However, given limitations on geologic formations, and the option of using the above ground storage, it may be more viable to deploy CAES with lower storage capacity. The technology is based on the simple well-known and commercialised conventional technology of gas turbine and uses the elastic potential energy of compressed air (Daniel, 2011). CAES can be classified as diabatic, adiabatic and isothermal as in Figure 2.1 (Daniel, 2011).

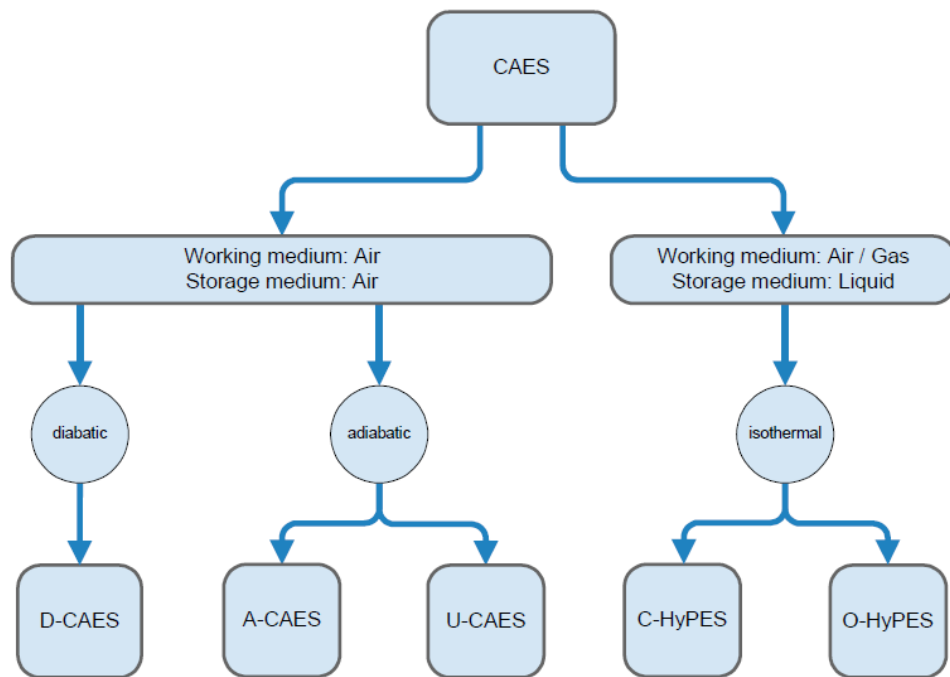


Figure 2.1 Classification of CAES (Daniel, 2011)

A diabatic CAES (D-CAES) is also referred to as conventional or first generation CAES. It is a configuration in which the heat developed through compression is not recovered and stored but dissipated by cooling and the stored compressed air must be heated up before expansion in the turbine using an auxiliary fossil fuel power source (Succar & Williams, 2008). This leads to pollution and round-trip efficiencies that are low and below 50% (Succar & Williams, 2008). The low efficiencies stems from the thermal losses during the compression and expansion modes, leakage of air during the whole CAES

system, the internal energy losses due to the air compressibility, etc. Other shortcomings of the conventional CAES systems include the requirement for an underground cavern, its dependence on fossil fuel, dissipation of heat into the atmosphere, and generation of pollutant emissions from their combustion processes. The above shortcomings have impacted negatively on wide scale deployment of the D-CAES for electricity generation. A diagrammatic representation of the conventional CAES is shown in Figure 2.2.

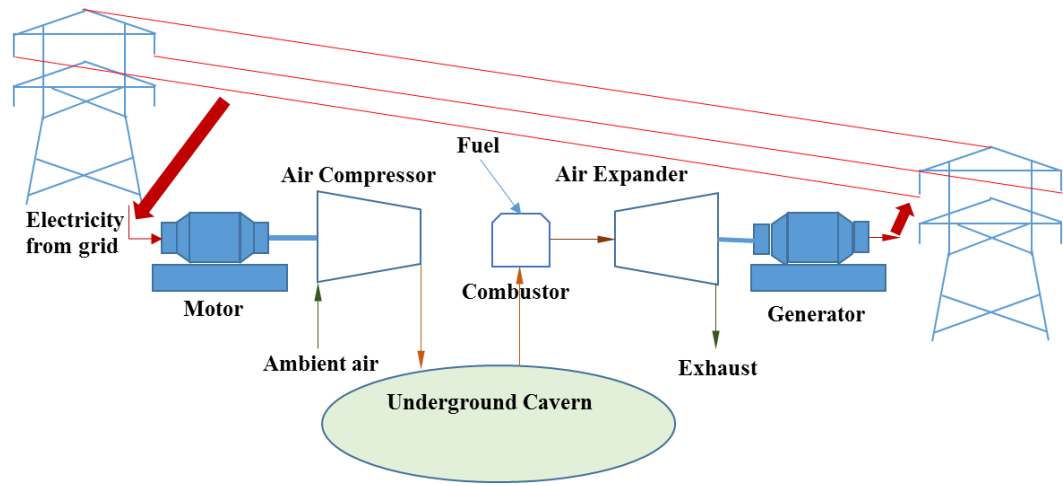


Figure 2.2 Conventional CAES plant

During charging, excess electrical energy is used to drive a motor unit to compress air and store it as a pressurised air in an underground cavern. During discharging when there is a deficit of electricity supply or generation, the highly pressurised air is mixed with natural gas, burned and expanded in a modified gas turbine (turbo expander) which drives a generator to re-generate the stored electrical energy. Thermal energy from combustion of gas is used to preheat the air to prevent the turbo expander blades from freezing during the adiabatic expansion process (Succar & Williams, 2008).

Conventional gas turbines utilize about 67% (two-third) of their input fuel to generate electricity but D-CAES utilizes less than 40% of the fuel used by conventional gas turbines to produce the same amount of electric power (Succar & Williams, 2008; Daniel, 2011). In addition, the technology has a fast ramp rate or start up time. In emergency start-ups, D-CAES plants have the capacity of ramp rates of about 9 minutes and about 12 minutes under normal conditions, whereas conventional gas turbine peaking

plants characteristically require 20 to 30 minutes for a standard start-up (Succar & Williams, 2008; Chen et al., 2009 and Daniel, 2011). The major components of a D-CAES plant include compressor, underground cavern, generator and air turbine.

The second generation CAES is a slight improvement of the first generation CAES. The attention was to improve on the efficiency through improvement in the compression and expansion phase using the techniques of air injection. The techniques employed include adding intercooling the air during the compression process, after cooling, reheating and recuperating as design options. An example of the second generation CAES is the Air Injection (CAES-AI) technology patented by Energy Storage and Power Corporation (ESPC) (EPRI, 2008). The idea is centered on injecting the stored and preheated air directly into Solar Mercury gas turbine (GT) and storing the compressed air in a steel pipes located near the GT (Agrawal et al., 2011).

Third generation CAES comprises of three main types:

1. Adiabatic(A-CAES) and advanced adiabatic (AA-CAES),
2. Isothermal (I-CAES) and
3. Polytropic (P-CAES)

They were proposed to solve the challenges of the first and second generation CAES (Daniel, 2011; EPRI, 2008; Succar & Williams, 2008).

What distinguishes adiabatic CAES (A-CAES) from other CAES technologies is that the use of gas or fuel by CAES technology is tried to be reduced or possibly even eradicated by deploying thermal energy storage (TES) to capture and store the heat developed during compression and also the heat recovered from the turbine during generation. CAES can be used to perform different applications. CAES can greatly reduce GHG emission when coupled with fossil fuel power plants (Denholm & Kulcinski, 2004). It has been studied for use in isolated islands with favourable results (Kaldellis, 2008). CAES has also been studies for peak shaving applications when coupled with wind electricity with positive results (Strbac et al., 2007).

Despite the benefits derivable from CAES, previous researches state that TES is associated with high capital costs (EPRI, 2008; Succar & Williams, 2008; Daniel, 2011). The capital cost of the TES unit has to be warranted before A-CAES can be commercialised.

The means of storage of heat can be through a solid (e.g. concrete or stone), or a fluid such as hot oil or molten salt solution (Chen et al., 2009). A diagrammatic representation of an A- CAES is shown in Figure 2.3

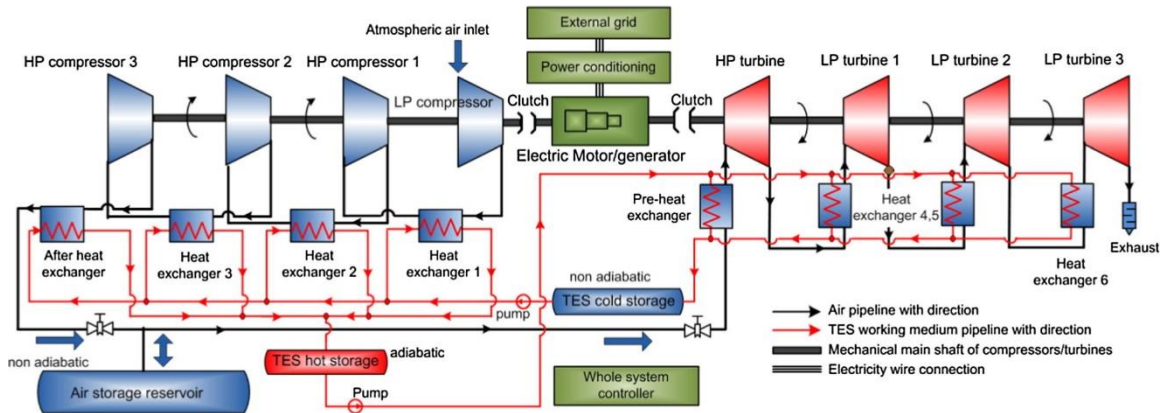


Figure 2.3 Layout of adiabatic compressed air energy storage (Luo et al., 2016)

During the charging period heat is extracted from the compressed air stream using the heat exchangers and stored in the TES hot storage. During discharging, when energy is required by the grid, the compressed air from the air storage reservoir is preheated and reheated before and after expansion in the turbines respectively using the stored TES hot storage thus eliminating the use of gas heating.

Advanced Adiabatic CAES (AA-CAES) is an improvement of the adiabatic case that comes with improved compressor and turbine design along with improved TES technologies. Its overall efficiency is estimated to lie between 70- 75% (Daniel, 2011). However, currently there is no AA-CAES plants existing in the world because it is still in its infant stage of trials and has not yet attained commercial status. The quoted efficiency depends on the assumed thermodynamic efficiency values of the compressors and turbines and the effectiveness of the heat exchangers used (Daniel, 2011).

Isothermal CAES (I-CAES) technology aims to address some of the pitfalls of the first generation diabatic and second generation adiabatic CAES, by exterminating the necessity for gas and high temperature TES, thus, giving a superior round trip efficiency ranging from 70 to 80% (Daniel, 2011) . As the name implies, in I-CAES process, the air is compressed at a constant temperature, consequently decreasing the work needed for compression while maximizing the work output during expansion, through effective

transfer of heat with surroundings of the air vessel. The P-CAES is still being seen as a theoretical concept. Being polytropic, heat enters or leaves the system and input work appears as both increased pressure and increased temperature above adiabatic (Daniel, 2011).

The performance of a CAES plant is quantified by its round trip efficiency which is the ratio of electricity generated from discharging the TES to that used to store or charge the TES (Freund et al., 2012). Currently, the use of CAES systems is not widespread. Two CAES systems exist in the world so far; the first is the Huntorf CAES plant in Germany and the second is in McIntosh, Alabama that operates by utilizing off-peak electricity to compress air and store it in an underground cavern (Daniel, 2011). The two CAES plants utilize the heat from the combustion of natural gas-fired combustors to preheat the compressed air from the cavern before expansion in the turbine to generate electricity during times of peak demand.

The Huntorf Plant in Germany, built in 1978 is the world's first utility-scale CAES plant (Succar & Williams, 2008). It is now being run by Eon (Freund et al., 2012) and utilizes two salt domes as the storage caverns located 640-790 m below the surface to store a total volume of 311485 m³ at pressures up to 69 bar. The plant produces 425 kilograms per second (kg/s) of compressed air (pressure up to 70 bars) in a daily cycle of compressed air charging for 8 hours and a 2 hour of operation at a rated power of 290 MW (Succar & Williams, 2008; Chen et al., 2009). This plant serves the purpose of providing peak shaving, load shifting, frequency and voltage control, back-up to local power systems and additional electrical power to bridge the disparity between electricity produced and demand. It also provides black-start power to nuclear units. It was designed by Brown Boveri Company, Mannheim. It can attain full load in 11 min from idle position or in about 6 min from a quick-start position attaining synchronous speed in 2 min (Foley & Díaz Lobera, 2013). The plant has been in operation since it was built over 32 years ago with excellent performance of 90% availability and also 99% starting reliability respectively (Succar & Williams, 2008; Chen et al., 2009). The round-trip (cycle) efficiency of this plant is about 42% (Freund et al., 2012). The McIntosh CAES plant was commissioned in 1991 and is fitted with a recuperator to recuperate waste heat from the gas turbine exhaust and increase the power system efficiency (Succar & Williams, 2008; Chen et al., 2009)

There is also hybrid CAES projects called the solar-assisted Solar CAES (Agrawal et al., 2011). It works just like a conventional CAES system but incorporate concentrated solar power (CSP) to supply the extra energy needed for air preheat and thus minimise or remove the need for fossil fuels. A solar-assisted CAES is being developed by Brayton Energy, LLC and Southwest Solar Technologies, Inc. in Arizona as in Figure 2.4. The hybrid solar-heated system is made of a power generation turbine system a 320-m² array of parabolic dish concentrators. The power generation turbine is installed with intercooled recuperated reheat gas turbine built to accommodate a range of pressures (10 to 64 bar). The systems has a net solar-to-electric system efficiency of about 30%, which is arguably one of the best in terms of efficiency of all solar power conversion systems (Agrawal et al., 2011).

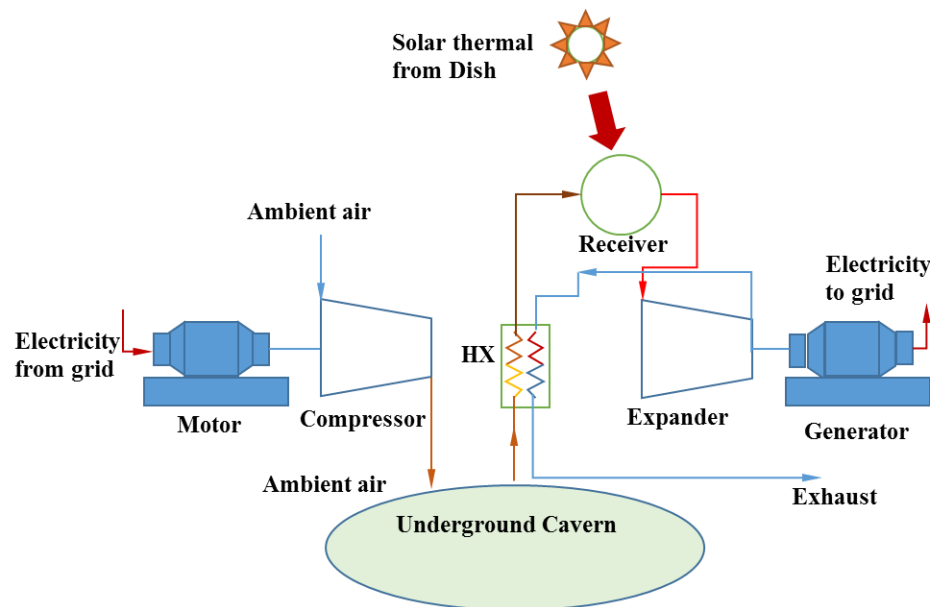


Figure 2.4 Solar assisted CAES

2.3 Classification of A-CAES

Depending on the temperature range involved, the A-CAEs process can further be classified as low (<200 °C), medium (200-400 °C) or high (>400 °C) temperature A-CAES.

Low-temperature adiabatic compressed air energy storage (LT A-CAES) involves a comparatively low storage temperatures of 95–200 °C (Wolf & Budt, 2014). It takes advantage of the fact that cycle efficiency of A-CAES plants is not determined by the

Carnot efficiency. Thus, low TES temperatures still gives rise to appropriately high roundtrip efficiencies (Wolf & Budt, 2014). Because of the low temperature involved in the process, only water and thermal oil are used. Water has the advantage of having a higher heat capacity and is both of lower cost and chemically stable. However, if water is used above 95 °C, it needs to be pressurised to prevent evaporation and this adds to cost tremendously (Dincer, 2002; Wolf & Budt, 2014). In this case, water cannot be used above its critical point, namely 374.3 °C (Dincer, 2002).

To maintain the low temperature, intermediate cooling of air at exit of the compressors is done. Compressors designed for high pressure ratios like the axial turbo compressors are not applied here because they do not allow intermediate re-cooling of the air (Wolf & Budt, 2014). Though, radial type inline compressors can be intercooled between the stages, they are not suitable for LT A-CAES applications because of their limited number of five stages. Thus the most suitable compressor types for LT A-CAES-plants are integrally geared radial turbo compressors with up to ten intercooled stages (Wolf & Budt, 2014). The main advantage of LT A-CAES is the use of liquid media which makes possible the use of conventional heat exchangers. Also storage plants of this type has a short start up time of about 5 minute

In Medium temperature A-CAES (MT-ACAES) process, the process temperature lies between 200 and 400°C. Because of the low temperature range involved, it makes use of the off the shelf compressors and TES media like thermal oil and molten salts. Storage of thermal energy using packed beds is also possible. Due to its high thermal stress, the start-up time of MT A-CAES is high in the range of 10-15min (Budt et al., 2016)

High Temperature A-CAES (HT A-CAES) takes place at temperatures above 400 °C with a start-up time in the range of 10-15 min. Because of its high temperature of operation, it has the highest cycle efficiency of all the three types. Its cycle efficiency can be up to 70%. Though technically feasible, at the moment there are no off the shelf compressors and turbines that can operate at the high temperature range of operation of the HT A-CAES and still maintain the outlet temperatures at the discharge of the compressors below a certain temperature limit. Presently, this temperature limit for industrial compressors is about 400 °C (Yang et al., 2014).

2.4 Review of previous work on CAES

2.4.1 CAES Configurations

A basic energy storage systems configuration is made of three main parts, the charging or input, storage and the output/discharging. The makeup of the components depends on the type of energy source involved, the TES configuration and heat transfer storage used. A regenerative solid or recuperative liquid TES can be used (Freund et al., 2012). Several research has been done to improve the efficiency and reduce cost of CAES through analysis of different TES configurations (Grazzini & Milazzo, 2012; Zhang et al., 2013; Aldoss & Rahman, 2014 and Barbour et al., 2015).

Hartmann et al. (2012) analysed different configurations of CAES using thermodynamic analysis. The options analysed include one-stage polytropic CAES, two-stage polytropic CAES, three-stage polytropic CAES, and isentropic CAES. Their results suggested that the two stage configuration is the best and has efficiency that varies between 52 and 62% depending on the cooling and heating demand. It was also reported that the efficiency of the polytropic configuration is about 60%, and lower than that of adiabatic CAES of about 70% quoted in the literature. To optimise the CAES operation, the development of high temperature thermal storages (operable at a temperature above 600 °C) and temperature resistant materials for compressors was suggested (Hartmann et al., 2012)

In the work of Kim et al. (2012) Innovative concepts of A-CAES, I-CAES and constant pressure CAES combined with PHS was proposed to address the shortcomings of CAES and broaden its scope. The proposed configurations were analysed using energy and exergy analysis. Result of their analysis suggested that the energy loss by throttling during expansion in the current CAES could be reduced by a combination of the constant-pressure CAES and PHS plants. This combination, according to them (Kim et al., 2012) will require half the storage volume of container for existing CAES plants.

2.4.2 Analysis methods

Several methods have been deployed by various authors to analyse and optimize the efficiency and cost of CAES. Such methods include, energy analysis, exergy analysis, thermo economic modelling, techno-economic analysis, etc. In the works of the authors

(Grazzini & Milazzo, 2008), a thermodynamic analysis was carried out for CAES/TES systems for renewable energy plants. In their analysis, the storage volume was optimized and a system layout with thermal storage (TES) and variable configuration was designed. It was reported that a variable configuration system based on compressed air and a heat reservoir is a viable option for energy storage with performance that can compete with other energy storage technologies.

In another study, a multi adiabatic CAES was analysed thermodynamically by the authors (Grazzini & Milazzo, 2012). The analysis was dedicated solely to the optimization of its heat exchangers since the compressors and turbines used in a typical CAES plant are off the shelf components with limited margins for optimization. Barbour et al. (2015) carried out a thermodynamic analysis of an A-CAES plant using packed bed regenerators. A validated numerical model was used by the authors to analyse the packed bed system and concluded that efficiencies are between 70.5% and 71.1% for continuous operation (Barbour et al., 2015). Other authors have also carried out analysis of A-CAES packed bed thermal energy storage (Peng et al., 2015; Ortega-Fernández et al., 2017; Tola et al., 2017). To analyse the effect of TES on the performance of A-CAES plant, the authors (Zhang et al., 2013) carried out a thermodynamic effect of thermal energy storage on CAES system and concluded that the utilization of stored heat in a CAES TES store is affected by the pressure in the air storage chamber. They suggested appropriate selection of pressure limits will help to optimize the CAES operation.

Thermo economic modelling of CAES has been presented by Buffa et al. (2013) in a paper titled “Exergy and Exergoeconomic Model of a Ground-Based CAES Plant for Peak-Load Energy Production”. They reported overall exergy efficiency of about 52%. It was further reported that the major exergy destructions arise in the expanders, compressors, and in the compressor intercoolers. The design and off-design analysis of a compression and storage system for small size compressed air energy storage (CAES) plants was carried out by Salvini et al. (2017). The system consists of 4-stage reciprocating compressor coupled with an artificial air reservoir. Capacity control devices are equipped to the compressor so as to timely vary the absorbed power in accordance with the grid requirements. In another related study by Salvini, (2015), a techno economic analysis of a small size second generation CAES plants based on a 4600 kW mercury recuperated gas

turbine equipped with an artificial compressed air storage system has been investigated. Evaluation of the investment cost and operation and maintenance (O&M) costs was carried out by varying the air storage pressure from 2000 to 10000 kPa. It was reported that low pressure values result to very high investment and maintenance costs that are not offset by the relatively low cost of the purchased electricity. It was further reported by the author that air storage pressure of 4000 kPa gives rise to a minimum equivalent annual cost of about 210,000 Euros. Other authors have also carried out analysis of A-CAES packed bed thermal energy storage (Fertig & Apt, 2011; Grazzini & Milazzo, 2012; Mason & Archer, 2012; Jubeh & Najjar, 2012; Kim et al., 2012; Wolf & Budt, 2014; Zhao et al., 2014 and Tessier et al., 2016)

2.4.3 Different TES configuration/storage media

The TES component is central to the operation and overall performance of a thermal power plant. Most of the TES systems in operation deploy sensible heat storage (Nithyanandam et al., 2012). Nevertheless, storing heat in the form of latent heat of fusion of phase change material (PCM) in addition to sensible heat considerably increases the energy density (Nithyanandam et al., 2012). Amongst the numerous heat storage methods, latent heat storage has received noteworthy attention from researchers over the recent years owing to its capability to offer huge heat storage capacity and constant temperature behaviour during the charging and discharging processes. The other benefits of LH TES include lesser temperature change between charging and discharging cycles, compactness in sizes and small weight per unit capacity of storage (Gong & Mujumdar, 1997a).

As a result of the above benefits, latent heat thermal energy storage (LH TES) systems have been extensively used in electrical power load shifting application, industrial waste heat recovery and solar energy utilization, in recent years (Gong & Mujumdar, 1997a).

Aldoss & Rahman (2014) carried out a comparison between the design of a TES using single-PCM and multi-PCM TES design. To maximize heat transfer rate, the PCM capsules were packed in the bed at different sections in such a way that their melting temperatures match the heat transfer fluid (HTF) temperature profile along the bed. In their results, it was reported that Multi-PCM design is found to increase the charging and

discharging rate as reported by many other researchers (Gong & Mujumdar, 1996; Gong & Mujumdar, 1997b and Chiu & Martin, 2013;). In furtherance of their analysis, the authors further investigated the degree of improvement as the number of stages increases. Single-PCM design and multi-PCM design of two and three stages were investigated and compared. The comparison was done with the aid of calculated performance indices such as charging and discharging rate, rate of heat transfer, and storage capacity. According to their findings, as the number of stages increases, the performance of the multi-PCM TES increases. However, using more than three stages does not bring any added improvement in performance.

Tessier et al. (2016) analysed the performance of a novel A-CAES system using cascaded PCMs as storage media through exergetic and energy analysis. It was reported that as the number of PCM increases, the roundtrip efficiency also increases up to as high as 85%, representing a 15% increase over conventional designs that do not use PCM storage. In the analysis, it was assumed that the phase change takes place at constant temperature. However, the assumption is not fully correct as phase change takes place at a range of temperature.

In the work of Zhang et al. (2013), the influence of TES on CAES efficiency was analysed. Further, their research also evaluated the impact of pressure and on the utilization of thermal energy in TES. It was reportedly found that there is always a quantity of thermal energy left in TES even after power efficiency has peaked to its maximum. It was also reported that the air storage vessel pressure can affect the use of heat in TES and also the use of stored compressed air can be optimized with appropriate selection of pressure limits (Zhang et al., 2013).

2.4.4 CAES hybrid configurations

Hybrid energy system (HES) combine two or more energy conversion systems to form a single unit called a hybrid system. The individual energy system complement each other to a degree and realize greater total energy efficiency than what may possibly be gotten from a lone RE source unit, thus overcoming limitations inherent in each. HES can solve shortcomings that has to do with fuel flexibility, efficiency, reliability, emissions and / or economics (Wichert, 1997; Baños et al., 2011). Owing to this characteristic, lately HES

have caught the attention of the global research community. The applications of HES is more popular in distributed generation or micro-grids. Lately, HES have received increased attentions due to their high thermal efficiency, low operating cost per energy output, and low greenhouse gas (GHG) emissions. The process of design of HES systems necessitates the selection and sizing of the most appropriate blend of energy sources, TES systems and power conditioning devices together with the execution of an efficient energy dispatch scheme (Wichert, 1997).

The selection of the appropriate combination from renewable energy power systems to form a HES depends on the availability of the renewable resources in the location where the HES is proposed to be mounted. Other than that, additional factors that needs to be weighed in for an optimum HES design are the load requirements, efficiency of energy conversion, greenhouse gas emissions during the expected life cycle of the system, economic aspects and social impacts (Baños et al., 2011)

In a bid to increase the efficiency of A-CAES, different hybrid configurations of A-CAES has been explored by researchers as reported in the literatures

(Grazzini & Milazzo, 2008; Li et al., 2011; Zhao et al., 2014 and Arabkoohsar et al., 2015). Zhao et al. (2014) proposed and thermodynamically analysed a hybrid A-CAES and flywheel energy storage system (FESS) and concluded that the hybrid energy storage system is more suitable for smoothing out the variability of wind power. Another configuration of a novel compressed air energy storage that makes use of near isothermal compression/expansion and energy storage before conversion to electrical energy was proposed and analysed by Li et al. (2011). This approach differs from conventional CAES approaches in that air compression and expansion is accomplished by means of liquid piston compression/expansion using sea water as the liquid. The liquid piston generates a positive gas seal that makes possible a compression space with high surface area for the transfer of heat and it makes use of the ocean as heat source or sink (Li et al., 2011). A sizing and thermo-economic study of a hybrid of CAES and PV plant was carried out by the authors (Arabkoohsar et al., 2015). Net present value (NPV) method was employed for the economic analysis and it was reported that the hybrid system have a payback period of less than 9 years.

Also in another study, Garrison and Webber (2011) proposed a novel configuration for CAES system in which the CA exiting the cavern is preheated by solar energy as opposed to natural gas before expansion in the expander. They reported an overall efficiency of 46% for the hybrid solar-CAES system. In another hybrid configuration, Zhang et al. (2017) analysed a hybrid diesel DG system integrated with compressed air energy storage (CAES) and thermal energy storage (TES). They reported exergy efficiency of 41.5%, and the primary fuel saving ratio of 23.13%. In another study by the authors, (Singh & Baredar, 2016), a techno-economic assessment of a solar PV, fuel cell, and biomass gasifier hybrid energy system was implemented. The cost of energy (COE) and net present cost of the system was reported to be 15.064 Rs per kWh and Rs. 5, 189,003 respectively.

A biomass-fired combined cooling, heating and power system with thermal energy storage system was studied by the authors (Caliano et al., 2017). In another related study Singh et al. (2016) carried out a feasibility study of an island micro-grid in rural area consisting of PV, wind, biomass and battery energy storage system. A Hybrid solar–biomass power plant without energy storage was studied by the scholars (Srinivas & Reddy, 2014). Their result indicated that the plant fuel energy efficiency increases from 16% to 29% with an increase in solar participation from 10% to 50% at the boiler pressure of 20 bar. Using thermodynamic modelling and thermo-economic assessment, Pantaleo et al. (2017) studied the system integration and economic analysis of Solar/biomass hybrid cycles with thermal storage and bottoming organic rankine cycle (ORC). Results of energy performance reported shows higher global conversion efficiencies when using CSP integration and reports of the thermo-economic analysis showed a higher NPV of the investment when solar energy is integrated, due to the increased electric generation and higher value of solar-based electricity. To provide a solution for managing excess heat production in tri-generation plant and thus, increases the power plant annual efficiency, a hybrid optimization model of biomass tri-generation system combined with pit thermal energy storage was studied by the authors (Dominković et al., 2015). Matlab software was used to model the system on hourly basis and hybrid optimization model was deployed to maximize the net present value (NPV). It was reported that the NPV become favourable if the economy-of-scale of both power plant and pit thermal energy storage can be utilised.

The closest work in the literature to the proposed A-CAES+BMGES system in this thesis is the work by the authors (Denholm, 2006). They analysed the technical, environmental and social performance of a base load bio-fuelled wind/CAES system using biomass-based energy storage. In the system, the low-grade waste heat generated in both the compression and combustion stages were employed to dry raw biofuels and increase the gasifier efficiency and biofuel replaced air and natural gas used in the compressors/turbines and combustors of conventional diabatic CAES respectively. In the system, the CAES turbine was adapted to operate on properly conditioned biomass syngas fuel. The authors concluded that the base load wind system based on wind generation and CAES is an economically viable method of generating electricity, mainly when considering carbon emission constraints. The delivered cost of electricity from the system was reported to vary widely depending on wind resource assumptions and project financing.

Hence from the literatures reviewed so far and within the limits of the author's knowledge, there has been no technical and economic modelling done on an integrated A-CAES and downdraft biomass gasification energy storage system for distributed power generation in the UK northern region. Therefore, the present study seeks to bridge this gap by assessing the technical and economic potential of coupling a biomass gasifier with dryer to A-CAES plant.

2.5 Phase change thermal energy storage

2.5.1 Introduction

Phase change thermal storage involves using storage materials for storing thermal energy that can be released as sensible heat (SH) and latent heat (LH) when required. The application of this ES technique became a key component of energy management following the 1973–1974 energy crisis (Pielichowska & Pielichowski, 2014). Nowadays, the depleting nature of fossil fuels reserves and the variability associated with RE substitutes make the effective utilization of energy an important subject. Using LH based TES in a CAES system provides a smart and realistic solution to increase the efficiency of the storage and retrieval cycles (Pielichowska & Pielichowski, 2014). In addition, use of LH TES in CAES will help to improve the performance and reliability of energy distribution

networks and plays an important general role in conserving energy (Pielichowska & Pielichowski, 2014). In general, a well-designed TES system offers the following advantages (Rosen et al., 2000):

(a) lower energy costs, (b) reduced auxiliary energy consumption, (c) (d) increased flexibility of operation, (e) lower initial and maintenance costs, (f) compact equipment size, (g) increased efficiency and effectiveness of equipment utilization, (h) conservation of fossil fuels, and (i) reduced pollutant emissions.

2.5.2 Materials

The latent heat material used for thermal energy storage is called phase change material (PCM). PCMs exhibit a high heat of fusion with the capacity, of storing and releasing large amounts of energy in a relatively small volume as latent heat during melting and solidification at a constant temperature, called the melting and solidification temperature respectively.

The selection of PCMs as the storage material in the research work has been based on the many advantages of latent heat storage (LHS) over sensible heat storage (SHS) as has already been enumerated in the previous section

2.5.3 Classification of PCMs

PCMs can be categorized as organic, inorganic or eutectic depending on the material nature as in Figure 2.5. Both organic and inorganic materials can be used for thermal storage at low, medium and high temperature but with different characteristics and performances

Organic PCM consists of all PCM that contains carbon atom. The organic PCM are further grouped into paraffin and non-paraffin. PCM with the universal chemical formula C_nH_{2n+2} are considered under paraffin (Raam Dheep & Sreekumar, 2014). In paraffin, the melting point and heat of fusion increases as the number of carbon atoms increases. Non-paraffin PCM comprises the compounds with functional groups such as glycols, esters, fatty acids and alcohols. Organic PCM's are obtainable for a wide range of temperatures which are stable up to 300 °C (Raam Dheep & Sreekumar, 2014). They are generally of low melting points and can only be used for room-heating thermal storage.

The main advantages of organic PCMs are; chemical stability, high heat of fusion, no tendency of super cooling, no tendency to segregate and compatibility with all containment vessels excluding plastic at high temperature. The disadvantages include high cost, low thermal conductivity, flammable sometimes and corrosive to containers (Raam Dheep & Sreekumar, 2014)

Inorganic PCMs are materials which comprise of nitrates, metallic's and salt hydrates. They can be utilised in higher temperatures applications up to 1500°C. Inorganic PCMs have superior performance in terms of ease of availability, high thermal conductivity, lower volume change, low cost, high heat of fusion and sharp melting point. It is linked with disadvantages such as materials degradation, segregation, and decrease in heat of fusion after few cycles due to incongruent melting, corrosion of heat exchangers, low specific heat and super cooling (Raam Dheep & Sreekumar, 2014).

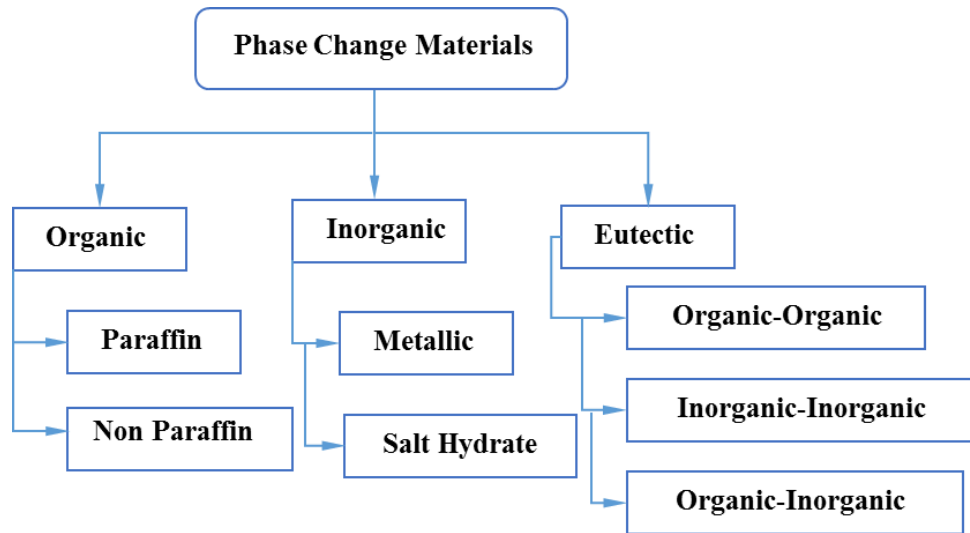


Figure 2.5 Classification of PCM

Eutectic PCMs are mixture of two or more compounds at a certain composition to give desired properties. The combination can be of any order like organic–inorganic, inorganic–inorganic and organic-organic. PCMs of this type melt and freeze congruently without any segregation (Raam Dheep & Sreekumar, 2014).

PCMs can further be classified based on the temperature range over which the phase transition of the TES occurs (Pielichowska & Pielichowski, 2014). The classification include: (i) low temperature PCMs (LT-PCMs) (ii) medium temperature PCMs (MT-PCMs) and (iii) high temperature PCMs (HT-PCM).

LT-PCMs have a phase transition temperatures below 15 °C and they are typically used in air conditioning applications and in the food industry. MT-PCMs operate in a phase transition temperature range between 15-90 °C. This set of TES system has been extensively investigated and developed. Application areas of MT-PCM systems include; energy saving storage applications for heating and cooling homes, thermal storage of solar energy, passive storage in bio-climatic building, protection of electrical devices and application in off-peak electricity for cooling and heating (Agyenim et al., 2010). HT-PCMs have a phase transition above 90 °C. They find applications in storage for solar power plants based on parabolic trough collectors, direct steam generation and CAES based on PCM TES and other industrial and aerospace applications. HT-PCMs comprise pure salts, salt eutectics, metals and metal eutectics. Amongst them, the PCMs with melting temperatures ranging from 200 to 550 °C can be possibly used as energy storage media for CAES plants Error! Reference source not found. shows some of the selected properties of medium to high temperature PCM that can be used in RE systems obtained from a list of compiled PCM properties from the authors (Agyenim et al., 2010). Full list of potential Phase Change Materials (PCM) for usage in thermal energy storage systems is given by the following authors: Sharma et al. (2009), Kenisarin (2010) and Agyenim et al. (2010). In particular, Kenisarin (2010), listed hundreds of inorganic salts and salt composites for LHS in the temperature range from 120 to 1000°C. Despite the important benefits of PCM in energy storage applications, they suffer from a limitation of poor thermal conductivity.

However, research findings by many scholars has shown that the low thermal conductivity of PCMs might be improved by the following methods (Kenisarin, 2010; de Gracia & Cabeza 2015):

- improving the thermal conductivity of the PCM by compositing high conductive materials,
- using intermediate heat transfer medium or heat pipes,
- maximizing the heat transfer area by use of fins and capsules

- Employing multiple PCMs.

Table 2.1 Thermo physical properties of PCMs investigated for different applications (Agyenim et al., 2010)

Compound	Melting temp, (°C)	Heat of fusion, (kJ kg ⁻¹)	Specific heat capacity, (kJ kg ⁻¹ K ⁻¹)		Thermal conductivity (W m ⁻¹ K ⁻¹)		Density, (kg m ⁻³)	
			l	s	l	s	l	s
Mg(NO ₃) ₂ ·6H ₂ O	89	162.8		–	0.49	0.61	1550	1636
MgCl ₂ ·6H ₂ O	116.7	168.6	2.61	2.25	0.57	0.70	1450	1570
Erythritol	117.7	339.8	2.61	2.25	0.33	0.73	1300	1480
Na/K/NO ₃ (50:50)	220	100.7		1.35		0.56	-	1920
ZnCl ₂ /KCl(32:68)	235	198	-	–		0.8	-	2480
NaNO ₃	310	172	1.82	1.82		0.5	-	2260
KNO ₃	330	266	1.22	1.22		0.5	-	2110
NaOH	318	165	2.08	2.08		0.92	-	2100
KOH	380	149.7	1.47	1.47		0.5	-	2044
ZnCl ₂	280	75	0.74	0.74		0.5	-	2907
LiF-CaF ₂ (80:20)	767	816	1770	1.77	1.70	3.8	2390	2390

l=liquid, s=solid

Each type of PCM has their own advantages and limitations, therefore the selection of a particular type of PCM has to be carried out based on the requirements of a given application.

Chemical and thermal reliability have been the critical issues so far. Organic PCMs generally have low melting points and can only be used for room-heating thermal storage. For high temperature TES, molten salts have been extensively studied by researchers (Xu et al., 2015). When the application involves medium to high temperature heat sources like in solar salts, compressed air energy storage, nitrate and nitrite salt phase change materials have been widely investigated (Xu et al., 2015).

The choice of PCM for TES application depends on a number of factors. First it is required that the melting temperature of the PCM lie within the practical range of application of the TEST process (Agyenim et al., 2010). Once the PCM has been selected based on temperature range, other thermo physical properties has to be met as well. **Error!**

Reference source not found. summarises the desirable characteristics of PCMs for TES applications (Zalba et al., 2003).

Table 2.2 Desirable characteristics of PCM for TES application (Zalba et al., 2003)

Thermal properties	Physical properties	Chemical properties	Economic properties
Suitable temperature range	Low density	Good chemical Stability	Cheap
High change of enthalpy near temperature of use	variation	No phase separation	
High thermal conductivity in both liquid and solid phases	High energy density	Compatibility with container materials	abundant
	Small or no undercooling	Non-toxic, non-flammable, non-polluting	

2.5.4 Latent heat TES systems/modelling

As already discussed in the previous section, LH TES systems can be classified as single or cascade designs. Studies on the utilization of single/multiple PCM systems can be classified according to the geometry of the storage system. According to the literature, shell and tube systems, spiral, coil, double pipe, plate and packed bed or rectangular slabs have been used (Esen et al., 1998; Agyenim et al., 2010). However, the rectangular and cylindrical containers (Figure 2.6) are the most widely studied geometries in the literature with the shell and tube type accounting for over 70% probably because most engineering systems employ cylindrical pipes and heat loss from the shell and tube system is minimal (Agyenim et al., 2010). Three variants of cylindrical PCM container arrangements exist (Agyenim et al., 2010). In the first arrangement called the pipe model (Figure 2.6a), the PCM fills the shell and the HTF flows through a single tube. The second arrangement involves a case where the PCM fills the tube and the HTF flows parallel to it (Figure 2.6b). The third arrangement is called the shell and tube system. It is normally used to improve heat transfer in PCMs.

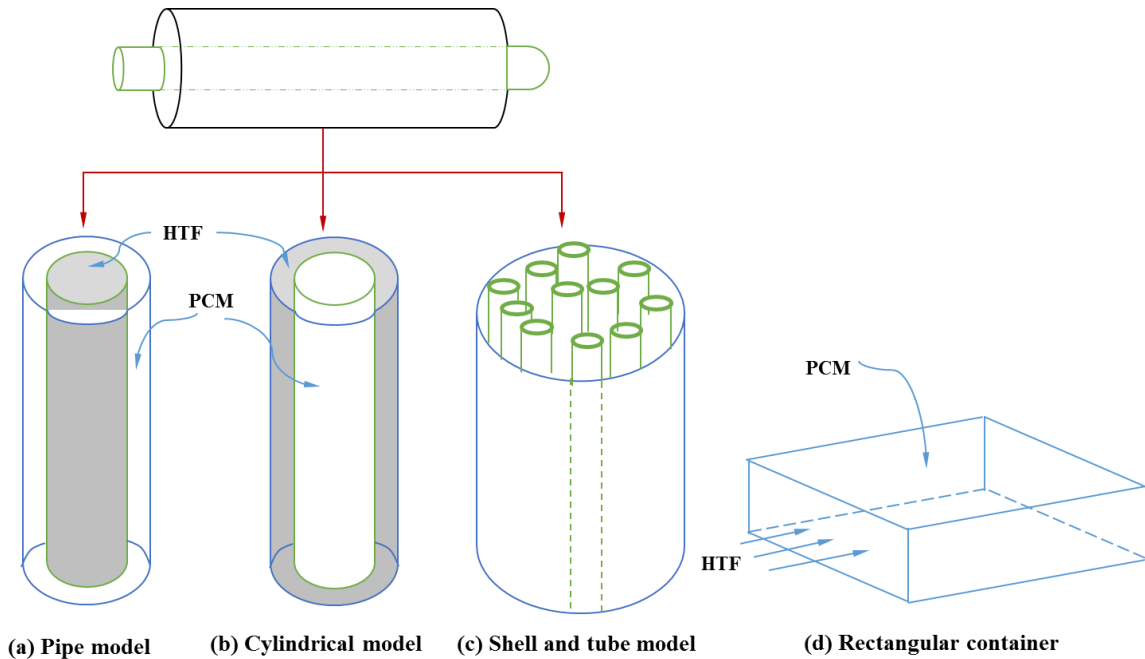


Figure 2.6 Classification of commonly used PCM containers in terms of the geometry and configuration

Esen et al.(1998) studied the first and second arrangements theoretically by comparing the effects of various thermal and geometric parameters such as cylinder radii, total PCM volume, mass flow rates and inlet temperatures of HTF on the storage time and reported that the pipe model is better because it showed a shorter melt time.

Thus the cylindrical LH packed bed system has been selected for the modelling of the LH thermal energy system of the A-CAES system in this research work

2.6 Mathematical modelling of LH-TES systems

Mathematical modelling involves representing the behaviour of a phenomenon, systems and devices in mathematical terms so that we can model, observe, predict or explain the phenomenon, device or process. The first numerical study on packed bed modelling was conducted by Schumann (1929). Building on Schumann's work, a number of mathematical models have been reported in the literature for calculating the thermal performance of a LH TES packed bed system (Tailor, 1981; Ismail & Henríquez, 2002; Benmansour et al., 2006; Felix et al., 2009; Xia et al., 2010; Karthikeyan & Velraj, 2012;

Oró et al., 2013 and Mertens, et al., 2014). These models can be categorized into two groups: single phase models and two phase models (de Gracia & Cabeza, 2016)

2.6.1 Single Phase model (SPM)

In the single phase models (SPM), the temperature of the HTF phase and the solid/PCM phase are considered the same. This model is suitable for studying fixed beds whose both thermal capacity and thermal conductivity is high and more than that of the HTF. The two- dimensional heat equation for the solid and HTF can be written in the following form (Ismail & Stuginsky Jr, 1999):

$$\begin{aligned} \epsilon \rho_F C_{p,F} \frac{\partial T}{\partial t} + (1 - \epsilon) \rho_{PCM} \frac{\partial H}{\partial t} + \rho_F C_{p,HTF} \cdot u \cdot \frac{\partial T}{\partial y} \\ = k_{eff} \frac{\partial^2 T}{\partial y^2} + k_{,eff} \left(\frac{\partial^2 T}{\partial r^2} + \frac{\partial T}{2 \cdot \partial r} \right) \end{aligned} \quad (2.1)$$

Where $\epsilon, \rho, C_p, k, u, y, r$ denote porosity, density (kgm^{-3}), specific heat at constant pressure ($\text{Jkg}^{-1}\text{K}^{-1}$), thermal conductivity ($\text{Wm}^{-1}\text{K}^{-1}$), velocity (ms^{-1}), axial distance (m) and radial distance (m) respectively. The subscripts F,PCM and eff denote fluid, Phase change materia and effective respectively.

2.6.2 Two phase model (TPM)

In contrast, in the two phase models (TPM), the temperature of HTF and PCM are not equal and treated separately. The boundary between the solid and the fluid interface is described by means of Nusselt correlations (Ismail & Stuginsky Jr, 1999; de Gracia & Cabeza, 2016). The TPM is further divided into three different typologies: the concentric dispersion model, the continuous solid phase model, and the Schumann's model (de Gracia & Cabeza, 2016).

2.6.2.1 Continuous solid phase models (CSFM)

In the CSFM, the fluid phases and the solid PCM spheres in the packed bed are treated as being in one phase with conduction as the heat transfer mechanism in both the axial and radial direction (Xia et al., 2010). The energy equations for the fluid (F) and solid phases (P) can be written as (Ismail & Stuginsky Jr, 1999), respectively.

$$\epsilon \rho_F C_{p,F} \left(\frac{\partial T}{\partial t} + u_\infty \frac{\partial T}{\partial x} \right) \quad (2.2)$$

$$= k_{,eff} \frac{\partial^2 T}{\partial x^2} + k_{f,x} \left(\frac{\partial^2 T}{\partial r^2} + \frac{1}{r} \frac{\partial T}{\partial r} \right) + h_p A_p (\theta - T) - U_w A_w (T - T_0)$$

$$(1 - \epsilon) \rho_P \frac{\partial H}{\partial t} = k_{P,x} \frac{\partial^2 T}{\partial x^2} + k_{P,x} \left(\frac{\partial^2 \theta}{\partial r^2} + \frac{\partial \theta}{r \partial r} \right) - h_p A_p (\theta - T) \quad (2.3)$$

Where h is heat transfer coefficient ($Wm^{-2}K^{-1}$) between fluid and particle, U is overall heat loss coefficient ($Wm^{-2}K^{-1}$), A is area (m^2), r is radius (m) and θ is temperature of PCM ($^{\circ}C$). Subscript P and w and x denote particle, wall and position respectively.

2.6.2 .2 Schumann's model

Schumann pioneered the mathematical basis for modelling the fluid-to-particle heat transfer in packed beds, with the single phase flow. His model is a one-dimensional model and involved two main assumptions (Schumann, 1929; Taylor, 1981 and Ismail & Stuginsky Jr, 1999):

- Fluid is in plug flow and
- No temperature gradients in the solid phase

Implementing the above assumptions simplify the numerical equations describing the heat transfer in the HTF and solid to a simple system of partial differential equations that can easily be solved using elimination or substitution methods. The resulting system of equations for the HTF and PCM appear in the form of Eq 2.4 and 2.5 respectively (Ismail and Stuginsky Jr 1999):

$$\epsilon \rho_F C_{p,F} \left(\frac{\partial T}{\partial t} + u_\infty \frac{\partial T}{\partial x} \right) = h_p A_p (\theta - T) - U_w A_w (T - T_0) \quad (2.4)$$

$$(1 - \epsilon) \rho_P \frac{\partial H}{\partial t} = -h_p A_p (\theta - T) \quad (2.5)$$

Barbour et al. (2015) used Schumann's model in their work on Adiabatic Compressed air Energy storage with packed bed thermal energy storage.

2.6.2.3 The Concentric Dispersion model (CDM)

The CDM is based on a two-phase model and it is the most widely practiced models in the analysis of transient problems of heat and mass transfer in packed beds (Wakao and Kagei, 1983). The CDM models allow for thermal gradients inside the solid particles (Ismail & Stuginsky Jr, 1999). It is developed by considering axial conduction in the fluid phase but neglecting axial conduction in solid phase (Tailor, 1981). Hence a differential equation may be written by energy balance for the fluid phase.

Fluid phase:

$$\frac{\partial T}{\partial t} = D_{af} \frac{\partial^2 T}{\partial x^2} - u \frac{\partial T}{\partial x} - \frac{h_{pf} A_p}{\epsilon \rho_F C_{p,F}} (T - \theta) - U_w A_w (T - T_0) \quad (2.6)$$

Solid phase:

$$\frac{\partial \theta}{\partial t} = \alpha_p \left(\frac{\partial^2 \theta}{\partial r^2} + \frac{2}{r} \frac{\partial \theta}{\partial r} \right) \quad (2.7)$$

Where α represents thermal diffusivity ($m^2 s^{-1}$)

The CDM is implemented on two assumption (Wakao and Kagei, 1983);

- i. The fluid have dispersed plug flow and
- ii. The intraparticle temperature profile is symmetric

However, in practical application, the axial heat conduction takes place in both phases (Tailor, 1981). To make up for this inadequacy, solid phase axial heat conduction has to be superficially included in the fluids thermal dispersion term by Wako in his DCM by assuming that the axial conduction in the solid phase is proportional to the temperature gradient in the fluid phase (Wakao & Kagei, 1983). Hence, Wakao and Kagei (1983) proposed a modified axial fluid dispersion coefficient D_{af}^* to replace D_{af} in Eq 2.6.

$$D_{af}^* = \frac{k_f}{\epsilon \rho_F C_{p,F}} + 0.5 D_p u \quad (2.8)$$

The first and second terms in the RHS of Eq 2.8 are the contribution independent of flow and the turbulent contribution given by an axial Peclet number of 2.0 respectively. As in Eq 2.9 and 2.10 respectively (Tailor, 1981).

$$k_{eaf} = D_{af}\epsilon\rho C_p \quad (2.9)$$

$$Pe_{af} = \frac{GC_p D_p}{k_{eaf}} = \frac{uD_p}{D_{af}} \quad (2.10)$$

Where k_{eaf} is effective axial fluid thermal conductivity ($Wm^{-1}K^{-1}$) and D is diameter (m), Pe_{af} is effective axial fluid peclet number and G is superficial mass velocity($kgs^{-1}m^{-2}$). Subscripts e, a, f stands for effective, axial and fluid respectively.

The CDM is the only one that solves for the temperature distribution inside the solid particles. However the phase change process must be incorporated in the solution method. In the numerical modelling using CDM, the cylindrical vessel containing the solid (PCM) is divided into elements in the axial direction in which fluid temperature is considered uniform (de Gracia & Cabeza, 2016). All the PCMs at the same height are treated to behave similarly and the energy equation must only be solved for a single sphere at each axial position of the cylindrical vessel. Once obtained, its temperature profile represents that of all other PCMs at the same axial location. Table 2.3 highlights the comparison between the three different models.

A good number of LH TES system using either the single phase models or any of the four variants of the two phase models already reviewed have been designed. The different solution methods applied include analytical, experimental and numerical using one-dimensional, two-dimensional or three-dimensional models. Farid and Kanzawa (1989) carried out a mathematical modelling of the thermal performance of a cylindrical heat storage module. The heat storage unit were filled with cylindrical PCM capsules of different melting temperatures, with air flowing across them for heat exchange. The mathematical model developed was based on solving the heat conduction equation in both liquid and solid phases in cylindrical coordinates, while accounting for the radial temperature distribution in both phases. They showed that a substantial improvement in charging and discharging rate when multiple PCMs of different melting temperatures were used. This is in agreement with the work of Gong and Mujumdar (1996b) who carried out numerical study of multiple PCMs in the shell side of a cylindrical container and discovered that at a steady reproducible state, the charge and discharge rates can be significantly enhanced using composite PCMs with different melting points as compared

with using a single PCM. Notably, the magnitude of the enhancement depends on the arrangements of the PCMs, their thermo physical properties and the boundary conditions applied.

Another similar numerical study by Fang and Chen (2007) indicated that the melting temperatures and melted fraction also play a significant role in the performance of the LH TES unit. Hence, proper selection of the multiple PCMs is critical to the performance improvement of the LH TES unit. Felix et al. (2009) carried out a numerical investigation of a packed bed LH TES system using paraffin wax PCM capsules. In the model the energy balance equation for the HTF and PCM were represented with fundamental equations similar to those of Schumann, the only difference being that the phase change process of PCM inside the capsules were analysed by enthalpy method. The equations are numerically solved, and the results obtained concluded that the phase change temperature range of the PCM must be accurately known to be able to model the performance of the system accurately. In a related study using Schumann's model, Barbour et al. (2015) numerically simulated an adiabatic compressed air energy storage with sensible heat packed bed thermal energy storage. The result obtained was validated against analytical solution and suggest that an efficiency in excess of 70% could be achieved by the system, which is more than several previous estimates for A-CAES systems using indirect-contact heat exchangers. In furtherance of their study, an exergy analysis carried out showed that the highest losses occur in the compressors and expanders (accounting for nearly 20% of the work input) and not in the packed beds.

Wu et al. (2014) applied a two dimensional transient DCM model adapted to account for the phase change process within PCM capsules to examine the phase change front and distribution temperature within each capsule. Molten salt was used as the HTF and results of their analysis suggested that an increase in effective discharging efficiency of the system can be attained by increasing the phase change temperature (PCT), reducing the inlet velocity of the molten-salt HTF or the diameter of the capsule.

To exploit off-peak electrical energy for space heating, Costa et al. (1998) designed a LH TES system using enthalpy formation and a fully implicit finite difference technique. Comparison was made of the thermal performance of the TES unit, with and without fins. It was found that the magnitude of the melt fraction obtained with TES with fins dominated

that without fins. In another related study with objective to solve intermittent energy supply problems associated with concentrated solar power plants, Bellan et al. (2015) experimentally and dynamically analysed the thermal performance of a packed bed LH TES operating at a high temperature. Air was used as the HTF and the PCMs used are spherical capsules encapsulated by sodium nitrate. Transient two-dimensional continuous solid phase models were deployed and results obtained was validated against experimental results. In furtherance of their analysis, a parametric study on the influence of key parameters (mass flow rate, Stefan number, thickness and the thermal conductivity of the shell) were undertaken.

It was concluded that that the Stefan number greatly influences the overall heat storage capacity of the TES due to sensible heat. In addition it was reported that the thermal performance of the system was significantly affected by shell properties of the capsule. That is; as the shell thickness increases (decreases), the thermal conductivity of the shell becomes low (high).

The work of Peng et al. (2014) on the performance of a LH packed bed TES system utilizing molten salt as a HTF has indicated that decreasing the diameter of PCM capsule, fluid inlet velocity, or increasing the storage height improves the performance efficiency of the system. A numerical and experimental performance analysis was carried out by Ismail et al. (2001) using finned tube for application in TES systems. The model was based on pure heat transfer conduction mechanism, the control volume method and the enthalpy formulation approach

Table 2.3 Comparison of Schumann's model, Continuous solid phase models and concentric dispersion model

	Schumann's model	Continuous solid phase models	Concentric dispersion model
Assumptions	<ul style="list-style-type: none"> • Fluid is plug flow • Temperature gradient does not exist within the solid/particles • No heat conduction in the radial direction, • No heat conduction in the fluid 	<ul style="list-style-type: none"> • Solid behaves as a continuous medium and not as a medium composed of independent particles. • Fluid is in dispersed plug flow • Axial conduction in both the solid and liquid phases are taken into account through the inclusion of an effective thermal conductivity in the solid and fluid energy equation 	<ul style="list-style-type: none"> • thermal gradient inside the solid particles • Intra-particle temperature is symmetrical along the radial direction
Computation time	least	High	Highest
Complexity and accuracy	Simplest and least accurate	More complex and accurate than Schumann's model	Complex and most accurate
Allowance for Dispersion	No account is taken of axial conduction and dispersion in the solid energy equation (Wakao & Kaguei, 1982)	No account is made of dispersion and the effective thermal conductivity of the liquid and solid are to be determined experimentally	Allows for dispersion

A numerical model of a shell and tube LH TES based on the conservation of energy equations was developed and validated with experimental data by the authors (Adine and El Qarnia 2009). The shell side of the cylindrical TES tube was packed with two PCMs with different melting temperatures of 50 °C and 27.7 °C respectively and water was the HTF. Numerical investigations were carried out by the authors to study the effect of critical parameters on the performance of the unit with one and two PCMs respectively. Parameters studied include the inlet mass flow rate and temperature of the HTF and the proportion mass of PCMs.

Apart from the above quoted studies, there are still many studies on LH TES problems that we cannot comprehensively review here for want of space. Different numerical schemes have been used to deal with the phase change phenomenon in the mushy region. The schemes include the apparent capacity method, the effective heat capacity method, the heat integration method, the source based method, the enthalpy method. As a huge amount of outstanding research papers exist in this area, it is impossible to make a fully comprehensive review. Rather, the various schemes that have been used can be found in the work of the following Authors: Hu and Argyropoulos (1996) and Bannach (2014).

2.7 Summary

As discussed in the preceding Section, there have been many studies on A-CAES, biomass gasification and PCM TES. Also many hybrid studies on biomass and A-CAES has been done.

However, the concept of a hybrid adiabatic compressed air energy storage with PCM thermal storage and biomass gasification energy storage system for distributed combined heat and power application has gained very little interest so far. The present work aims to address the above gap by developing a comprehensive model for the integrated system capable of performing thermodynamic and economic analysis of the system.

Chapter 3

Modelling of PCM based thermal energy storage for A-CAES

3.1 Introduction

In this chapter, a charging mode of adiabatic compressed air energy storage (A-CAES) different from the conventional system and using a phase change material (PCM) based thermal energy storage (TES) is proposed. A mathematical formulation of the PCM TES for the A-CAES process is presented. In this formulation, the PCM based TES system under study is treated with a one dimensional dispersion concentric model (DCM). Equations at the various nodes for computing the temperature of the nodes are developed using an implicit finite difference method and coupled with appropriate initial and convective boundary conditions. Comparison is made between the proposed mode and the conventional mode to know which of the two charging modes is better. The effects of different arrangement of PCM in the thermal energy storage tank for the two modes have been discussed for charging processes.

The main contributions of the work presented in this Chapter are:

4. Comparison of the two different modes of operation of the LH TES system which has not been reported in the literature, to the best of the author's knowledge.
5. Although DCM has been used extensively in other areas of TES, to the best of the author's knowledge, no dispersion concentric model has been used in studies related to A-CAES.

Before using the model to carry out analysis on the thermal storage performance of the two modes, experimental validation of the model was carried out by comparing model predictions with experimental data from literature. At the end of this chapter the results of the comparison between the two charging modes proposed will be presented. The results will aid the design of the integrated A-CAES+BMGES system in chapter 5.

3.2 Two charging modes of A-CAES

Many authors (Gong & Mujumdar, 1996a; Liu et al., 2006; Nallusamy et al., 2007 and Peng et al., 2015), have investigated the influence of temperature and mass flow rate respectively on the performance of a latent heat (LH) thermal energy storage tank (TEST) and have established that the charging and discharging performance of the LH TES system increases with increasing the temperature or mass flow rate of the HTF (Nallusamy et al., 2007; Peng et al., 2015), respectively. Since both air mass flow rate (\dot{m}_f) and temperature (T) affect the performance of a LH TEST, what then happens when the inlet fluid temperature increases and the mass flow rate reduces simultaneously in the same charging process? To answer that question, two modes of operation of a thermal energy storage tank (TEST) will be investigated.

The block diagram of the physical system showing the two charging modes considered for an adiabatic compressed air energy storage system (A-CAES) is as shown in Figure 3.1. The two modes are referred to as mode 1 and mode 2 respectively.

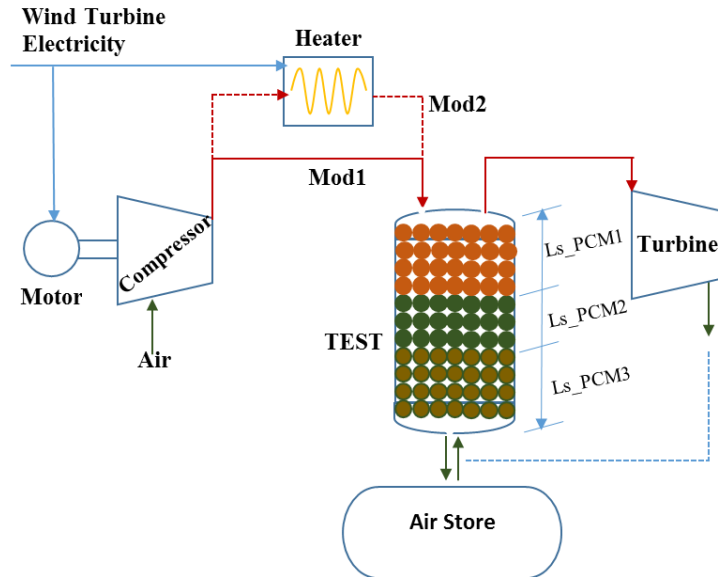


Figure 3.1 Schematic of TEST showing two charging modes

3.2.1 Model1

This mode is the conventional operating mode of the A-CAES system. During the energy-charge period, the excess electricity from a wind turbine power plant is used to

power the air compressor (AC) to compress air to a practicable very high temperature in the A-CAES system. In this conventional operating mode, hereafter called **mod1**, the whole excess electricity of the wind turbine is used to power the compressor to compress air and the thermal energy contained in the high pressure compressed air (CA) exiting the compressor is absorbed and stored in the latent heat (LH) TES unit. For a given pressure ratio and ambient conditions, the power input to the compressor determines the mass flow rate of air from the compressor. The higher the temperature and/or mass flow rate of the compressed air entering the TEST, the better will the performance of the TEST be. In this mode of operation, the maximum entrance temperature and mass flow rate of compressed air (CA) to the LH TEST is limited by the maximum limit of the CA exit temperature which is set by the possible maximum exit temperature limit of the compressor and pressure ratio respectively.

The maximum limit of the CA exit temperature are placed on the machine mainly by the manufacturer based on the maximum discharge temperature that is tolerable for the compressor material.

3.2.2 Mode2

In the second operating mode hereafter referred to as **mod2**, the shortcoming of operating mod1 is overcome. That is, the maximum temperature limit of the CA exiting the compressor and entering the TES tank is overcome. This is achieved by using some part of the residual electricity of the wind turbine to power the compressor to compress air while the remainder is used to operate an electric filament to heat up the hot CA exiting the AC to a higher temperature before it enters the TEST. Although, this method leads to a higher CA inlet temperature to TEST, it however comes with a penalty of reduction in the mass flow rate of the compressed air from the compressor.

The high pressurised CA (HTF) is introduced into the bed from the top and it releases some of its heat to the PCM capsules as it flows past them exiting from the bottom port. Simultaneously, the solid PCMs absorb and store the heat from the air and melts to liquid phase. After exchanging heat with the PCMs, the now cold CA is stored in the air store (AS). During the energy-recovery period, the cold HTF from the AS enters the bed from the bottom and extracts the thermal energy already stored in the PCM. The extracted

energy which is contained in the CA is delivered to the air expander/turbine (AE) for generating the electricity back. The PCMs solidify on releasing all their energy to the HTF.

Having identified the two operating modes: mod1 with higher mass flow rate (\dot{m}_f) and low temperature (T) and mod 2 with higher temperature and low mass flow rate, it is necessary to evaluate them using charging duration, energy and exergy efficiency metrics to provide answer to the question; of the two operating modes which one is better and why? Although, the influence of temperature or mass flow rate on the performance of a LH TES system has been carried out by many authors (Nallusamy et al. 2007; Peng et al., 2015), these treatments have been carried out by varying one quantity and keeping the other constant. To the best of our knowledge, no treatment have been carried out for a case where both quantities (\dot{m}_f , T) vary inversely with each other like in the two modes as can be seen from the operating characteristics of the two modes contained in Table 3.1. Hence there is the need to investigate the dynamic thermal performance of the two alternative charging modes of a PCM based TES system for A-CAES application in order to know the operating characteristics of the two modes and which is best between them.

To reveal the thermal response of the TEST for the two operational modes and the phase change process within PCM capsules during the charging and discharging process, a transient two-dimensional concentric dispersion model (CDM) of a TEST system using multiple heat storage PCM is developed. The PCMs are immiscible and separated by thermally thin barriers. Thermodynamic performance calculations have been carried out to study and analyse/know the operating characteristics of the two different operation modes. Performance indicators such as storage efficiency and overall energy and exergy efficiency were calculated and reported. In addition, the effects of capsule arrangement and number of multiples on the performance of the two modes are evaluated. Numerical results offer guidance for selection of the appropriate operating mode.

3.3 Description of the PCM based TES tank unit

The thermal energy storage tank (TEST) is made of a cylindrical steel tank which has a thermal conductivity of $16.0 \text{ Wm}^{-1}\text{K}$, a density of 7920 kgm^{-3} and a specific heat of $499 \text{ Jkg}^{-1}\text{K}$ (Wei et al., 2005). Its height and diameter are determined as 10 mm and 6 mm,

respectively as detailed in section 3.4. The whole surface of the TES tank is covered with 0.05 m thickness of glass wool insulation and an outer covering of 0.001 m thickness of steel plate (Öztürk, 2005).

The TES tank is divided into three sections and filled with three different phase change materials (PCMs) referred hereafter as PCM1, PCM2, and PCM3, respectively. The heat stored in a LHS system consists of three terms (Sattler et al., n.d.); the sensible heat required to heat up the PCM from a solid state at temperature (T_s) to the melting temperature (T_m), the latent required for melting the PCM (L_m) and the sensible heat required for heating the liquid PCM to the storage maximum temperature (T_1).

The temperature ($T_{TEST,i}$) and mass flow of air (\dot{m}_{AC}) entering the TEST for mod1 has been estimated using the following two equations respectively.

$$T_{TEST,i} = T_{amb} \left[1 + \frac{\beta^{\frac{\gamma-1}{\gamma}} - 1}{\eta_{isen}} \right] \quad (3.1)$$

$$\dot{m}_{a,AC} = \frac{\dot{W}_{WT} \eta_{isen} \eta_m}{C_{p,a} \left(\beta^{\frac{\gamma-1}{\gamma}} - 1 \right)} \quad (3.2)$$

Where \dot{W} , T , β , γ , η , C_p denote power (W), temperature (K), stage pressure ratio, ratio of air specific heat, efficiency and constant pressure specific heat ($\text{Jkg}^{-1}\text{K}^{-1}$) respectively. Subscripts WT, i, m, isen, amb AC, and a denote wind turbine, in/inlet/input, mechanical, isentropic, ambient, air compressor and air or HTF respectively. The power consumed by each air compressor (AC) stage (\dot{W}_{AC}) is given as follows:

$$\dot{W}_{AC} = \dot{m}_{a,AC} [h_e - h_i] \quad (3.3)$$

Where h represents enthalpy (Jkg^{-1}) and subscript e denotes exit.

In mod2, assuming negligible losses, heat is transferred from the hot air electric heater to the hot compressed air from the compressor at a rate according to the following equation:

$$Q_{heater} = \dot{m}_{a,AC} C_{p,a} (T_{a,e} - T_{a,i}) \quad (3.4)$$

The heater raise the temperature of air by a certain temperature difference (ΔT) for a given power input and mass flow rate. Assuming a fraction of the wind turbine power used to power the electrical heater to be denoted by ψ , the temperature and mass flow rate

of the HTF entering the bed is given by equations 3.5 and 3.6 respectively. Table 3.1 shows the summary of the operating characteristics of the two modes. A hypothetical heater power of 10% of the wind turbine power is selected for the analysis.

$$T_{\text{TEST},i} = T_{\text{amb}} \left[1 + \frac{\beta^{\frac{\gamma-1}{\gamma}} - 1}{\eta_{\text{isen}}} \right] + \psi \dot{W}_{\text{WT}} / \dot{m}_{\text{a,AC}} C_{p,a} \quad (3.5)$$

$$\dot{m}_{\text{a,AC}} = \frac{\dot{W}_{\text{WT}} \eta_{\text{isen}} \eta_m [1 - \psi]}{C_{p,a} \left(\beta^{\frac{\gamma-1}{\gamma}} - 1 \right)} \quad (3.6)$$

Table 3.1 Operating characteristics of the two modes

Characteristics	mod1	mod2
Power of wind turbine (\dot{W}_{WT}), MW	10	10
Heater power , (Q_{heater}) MW	0	1
TEST Inlet Temperature ($T_{\text{TES},i}$), °C	327	360
HTF mass flow into bed ($\dot{m}_{\text{a,AC}}$), kgs^{-1}	32.9	29.64
HTF mass flow out of bed ($\dot{m}_{\text{a,AC}}$), kgs^{-1}	32.9	29.64

The mass flow rate of HTF during the discharge operation is the same for the two modes but the temperature of the charging PCM is different.

3.4 The thermal capacity of the TEST

The maximum energy storage capacity of the TEST is based on the maximum thermal output obtainable from the A-CAES plant. For a given temperature of air input into TEST ($T_{a,i}$), using heat exchanger effectiveness (ε) relations and assuming $\dot{m}_{\text{a,AC}} C_{p,a} > \dot{m}_{\text{PCM}} C_{p,\text{PCM}}$, the maximum exit temperature of air from the TEST during charging is gives as:

$$T_{a,e} = T_{\text{TEST},i} - \varepsilon [T_{\text{TEST},i} - T_{\text{PCM},c}] \quad (3.7)$$

Where $T_{\text{PCM},c}$ is the initial temperature of the PCM or TEST in °C. Thus, the maximum thermal capacity of the TES ($Q_{\text{Th,TEST}}$) is estimated as follows:

$$Q_{Th,TEST} = \dot{m}_{a,AC} C_{p,a} \varepsilon [T_{TEST,i} - T_{PCM,c}] \times t_{ch} \quad (\text{kWh}) \quad (3.8)$$

From the above equation, the average thermal capacity of 44 MWh is estimated for the TEST when the initial temperature of the PCM is 175 °C at a maximum charging time of 12 hours and ε of 0.7. To reduce the size of the TEST, the thermal capacity is split into two, such that half the mass flow rate from the compressor now split flow between them and each having a thermal capacity of 22 MWh.

The mass of the PCM (m_{PCM}) required to store the thermal capacity is estimated using (Sattler et al., n.d.) :

$$m_{PCM} = \frac{Q_{Th,TEST}}{[C_{p,s} \cdot (T_m - T_s) + L_m + C_{p,l} \cdot (T_l - T_m)]} \quad (3.9)$$

Where L represents latent heat (Jkg^{-1}) and subscripts s, m and l denote solid, melting and liquid respectively. Thermo-physical properties of NaNO_3 with melting point of 306 °C has been used to estimate the mass of PCM required. Table 3.2 contains the Thermo-physical properties of NaNO_3 . From the known mass of the PCM, the average volume of the thermal energy storage tank (V_{TEST}) required is estimated using:

$$V_{TEST} = \frac{m_{PCM}}{f_{uf} \rho_{PCM}} \quad (3.10)$$

Where ρ is density of the PCM (kgm^{-3}) and f_{uf} is the actual storage material utilization coefficient, taken as 0.95 (Sattler et al., n.d.). Using length to diameter ratio (L/D) of 1.875, an average height and diameter of 10 and 6 m respectively is calculated for the TEST in the two modes.

For multiple PCM storage, the volume of the TEST is shared by the PCMs according to the height each occupy in the TEST. If the PCM are desired to occupy the same height in the storage tank, the total volume is divided equally according to the number of the PCMs. In this case, the height of the tank occupied by the PCMs remains the same but their masses vary since their densities are not the same.

3.5 Selected phase change materials

The performance of LH thermal storage systems depends on the thermo physical properties of the PCM selected including the melting range. In the selection of PCM used for the present analysis, the first step is the consideration of PCMs whose temperature fall

in the range of application. Then some desirable properties of a good PCM for thermal energy storage applications were taken into consideration. The properties considered include: high latent heat of fusion per unit mass, chemical stability, small volume changes during the phase transition, self-nucleating and fast phase transition, little sub cooling during freezing, availability in large quantities, non-corrosiveness to construction materials, easily packaged and inexpensive (Öztürk, 2005). Inorganic type of PCMs were selected because of their advantages as already enumerated in chapter 1. Table 3.2 shows the some of the most important properties of the selected PCMs. The properties were taken from the following sources: Michels and Pitz-Paal (2007), Peng et al. (2015) and Xu et al. (2015) for NaNO_3 , NaNO_2 and $\text{NaNO}_3 - \text{KNO}_3$ respectively.

Table 3.2 Selected PCM properties

No	PCM	$T_m(^{\circ}\text{C})$	$c_p(\text{kJkg}^{-1}\text{K})$		$k(\text{Wmk}^{-1})$		$L_m(\text{kJkg}^{-1})$		$\rho(\text{kgm}^{-3})$	
			s	l	s	l	s	l	s	l
1	NaNO_3	306	1100		0.5		172		2100	
2	NaNO_2	277-303	1385	1514	0.56	0.48	199.6		2097	1873
3	NaNO_3 – KNO_3	220	950	1360	0.56		100.7		1790	

s in the table denote solid and l, liquid.

PCM capsules can come in four different forms; sphere, cylinder, plate and tube. In the present analysis, spherical PCMs capsules has been investigated. The capsule material is made of stainless steel, with a thermal conductivity of $16.0 \text{ Wm}^{-1}\text{K}^{-1}$, density of 7920 kgm^{-3} and a specific heat of $499 \text{ Jkg}^{-1}\text{K}^{-1}$ (Wei et al., 2005).

3.6 Previous models on LH TES based on CAES

The design of a CAES system using LH TES system has gained attention lately. An interesting feature of this system is that it stores excess electrical energy from wind turbine and at the same time helps to reduce the operating temperature of the compressed air entering the next stage compressor which results in increased efficiency of the compression process. An overview of the existing models that are well related to the current

work are presented in this section. The relevant models include models developed by Barbour et al. (2015), Peng et al. (2015) and Tessier et al. (2016).

Peng et al. (2015) numerically modelled the heat storage performance of compressed air in a packed bed system using phase change material (PCM) particles filler. An unsteady continuous two phase model was used to describe the heat transfer in the packed for the HTF and the solid. Implicit difference formulation was applied to discretize the equations and the resulting tri-diagonal matrix was solved numerically using **complex Jacobi iteration method**. It was found that the charge efficiency increases with an increase in compressed air inlet pressure.

In developing Peng et al. (2015) model, the following assumptions were made:

(i) The properties of CA are homogeneous and calculated at an average temperature $T_{ave} = (T_{in} + T_{out})/2$. (ii) Variation of temperature along the radial direction is neglected (iii) **Uniform distribution porosity is applied to the packed bed** (iv) the volume change of fluid and solid particle caused by the temperature change is ignored (v) Internal heat generation is not considered in packed bed and (vi) Radiation is negligible.

In another study, Tessier et al. (2016) carried out an exergy analysis of an A-CAES using a cascade of four PCMs. Unlike the above work of Peng et al. (2015), this research did not use numerical methods. Rather the temperature of the HTF and PCM were related to each other by heat exchanger temperature-effectiveness relations and the optimum melting temperatures of each of the four PCM were determined using a grid search algorithm. It was found by the authors that efficiencies of storage and recovery using this approach are as high as 85% representing a 15% increase over A-CAES using sensible heat (SH) TES.

Using Schumann's model (Schumann, 1929), Barbour et al. (2015) numerically simulated an adiabatic compressed air energy storage with sensible heat packed bed thermal energy storage. The model was validated against analytical solution. Results reported suggest that an efficiency in excess of 70% could be achieved by the system, which is more than several previous estimates for A-CAES systems using indirect-contact heat exchangers. In furtherance of their study, an exergy analysis carried out showed that the highest losses occur in the compressors and expanders (accounting for nearly 20% of the work input) and not in the packed beds.

3.7 Mathematical formulation

Among the three related model reviewed above, the very good work by Peng et al. (2015) is worth commenting on because it is related to energy storage in A-CAES using LH TES. In Peng's assumption (Peng et al., 2015) iii, Uniform distribution porosity was applied in the modelling. This assumption seem to be imprecise since according the authors (Klerk, 2003), the porosity of the bed is influenced by the mode of packing, the ratio of the bed to particle diameter (D/d), the shape of the particle, the particle size distribution, the height of bed and the roughness of the surface of the particle. In addition, a simpler method could be used than the **complex Jacobi iteration method** deployed in Peng et al. (2015) good work.

Hence the CDM has been selected to model the current PCM TES design problems with appropriate initial and boundary conditions. In particular, the variation in the porosity of the packed bed with the ratio of TEST to PCM diameter (D/d) ratio have been accounted for by using the following Equation (Benmansour et al., 2006):

$$\epsilon = 0.4272 - 4.516 \times 10^{-3}(D/d) + 7.881 \times 10^{-5}(D/d)^2 \quad (3.11)$$

In addition, the matrix inversion technique has been used because of its easiness of solution, against the complex interactive method adopted by Peng et al. (2015). As already afore mentioned in chapter two, the CDM is selected for our present research because of its wide acceptance due to the ease with which heat losses can be implemented in such models (Tailor, 1981). In addition, the CDM is the only approach that solves the thermal distribution inside the solid particles (Ismail & Stuginsky Jr, 1999).

A multi PCM TES has been considered in this work because storing thermal energy using multiple PCMs has been proven to be better and effective at recovering and storing thermal energy for power generation (Gong & Mujumdar, 1997a) and their use have gained increasing attention lately as a result of their potentially improved efficiency (Gong & Mujumdar, 1997a). Other reasons of using multiple PCMs have been given in chapter two.

3.7.1 Assumptions

A vital step in order to introduce the LH TEST model in the A-CAES component of the integrated system is to simulate its thermal behaviour and hence temperature fields of PCM and HTF during charging and discharging processes. To do so, the energy conservation differential equations are modelled for the heat transfer fluid (HTF), which is compressed air in this case and PCM with the following assumptions:

- The fluid flow is laminar and incompressible and the flow rate is constant with time
- Thermo-physical properties of HTF are temperature independent but evaluated at mean average temperature $T_{ave} = 0.5(T_{TEST,i} + T_{amb})$
- The convection effects existing during the melting of the PCM are accounted for via the use of an effective conduction coefficient (k_{ef}) in the energy equation.
- The PCMs in the TEST are immiscible and each is isotropic and homogenous;
- The thermo-physical properties of PCM's do not depend on temperature but differ for solid and liquid phases
- The PCM is originally in solid state
- Heat loss from the TEST reservoir is by conduction and convection only
- Thermal conduction in the PCM in the axial direction is ignored

3.7.2 Governing mathematical equations for HTF and PCM

From the foregoing assumptions, the governing mathematical energy conservation equation for the transfer of energy in the HTF is (Zanganeh et al., 2012):

$$\frac{\partial(\rho_a H_a)}{\partial t} + \frac{\partial(\rho_a v_a H_a)}{\partial z} = \dot{Q} \quad (3.12)$$

Where ρ , H , v_∞ , z , t denote density (kgm^{-3}), specific enthalpy (Jkg^{-1}), velocity (ms^{-1}), axial distance (m) and time (s) respectively. The two terms on the left hand side of Equation 3.12 represents the rate of change of specific enthalpy and the net enthalpy per space associated with the fluid flow in the control volume respectively. \dot{Q} Accounts for the net flux in and out of the fluid face due to conduction and transport. The net flux (\dot{Q}) is given as follows (Zanganeh et al., 2012) :

$$\dot{Q} = Ah_v dz \Delta T_{pa} + U_{wall} C_w dz \Delta T_{amb,a} + \nabla \cdot (k_{a,ef} \nabla T_a) \quad (3.13)$$

Through the specific enthalpy of the control volume given by $H_a = \epsilon Ah_a dz$ and mass flow rate given as $\dot{m} = \rho v_a \epsilon A$, the energy conservation equation for HTF becomes:

$$\begin{aligned} \frac{\partial(\epsilon Ah_a dz)}{\partial t} + \dot{m}_a \frac{\partial(h_a dz)}{\partial z} \\ = Ah_v dz \Delta T_{p,a} + U_w C_w dz \Delta T_{amb,a} + Adz \cdot \nabla \cdot (k_{a,ef} \nabla T_a) \end{aligned} \quad (3.14)$$

Where T and θ are the CA and PCM temperatures respectively. C_w is the circumference (m) of cylindrical bed, $\Delta T_{p,a} = (\theta - T_a)$ and $\Delta T_{a,amb} = (T_a - T_{amb})$, A is the superficial area of the bed (m^2), h is enthalpy (Jkg^{-1}), ϵ is porosity, z is axial coordinate (m), U is overall heat transfer coefficient ($Wm^{-2}K^{-1}$), v_a is superficial velocity of CA entering TEST in ms^{-1} , h_v is volumetric heat transfer coefficient ($Wm^{-3}K^{-1}$) and subscripts p, a, ef and w denote PCM, air, effective, and wall, respectively.

The PCM is modelled using the general equation for radially symmetric heat conduction in polar coordinates given as (Cengel, 2002):

$$\frac{1}{\alpha} \left(\frac{\partial \theta}{\partial t} \right) = \frac{1}{r^\sigma} \nabla \cdot (r^\sigma \nabla \cdot \theta) = \left[\nabla \cdot (\nabla \theta) + \frac{\sigma}{r} \nabla \theta \right], \text{ for } r \neq 0 \quad (3.15)$$

Where $\sigma=0$ for a plane wall, $\sigma=1$ for a cylinder, and $\sigma=2$ for a sphere (Cengel, 2002) and k is thermal conductivity ($Wm^{-1}K^{-1}$), ρ is density (kgm^{-3}) and α is thermal diffusivity in m^2s^{-1} which is expressed as $\alpha = k/\rho C_p$. Values of ρ , C_p and k are dependent on the temperature of PCM.

In Equations 3.15, the term on the left hand side represents the rate of change of enthalpy of the solid within the control volume while the term on the right hand side is the heat conduction in the radial direction (Ismail & Stuginsky Jr, 1999). The effective thermal conductivity of the air ($k_{a,ef}$) is calculated with the correlation proposed by Wakao and Kaguei (1983):

$$\frac{k_{a,ef}}{k_a} = \frac{k_{se}^0}{k_a} + 0.5 P_r Re_c \quad (3.16)$$

Where k is thermal conductivity ($Wm^{-1}K^{-1}$), $k_{s,e}^0$ is the effective stagnation thermal conductivity estimated from $k_{se}^0 = k_a \left[\frac{k_s}{k_a} \right]^q$ and subscript s denote solid.

$$q = 0.280 - 0.757 \log \epsilon - 0.057 \log \left[\frac{k_s}{k_a} \right] \quad (3.17)$$

The external convection heat transfer coefficient (h_c) is obtained for the relation proposed by beek for the case of fluid flow in between the spheres arranged in a random form (Beek, 1962):

$$h_c = \frac{k_a \text{Nu}_c}{d_c} \quad (3.18)$$

Where

$$\text{Nu}_c = 3.22 \text{Re}_c^{1/3} \text{Pr}_c^{1/3} + 0.117 \text{Re}_c^{0.8} \text{Pr}_c^{0.4} \quad (3.19)$$

For spherical particles of cubic arrangement,

$$\text{Nu}_c = 2.42 \text{Re}_c^{1/3} \text{Pr}_c^{1/3} + 0.129 \text{Re}_c^{0.8} \text{Pr}_c^{0.4} + 1.4 \text{Re}_c^{0.4} \quad \text{for } \text{Re}_c > 40 \quad (3.20)$$

Where Re is Reynolds number, Pr is Prandtl number. Perry and Green (de Gracia & Cabeza, 2016) proposed another correlation of the nusselt number that is a function of porosity of the bed:

$$\text{Nu}_c = \{6(1 - \epsilon)\} [2 + 1.1 \text{Re}_c^{0.6} \text{Pr}_c^{1/3}] \quad (3.21)$$

The volumetric heat transfer coefficient (h_v) for the capsule is estimated with:

$$h_v = \frac{3(1 - \epsilon)}{(r_{p,i} + x_p)} h_{ef} \quad (3.22)$$

Where x is PCM capsule thickness (m), $r_{p,i}$ is capsule internal radius (m) and h_{ef} is the effective heat transfer coefficient ($\text{Wm}^{-2}\text{K}^{-1}$) which is given as:

$$h_{e,f} = \frac{1}{R_{\text{conv}} + R_{\text{cond}}} \quad (3.23)$$

R_{conv} is the thermal resistance due to convection on the external surface of the PCM spherical shell and R_{cond} is the thermal resistance due to conduction through the shell thickness (Ismail & Henríquez, 2002). Thus;

$$R_{\text{cond}} = \frac{\left((r_{p,i} + x_p) - r_{p,i} \right)}{k_p} \left\langle \frac{r_{p,i}}{(r_{p,i} + x_p)} \right\rangle \quad (3.24)$$

$$R_{\text{conv}} = \left[\frac{r_{p,i}}{(r_{p,i} + x_p)} \right]^2 \left\langle \frac{1}{h_c} \right\rangle \quad (3.25)$$

The Reynolds number (Re) is calculated from the relation

$$Re = \rho v_a d_p / \mu \quad (3.26)$$

Where d_p is capsule diameter and μ is HTF viscosity. One of the problems of PCMs is their low thermal conductivity (k). For PCMs with large diameters, the overall heat transfer coefficients will be low because of the high internal thermal resistance (r/k) in the PCM balls. To account for this, the fluid-solid heat transfer coefficient is multiplied by a degradation factor $1/(1 + 0.2Bi)$ proposed by Jeffreson (1972) to obtain a new effective heat transfer coefficient. The modified effective heat transfer coefficients between air and the PCM spheres now becomes:

$$h_{ef,m} = \frac{h_{ef}}{(1 + 0.2Bi)} \quad (3.27)$$

Where $h_{ef,m}$ is the new effective heat transfer coefficient to replace h_{ef} in Eq. 3.22. The corrected effective heat transfer coefficient is used anywhere where h_{ef} is required.

3.7.3 Boundary and initial conditions

The specification of the correct initial and boundary conditions (IC and BC) is an important phase in describing the physical system of the thermal energy storage tank (TEST) being modelled and also crucial for the accuracy of the results obtained.

HTF

In the analyses, the physical domain of the TEST is a rectangular matrix with dimensions length (L) and time (t) as shown in Figure 3.2. During charging, the thermal energy storage tank (TEST) top and bottom surfaces are represented by the plane $x = 0$ and $x=L$, respectively. The compressed air enters the matrix at the top and exits at the bottom face $x = L$. The mass flow rate of air at all the nodes is assumed constant.

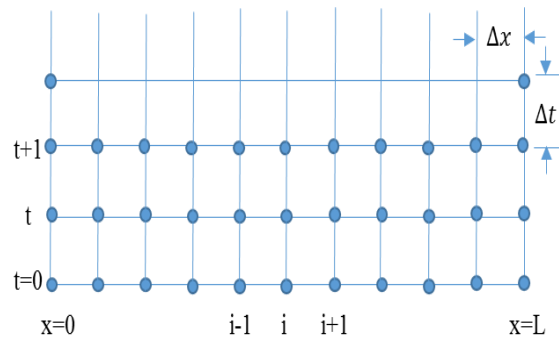


Figure 3.2 Finite difference grid for the TEST

The temperatures in all the nodes and the inlet at the initial state are equal to the initial temperature of the bed. Mathematically, the boundary and initial conditions for the matrix and fluid energy equation at the top/entrance is thus:

For the HTF;

$$T_a(x, t = 0) = T_{\text{initial}} \quad 0 \leq x \leq L \quad (3.28)$$

$$T_a(x = 0, t) = T_{\text{TEST},i}(t) \quad 0 \leq x \leq L \quad (3.29)$$

At the end node boundary of the TEST, the boundary condition applied is as follows:

$$\frac{\partial T(x, t)}{\partial x} = 0; \quad \text{at } x = L \quad (3.30)$$

PCM

For the PCM, we considered a cross section of the spherical ball with series of nodes, which span from the surface to the centre. For the melting process, the PCM is initially solid, at $t = 0$ and the PCM and the surrounding heat transfer fluid are all at the same initial temperature. For freezing, the PCM is liquid initially and its temperature is the temperature it was charged to during the charging mode. The exact value of this temperature is dependent on last condition of melting during the charging period. Mathematically, the initial conditions is expressed as follows:

$$\theta(r, t = 0) = T_{\text{initial}} = T_{\text{PCM},c} \quad 0 \leq x \leq L \quad (3.31)$$

At the surface of the PCM shell, a convective and conductive boundary condition is applied such the heat transferred from the PCM wall must equal the heat conducted and convected into the bed by the air. Thus:

$$-k_w \frac{\partial \theta(r, t)}{\partial r} = h_p(T_a - \theta_w) \quad \text{at } r=0 \quad (3.32)$$

A thermally adiabatic condition exists at the centre of the spherical shell inside the TEST such that;

$$\frac{\partial T(r, t)}{\partial r} = 0, \quad \text{at } r = R \quad (3.33)$$

The HTF outlet temperature after charging is maintained at or near the initial bed temperature, demonstrating efficient and complete absorption of the energy that is carried in by the HTF. The PCM outlet temperature after charging is also maintained at the initial

temperature of the HTF at the beginning of the charging phase. The reverse is the case during the discharging process.

3.8 Solution Method

Energy conservation Equations (3.14) and (3.15) for the air and PCM respectively, are coupled, nonlinear partial differential equations describing the flow and heat transfer in the TEST and PCM capsule. The common method for the solution of the equations are the finite-difference method, which allows the approximation of the partial derivatives through discretization by Taylor Series expansion involving the independent and dependent variables. This technique can be realized by Crank-Nicholson, implicit or Euler/explicit method (Ghoshdastidar, 1998), using forward, backward or central difference respectively and results into a set of algebraic equations in the dependent variable from which the final value of the temperature can be estimated.

Each of the methods has advantages and disadvantages. An explicit technique requires small time steps for a given value of Δx . Thus more computational time step is required to obtain the solution at a particular point in time. The crank Nicolson scheme despite being unconditionally stable gives erroneous results if the time step is too large. The implicit technique does not have a time-step limitation. It is also unconditionally stable but may require the solution of a large algebraic matrix (Ghoshdastidar, 1998) which can be easily solved using the many computing resources available today.

In this study, an implicit backward difference in space and forward difference in time finite difference technique is used to obtain solutions for the transient temperature history of the air and PCM in the TEST for the charging and discharging processes. The choice of the implicit method are due to its merits (Ghoshdastidar, 1998) over the other methods mentioned above.

3.8.1 Implicit difference equation formulation for the HTF

The storage tank is divided into a number of grid points of equal thickness (Δx) made up of two continuous independent variables (x, t) as shown in Figure 3.2. An implicit finite difference equation for each grid point (i, t) can be written for the equations of the HTF and PCM.

For the HTF phase, HTF equation (3.14) is discretized as follows:

$$\rho \epsilon A C_p \frac{T_i^{t+1} - T_i^t}{\Delta t} = -m \dot{C}_p \left(\frac{T_i^{t+1} - T_{i-1}^{t+1}}{\Delta x} \right) + A h_v (\theta_i^t - T_i^{t+1}) + \quad (3.34)$$

$$+ U_w C_w (\theta_\infty - T_i^{t+1}) + kA \left(\frac{T_{i+1}^{t+1} - 2T_i^{t+1} + T_{i-1}^{t+1}}{\Delta r^2} \right)$$

Rearranging and collecting like terms reduces to:

$$T_{i-1}^{t+1}(-A - B) + T_i^{t+1}(1 + 2B + A + C + D) + T_{i+1}^{t+1}(-B) \quad (3.35)$$

$$= T_i^t + \theta^t(C) + T_\infty(D)$$

Where

$$A = \frac{m \Delta t}{\epsilon \rho A \Delta x}, B = \frac{k \Delta t}{\epsilon \rho C_p \Delta x^2}, C = \frac{h_v \Delta t}{\epsilon \rho C_p} \text{ and } D = \frac{U_w C_w \Delta t}{\epsilon \rho C_p A} \quad (3.36)$$

A set of equations similar to Eq. 3.35 can be written for all the internal nodes of the storage tank. At the boundary nodes ($x=0$ and $x=L$), boundary conditions of section 3.8.1 are invoked thus;

At the end node, $x=L$, $i = i_{\max}$ and $\partial y / \partial x = 0$, $\rightarrow T_{i-1} = T_{i+1}$

Substituting $i=i_{\max}$ in Eq. 3.35 and replacing T_{i-1} with T_{i+1} , we arrive at the expression for the nodal temperature at the end of the TEST as in Eq.3.37

$$T_{i_{\max}-1}^{t+1}(-A - 2B) + T_{i_{\max}}^{t+1}(1 + 2B + A + C + D) = T_i^t + \theta^t(C) + T_\infty(D) \quad (3.37)$$

At any given time(Δt), Equations (3.35 and 3.37) can be written for each layer-giving rise to a system of $i \times t$ simultaneous equations.

3.8.2 Discretizing the PCM equation

Consider a cross section of the spherical ball with series of nodes, which span from the surface to the centre as in Figure 3.3.

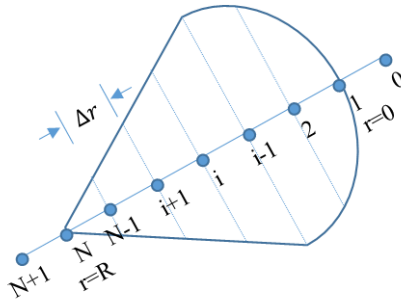


Figure 3.3 Grid points in the PCM

We imagine the spheres as being composed of n spherical shells of equal thickness Δr . Sweeping from the surface to the centre, the temperature at the interphase of these shells will be designated as θ_i ($i = 1, \dots, \dots, \dots, N$) with θ_1 at $r=0$ and θ_N at $r=R$

Thus;

$$dr = \frac{R}{N} \quad (3.38)$$

$$R_i = (i - 1)dr, \quad i = 1, \dots, \dots, N + 1 \quad (3.39)$$

$$\Delta r = R - (i - 1)dr, \quad i = 1, \dots, \dots, N + 1 \quad (3.40)$$

At any general interior grid point i , the PCM energy equation (3.15) can be discretized by substituting the implicit difference approximations for the derivatives (Ghoshdastidar, 1998). Thus:

$$\frac{\theta_i^{t+1} - \theta_i^t}{\Delta t} = \frac{k}{\rho C_p} \left\langle \frac{\theta_{i+1}^{t+1} - 2\theta_i^{t+1} + \theta_{i-1}^{t+1}}{\Delta r^2} + \frac{\sigma \Delta r}{2R_i} \left(\frac{\theta_{i+1}^{t+1} - \theta_{i-1}^{t+1}}{\Delta r^2} \right) \right\rangle \quad (3.41)$$

Collecting like terms, we have

$$\theta_{i-1}^{t+1} \left\langle -E - \frac{E\sigma\Delta r}{2r} \right\rangle + \theta_i^{t+1} \langle 1 + 2E \rangle + \theta_{i+1}^{t+1} \left\langle \frac{E\sigma\Delta r}{2r} - E \right\rangle = \theta_i^t \quad (3.42)$$

Where

$$E = \frac{k\Delta t}{\rho C_p \Delta r^2}$$

For pure solids, the value of E remains the same throughout the simulation but for a PCM, the values of E vary with the state of the PCM at the instant and are updated accordingly.

Equation (3.42) is descriptive of any i^{th} node except the surface ($r=0$) and centre ($r=R$) nodes. To solve for the temperature at the surface and centre nodes, the boundary conditions of the PCM as set out in Equations 3.32 and 3.33 are applied.

At the outer boundary, that is at the surface of the spherical PCM where $r = 0$ and $i=1$, substituting $i=1$ in equation 3.42 results to the following grid point finite difference equation at the outer boundary.

$$\theta_0^{t+1} \left\langle -E + \frac{E\sigma\Delta r}{2r} \right\rangle + \theta_1^{t+1} \langle 1 + 2E \rangle + \theta_2^{t+1} \left\langle \frac{E\sigma\Delta r}{2r} - E \right\rangle = \theta_1^t \quad (3.43)$$

The fictitious θ_0^{t+1} term in equation 3.43 falls outside the boundary of the nodes under consideration. To circumvent the fictitious value θ_0^{t+1} , we invoke the finite difference

discretisation of the convective boundary condition of equation 3.32 (Ghoshdastidar, 1998). Thus;

$$\frac{T_{a,i} - \theta_1^{t+1}}{1/hA} = \frac{T_{a,i} - \theta_2^{t+1}}{1/hA + \Delta r/kA} \quad (3.44)$$

$$(T_{a,i} - \theta_1^{t+1})(1/hA + \Delta r/kA) = (T_{a,i} - \theta_2^{t+1})(1/hA) \quad (3.45)$$

Solving and simplifying, the temperature describing the surface node reduces to;

$$\theta_1^{t+1}(1 + B_i) - \theta_2^{t+1} = B_i(T_{a,i}) \quad (3.46)$$

Where $B_i = h\Delta r/k$

From Eq. 3.46, the temperature of the node immediately below the surface ($N= 2$) can be solved at any time step, since the temperature of the HTF entering the first node at any time step is known.

At the centre, that is at $r=R$ and $i = N$, the term (θ_{i+1}^{t+1}) in the discretised equation (3.42) becomes a fictitious value since it falls outside the computational domain. However, since the PCM have symmetry at the origin; according to (Adebiyi, 1991, Benmansour et al., 2006), the following form of the heat equation is valid at the centre

$$\frac{\partial \theta}{\partial t} = (\sigma + 1)\alpha \frac{\partial^2 \theta}{\partial r^2} \quad (3.47)$$

Equation 3.46 is expressed in terms of its finite difference (FD) equivalent thus:

$$\frac{\theta_i^{t+1} - \theta_i^t}{\Delta t} = (\sigma + 1)\alpha \left(\frac{\theta_{i+1}^{t+1} - 2\theta_i^{t+1} + \theta_{i-1}^{t+1}}{\Delta r^2} \right) \quad (3.48)$$

Substituting the FD approximation of boundary condition of equation 3.33 ($\theta_{i-1} = \theta_{i+1}$) and simplifying reduces to the following finite difference formula for the nodal point located at the origin given as:

$$\theta_{i_{max}-1}^{t+1}[-2E(1 + \sigma)] + \theta_{i_{max}}^{t+1}[1 + 2E(1 + \sigma)] = \theta_{i_{max}}^t \quad (3.49)$$

The system of the discretized nodal equations (3.35, 3.37) for the HTF and (3.43, 3.46, 3.49) for the PCM take the matrix form $[A] [T] = [b]$. Here, $[A]$ is an i by t matrix containing the coefficient matrix that includes all implicit or unknown parts T at time $t+1$ while $[T]$ is an i by 1 column vector of the temperatures of each node at time $t+1$. The RHS term $[b]$ is an i by 1 column vector of all known parts of the system of the equations and i is the number of nodes in the simulation. Thus for i grid points, the finite difference system of the HTF and PCM to be solved may be written generally as (Buttsworth 2001):

$$\theta_{i-1}^{t+1}X_i + \theta_i^{t+1}Y_i + \theta_{i+1}^{t+1}Z_i = \text{RHS}_i^t \quad (3.50)$$

or

$$\begin{bmatrix} Y_1 & X_1 & 0 & 0 & 0 & 0 \\ X_2 & Y_2 & Z_2 & 0 & 0 & 0 \\ 0 & \dots & \dots & \dots & 0 & 0 \\ 0 & 0 & X_n & Y_n & Z_n & 0 \\ 0 & 0 & 0 & \dots & \dots & \dots \\ 0 & 0 & 0 & 0 & X_{i_{\max}-1} & Y_{i_{\max}} \end{bmatrix} \begin{bmatrix} \theta_1^{t+1} \\ \theta_2^{t+1} \\ \dots \\ \theta_n^{t+1} \\ \dots \\ \theta_{n-1}^{t+1} \end{bmatrix} = \begin{bmatrix} \text{RHS}_1^t \\ \text{RHS}_2^t \\ \dots \\ \text{RHS}_n^t \\ \dots \\ \text{RHS}_{i_{\max}}^t \end{bmatrix} \quad (3.51)$$

To advance the solution forward in time, matrix inversion method was applied by means of a Matlab written computer code to obtain the complete profile of the nodal temperatures by multiplying the RHS [b] matrix by the inverse of the LHS [A] matrix. The charging/discharging process is deemed completed if the set cut off temperature is attained. The cut off values of the discharging mode is set as the temperature of the charging HTF as reported in table 3.1 while that for the charging mode is set as the initial temperature of the PCM which set as 175 °C.

3.8.3 State judgment system (SJS)

The heat transfer process in phase change phenomenon is a very complex issue because the processes (solidification and melting) are nonlinear in the mathematical sense due to the fact that the solid/liquid interface moves depending on the speed at which the latent heat is absorbed or lost at the boundary (Agyenim et al., 2010). The location of the interface is unknown and forms part of the solution.

If the PCM discretised equations derived above are for sensible heat storage involving ordinary heating or cooling problem not involving phase change, the implementation of the heat transfer calculation is straight forward. However, since latent heat storage (LHS) involves phase change (melting or freezing), the calculation of the temperature histories is more complicated because the determination of the liquid fraction of each node is required to decide the thermal state of a node. To account for change of the phase problem in the PCM, several methods are employed to estimate the heat capacity.

They include the enthalpy method, the apparent heat capacity method and a combination of both methods (Peng et al., 2015).

In this research, effective heat capacity method is employed because of its simplicity to use as it does not necessitate alteration of the dispersion concentric energy equations. The technique is centred on the use of an apparent heat capacity over the melting range, directly proportional to the latent heat of phase change. It basically captures the storing and releasing of latent heat by augmenting the heat capacity and thermal conductivity over a temperature range.

To integrate the melting/solidification effect in the solution, a phase change state judgment system (SJS) is built in, which analyses the information in every node according to its present state to determine the state of the node. The algorithm makes use of equivalent temperature dependent thermo physical property of the PCM that meets the characteristics of the phase change Process inside the PCM.

The SJS can be explained with the aid of Figure 3.4 s can be seen, the phase change process is divided into three sub process for the charging and discharging mode. For the charge, the three sub processes are; the solid phase (region AB), the transition phase (region BC) and the liquid phase (region CD). Latent heat is characterised as a sensible heat (SH) spread over finite temperature difference($T_l - T_s$).

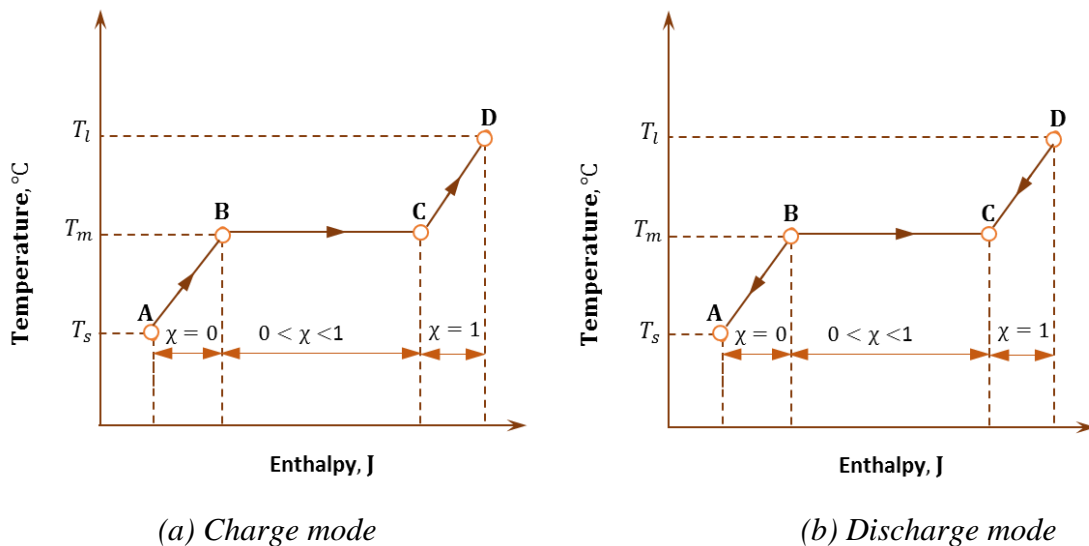


Figure 3.4 Node temperature vs. enthalpy for the SJS

In Figure 3.4, three temperature ranges of the effective specific heat within the system for charge(discharge) mode can be observed: Before melting/solidification (AB), during melting/solidification (BC) and after melting/solidification (CD).

In the charging mode (**Figure3.4a**)/discharge (**Figure 3.4b**) mode, in order to estimate the temperature of the PCM in each node, the temperature of the PCM (T_{PCM}) is compared to its melting/solidification temperature(T_m) and decision on the state of the PCM made with SJS. Table 3.3summarises the computational judgment of the (SJS) whereas the flow chart of the whole computational procedure is given in Figure 3.5.

Table 3.3 Computational decision of the SJS

Charge mode: $T_{HTF} > T_{PCM}$		
Region	Condition	decision
Solid- region (AB)	If $T_{PCM} \leq T_s$	$\chi = 0$ $C_p = C_{p,s}$
Transition Phase (BC)	If $T_s < T_{PCM} < T_l$	$\chi = 1/(T_l - T_s), 0 < \chi < 1$ $C_p = 0.5(C_{p,s} + C_{p,l}) + \chi \cdot L$
Liquid Phase (CD)	If $T_{PCM} \geq T_l$	$\chi = 1, C_p = C_{p,l}$
Discharge mode: $T_{HTF} < T_{PCM}$		
Region	Condition	decision
Liquid Region (DC)	If $T_{PCM} \geq T_l$	$\chi = 1$ $C_p = C_{p,s}$
Mushy region (CB)	If $T_l < T_{PCM} < T_s$	$\chi = 1/(T_s - T_l), 0 < \chi < 1$ $C_p = 0.5(C_{p,s} + C_{p,l}) + \chi \cdot L$
Solid region (BA)(If $T_{PCM} \leq T_s$	$\chi = 0$ $C_p = C_{p,l}$

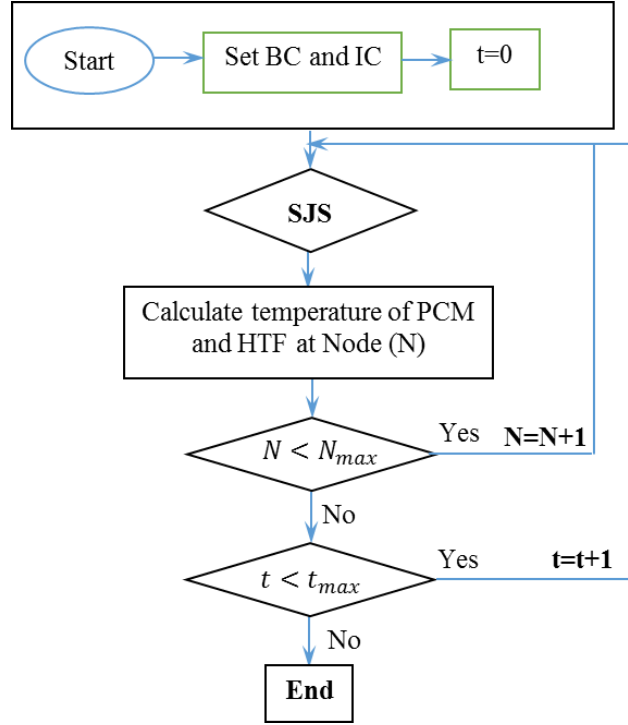


Figure 3.5 Flow chart of solution method

3.9 Estimation of model parameters

3.9.1 Density and thermal conductivity

The effective thermal conductivity is taken as the average thermal conductivity of the solid (k_s) and liquid (k_l) PCM. In addition, the density at the mushy state was taken as the average densities of the PCM in the liquid and solid states. They can also be estimated with the following expression:

$$k_e = k_s(1 - f_l) + f_l k_l \quad (3.52)$$

$$\rho_e = \rho_s(1 - f_l) + f_l \rho_l \quad (3.53)$$

The specific heat capacity at constant pressure ($C_{P,a}$), thermal conductivity (k_a), viscosity (μ_a) and density (ρ_a) for air respectively were estimated at the average temperature (T) using the following equations (Toyama et al., 1983; Toyama et al., 1987):

$$C_{P,a} = 0.9992 \times 10^3 T^0 + 1.4319 \times 10^{-1} T^1 + 1.1010 \times 10^{-4} T^2 - 6.7851 \times 10^{-8} T^3 \quad (\text{Jkg}^{-1}\text{K}^{-1}) \quad (3.54)$$

$$k_a = 0.0244 + 0.7673 \times 10^{-4}T \quad (\text{Wm}^{-1}\text{K}^{-1}) \quad (3.55)$$

$$\mu_a = 1.718 \times 10^{-5} + 4.620 \times 10^{-8}T \quad (\text{kgm}^{-1}\text{s}^{-1}) \quad (3.56)$$

$$\rho_a = \frac{353.44}{(T + 273.15)} \quad (\text{kgm}^{-3}) \quad (3.57)$$

Where T is in °C

3.9.2 The pressure drop along the bed

The pressure drop along the TEST depends on the geometry, arrangement and velocity of the HTF in the TEST (Beek, 1962). It is calculated using the Ergun pressure drop correlation expressed as follows:

$$\Delta P = \frac{LG^2}{\rho_a d_p} \left[\left(\frac{(1-\epsilon)}{\epsilon^3} \right) \left(175 + 150 \frac{((1-\epsilon))}{\text{Re}_m} \right) (\text{Nm}^{-2}) \right] \quad (3.58)$$

Where G is mass flux given as $\dot{m}_a/A_{\text{TEST}}$ ($\text{kgm}^{-2}\text{s}^{-1}$), Re_m is the modified Reynolds number defined as Gd/μ_a where μ_a is the fluid viscosity and d is the diameter of the PCM.

3.9.3 The overall heat loss coefficient (U)

The heat loss from the TEST was assumed to be by conduction and convection only. Heat was assumed to be transferred from the top lid cover, the side walls and the bottom with each part assumed to have a different heat transfer coefficient. The top part of the storage is treated as a flat circular plate (Cengel, 2002). Heat loss coefficient of the top cover (U_t) is calculated as follows:

$$U_t = \frac{1}{1/h_1 A_t + t_{\text{steel}}/k_{\text{steel}}A_t + t_{\text{ins}}/k_{\text{ins}}A_t + 1/h_t A_t} \quad (\text{WK}^{-1}) \quad (3.59)$$

The top natural convection heat transfer (h_t) coefficient is calculated as $h_t = \frac{\text{Nu}_L k}{L}$ ($\text{Wm}^{-2}\text{K}^{-1}$). Applying the Empirical correlations for the average Nusselt number for natural convection over the upper surface of a hot plate, as documented in (Cengel, 2002), the nusselt number is thus given as:

$$\text{Nu} = \begin{cases} \text{Nu} = 0.54\text{Ra}_L^{0.25} & (10^4 \leq \text{Ra}_L \leq 10^7) \\ \text{Nu} = 0.15\text{Ra}_L^{0.25} & (10^7 \leq \text{Ra}_L \leq 10^{11}) \end{cases} \quad (3.60)$$

The heat loss coefficient of the bottom (U_b) is calculated as follows:

$$U_b = \frac{1}{\frac{1}{h_1} A_b + \frac{t_{\text{steel}}}{k_{\text{steel}} A_b} + \frac{t_{\text{ins}}}{k_{\text{ins}} A_b} + \frac{1}{h_b} A_b} \quad (\text{WK}^{-1}) \quad (3.61)$$

The natural convective heat transfer coefficient of the bottom cover is given by the following formula (Incropera & DeWitt, 1996; Cengel, 2002):

$$\text{Nu} = 0.27 \text{Ra}_L^{0.25} \quad (10^5 \leq \text{Ra}_L \leq 10^{10}) \quad (3.62)$$

$$\text{Ra}_L = \frac{g\beta L^3 (T_s - T_\infty)}{\alpha\mu} \quad (3.63)$$

Where $L = \frac{A_s}{P}$ and A_s and P are perimeters and cross sectional areas respectively.

Heat loss coefficient from the side walls (U_s) based on the outer diameter (D_o) is given as (Morvay & Gvozdenac, 2008; Incropera & DeWitt, 1996) :

$$U_s = \frac{1}{R_i + R_1 + R_2 + R_o} \quad (3.64)$$

$$= \frac{1}{\frac{D_3}{D_1 h_{i,w}} + \frac{D_3 * \ln(D_2/D_1)}{2 * k_{\text{pipe}}} + \frac{D_3 * \ln(D_3/D_2)}{2 * k_{\text{insulation}}} + \frac{1}{h_{e,w}}} \quad (\text{WK}^{-1})$$

Where R_i = the resistance of a "boundary layer" of air on the inside surface, R_2 is the resistance due to steel tank thickness, R_3 is the resistance due to wool insulation thickness and R_o is the resistance of the "air boundary layer" on the outside surface of the wall

The heat transfer coefficient between the air inside the tank and the internal wall is estimated using a correlation proposed by Beek (1962) as cited in (Ismail & Stuginsky Jr, 1999) as follows:

$$h_{i,w} = \left(\frac{k_f}{d_{p,e}} \right) \left[2.576 \text{Re}^{1/3} \text{Pr}^{1/3} + 0.0936 \text{Re}^{0.8} \text{Pr}^{0.4} \right] \quad (3.65)$$

The external wall natural convection heat transfer coefficient ($h_{e,w}$) is estimated using a correlation in the open literature for a vertical cylinder (Incropera & DeWitt, 1996) given as $h_{e,w} = \frac{\text{Nu}_L k}{L}$ ($\text{Wm}^{-2}\text{K}^{-1}$).

Where Nu is given as (Cengel, 2002):

$$\overline{Nu} = \left\{ 0.825 + \frac{0.387Ra_L^{1/6}}{\left[1 + (0.492/Pr)^{9/16} \right]^{8/27}} \right\}^2 \quad (Ra_L \leq 10^9) \quad (3.66)$$

The heat loss from the TEST is estimated with the following equation:

$$Q_l = UA_{TEST}(T_{ave} - T_{amb}) \quad (3.67)$$

Where $U = U_s + U_t + U_b$ and T_{ave} is the average temperature of all the nodes of the TEST.

3.10 Performance metrics

The performance of a LH TEST system is commonly assessed in terms of energy input or output from the HTF and the accumulated energy stored or discharged from the unit during its operating cycle (Rady, 2009). The rate of energy input ($q_i(t)$) to the storage unit during the charging period (t) is estimated using the following equation (Dincer, 2002; Öztürk, 2005) :

$$q_i(t) = \dot{m}_{a,i} C_{p,a} (T_{a,i}(t) - T_{a,e}(t)) \quad (W) \quad (3.68)$$

The heat stored ($q_{st}(t)$) in the TEST was determined as follows (Öztürk, 2005):

$$q_{st}(t) = q_i(t) - q_{loss}(t) \quad (W) \quad (3.69)$$

The energy efficiency for the charging cycle ($EnEff_{ch}$) is estimated as the ratio of the stored energy at the end of the cycle ($q_{st}(t)$) to the net input and pumping energy ($q_{ch,p}$):

$$EnEff_{ch}(t) = \frac{q_{st}(t)}{q_i(t) + q_{p,ch}} \quad (3.70)$$

For the discharging process the energy efficiency is defined as the ratio between the energy recovered from the tank to the maximum energy stored, and can be expressed as:

$$EnEff_{dch}(t) = \frac{q_e(t)}{q_{st}(t) + q_{p,dch}} \quad (3.71)$$

Where

$$q_e(t) = \dot{m}_{a,i} C_{p,a} (T_{a,e}(t) - T_{a,i}(t)) \quad (W) \quad (3.72)$$

The round trip efficiency of the system (RTE) is defined as the ratio of the rate of energy recovered during the discharging mode to the rate of energy input during the charging mode. It can also be expressed as the product of the charging and discharging energy efficiency.

$$\text{RTE}(t) = \frac{q_e(t)}{q_i(t)} = \text{EnEff}_{\text{ch}} \times \text{EnEff}_{\text{dch}} \quad (3.73)$$

Energy efficiency alone is not enough to compare the performance of a LH TEST system. Exergy analysis has been proven as a better comparison metric since unlike the energy efficiency, it can reveal the exact point and extent of irreversibility in the TEST. In this work, the exergy efficiency of the charging process is calculated with respect to the exergy charged into the bed by the hot air and the thermal exergy loss.

The rate of input exergy during charging period, which comes from the hot compressed air to the TEST is given as:

$$\dot{E}x_i(t) = \dot{m}_{a,AC} C_{p,a} \left(C_{p,a} (T_{a,i}(t) - T_{a,e}(t)) - T_{\text{amb}} \left(C_{p,a} \ln \frac{T_{a,i}(t)}{T_{a,e}(t)} \right) \right) \quad (W) \quad (3.74)$$

The stored exergy in the TEST is calculated by the equation below (Rezaei et al., 2013):

$$\dot{E}x_s(t) = \dot{E}x_i(t) - Q_{\text{loss}}(t) \left[1 - \frac{T_{\text{amb}}}{T_{\text{ave}}(t)} \right] \quad (W) \quad (3.75)$$

Finally, the exergy efficiency (ExEff) is the ratio of the stored exergy to the exergy input:

$$\text{ExEff}(t) = \frac{\dot{E}x_s(t)}{\dot{E}x_i(t)} \quad (3.76)$$

During the discharging cycle, the exergy output of the TEST is calculated by the equation below:

$$\dot{E}x_e(t) = \dot{m}_{a,AE} C_{p,a} \left(C_{p,a} (T_{a,e}(t) - T_{a,i}(t)) - T_{\text{amb}} \left(C_{p,a} \ln \frac{T_{a,e}(t)}{T_{a,i}(t)} \right) \right) \quad (3.77)$$

In addition, the exergy efficiency of the discharging process is the ration of the exergy output to the stored exergy, taking the exergy loss into consideration as follows:

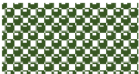

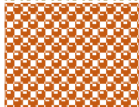
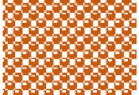

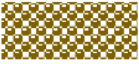
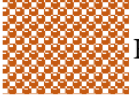
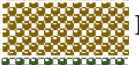
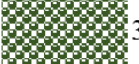
$$\text{ExEff}(t) = \frac{\dot{E}x_e(t)}{\dot{E}x_s(t)} \quad (3.78)$$

Finally the overall exergy efficiency of the charge and discharge cycle is the product of the charging and discharging exergy efficiency.

3.11 Parametric analysis

Numerical parametric study was carried out to investigate the influence of the height of the TEST that is occupied by each of the three PCM used on the performance of the two operating modes considered. Three different PCM height arrangement were considered here. Table 3.4 shows the summary of the PCM arrangements considered in the parametric analysis

Table 3.4 PCM arrangement (Ar) options for parametric analysis

Ar1	Ar2	Ar3
PCM1  3H/8 PCM2  H/8 PCM3  H/2	PCM1  H/2 PCM2  3H/8 PCM3  H/8	PCM1  H/2 PCM2  H/8 PCM3  3H/8

3.12 Results and discussion

3.12.1 Grid independent study

Research has shown that the accuracy of numerical simulation results might depend on both the time step and grid spacing used in the model. (Ghoshdastidar, 1998). To ensure the model prediction does not depend on the grid spacing and time step, a grid independent study was carried out by continuously refining the grid meshing until a negligible change in the variations in the temperature histories of the HTF is observed. As can be seen in Figure 3.6, as the number of nodes increased from 120 (axial) × 40 (radial) to 480(axial) × 40 (radial) there was a remarkable difference in the temperature histories of the HTF

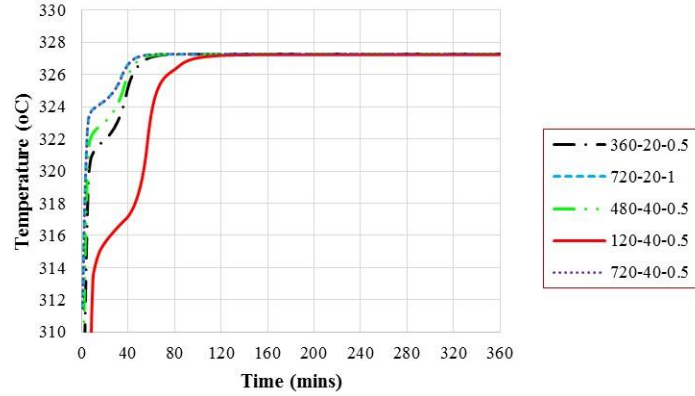


Figure 3.6 Temperature histories of the HTF at different computational grids

but between the nodes 480(axial) \times 40 (radial) to 720(axial) \times 40 (radial), a negligible difference in the histories of the HTF is observed.

In addition, as can be observed from Table 3.5 as the number of nodes of the TEST and the PCM in the axial and radial direction ($N_x \times R_x$) increased, respectively, from 120 (axial) \times 20 (radial) elements in the PCM with a time step of 1.0 min and 480 \times 20 elements with a time step of 1min, the percentage difference in the stored energy is about 0.55%.

Table 3.5 Stored energy at different computational grid.

Grid ($N_x \times R_x$)	Δt (mins)	Average stored heat (MW)
120 \times 40	0.5	2.379
360 \times 20	1	2.385
480 \times 20	1	2.386
480 \times 40	0.5	2.392
720 \times 40	0.5	2.395
720 \times 20	1	2.395
1200 \times 40	1	2.396
1200 \times 20	1	2.395

As the meshing is increased further to 1200 \times 40 at $\Delta t = \mathbf{1min}$, the stored energy predicted from the two grids are close to each other, and the percentage differences of 0.17% between the predictions of two grids are insignificant. An implicit time-

discretization scheme is used in the model discretization. This scheme does not have a time-step limitation. i.e., it is unconditionally stable for all values of time step (Ghoshdastidar, 1998). Hence, taking into account both the accuracy and calculation time, simulations reported in this study were all conducted with a 720 x 40 computational domain at a time step of 1 min.

3.12.2 Validation

The developed numerical model is validated with the experimental result of Benmansour et al. (2006) for a cylindrical TES unit made of stainless steel bed container of 60 mm height and 20 mm diameter whose wall thickness is 1mm. The system with mean void fraction and bed-to-particle diameter ratio 0.4056 and 6 respectively is covered with wool insulation and filled with PCM packing of 31.8 mm diameter. The simulation used the same conditions as in the experiment. The thermo-physical properties of the PCM is shown in Table 3.6 .

Figure 3.7 shows the comparison of the simulation results obtained with the model to that of the experiment for charging temperature history of PCM. As can be observed from the diagram, both experimental (Benmansour et al., 2006) and model predicted temperatures follow the same trend.

Table 3.6 Thermo physical proprieties of the paraffin wax. (Benmansour et al., 2006)

Melting temperature	60 °C
Latent heat of fusion	189 kJkg ⁻¹
Thermal conductivity	0.2406 Wm ⁻¹ K ⁻¹
Specific heat of Solid phase	8.4 kJkg ⁻¹ K ⁻¹
Specific heat of Liquid phase	2.1 Jkg ⁻¹ K ⁻¹
Solid phase density	920 kgm ⁻³
Liquid phase density	795 kgm ⁻³

In addition, it can be seen that the values of temperature predicted by the model agreed fairly closely with that of the experiment to a reasonable degree

The difference between the model result and the experimental result could be because of the various assumptions, approximations and fluid property correlations used. One other

reason for the difference between the model prediction and experimental results is in the material properties of the PCM. The properties of the PCM at the mushy region was taken as an average of the solid and liquid state properties. If the temperature dependent material properties are known, the numerical results will be more accurate. Therefore, the temperature dependent material properties of the PCM should be well known so as to obtain adequately precise results with the numerical prediction.

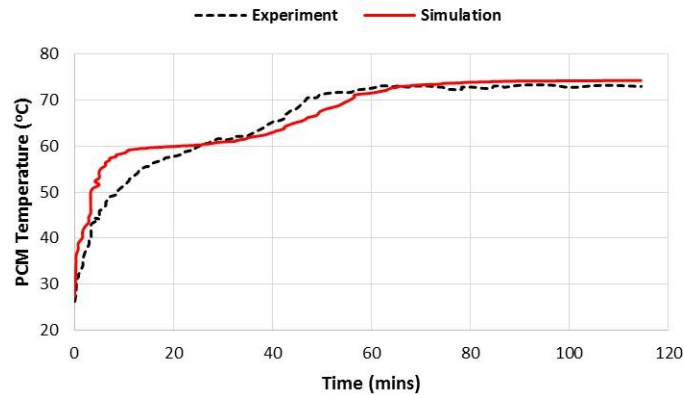


Figure 3.7 Experimental vs. Model predicted temperature histories of the PCM

Moreover, the differences between the numerical and experimental results could be as a result of the selected phase change temperature range of the PCMs used in the model. However, the general trend of evolution of temperature agrees and the deviation is less than 20% which is acceptable owing to the fact that natural convection inside the melted PCM may not have been well captured in the model

3.12.3 Charging mode general charging behaviour

The overall behaviour of the two charging modes of the compressed air TEST system using spherical PCM capsules is analysed in this section. Figure 3.8 shows the PCM surface temperature distribution at axial distance of $x=H/45$ in the TEST for the two modes analysed against charging time. It can be observed that, generally four distinct stages, namely a, b, c and d can be observed thorough the charging process in the two modes. Notice that at the initial stage of charging, about 5 minutes, before the hot HTF arrives at the surface of the capsule, the PCM capsule does not start to absorb any heat but remains

at its initial temperature of 175 °C. After this period, the PCM surface temperature begins to increase fairly sharply. The PCM temperature increased from 175 to about 306 °C from charging moment of 5 to 44 minutes without the PCM melting in both modes. This stage (a) is called the first temperature rising period in which the energy charged by the HTF is stored inside the PCM capsules as sensible heat up until the melting temperature of PCM is reached (at about 44 minutes). In mod1, from about 44 minutes, the PCM remained at the temperature of 306 °C until at about 196 minutes. This stage (b) is called the isothermal charging region where the latent heat is stored. In this period, each grid in the PCM capsule experiences a change of state from solid to mushy and the liquid fraction in solid state increases continuously with the storage of latent heat. Observe that the time spent by mod1 in region b is more than that spent by mod2. This is because mod2 operated at a higher temperature which led to more heat transfer rate in mod2 compared to mod1.

At about 196 minutes, in mod1, the heat absorbed by the PCM equals its latent heat and the node liquid fraction increases to unity. Thus the PCM capsule surface becomes completely liquid and thereafter, more regions in the PCM capsule become liquid and the solid-liquid front moves towards the centre. As the charging process continued between charging time of 196-214 minutes (zone c) in mod1, the additional heat added by the charging HTF finally raises the node temperature to its highest temperature and the energy is then stored as sensible heat in the melted PCM. After the PCM is fully charged to its highest temperature, it stays at this highest temperature for the duration of the charging mode (region d) until thermal equilibrium is reached between the PCM and the HTF.

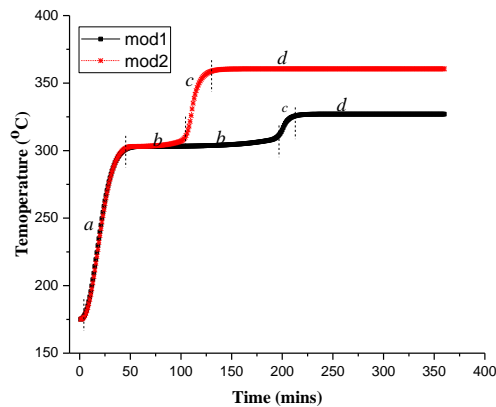
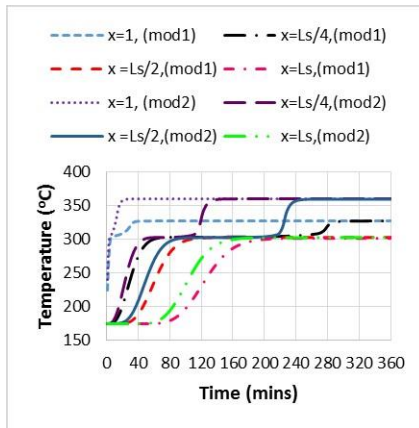


Figure 3.8 PCM surface temperature profile ($x=H/45$, $r=0$) VS charging time in the TEST

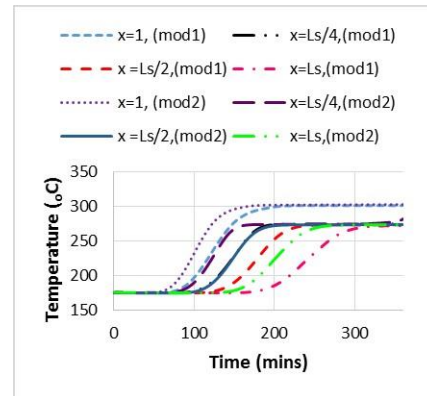
Mod2 stayed longer in the highest temperature of the PCM than mod1. This is because of the high HTF temperature in mod2 compared to mod1. Although, mod1 has a higher mass flow rate, the effect of higher HTF temperature in mod2 dominated the contribution of higher mass flow rate in mod1.

3.10.12.1 Temperature histories of the PCM and HTF

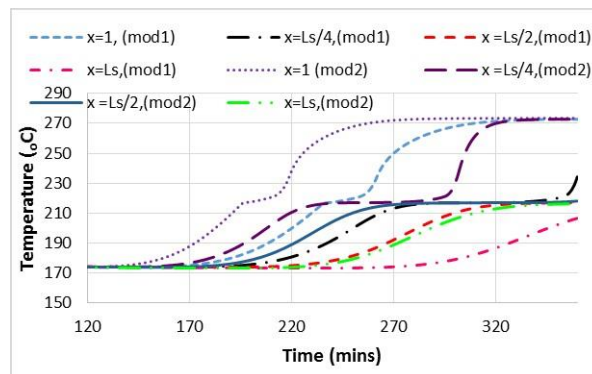
In the model, the TEST was divided into three equal sections (top, middle and bottom) with each having length designated as L_s and filled with PCM of different characteristics. It will be interesting to observe the PCM charging features in those sections for the two modes. Hence, Figure 3.9 (a-c) shows the temperature histories of the PCM at four different axial locations ($x = L_s/4, L_s/2,$ and L_s) in the three sections (top, middle and Bottom) of the TEST being filled with different PCM for the two modes.



(a)



(b)



(c)

Figure 3.9 : PCM outlet temperature at four locations of the TEST (a) top section , (b) middle section, (c) bottom section

It is seen that in the two modes, the temperature histories of the PCM along the axial direction show related trends in the three sections of the TEST. That is, in the two modes, the melting time of the PCMs in the three sections increased from the top section to the last section. This is because during the charging process, the temperature of the charging HTF decreases along the tank height as the charging progresses and consequently the temperature differences between HTF and PCM are reduced along the length of the TEST in the two modes, which leads to a slower charging rate for the PCMs in the sections with greater heights.

In Figure 3.9a, it can be observed that for both modes, the initial period of charging is characterised by high rate of heat transfer between the HTF and the PCM leading to a sharp increase in the temperature of the HTF and PCM at a very fast rate in all the three sections of the TEST until the melting temperature of the PCM is attained. After reaching the melting temperature, the rate of heat transfer between the HTF and the PCM capsules happen at a comparatively constant rate. This is revealed in the very slow rise in the outlet temperature of the HTF. This phase is called the latent heat phase. It is the point where the latent heat is dominant and most of the energy is stored in this phase. Following the latent heat phase is another sensible heat storage phase. At this period, the temperature of the PCM gradually increases to its liquidus temperature and there is a gradual drop in the rate of heat transfer between the HTF and the PCM, which consequently leads to a lengthier time required for storing energy.

As can be observed, in the top section of the TEST ($x=1$) (Figure 3.9a), mod2 attained a higher temperature than mod1 and the rate of increase of the temperatures is more in mod2 compared to mod1. The reason for the observed trend is that the HTF in mod2 is at a higher temperature because it was heated further with an electric heater powered by some part of the excess wind power thus leading to a high heat transfer rate between the HTF and the PCM in mod2. Though, the mass flow rate also influences heat transfer rate positively. However, the rate of increase in heat transfer induced by the high temperature in mod2 is more than that induced by the high mass flow rate of HTF in mod1. Thus temperature has a more dominant effect than mass flow rate.

Figure 3.9b shows the temperature map of the middle section of the TEST for both modes. It is noteworthy to observe that the PCMs occupying this section of the TEST took

a longer time to melt when compared to the top section. This is because, as the time elapses, the temperature difference between the PCM and HTF reduces and heat absorbed by the PCMs in this section of the tank are no longer enough to cause immediate melting of the PCMs. Rather the PCMs absorb heat gradually until a minimum threshold of temperature called the melting temperature of the PCMs is attained and they melt. Although, the two modes, (mod1 and mod2) attained almost the same highest temperature of about 290 °C, it can be observed that the rate of increase of the PCM temperature for mod2 is still higher in this section than for mod1. In other words, mod2 melted faster, having taken about 150 minutes to melt when compared to mod1 that melted at about 200 minutes. This can be explained by making reference to temperature plot of the HTF along the height of the TEST as depicted in Figure 3.10. As can be seen, in the first section of the TEST ($H \approx 0 - 4 \text{ m}$), the exit temperature of the HTF in mod2 is higher than in mod1. Hence, owing to the higher temperature of the entering HTF in mod2, there is higher heat transfer rate and hence the rate of increase in temperature of the PCM in the middle section of the TEST is more in mod2 compared to mod1. The same trend is observed for the temperature profile of the HTF.

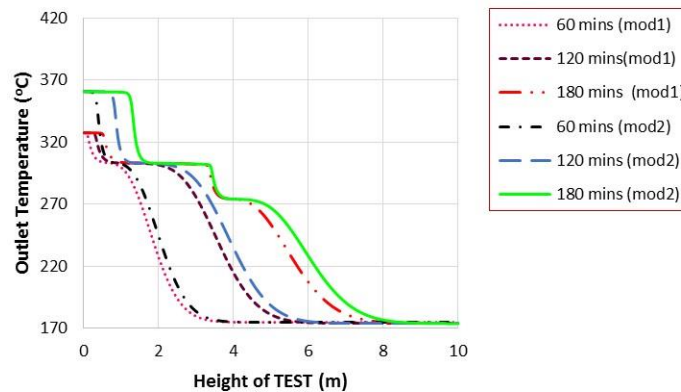


Figure 3.10 Temperature distribution of the HTF along the TEST during charging

In the last section of the TEST for the charging operation (see Figure 3.9c), the same trend observed in the top and middle sections of the TEST is equally observed here. The temperature profile at different heights in this section just like the other first two sections (Top and middle of TEST) presented the lowest phase change because the heat

exchange between the HTF and the PCM is much slower here, because of lower HTF temperature than the middle and top sections of the TES as in Figure 3.10. In the last section of the TEST, mod2 melted at a shorter time of about 198 minutes and equally took a shorter time to attain a highest temperature of 270 °C. In contrast, mod1 took a longer time to melt, about 230 minutes. With reference to the melting time observed in the second section of the tank, mod2 took about 32% more time to melt in the bottom section of the TEST. For mod1, about 15% more time is taken to melt.

In summary, the temperature evolution at different axial positions for the two mode display similar trends throughout the charging/discharging duration. As shown in Figs 3.9 (a-c) the temperature of the PCM in both modes increases speedily initially because of high heat transfer rate but the rate of increase reduces as the PCM temperature increases, and finally approaches the melting point where the temperature of the PCM remains constant. The time for attaining the melting point varies with the axial position (x) in both modes with PCMs at the top of the storage tank melting faster than those at the bottom. The PCMs in mod2 melted faster than those in mod1. The PCMs positioned near the bottom sections of the TEST remains solid, even for large operating times. This is because the energy carried by the HTF at these locations is not sufficient to achieve complete melting of the PCM.

3.12.3.2 Stored and accumulated energy

Figure 3.11 shows the variation of the stored (Q_s) and accumulated energy (Q_{ac}) against time for the two modes. It can be seen that the stored energy for the two modes is constant at first until after about 275 minutes in mod2 and 225 minutes in mod1 when the stored energy started decreasing relatively sharply as the charging continued. This is because, as already observed from the outlet temperature profile of PCM (Figure 3.9 a) for the two modes, the first sensible heat stage is very short while the latent heat stage is very long and a significant amount of energy storage takes place during the PCM change of phase stage. Thus, the high difference between the temperature of the HTF and the PCM melting temperatures leads to high and constant values of charging rate thus reinforcing the advantage of a LH TES system to provide constant heat rates (Rady, 2009). After the phase change period, there is a gradual increase in the outlet air temperature due to sensible heating of the melted PCM. This is because, as the sensible heating the PCM starts, the

PCM nears its fully charged state, making the heat transferred by HTF to the PCM to reduce increasingly as the PCM approaches the end of the charging duration. This leads to a decrease in the temperature difference between the HTF and the PCM in the TEST as the charging operation progressed leading to a reduction in energy transferred to the PCMs. Hence the energy stored reduces over time. Moreover as the charging progressed, the cumulative heat absorbed by the storage materials in the TEST increases leading to increase in the temperature of the TEST tank and its contents. This results in increased heat loss from the storage tank as can be seen from Figure 3.12.

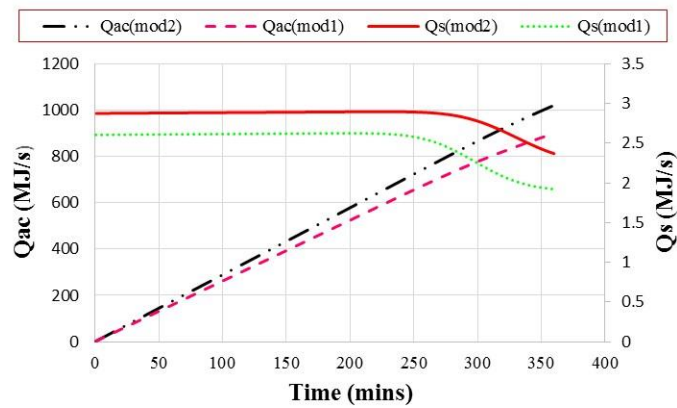


Figure 3.11 Stored and accumulated energy VS time

This also played a part in the observed decrease in the magnitude of the stored energy in both modes over time. There is a small-observed difference in the value of stored energy for the two modes. However, mod2 stayed longer in the constant energy storage zone than mod1. This is because mod2 operated at a higher temperature compared to mod1 and when the HTF inlet temperature rises, there is an increase of sensible heat in capsules and the rate of heat transfer between the HTF and the PCM which is proportional to the temperature difference between the air and the PCM is increased thus enhancing the heat transfer coefficient (Li et al., 2018).

Figure 3.11 also presents the characteristic variation of accumulated power with time for the two modes. As can be observed from the diagram, the relationship between the charging time and the accumulated heat is essentially linear during the charging period.

The observed trend can be explained by the nearly constant PCM melting rate as can be seen in Figure 3.8. Similar trend was obtained by Liu et al. (2006) in his experimental study involving PCM and water as HTF. Mod2 has a sloppier graph and thus has a higher accumulated heat per time. This is because since mod2 operated at a higher temperature, as the HTF inlet temperature increases, the charging rate increases obviously due to the increase in the sensible heat in capsules thus making the charging time to reduce. In addition, the increased temperature of the HTF in mod2 enhances the heat transfer coefficient leading to the observed higher accumulated heat per time in comparison to mod1.

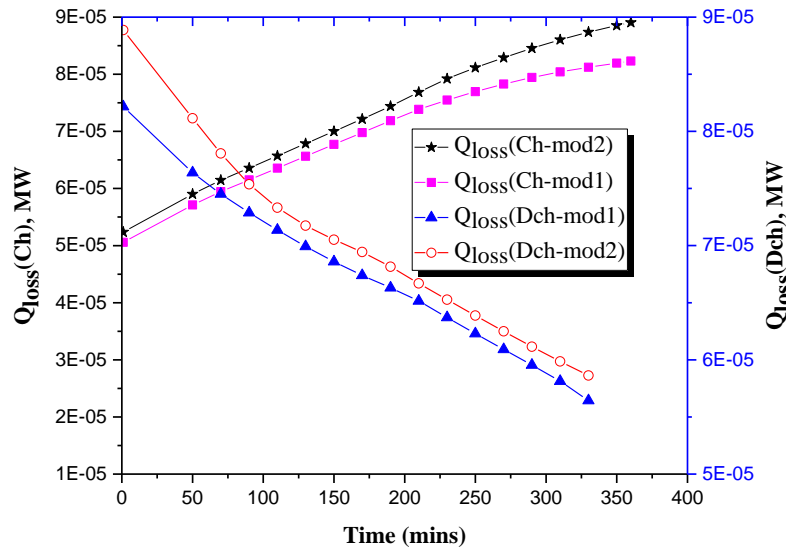


Figure 3.12 Heat loss during charging and discharging mode

3.12.4 Discharging mode general discharging behaviour

During the discharge mode, the mode of travel of the HTF is reversed. The HTF enters from the bottom of the TEST and exits from the top. At the beginning of the discharging operation, all the PCM in the three sections of the TEST are in liquid phase and consequently, the overall thermal conductivity of the PCM is enhanced very well by the natural convection effect within the liquid PCM. Through the continuous flow of the cold compressed air over the PCMs from the bottom and out through the top, the PCM

capsules in the TEST bottom release their heat to the HTF gradually until after some minutes when the PCMs in the bottom part begins to solidify partially while those at the middle and top sections still remain in liquid state. As the charging time progresses, more of the PCMs in the other sections of the TEST take part in solidification. The dynamics of the solidification curves in each section of the TEST during the discharging operation in the two modes analysed in this research can be divided into three main phases. The first phase is the cooling phase. It is characterised by transfer of sensible heat from the PCMs to the cold compressed air, during which the temperature of the PCM decreases rapidly to its melting point and the heat recovered from the PCM by the HTF is thus, primarily the sensible heat of the liquid PCM (Liu et al., 2006). This phase is followed by quasi-isothermal latent heat stage phase called solidification phase, during which the temperature of the PCM remains almost constant due to latent heat energy storage. The last phase is the sensible heat storage sub-cooling phase during which the temperature of the PCMs reduces sharply to their final lowest temperature and the charging operation stops. Obviously, the heat recovered by the cold compressed air after the solidification is completed is again the sensible heat of the PCM, and this surely speeds up the decreasing of the PCM temperature. Figure 3.13 (a-c) show the temperature histories of the PCM at three axial locations ($x = 1, x = 0.25L_s$ and $x = 0.5L_s$) in each of the three sub-sections of the TEST, namely, bottom sub section (Bs), middle sub section (Ms) and top sub-section (Ts) filled with different PCMs and each with length ($L_s = H_{TEST}/3$).

As can be observed from Figure 3.13a, the first sensible heat stage for the PCMs at the Bs of the TEST is very short and a substantial amount of energy discharge takes place at constant temperature during the phase change. After about 10 minutes, the PCMs at the entrance ($x=1$) get solidified completely in both modes. This can be explained by the high temperature difference between the HTF and the PCM in the bottom section of the TEST. The temperature profile at the middle (Ms) and bottom (Bs) sub sections of the three sections of the TEST is shown in Figure 3.13b and c. Observe that for the same axial distance ($x=1$) it takes longer time for the PCM to solidify in the middle (Ms) and top (Ts) sub-sections of the TEST. While the PCM solidifies almost immediately the discharging operation starts in the bottom sub section of the TEST (Figure 3.13a), it takes about 175 minutes for the PCM to solidify completely in the middle sub-section of the TEST at $x=1$

whereas in the top sub-section, it takes about 225 minutes for the PCM to be completely solidified at the same axial location($x=1$). The reason for this is because the temperature of the HTF increases successively as it moves from the bottom of the TEST to the exit as can be seen in Figure 3.14.

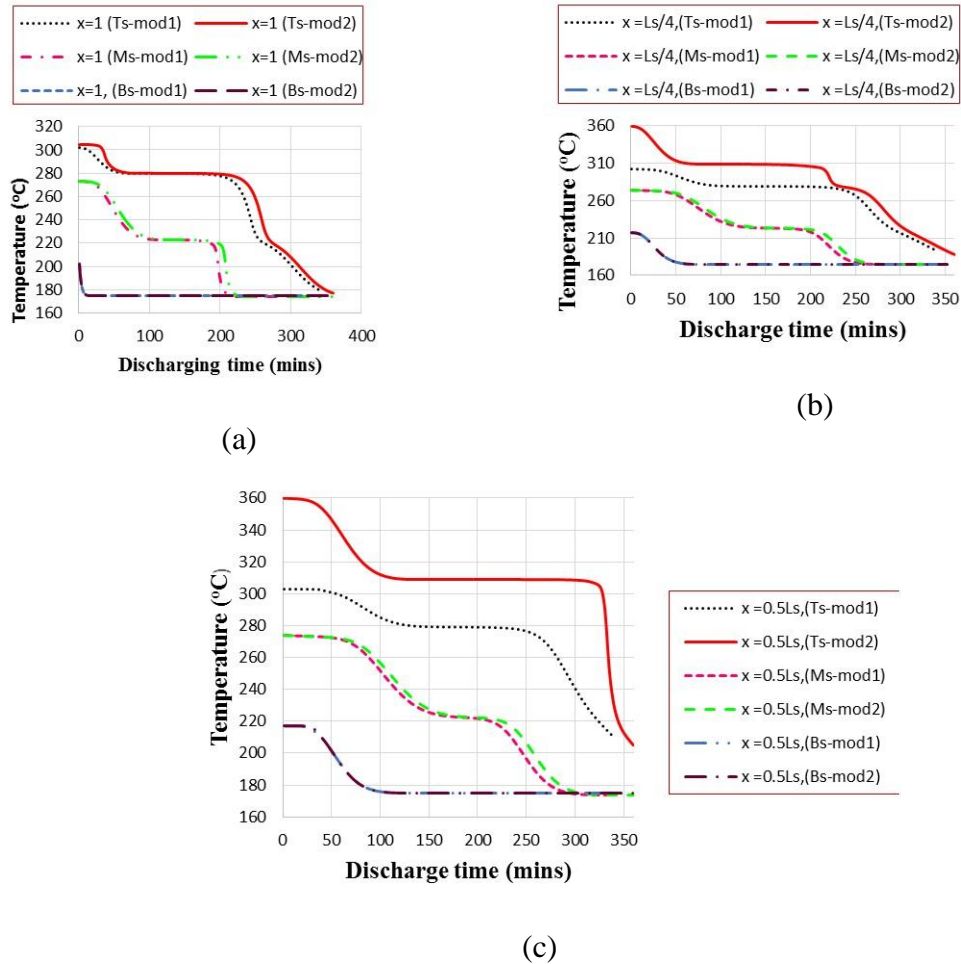


Figure 3.13 Outlet temperature of PCM during discharge mode (a) Top section (Ts), $x=1$ (b) Middle section, $x=0.25Ls$ (Ms) (c) Bottom section (Bs), $x=0.5Ls$

The increased temperature leads to a successive decrease in temperature difference between the PCM and the HTF leading to the reduction in the charging energy and hence increased solidification time.

In the temperature profile at the middle for the three sub sections of the TEST as shown in Figure 3.13b, using the temperature features at the bottom section (Bs) as an example, in contrast to the temperature features at the bottom in Figure 3.13a, it can be

observed that the first sensible heat discharging stage is very visible and the phase change stage takes place much later, at about 50 minutes (in both modes) compared to the bottom section in Figure 3.12a. Also observe that the discharging rate in the middle sub-section of the TEST is relatively lower than at the bottom sub-section. At $x=1/4L_s$ in Ms of the TEST (Figure 3.13b), about 250 minutes is required in mod1 and 265 minutes in mod2 for the PCM to be completely discharged.

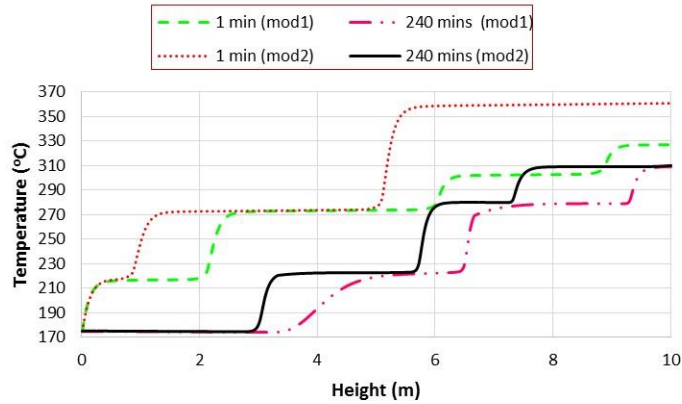


Figure 3.14 Temperature map of HTF during discharging mode

This is in contrast to lower discharging time of 210 and 225 minutes at the Ms of the bottom section (Figure 3.13c). Although the difference between the discharging time are almost the same for the two modes at Ms, $x=1/4 L_s$ (Fig 10.13b), and Ms, $x= 0.5L_s$ (Fig 10.13c), mod2 has a higher discharge time because during the charging mode, it stayed longer in the constant temperature phase change region than mod1 owing to its higher temperature and thus possess more energy in the latent heat region compared to mod1. It is pertinent to note that in all the sections of the TEST, the decreasing rate of the PCM temperature is fastest in the first sensible heat phase than in the other phases. This is owing to the fact that the sensible heat is much smaller than the latent heat

The same trend observed in the Ts and Ms of the TEST sections is also observed in the Bs as can be seen in Figure 3.13c At axial distance equivalent to a half the length of each TEST section ($x=0.5L_s$), the discharge time for the PCM increased to about 300 min for mod1 and 310 minutes for mod2 at Ms. It is interesting to observe that at the top section (Ts) of the tank, mod2 took a shorter time to start melting than mod1. This can be explained by the higher temperature difference and hence higher heat transfer rate in mod2 owing to

its higher final charge state temperature of about 360 °C compared to about 320 °C for mod1. One of the reasons for carrying out this study is to find out which has more effect on the performance of a TES system between mod1 with higher flow rate and low temperature or mod2 with higher temperature and low flow rate. Although both high flow rate and temperature have been found to improve the performance of a TES system by reducing the melting time of the PCMs (Liu et al., 2006; Li et al., 2018), the results of the analysis carried out here suggest that temperature has a much stronger influence than the flow rate. This may be explained thus; from basic convective heat transfer theory, it is known that high mass flow rate of the HTF can only improve the convection heat transfer between the hot compressed air and the inside wall of the TEST and according to Liu et al. (2006), the thermal resistance of this process of convection heat transfer is of insignificant value when compared to the thermal conduction resistance of the PCM owing to the very low thermal conductivity of the PCM. In addition, for spherical particles of cylindrical arrangement, the heat transfer coefficient due to convection is in direct proportion to the n^{th} power of the flow rate, where n is a constant between 0.3 and 0.8. This additionally plays a part to the insignificant effects of the high mass flow rate of the HTF in mod1.

3.12.5 Energy and exergy efficiency

The plot of the variation in energy (exergy) efficiency (EnEff, ExEff) during charging for the two modes is shown in Figure 3.15. The results obtained shows that the performance of the two modes differ a lot from energy analysis to exergy analysis. Similar to the trend of the stored energy, the energy and exergy efficiency for the two modes analysed is high and fairly steady at first and decreased relatively at a constant rate with time as the charging progressed. This is because of the reason already advanced for the case with energy stored in both modes. The EnEff ranges from 97.6 to 96.7% with an average of 97% in mod1. In mod2, EnEff varies from 98.3 to 97.8% with an average of 98%. Again mod2 has an average energy efficiency which is higher than that of mod 1. However, the difference between the energy efficiency in both modes is small and below 3%. The efficiency values computed above, is within the range of typical values reported in the literature. Specifically Peng et al. (2014) determined charging energy efficiency values that ranges from 98.5 to 96% for a PCM based TES packed bed with height of 5m,

Diameter of 1m, T_{HTF} of 400 °C and T_c of 250 °C. In another study, Li et al. (2018) experimentally investigated the impact of various HTF temperatures of 425, 445, and 465 °C respectively at constant mass flow rate of 260 kg/h on the performance of a PCM based thermal energy storage tank. They reported charging efficiencies of 83.8, 89.8 and 91.1% respectively. The higher energy efficiency reported by the current model could be due to inability to fully account for all the heat losses taking place in the model implementation. The exergy efficiency ranges from 69.6 to 53.3% in mod1 with an average value of 65%. In mod2, the exergy efficiency fluctuated from 74.3 to 61% with an average value of 72%. Percentage exergy efficiency variation of 7.2% is estimated for mod1 and 3.5% for mod2. The smaller variation in energy efficiency in mod2 could be because of the longer phase change temperature observed in mod2. A higher energy efficiency in mod2 suggests higher amount of heat charged into the TEST in mod2 compared to mod1. The exergy efficiency values obtained are within the range reported by other researchers. Elfeky et al. (2018) reported exergy efficiency of 75.2% for three stage PCM TEST in their study on numerical comparison between single and multi-stage PCM based high temperature TES for CSP tower plants.

Comparison of the exergy and energy efficiency results of both modes suggests that the energy efficiency is always more than the exergy efficiency. This is anticipated since the entire energy content of the charging compressed air is taken into account in the estimation of energy efficiency. In other words, to estimate the energy efficiency, the quality of the energy transferred is neglected while the quantity of energy transferred is taken into account but in exergy efficiency estimation, the quality of the available energy extracted from the compressed air is taken into account and this quality degrade over time due to thermal exergy loss resulting from internal irreversibility.

Since mod2 operated longer in the stable constant efficiency region than mod1. This implies that in applications requiring a longer and efficient stable operation, mod2 will be preferred since it is apparent that mod2 can guarantee a more uniform outlet energy efficiency in the charge process than mod1. The fluctuation in the energy efficiency for the two modes over the charging time analysed is negligible and below 5% further reinforcing the advantage of a LH TES system to provide a relatively constant efficiency over its charging cycle.

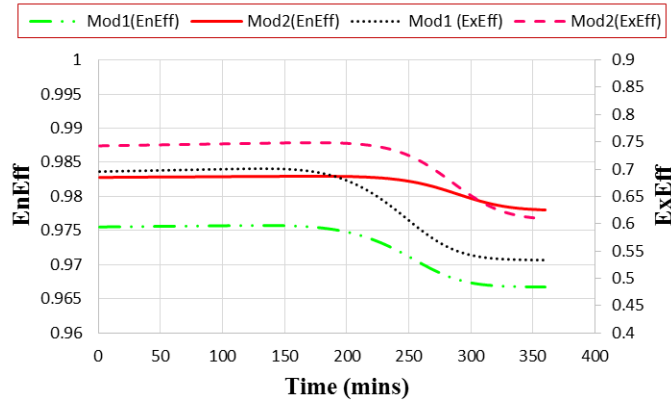


Figure 3.15 Energy and exergy efficiency of charging mode

Figure 3.16 shows the variation of energy (EnEff) and exergy (ExEff) efficiency for the two modes analysed during the discharging mode. Both metrics show similar trend with the charging mode but on a smaller magnitude. Again, energy efficiency of mod2 is higher than that of mod1. The energy efficiency varied from a maximum value of 87% in mod1 and 97% in mod2 to a minimum value of 77% in mod1 and 79% in mod2 respectively. This translates to average discharging efficiencies of 78 and 80% for mod1 and mod2 respectively over a charging time of 250 minutes. Again, the values of the discharging efficiency is within the range of reported values in similar published works. Wu et al. (2014) reported a discharging efficiency of 98.3 and 94.8% respectively for capsule diameters of 0.02 and 0.04m at discharging time of 5.57 and 5.37 hours respectively.

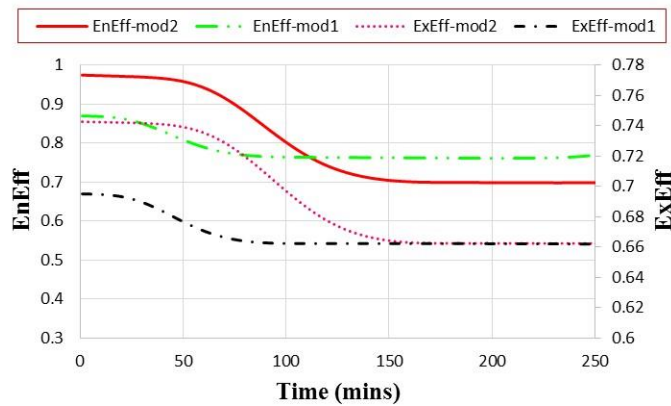


Figure 3.16 Energy and exergy efficiency of discharging mode

As expected, the exergy efficiency is lower than the energy efficiency and varied from maximum values of 66 and 74% to a minimum value of 60 and 69% in mod1 and mod2 respectively. Again, this translates to average ExEff of 66 and 68% for mod1 and mod2 respectively.

Figure 3.17 shows the RTE and overall exergy efficiency (ExEo) for the two modes. The overall energy efficiency or RTE of the two modes varied just like the charging and discharging energy efficiencies. The RTE of mod1 varied from 87 to 77% with an average of 76% while that for mod2 varied from 97 to 79% with an average of 78%. Again, the values of the RTE are comparable to values of 77, 84 and 86% reported as the overall energy efficiency by Li et al. (2018) in their experimental investigation of the impact of various HTF temperatures of 425, 445, and 465 °C at a constant mass flow rate of 260 kg/h on the performance of a PCM based thermal energy storage tank.

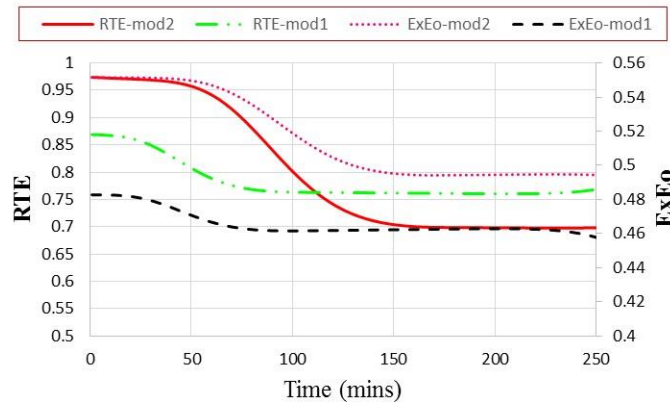


Figure 3.17 Overall energy and exergy efficiency

Similarly, the overall exergy efficiency varied from a maximum value of 0.48 and 0.55 to minimum value of 0.33 and 0.44 in mod1 and mod2 respectively over a charging/discharging time of about 250 minutes. This translates to average efficiencies of 0.45 and 0.51 in mod1 and mod2 respectively.

3.12.6 Parametric analysis results

The influence of key parameters used in the model on the performance of the TEST charging and discharging performance was examined. This sections reports the results obtained.

3.12.6.1 Influence of packing height

The influence of the different PCM arrangement options considered in the sensitivity analysis on the performances of the two modes during charging are presented in terms of the temperature profile of the PCM at the same TEST sub-section height of $2L_s/3$, energy (exergy) efficiency as shown in Figure 3.17 and Figure 3.18 respectively for the charging mode. The PCM temperature profile indicates the rate of melting or freezing of the PCMs in the TEST. The gradient of the curve represents how fast the rate of charging and discharging process is. Sharper slope means better dynamic performance of the system. Energy efficiency measures the rate of energy transfer and the exergy efficacy indicates the quality of energy transfer and recovery.

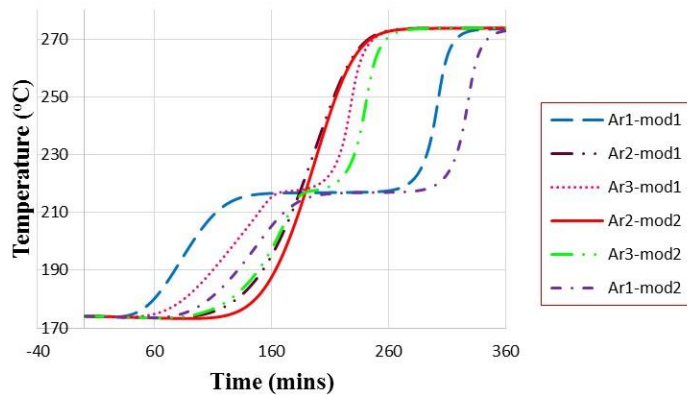


Figure 3.18 Temperature profile of PCM at height of $2L_s/3$

As can be observed from Figure 3.18, increasing the length of tank occupied by the PCMs (from the top to the bottom) results in shorter isothermal phase change period for the surface temperature of the PCM and hence the melting point. From Figure 3.18, it can be observed that the order of PCM melting time from the lowest to the highest is Ar2, Ar3, and Ar1 respectively. This is because Ar2 has the highest number of PCMs with high melting temperature in the Ts and Ms of the TEST while Ar1 has the least. Large amount

of energy storage takes place during the phase change period (Aldoss & Rahman, 2014). PCM2 and PCM3 has the highest latent heat value of the three PCMs considered in that order and since Ar2 has the highest number of PCMs with high latent heat in the Ts and Ms of the TEST where the compressed air temperature is still high, the charge time decreases because of increases in sensible energy extraction rate as a result of more heat transfer interfacial area for thermal energy extraction and subsequent storage by the PCM.

Figure 3.19 (a) and (b) compares the average energy and exergy efficiency of the different arrangements with that of the base case designs using the PCMs involved during the charging process. The results are obtained at the same charging times for all cases. During the charging process, Ar2-mod2, attains the highest energy and exergy efficiency followed by the base case mod2. The worst performance is exhibited by Ar1-mod1.

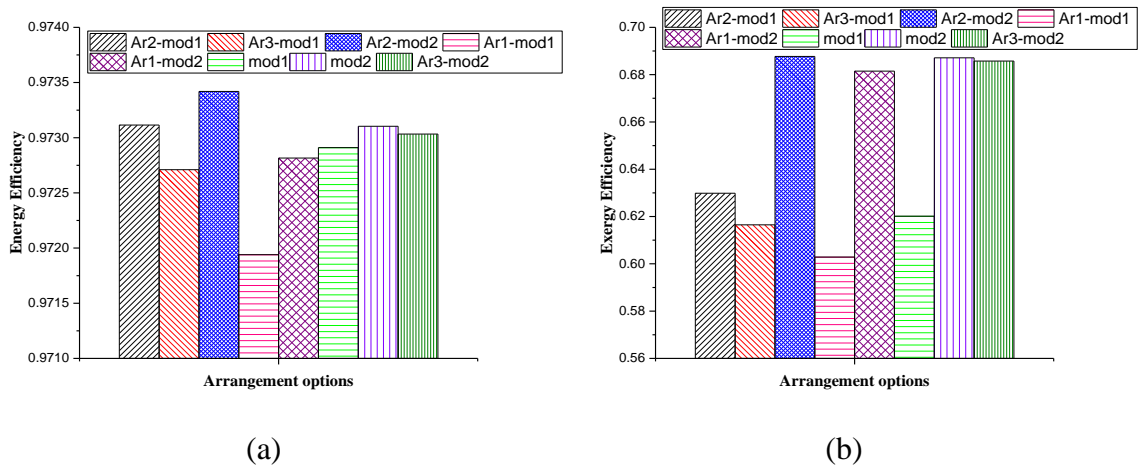


Figure 3.19 Energy and Exergy efficiency for various arrangements

The observed trend again has to do with the arrangement and thermo-physical properties of the PCMs, including the HTF inlet temperature. Because of high temperature of HTF in Ar2-mod2 and since Ar2 has the highest number of PCMs with high latent heat in the Ts and Ms of the TEST where the compressed air temperature is still high, there is a high rate of energy transfer from HTF to the PCM during charging process which was able to completely melt all of the PCM thus accounting for the best performance recorded. However, for the AR1-mod1 with the worst performance, the PCM at the bottom of the tank took a longer time to melt due to the twin reason that the temperature of the HTF is low and also the AR1-mod1 has least number of PCMs with high latent heat in the Ts and

Ms of the TEST. Thus there is a smaller temperature difference between the PCM and HTF leading to lower charging rate.

3.12.6.2 Effects of number of multiple PCM

The performance of a LH TES system has been proven to improve with multi PCM configuration (Aldoss & Rahman, 2014). Two and three PCM multi configuration arrangement options were analysed in the parametric analysis to study its impact on the performance of the two charging options analysed. The thermal performances of two multiple PCM combinations are presented in terms of the accumulated stored energy (Q_{ac}), round trip efficiency (RTE) and overall exergy efficiency (ExEo) for the charging process.

Figure 3.20 shows the accumulated stored energy (Q_{ac}) of the PCMs during the charging mode for the 2PCM and 3-PCM combination analysed. In Figure 3.20, the following options were considered: the 2-PCM (mod1 and mod2) arrangement and, 3-PCM (mod1 and mod2) arrangement. The 3-PCM arrangement is the reference case analysed in the thesis. In the 2-PCM case, the bed is completely packed with PCM1 and PCM2 capsules with PCM1 on top and PCM2 below in the direction of the charging HTF. With reference to Figure 3.20, the gradient of the line signifies how fast the charging rate is. Sharper slope signifies better dynamic performance of the system (Aldoss & Rahman, 2014).

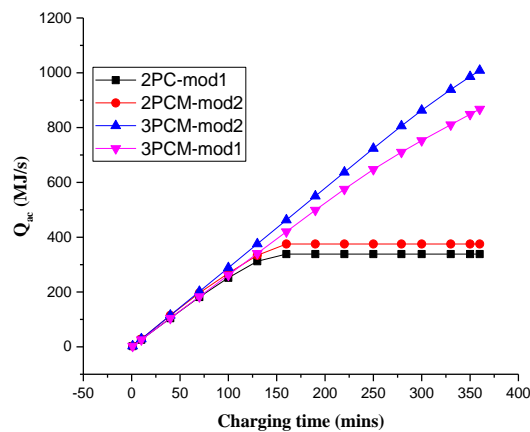


Figure 3.20 Accumulated stored energy of 3PCM vs. 2PCM

From Figure 3.20, it can be observed that that, the accumulated energy vs. time presents a basically straight-line relationship within the charging period for 3-PCM

arrangement. However, the accumulated energy in 2 PCM arrangement becomes constant after about 150 minutes while that for the 3 PCM arrangement continue to be linear with time. The three-stage PCMs case achieves the high performance since it has the best matching melting temperature distribution with the temperature profile of HTF (Aldoss & Rahman, 2014). In a 3 multiple PCMs arrangement, the three PCMs are arranged in decreasing order of melting points and the melting temperature of the last PCM is low (220 °C) and the HTF leaves each PCM interface at a temperature very near to the melting temperature of the lower PCM. Each of the lower PCM can exploit the exergy contained by the incoming flow stream to fast-track the phase transition process, thus stimulating superior usage of latent heat as well as sensible heat (Aldoss & Rahman, 2014; Elfeky et al., 2018). Thus the 3 PCM arrangement maintains a higher nearly constant PCM melting rate, especially in the later period of the charging process compared to 2 PCM arrangement (Liu et al., 2006). Whereas, in the 2 multiple PCM arrangement, the melting temperature of the last PCM (PCM2) in this instance is high (277 °C) which lead to less temperature difference between the PCM and the incoming HTF, and thus less heat flow driving force. After about 150 minutes in the charging cycle, most of the PCMs has undergone a change of phase, and shortly afterwards, the charging cut-of temperature is attained thus making the accumulated energy to remain constant.

Figure 3.21 shows the RTE (a) and ExEo (b) of the two options after about 140 minutes of charging and discharging.

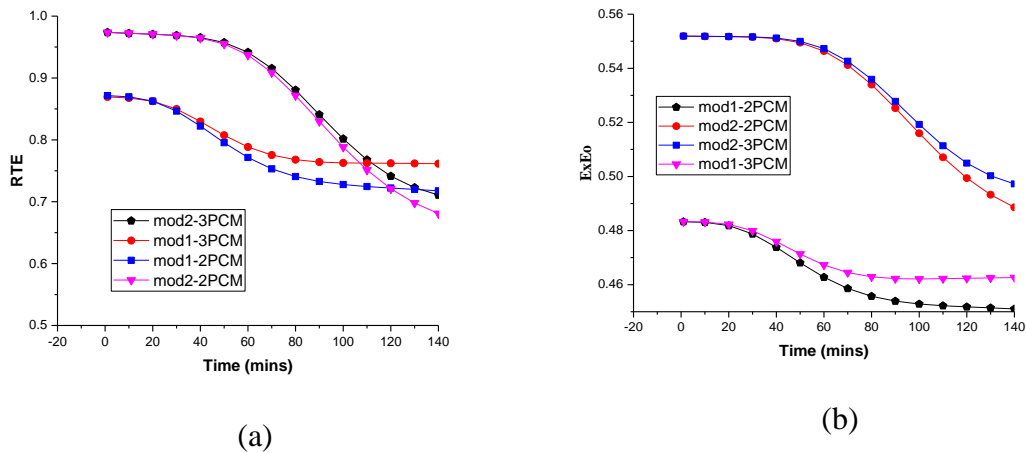


Figure 3.21 Energy efficiency and Exergy efficiency of 3PCM vs. 2PCM

From Figure 3.21(a), the result shows that the mod2- 3PCM arrangement has the highest RTE with an average efficiency of 87.5%. Arrangement mod2-2PCM is the second best in performance with an average RTE of 86.5% while mod1-2PCM arrangement has the lowest energy efficiency performance with an average RTE of about 70.1%. Although, the RTE of mod2-2PCM arrangement is close to that of mod2-3PCM, the variation of energy efficiency over the charging period is more pronounced in 2PCM arrangement than in 3PCM arrangement. Mod2-2PCM arrangement varied by about 30.1% from a maximum value of 97.4% at the beginning of charging operation to a minimum value of 68.1% whereas mod2-3PCM arrangement varied by about 26.9% from the same maximum value as mod2-3PCM to a minimum value of 71.1%. The reason for the observed better stable operation of mod2-3PCM Ar is because of the more uniform accumulated stored energy in mod2-3PCM (see Figure 3.20) due to higher nearly constant PCM melting rate, especially in the later period of the charging process compared to 2 PCM arrangement. Moreover, the melting temperature distribution in 3PCM arrangement matches the heat transfer temperature profile better than in the 2 PCM arrangement. This improves the heat transfer process, and increases the system dynamic performance (Aldoss & Rahman, 2014).

The corresponding overall exergy efficiency is as shown in Figure 3.21 (b). For all of the options, the exergy and energy efficiency decreases negligibly during the initial period of the charging process because of the very fast increase in the temperature of the PCM from its sensible state to the mushy region where it stayed much longer as it extracts energy from the HTF. As the charging progresses, the PCM is completely, melted and its temperature approaches the inlet temperature of the HTF and thus the temperature difference between the PCM and HTF reduces, leading to a reduction in the ExEo of the systems. Furthermore, mod2 3-PCM arrangement has almost the same ExEo value of about 53.0% as mod2 2-PCM arrangement. However, the variation of exergy efficiency over the charging/discharging time is higher in mod2-2PCm (11.5%) compared to variation of 9.39% estimated in mod2-3PCM. The mod1-2PCM still has the least exergy efficiency performance.

3.13 Conclusions

Two charging modes of a thermal energy storage tank system employing a multi-PCM system was simulated to compare their performance. Mod2 with higher temperature and lower mass flow rate was found to perform better than mod1 with higher mass flow rate and lower temperature in both the charging and discharging cycle. The specific results obtained are summarised as follows:

- The average daily net energy efficiency of the TEST is approximately 97 and 98% in mod1 and mod2 respectively during the charging periods. On the other hand, the average daily exergy efficiency is found to be 65 and 72% for mod1 and mod2 respectively.
- The net energy efficiency for the charging process in the two modes lies in the range of 97.6 to 96.7% in mod1 and 98.3 to 97.8% in mod2 respectively over a charging time of six hours. Their corresponding exergy efficiency is estimated to lie in the range of 69.6 to 53.3% in mod1 and 74.3 to 61.0% in mod2 representing a percentage exergy efficiency variation of 7.2% for mod1 and 3.5% for mod2.
- The round trip efficiency varied from a maximum value of 87% in mod1 and 0.97% in mod2 to a minimum value of 77% in mod1 and 79% in mod2 respectively. This translates to average efficiencies of 78 and 80% for mod1 and mod2 respectively
- The overall exergy efficiency varied from a maximum value of 48 and 55% to minimum value of 33 and 44% in mod1 and mod2 respectively. This translates to average efficiencies of 45 and 51% in mod1 and mod2 respectively.
- Results of parametric analysis on the influence of number of multiple systems on the performance of the system shows expectedly that the 3 –PCM arrangement are able to store and discharge more energy than 2 PCM arrangement. The mod2 3PCM arrangement has the highest RTE with an average efficiency of 87.5%. Arrangement mod2-2PCM is the second best in performance with an average RTE of 86.5% while mod1-2PCM arrangement has the lowest energy efficiency performance with an average RTE of about 70.1%.
- In addition, parametric analysis on the arrangement of the three PCMs in the TEST shows that due to the thermal properties of PCM1 and PCM2 and the larger

temperature difference experienced during the charging process, the mod2-3PCM Ar2 has the highest energy and exergy efficiency and stores more energy.

- The smaller temperature difference between the HTF and the PCM in mod1-AR1 coupled with the low values of latent heat leads to the system having the worst performance of the arrangement options considered.

These results confirm to already known fact that multiple (3 PCM) arrangement has a better energy and exergy performance over that of a single and double PCM system. While these results indicate a mod2 3-PCM system to be best between the two analysed modes, as the temperature of the HTF reduces, lesser number of PCMs used will have a greater impact. The results obtained from this section will be applied in the thermodynamic analysis of the integrated system in Chapter five. While the results give insight into crucial aspects of the performance of the two modes of the CA TEST system, additional research is required to determine the optimal operating conditions. In addition, the properties of the PCM at the mushy region was taken as an average of the solid and liquid state properties. If the temperature dependent material properties are known, the numerical results will be more accurate. Therefore, the temperature dependent material properties of the PCM should be determined experimentally to obtain adequately precise results with the numerical prediction.

Chapter 4

Modelling of biomass gasification

4.1 Introduction

One of the critical components of the A-CAES+BMGES is the downdraft gasification plant sub system. Its operational efficiency depends on various complex chemical reactions comprising drying, fast pyrolysis, partial oxidation of products of pyrolysis and subsequent gasification of the oxidized pyrolysis products including unreacted char and tar conversion.

In this chapter, a mathematical model that can capture these complex processes and enable the determination of syngas composition and hence its lower heating value (LHV) is presented. The developed model is validated with three different experimental results obtained from three different sources. The impact of some key gasification input variables, such as equivalence ratio, moisture content and ambient air temperature on the composition of the syngas and its calorific value are discussed.

This chapter starts with a general overview of biomass gasification. A succinct discussion is provided for different kinds of biomass gasification reactor design, with significance given to downdraft biomass gasification. This is followed by literature review on modelling methods that has been used for biomass gasification in the literature. Subsequently, a detailed literature review is provided for different modelling work done on downdraft biomass gasification. Finally methods for model development and validation is provided. At the end of this chapter the results of the syngas composition, cold gas efficiency and carbon conversion efficiency at various ranges of key input parameters of the system is presented. The results will aid the design of the integrated A-CAES+BMGES system to be carried out in chapter 5.

4.2 Overview of gasification

Biomass is converted to energy through pyrolysis, combustion gasification or liquefaction. Thermochemical gasification has been tipped to be the most cost effective

route (Gao & Li, 2008). It involves heating biomass and biomass derived wastes to a high temperature in the range of 500-1300 °C in a reactor with oxygen less than the stoichiometric requirement for complete combustion of the fuel to form volatile compounds (gases) and solid residues (char) (Basu, 2010; Sadaka, n.d.). The gaseous product from the biomass gasification is called syngas with the main constituents after removing water vapour as CO, CO₂, H₂, CH₄ and some minor components of higher hydrocarbons and tars. The syngas can be converted into desirable valuable gaseous fuel or chemical products which can further be exploited to produce power, thermal energy or applied in bio refinery applications to produce value added chemicals and liquid biofuels (Basu, 2010).

A thermochemical biomass gasification process typically involves the processes of drying, thermal decomposition/pyrolysis, partial oxidation of some gases, char and vapours and gasification of decomposition products (Basu, 2010). There are no distinct boundaries between these steps but in the mathematical modelling of gasification, these steps are usually treated as distinct processes for convenience and simplification purposes.

4.3 Classification of gasification reactors

Gasification reactors can be classified based on gasification agent, heat source, operating pressure and reactor type.

4.3.1 Gasification agent

The key gasifying agents used for gasification are air, oxygen, and steam. The heating value of the product gas depends on the choice of gasification agent. If air is used instead of oxygen, the nitrogen in it greatly dilutes the product gas (Basu, 2010). Hence, air gasification has the lowest heating value (4-7 MJN⁻¹m⁻³) followed by steam (10-18 MJN⁻¹m⁻³) and oxygen gasification has the highest heating value (12-28 MJN⁻¹m⁻³) but the gasification operating costs is very high due to the O₂ production costs. Syngas from air gasification is suitable for use in boiler, engine or turbine applications while that from oxygen is suitable for use as synthesis gas for conversion to methanol and liquid biofuels (Reed & Das, 1988).

4.3.2 Heat source

A gasifier can be classified as auto-thermal or allothermal. Auto-thermal gasifiers are also called direct gasifiers. They are self-sustaining and produce required heat by incomplete combustion of biomass. Allothermal gasifiers are also called indirect gasifiers. They use steam as gasification agent and the heat required for gasification is delivered from outside heat sources through a heat exchanger or recirculation of hot gas, char and hot bed material internally. The biomass moisture content has an effect on the heat requirement. At high moisture content (>20 wt.% for downdraft gasifiers and > 50 wt.% for updraft gasifiers), the heat essential for drying and heating up of the biomass to pyrolysis temperature rises significantly. Therefore, in the air/oxygen gasification process high fuel moisture content impacts negatively on the pyrolysis and gasification product distribution.

4.3.3 Operating pressure

A gasifier may be classified as atmospheric if it operates at atmospheric pressure or pressurised if it operates at pressure above atmospheric (can be as high as 62 bar). Pressurised gasifiers are more suitable for use in integrated gasification combined cycle (IGCC) process since the syngas pressure will be high enough to be fed directly into the gas turbine (GT) fuel control system. In atmospheric pressure gasifiers, there will be a need for a fuel gas compressor after the syngas clean-up processes. High pressure gasifiers also reduce the cost and improve the efficiency of the syngas clean-up process. Since the syngas volumetric flow is much lesser than it would be for an atmospheric gasifier, the clean-up equipment is smaller in size.

4.3.4 Reactor type

Numerous biomass gasification reactor designs exist and can be grouped into two basic classes: fixed bed and fluidised bed reactors (Quaak et al., 1999; Basu, 2006). Each is typically designed for particular feedstock feed rates and characteristics, and produces syngas with dissimilar quality. The selection of a gasifier type is dependent on the end use and the quality of producer gas required.

4.4 Fixed bed reactors

In a fixed bed reactors, the biomass feed travels either counter-current or co-current to the flow of gasification medium (steam, air or oxygen) as the fuel is converted to fuel gas (Quaak et al., 1999). The fixed bed reactors are comparatively simple to operate and largely experience minimum erosion of the reactor body. There are three basic fixed bed designs – updraft, downdraft and cross-draft gasifiers (Quaak et al., 1999).

4.4.1 Updraft gasifier

In a fixed bed updraft gasifier, the solid fuel is fed from the top and the material travels down over four zones: drying, pyrolysis, reduction and oxidation zones. Oxidant (air or O₂) is added via a grate in the bottom of the gasifier, which provides a bed for the feedstock and char, and the produced syngas flows upward, counter-current to the flow of the fuel feed and, exiting at the top of the gasifier as shown in Figure 4.1a. This type of gasifier operates at about (700-1100 °C), with syngas exiting at 200-400 °C (Basu, 2010).

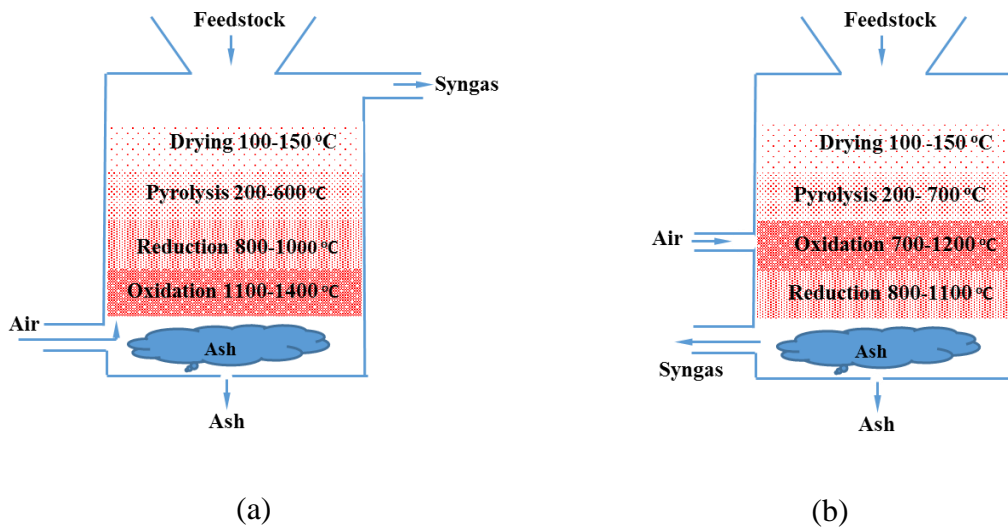


Figure 4.1 Updraft (a) and downdraft (b) biomass gasifier

The basic advantages of the updraft gasifier are its simplicity and high carbon conversion efficiency. The exit temperature of the producer gas is low because part of its sensible heat is transferred internally to the incoming fuel feed. As a result the updraft gasifier suited to high moisture content (up to 50 wt.%) biomass and wastes fuels.

Conversely, the major disadvantages of the updraft gasifier is it produces syngas with about 10 to 20 wt.% tar, which is considered in excess for many advanced applications (Sikarwar et al., 2016). The high tar content necessitates extensive gas cleaning if the producer gas is to be used in internal combustion engines (Reed & Das, 1988; Quaak et al., 1999). However, gas cleaning becomes less significant if the gas is to be used for direct heat appliances where the tars will simply be combusted (Reed & Das, 1988; Quaak et al., 1999).

Characteristics of updraft gasifiers are:

- Applied in the capacity range of 2-30 MW
- Fuel feed is dried first before it gets to the pyrolysis and gasification zones
- Suited to high moisture content (up to 50%) biomass and wastes fuels
- Partial oxidation of char supplies heat for endothermic gasification reactions
- Operates at about (700-1100 °C), with syngas exiting at 200-400 °C
- High amount of tar in syngas
- High efficiency

4.4.2 Downdraft gasifier

In a downdraft gasifier, oxidant (air or O₂) is added co-currently with the fuel feed as in Figure 4.1. (b) This type of gasifiers by their design minimise the production of tar to the range of 0.015 to 3.0 g per Nm³. The pyrolysis products undergo incomplete combustion in the oxidation zone, where the air that is less than the stoichiometric requirement is introduced. The heat evolved in the oxidation of the pyrolysis products supplies the heat necessary for the endothermic gasification reactions. This type of gasifier operates at a high temperature of about (800-1200 °C), with syngas exiting at 500-800 °C (Basu, 2010). Because of the high temperature reduction zone, thermal cracking and partial oxidation of tars takes place. This causes a filtering effect which helps to clean the syngas before it exits the gasifier. Tar conversion efficiency of this type of gasifier is more than 99%.

The main advantage of this type of gasifier is the low tar content (0.015-3.0 g per Nm³) of the syngas which makes it suitable for direct use in internal combustion engines without additional cleaning. It is the technology for small-scale processes in the range of

≤ 500 kWe (Quaak et al., 1999). Other advantages include simple design, very good carbon conversion, low capital cost and good compatibility with internal-combustion engines (Basu, 2006). Additionally, the time needed to ignite and bring the downdraft gasifier to working temperature is shorter (20–30 minutes) compared to the time required by an updraft gasifier (Basu, 2010). On the downward side, the downdraft gasifiers suffer from similar general limitations on feedstock properties as updraft gasifiers. The feed is required to have a moderately uniform particle size distribution with little fines, so as to sustain bed physical properties and reduce channelling. The moisture content of the feedstock is required to be below 20% to uphold the high temperatures necessary for cracking of tars (moisture content that is too high will cool the syngas). In addition, the fuel feed needs to have low ash content and high ash fusion temperatures to prevent slagging (Reed & Das, 1988; Quaak et al., 1999).

Characteristics of downdraft gasifiers are:

- Applied in the capacity range of 1-2 MW
- Low ash and low moisture (<20%) feed required
- partial oxidation of pyrolysis products provide heat for gasification reactions
- Operates at high temperature of about (800-1200 °C) which crack tars , with syngas exiting at 500-800 °C
- Tar content in syngas is low

4.4.3 The cross-draft gasifier

The cross draft gasifier is the simplest and lightest gasifier (Reed & Das, 1988). It is adapted for use of low ash fuels such charcoal instead of wood in gasification (FAO 1986). In the cross draft gasifier, air at high velocity enters via a single nozzle which causes considerable circulation, and flows across the bed of fuel and char. Charcoal gasification produces very high temperatures (1500 °C and higher) in a very small volume in the oxidation zone which can cause material problems (FAO, 1986). Due to high temperature, low tar syngas is produced, allowing engine load following capability. Insulation for the walls of the gasifier against the high temperatures in cross draft gasifiers is provided by the fuel (charcoal) itself thus allowing construction for all parts to be made of mild-steel except the nozzles and grates, which may require refractory alloys or some cooling (Reed & Das,

1988). The main advantages of the cross-draft gasifier is it can be used feasibly and economically at a very small scale (less than 10 kW) under certain conditions. This is due to its very simple gas-cleaning train consisting of only a cyclone and a hot filter which can be employed when using this type of gasifier in conjunction with small engines (FAO, 1986). In addition, it has a much faster start up time (5–10 min) than the downdraft and updraft gasifier. However, drawback includes minimal tar conversion capability and the consequent requirement for high quality (low volatile content) charcoal (FAO, 1986). Table 4.1 summarises the characteristics of the three fixed bed gasifier types.

Table 4.1 Characteristics of fixed bed gasifiers (Basu, 2010)

Feedstock (wood)	Updraft	Downdraft	Cross-draft
Moisture wet basis (%)	60 max	25 max	10-20
Dry ash basis (%)	25 max	6 max	0.5-1.0
Ash melting temperature (°C)	>1000	>1250	
Size (m)	0.005-0.1	0.02-0.1	0.005-0.02
Application range (MW)	2-3	1-2	<0.001 ^a
Operating Temperature range (°C)	700-1100	800-1200	>1500 ^a
Syngas exit temperature (°C)	200-400	500-800	1250
Tar (g(Nm ³) ⁻¹)	30-150	0.015-3.0	0.01-0.1
Syngas LHV (MJ/Nm ³)	5-6	4.5-5.0	4.0-4.5
Hot gas efficiency (%)	90-95	85-90	75-90
Turn down ratio (-)	5-10	3-4	2-3

^a (FAO, 1986)

4.5 Fluidised bed gasifiers

Fluidised bed gasifiers work on the principle of fluidization. Bed inert medium (alumina, sand or dolomite) are applied to mix the solid feed with gas phase and to help ensure steady operating temperature at the required level. The feedstock and the inert bed material behaves like a fluid. This behaviour is obtained by bowing fluidization medium (air, steam, steam/O₂ mixtures) over a bed of solid particles at a velocity sufficient enough to keep the solid particles in a state of suspension (Panwar et al., 2012). The bed is initially heated externally and the fuel feed introduced as soon a temperature that is sufficiently high is attained. The fuel feed is added through the bottom of the reactor. Immediately, they get mixed with the bed material and instantaneously heated up to the bed temperature

(FAO, 1986). Consequently, the pyrolysis of the fuel feed is very fast, resulting in a component mix with a quite massive quantity of gaseous materials. In addition, gasification and tar-conversion reactions take place in the gas phase. Most FBG are incorporated with a cyclone internally so as to lessen char blow-out as much as possible. Particles of ash are also agglomerated at the top of the reactor and have to be cleaned out if the syngas stream is to be used in engine applications (FAO, 1986).

FBGs are of two main types: bubbling FBG and circulating FBG. They have no separate reaction zones and drying, pyrolysis and gasification happens concurrently during mixing. The major advantages of FBGs, include: uniform temperature distribution in the gasification zone and easy control of temperature, feedstock flexibility, and ability to deal with fluffy and fine grained materials (sawdust) without the need of pre-processing (FAO 1986). However, FBGs are complicated and use expensive control systems. As a result, fluidised bed gasifiers tend to be commercially viable at bigger sizes (> 30 MW thermal output) (Quaak et al., 1999). Moreover, FBG suffer from high syngas tar content (up to 500 mg/m³ gas), incomplete carbon burn-out, and poor response to load changes (FAO, 1986).

4.5.1 Bubbling fluidised bed gasifier (BFBG)

In BFBG, the feedstock is introduced through the side, and/or beneath the bed, and the velocity of the gasifying agent is regulated such that it is just more than the minimum fluidization velocity of the bed material (Sikarwar et al., 2016). The syngas is collected from the top of the gasifier and ash is removed using a cyclone.

4.5.2 Circulating fluidised bed gasifier (CFBG)

The circulating fluidised beds operate at higher gas velocities (typically 3–10 m s⁻¹) than the BFBG, dragging the solid particles upwards with the gas flow (FAO, 1986; Sikarwar et al., 2016). CFBG has the following features: fast fluidization which improves heat and mass transfer and hence increase the rate of gasification. Char loss is reduced through the circulation of the char which increases the residence time of char so as to satisfy the need of reduction reaction (FAO, 1986). The CFBG can adapt to wide load changes.

4.6 Entrained flow gasifier (EFG)

In an entrained-flow gasifier (EFG), the biomass fuel particle is fed into the gasifier from the top in a coaxial flow of the gasifying medium (oxygen and steam, in some instances, carbon dioxide or a mixture of them). They are usually operated at pressures of 20-70 bar and at a temperature around 1200-1500 °C. Tar production is negligible, since the gases released pass through the very high-temperature (1000 °C) zone and are therefore nearly all converted into tar free syngas but with the penalty of oxygen consumption (Reed & Das, 1988; Zainal et al., 2001; Puig-Arnavat et al., 2010). EFGs have very short residence time, typically few seconds compared to the fluidised bed and fixed bed gasifiers. Detailed analysis of the various types of gasifiers can be found in the literatures (FAO, 1986; Reed & Das, 1988; Quaak et al., 1999; Basu, 2010; Diyoke et al., 2014 and Sikarwar et al., 2016).

4.7 Review of biomass gasification simulation models

Simulation models of a biomass gasifier can be categorized into thermodynamic equilibrium model (TEM), kinetic model, computational fluid dynamics (CFD) model and artificial neural network (ANN) model. Each of these models uses different approaches to predict the syngas composition. Nevertheless, the basic gasification reactions are common to each of them. A summary of the models is presented hereunder. For detailed work on each of the model, see the work of Puig-Arnavat et al. (2010).

4.7.1 Thermodynamic equilibrium models

Thermodynamic equilibrium models (TEMs) uses chemical and thermodynamic equilibrium, based on the concept of equilibrium constants or minimization of Gibbs free energy. In the chemical equilibrium approach, the system is assumed to attain chemical equilibrium. At such point, the system is taken to be at its best stable composition, which means the entropy of system is maximum, whereas its Gibbs free energy is minimised (Melgar et al., 2007). It pertinent to note that in the gasifier, chemical equilibrium is never attained in practice largely due to the fairly low operating temperatures (outlet temperatures of product gas range from 750 to 1000 °C) (Bridgwater, 1995). Nevertheless, TEM enables a rational prediction of the final syngas composition. Zainal et al. (2001) investigate the

influence of the moisture content and reaction temperature on the producer gas composition using a biomass gasification modelled based on TEM approach.

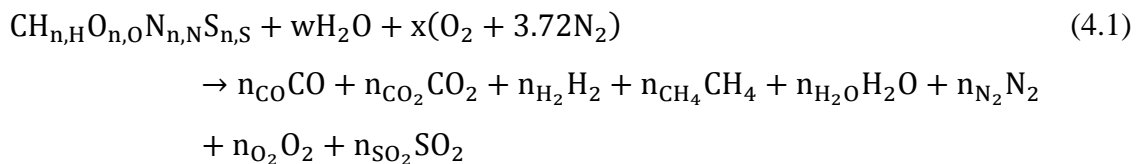
TEMs do not depend on gasifier design and hence lacks the capacity to predict the influence of geometric and design variables such as fluidizing velocity and gasifier height (Zainal et al., 2001; Puig-Arnavat et al., 2010). However, these models enables a reasonable prediction of the temperature of the system including the effect of biomass and process parameters on the syngas composition and yield.

The limitation of TEM is that the accuracy of results obtained with it is suspect. This is because, in model implementation, the carbon conversion is presumed to be 100% which is not factual in real gasification process and thus a kinetic model is preferred. Again, equilibrium is never attained at low reaction temperatures due to slow reaction rates and limited residence time. Moreover, TEMs are not suitable for simulation at different operating conditions (equivalent ratio, temperature). Before the model can be used to simulate process behaviours in different operating condition, a proper validation with at least three measurement in three different process conditions is recommended.

Many biomass gasifier models based on the TEMs exist. Some of them include the work done by: Zainal et al. (2001), Babu and Sheth (2006), Sharma et al. (2008), Gao and Li (2008) and Barman et al. (2012). TEMs can be implemented via the stoichiometric or nonstoichiometric approaches (Puig-Arnavat et al., 2010).

4.7.1.1 Stoichiometric equilibrium models

In this approach, a clearly defined reaction mechanism that integrates all species and chemical reactions involved is required. The model is based on choosing the species that are existing in the largest amounts, i.e. the ones with the lowest value of free energy of formation (Puig-Arnavat et al., 2010). SEMs can be implemented by treating the gasification reaction as one global gasification reaction as follows (Zainal et al., 2001; Sharma 2008):



Where C, H, O, N and S denote carbon, hydrogen, oxygen, nitrogen and sulphur and subscript n denote atoms and moles of the corresponding element in the biomass and pyrolysis species respectively. The variable w denote molar fraction of water in biomass. x corresponds to the molar quantity of air used during the gasification and depends on the equivalent ratio of the gasification process.

The overall gasification process can also be treated to be made up of sub processes such as drying, pyrolysis, oxidation and reduction and each of the sub process modelled separately and then linked together. For brevity, the first method is referred hereafter as the one step stoichiometric equilibrium models (Os-SEM) while the latter is referred to as Multi-step stoichiometric equilibrium models (Ms-SEM). The Ms-SEM offers more versatility and convenience than the Os-SEM since the molar composition and temperature at the various sub zones can be determined with the aid of a sub-model. Numerous combinations of the sub-models are possible depending on the model product requirement and choice/convenience.

4.7.1.2 Non-stoichiometric equilibrium models

Unlike in the SEM, the non-stoichiometric equilibrium models (NSEMs) is based on reducing the Gibbs free energy in the system without a reaction mechanism integrating all the reactions taking place. However, the moisture content and elemental composition of the biomass feed is required which is easily derivable from the ultimate analysis data of the feed. Consequently, this method is suited mainly to fuels like biomass whose exact chemical formula is not categorically known (Basu, 2010; Puig-Arnavat et al., 2010). Generally, some general assumptions are made in the implementation of equilibrium models (Puig-Arnavat et al., 2010):

- Steady state is assumed
- Ideal gas behavior of the gas phase;
- Residence time is infinite, so that reactions have huge time to occur;
- The gasifier operates isothermally and at atmospheric pressure
- No oxygen in the produced syngas;
- Negligible potential and kinetic energies
- Tar is modelled in the gaseous state;
- Nitrogen is considered inert

- Contribution of ash to the energy balance equation is ignored;
- Perfect mixing with uniform temperature and pressure;

Because of these assumptions, results obtained with SEMs are not very accurate under some conditions. For example at moderately low gasification temperatures, drawbacks include over prediction of H₂ and CO yields and the under prediction of CO₂, methane, tars and char (in fact, null values for these last three components above 800 °C) (Puig-Arnavat et al., 2010). To overcome this shortcoming, numerous scholars have modified and corrected the equilibrium model or used the quasi-equilibrium temperature (QET) approach (Puig-Arnavat et al., 2010). In QET approach, the equilibriums of the reactions in the model are estimated at a temperature that is lower than the actual process temperature (Panwar et al., 2012). More details of the QET approach can be found in (Panwar et al., 2012).

4.7.2 Kinetic rate models

In Kinetic rate models (KRM), kinetic rate expressions obtained from experiments is used to describe the conversion during biomass gasification including the char reduction process. KRMs have the capability to predict the syngas composition profiles and temperature within the gasifier. It can also reveal the overall gasifier performance for a given operating condition and gasifier configuration (Baruah & Baruah, 2014). KRMs takes into account both the kinetics of gasification reactions within the gasifier and the hydrodynamics of the gasifier reactor. Reaction kinetics entails the use of mass and energy balances including the knowledge of bed hydrodynamics to obtain the yields of gas, tar, and char at a given operating condition whereas reactor hydrodynamics involves the knowledge of the physical mixing process. This becomes important when the residence time necessary for full conversion is long which occurs when the reaction temperature is very low making the rate of reaction very slow. Therefore, KRM is found to be more appropriate and exact at moderately low operating temperatures compared to equilibrium model (Baruah & Baruah, 2014). As its name suggests, the fundamental principle of kinetic rate modes hinges on the Arrhenius equation as follows:

$$k = F \exp(AE/RT) \quad (4.2)$$

Where k is the reaction rate constant (s^{-1}), F_f the pre-exponential factor or frequency factor (s^{-1}), E is the activation energy ($Jmol^{-1}$), R is universal gas constant ($JK^{-1}mol^{-1}$); and T the absolute reaction temperature (K).

KRMs are detailed and enables a more accurate agreement between simulation and experimental data when the residence time of gas and biomass is relatively short. Unlike the TEMs that are limited at low reaction temperatures, the KRMs are more appropriate and accurate at moderate operating temperatures (below 800 °C) of the gasifier. At higher temperatures (above 1200 °C) when the rate of reaction is high, the TEM is more suitable. However, KRMs usually contain parameters that limit their applicability to different gasifiers. Consequently, TEMs, which do not depend on design of gasifier may be more appropriate for parametric analysis on the effect of the most important fuel and process parameters. Moreover, KRMs are computationally rigorous and its complexity depends on the level of desired outputs of the model. The more the desired out/accuracy, the more incorporation of detailed reaction kinetics and/or reactor hydrodynamics. To simplify the complexity, some reasonable simplifying assumptions are usually made (Baruah & Baruah, 2014). Many researchers have focused expansively on kinetic models of biomass gasification probably due to its accuracy. They include: Wang and Kinoshita (1993), Di Blassi (2000), Giltrap et al. (2003) Babu and Sheth (2006), Radmanesh et al. (2006) and Sharma (2008). Table 4.2 highlights the advantages and limitations of the biomass gasification simulation models discussed in the preceding sections.

Among the modelling techniques discussed in this chapter, the multi-step stoichiometric equilibrium model (Ms-SEM) was selected for use in the work presented in this thesis because this model has more capability than the single step stoichiometric equilibrium model since the syngas composition and temperature at different zone of the gasifier can be evaluated with it. In addition, downdraft biomass gasification has been selected because of its features and advantages as already highlighted in the preceding section. We therefore present in the following section a review of the work done exclusively on downdraft biomass gasification.

4.8 Review on models on downdraft biomass gasification

On the basis of any of the analysed biomass gasifier models above; so many qualitative downdraft gasification models exist: Gronli (1996), Zainal et al. (2001), Giltrap et al. (2003), Babu and Sheth (2006), Melgar et al. (2007) and Sharma (2008).

Sharma (2008) carried out a comparison of equilibrium and kinetic modelling of char reduction reactions in a downdraft biomass gasifier. In their approach, mass and energy balance were coupled with kinetic rate parameters (using varying char reactivity factor) to demonstrate the effect of reaction temperature on dry gas composition, un-reacted char and endothermic heat absorption rate in the reduction zone. An equilibrium model for predicting the syngas composition in a downdraft gasifier fed by solid waste was developed by Jarunghammachote and Dutta (2007). To improve the performance of the model, an amendment was made by multiplying the equilibrium constants with coefficients. The modified model was validated with experimental data from different researchers. Melgar et al. (2007) predicted the reaction temperature and final syngas composition using a combination of chemical equilibrium and thermodynamic equilibrium approach. Experimental studies have been published by Zainal et al. (2001), Jayah et al. (2003), Sheth and Babu (2009), Ratnadhariya and Channiwala (2010) and Sarker and Nielsen (2015). Sharma (2009) experimentally obtained temperature profile, gas composition, calorific value and trends for pressure drop across a porous gasifier bed.

Ratnadhariya and Channiwala (2009) developed a detailed model of a three-zone equilibrium and kinetic free model of biomass gasification in a downdraft gasifier. Qualitative agreement with experimental data is established. In another study, Blasi (2000) developed a comprehensive dynamic model for studying the behaviour of stratified downdraft gasifiers. Their results showed that the predictions of the gas composition are in agreement with experimental data.

Table 4.2 Advantages and limitations of biomass gasification simulation models

	TEMs	KM	ANN
Advantages	<ul style="list-style-type: none"> • Useful in prediction of gasifier performance under various different operational parameters • Easy to implement • Do not require any knowledge of the mechanisms of transformation • Independent of the reactor design and not limited to a specified range of operating conditions. 	<ul style="list-style-type: none"> • Potentially more accurate in deducing exit gas yield and composition • Good for gasifier design and improvement purposes • Can be applied to low-temperature gasification 	<ul style="list-style-type: none"> • Do not require extensive knowledge regarding process • Do not require the formulation of complex mathematical equations and they can learn and identify non-linear relations themselves (Sikarwar et al., 2016)
Limitations	<ul style="list-style-type: none"> • Only some reactions are taken into consideration • Not suitable for low temperature gasification • TEMs do not depend on gasifier design and hence lacks the capacity to predict the influence of geometric and design variables such as fluidizing velocity and gasifier height 	<ul style="list-style-type: none"> • All possible process reactions are not considered • Different model reaction coefficients and kinetics constants • Dependent on the gasifier design • More complex than TEMs 	<ul style="list-style-type: none"> • Depends on large quantity of experimental data

Gao and Li (2008) modelled the combined pyrolysis and reduction zone of a downdraft gasifier. Their model was made up of three parts: the pyrolysis, oxidation and reduction zone. In the model, it was assumed the products of pyrolysis were only CO, CH₄ and H₂O and only the pyrolysis and reduction zones were considered leaving out the combustion zone. The main weakness of their model is the inability to predict gas concentrations at the two zones and the omission of H₂ and tar in the assumed pyrolysis gas. Hence, an improvement to the model is necessary to extend its application and make it more robust.

In this chapter, the prediction of the pyrolysis and oxidation zone temperature are included. The reactor consists of three zones; pyrolysis, combustion and gasification zone where different reactions take place. The method adopted by Ratnadhariya and Channiwala (2009) was used in the estimation of the pyrolysis and oxidation product species. One of the differences between this model and Ratnadhariya and Channiwala's model is in the treatment of the water-gas shift reaction and tar. Ratnadhariya and Channiwala (2009) did not account for tar in the pyrolysis product composition and water gas shift reaction. Different from the work from Ratnadhariya and Channiwala (2009), tar in the composition of syngas was considered in this work using previously determined experimental tar measurements (Diyoke et al., 2018b). According to Cho and Joseph (1981), water-gas shift reaction is catalysed by the mineral matter in coal. Extending this to biomass, equation for this reaction have been incorporated in the model as well.

Furthermore, energy and material balances around the pyrolysis and oxidations zones are applied with some simplifying assumptions to obtain a more accurate representation of the temperature in the various sections of the reactor. Then a parametric study of the effect of operating conditions and fuel properties on the cold gas efficiency, gas yield, heating value and carbon conversion efficiency was carried out.

4.9 Model development

The biomass downdraft gasifier reactor under consideration is diagrammatically shown in Figure 4.2. The gasifier which operates at atmospheric pressure is made up of three dissimilar partitions where different chemical and physical events take place; heat

up/drying/pyrolysis, combustion and gasification. Biomass loaded into the reactor reacts with air to generate syngas consisting of largely hydrogen and carbon monoxide and lesser amounts of methane.

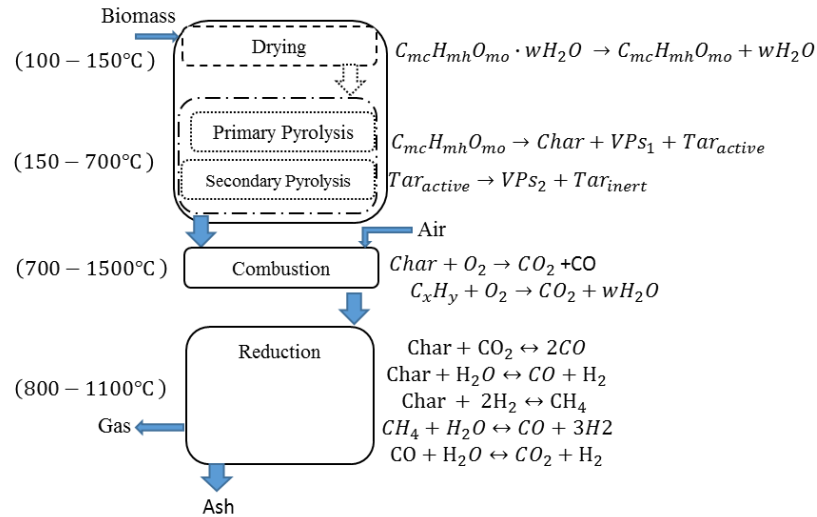


Figure 4.2 Three zone downdraft gasifier(Diyoke et al., 2018b)

The first zone is the drying zone where the biomass undergoes some moisture removal before proceeding to the pyrolysis zone (PZ). At the PZ, the dry biomass is initially cracked thermally into volatile products (VPs₁), char and active tar (Tar_{active}) in a primary reaction (Ngo et al., 2011; Diyoke et al., 2018b). The VPs₁ consist of the gases; CO, CO₂, CH₄, H₂, C₂H₄, and H₂O. The active tar denotes the primary tar that is formed first from the pyrolysis of the solid biomass (Morf et al., 2002; Diyoke et al., 2018b). The formation of the active tar is unavoidable, however, after their formation, the active tar simultaneously undergo secondary pyrolysis in which their mass and composition is altered to yield secondary volatile products (VPs₂) like CO, CO₂, H₂, some hydrocarbons like C₂H₂, C₂H₄, and C₃H₆, and inert tar (Wurzenberger et al., 2002; Ngo et al., 2011 and Diyoke et al., 2018b). Inert tar is the final tar formed after gasification which is assumed to be unreactive in the simulations.

According to the experimental investigation by Rath and Staudinger (2001), only 78% of the initial tar is cracked and 22% remains unchanged. The primary and secondary

pyrolysis reactions products make up the final pyrolysis product species. These species pass through the high temperature oxidation zone where additional reactions takes place at a very fast rate, releasing large amount of heat, which provides the energy necessary to sustain the endothermic gasification reactions (Sadaka, n.d.).

We present hereunder, the approaches adopted in modelling the physical and chemical events taking place in each zone of the gasifier.

4.9.1. Drying zone

The temperature reached in a biomass gasifier is influenced significantly by the moisture content of the fuel. The moisture content of fresh cut wood biomass is very high, ranges from 30 to 60 wt.% (Kaushal et al., 2010; Chen et al., 2012; Diyoke et al., 2018b). In order to produce a product gas with substantially high calorific value, biomass gasifiers prefer fuel feed with moisture content in the range of 5–20 wt.% (Kaushal et al., 2010). In the drying zone the moisture in the wet feed is detached by the heat produced by the incomplete combustion of some part of the fuel feed in the combustion zone. To model the drying process, a basic approach is assumed. It is supposed that the moisture in the biomass vaporises as its temperature gets to 100°C before pyrolysis starts. The amount of energy required to dry out moisture, Q_{dry} is the totality of the sensible energy to increase the moisture to a temperature of 100 °C plus the energy to vaporise it (Diyoke et al., 2018b) as follows:

$$Q_{dry} = w[c_{p,w}(\Delta T) + \Delta \dot{h}_{v,w}] \quad (\text{Jkg}^{-1}) \quad (4.3)$$

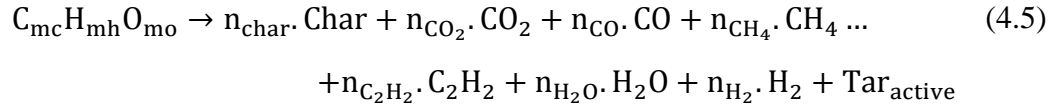
Where w represents the amount of moisture per mol of wood, $C_{p,w}$ is the specific heat of water ($\text{Jmol}^{-1}\text{K}^{-1}$), ΔT is the temperature difference between the initial and final state of moisture in the wood and $\Delta \dot{h}_{v,w}$ is latent heat of vaporization of water (Jmol^{-1}). The amount of water per kmol of wood, designated w is given as follows (Melgar et al., 2007):

$$w = \frac{Mw_B MC}{Mw_{H_2O}(1 - MC)} \quad (\text{kgmol}^{-1}) \quad (4.4)$$

Where Mw_B signifies the molar mass of the biomass (gmol^{-1}), Mw_{H_2O} is molar mass of water (gmol^{-1}) and MC is the biomass moisture content by weight.

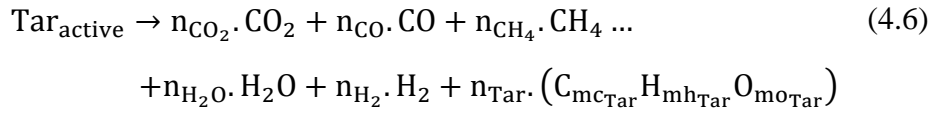
4.9.2. Pyrolysis zone

In the pyrolysis zone, the heat developed in the oxidation zone is used to crack down the biomass to primary pyrolysis products (gases and char) including primary or active tar (Shafizadeh & Chin, 1977) as shown in the following equation:



Where n is the number of moles of species of the respective pyrolysis product species and mc, mh and mo are the number of atoms of carbon, hydrogen and oxygen in the biomass.

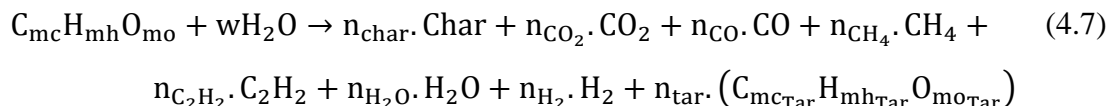
As reported by Radmanesh et al. (2006), the primary pyrolysis product is composed of 60% of active tar. The active tar instantaneously undergo secondary pyrolysis in a secondary reaction to produce secondary volatile products (VPs2) such as CO, CO₂, H₂, some hydrocarbons like C₂H₆, C₂H₄, and C₃H₆, and inert tar (Wurzenberger et al., 2002, Ngo et al., 2011) as depicted in the equation below:



The quantities mc_{Tar} , mh_{Tar} and mo_{Tar} denote the number of atoms of carbon, hydrogen and oxygen in the tar respectively. Higher aliphatic compounds formed in secondary tar cracking are lumped into methane formation in the model.

Rath and Staudinger (2001), found in their experimental investigation that only 78% of the initial tar is cracked while 22% remains unaffected.

The process of tar cracking is such a very complex phenomenon. In the thesis, the process of active tar cracking in the secondary reaction as in Eq. 4.6 was not considered separately since it is very difficult to do so. Rather, the total moles of the specific constituent released was predicted while relying on the supposition that the moles of the different volatiles including char produced during the primary and secondary pyrolysis reactions make up the overall moles of the individual gases in the pyrolysis zone. In the light of the above simplifying assumption, the overall pyrolysis process is assumed to be represented by the global one step pyrolysis model reaction (Shafizadeh & Chin, 1977):



4.9.2.1 Estimation of pyrolysis yields

The kinetic free, stoichiometric equilibrium modelling approach was applied in the model development and one of the features of the model is that the pyrolysis products are calculated using a combination of atomic balance approach and some simplifying relations under the assumption that the formations of the volatiles are independent of temperature. The same approach has been used in other validated published literatures in biomass gasification (Merrick, 1983; Radmanesh et al., 2006; Ratnadhariya & Channiwala, 2009 and Centeno et al., 2012).

To obtain the yields of the pyrolysis product species, a set of seven simultaneous equations were constructed, with the final mole of char and the six volatile matter species as unknowns. The species are: H₂, H₂O, CO, CO₂, CH₄ and C₂H₂. Predicting the concentration of tars produced in pyrolysis reaction is challenging since the process involves very complicated chemical reactions. Tar yield varies with biomass elemental composition and temperature. In downdraft biomass gasification, maximum tar yield is negligible and does not fluctuate considerably with temperature (Dogru et al., 2002). Therefore for simplicity and since tar is a less important variable to be predicted, tar was considered as an input variable. Tar yield was presumed to have fixed characteristic elemental composition of CH_{1.03}O_{0.33} (Tinaut et al., 2008) with a maximum inert tar yield of 4.5% by mass as reported by the authors (Tinaut et al., 2008; Barman et al., 2012) in their experiment (Diyoke et al., 2018b).

The first three equations are the elemental balance equations for carbon, hydrogen and oxygen respectively as depicted below:

$$mc = n_{\text{char}} + n_{\text{CO}_2} + n_{\text{CO}} + n_{\text{CH}_4} + 2 * n_{\text{C}_2\text{H}_2} + n_{\text{Tar}} * mc_{\text{Tar}} \quad (4.8)$$

$$mo = 2n_{\text{CO}_2} + n_{\text{CO}} + n_{\text{H}_2\text{O}} + n_{\text{Tar}}mo_{\text{Tar}} \quad (4.9)$$

$$mh = 4n_{\text{CH}_4} + 2n_{\text{C}_2\text{H}_2} + 2n_{\text{H}_2\text{O}} + n_{\text{H}_2} + n_{\text{Tar}}mh_{\text{Tar}} \quad (4.10)$$

Merrick (1983) found from his experimental measurements for coal, that it is possible to use the elemental hydrogen and oxygen content in the coal to relate its final volatile matter after pyrolysis. Precisely, the author found that the yields of CO and CO₂ can be predicted roughly by assuming that 18.5% and 11% of the oxygen content of the coal is evolved in these species. In addition, it was reported that the final yield of CH₄ and

C₂H₄ correspond approximately to 32.7% and 4.4% of the hydrogen content of the coal (Diyoke et al., 2018b).

Extending the above findings to biomass, the fourth and fifth equations are generated. Thus, the fourth and fifth equation are used to express water and hydrogen yield from the available oxygen and hydrogen in the biomass after tar formation respectively. It is assumed that 80% of the available oxygen in the fuel is evolved in water formation in the pyrolysis zone (Mott and Spooner 1940; Ratnadhariya & Channiwala, 2009) while half of the available hydrogen after water and tar formation is evolved as hydrogen gas (Ratnadhariya & Channiwala, 2009) as depicted in the following equations (Diyoke et al., 2018b).

$$n_{\text{H}_2\text{O}} = (m_{\text{O}} - n_{\text{Tar}}m_{\text{O}_{\text{Tar}}})0.8 \quad (4.11)$$

$$n_{\text{H}_2} = \frac{1}{2}(m_{\text{H}} - n_{\text{Tar}}m_{\text{H}_{\text{Tar}}} - 2n_{\text{H}_2\text{O}}) \quad (4.12)$$

The remaining two equations were used to express the molar yield of CO, CO₂, CH₄ and C₂H₂. The yield of CO and CO₂ were related to the available oxygen content of the biomass after water and tar formation while the yield of CH₄ and C₂H₂ is related to the biomass hydrogen content. It is assumed the remaining oxygen is evolved in the formation of CO and CO₂ with the mole of the species formed related according to the inverse of their molar mass (Mm) ratio (Storm et al., 1999; Berends, 2002; Ratnadhariya & Channiwala, 2009 and Diyoke et al., 2018b).

$$(m_{\text{O}} - n_{\text{Tar}}m_{\text{O}_{\text{Tar}}})0.2 = n_{\text{CO}_2} + n_{\text{CO}} \quad (4.13)$$

$$\text{where } n_{\text{CO}_2}/n_{\text{CO}} = \text{Mm}_{\text{CO}}/\text{Mm}_{\text{CO}_2} \quad (4.14)$$

The remaining hydrogen in the fuel is assumed to have evolved in the formation of CH₄ and C₂H₂ with the moles of each specie related according to the inverse ratio of their molar masses (Mm) (Storm et al., 1999; Parikh et al., 2002; Ratnadhariya & Channiwala, 2009 and Diyoke et al., 2018b).

$$0.5(m_{\text{H}} - n_{\text{Tar}}m_{\text{H}_{\text{Tar}}} - 2n_{\text{H}_2\text{O}}) = n_{\text{CH}_4} + 2n_{\text{C}_2\text{H}_2} \quad (4.15)$$

$$\text{where, } n_{\text{C}_2\text{H}_2}/n_{\text{CH}_4} = \text{Mm}_{\text{CH}_4}/\text{Mm}_{\text{C}_2\text{H}_2} \quad (4.16)$$

Other simplifying assumptions include the following (Diyoke et al., 2018b):

- All the elemental hydrogen and oxygen in fuel is released during de-volatilization; and hence the char formed is modelled as pure carbon (Sharma, 2011, Wen et al., 1982)
- Char yield in the gasifier is insensitive to pyrolysis temperatures encountered in the pyrolysis zone (Wen et al., 1982; Sharma, 2011)
- Temperature of the volatiles is the same as char temperature at every point in the gasifier (i.e. transfer of heat between gas and solid is instantaneous) (Wen et al., 1982)

Finally, the seven simultaneous equations were solved to obtain the moles of the formed pyrolysis product species n_j (n_{CO_2} , n_{CO} , n_{CH_4} , $n_{C_2H_2}$, n_{H_2O} and n_{H_2}). The mole of char (n_{char}) left after pyrolysis was calculated by elemental balance on the volatiles (Diyoke et al., 2018b).

4.9.3. Oxidation zone

In the oxidation zone, some of the combustibles volatiles and char from the pyrolysis zone react with oxygen that is below stoichiometric amount leading to incomplete combustion reaction. The reaction is exothermic causing a swift increase of temperature to about 1200 °C. The heat developed is then used to sustain the endothermic gasification reactions including the drying and further pyrolysis of the feed.

Since oxygen is inadequate in the oxidation zone, it is assumed the core reactions occurring in the oxidation zone are the hydrogen oxygen reaction, acetylene oxidation and char oxygen reaction (Centeno et al., 2012). The affinity between hydrogen and oxygen is more than that between oxygen with carbon. Thus hydrogen is assumed to first react with all the oxygen it requires to form water (Thring 1962; Amundson & Arri, 1978; Ratnadhariya & Channiwala, 2009) as follows:



In the above reaction, y is the actual air per kmol of wood for the biomass combustion reaction and is given as;

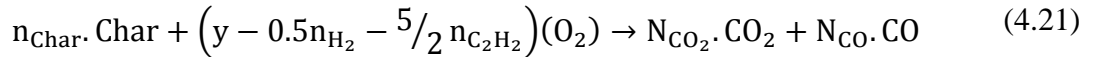
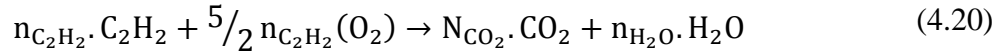
$$y = \frac{1}{ER} (mc + 0.5mh - 0.25mo) \quad (4.18)$$

ER is the equivalence ratio which denotes the ratio of stoichiometric air to actual air per unit quantity of fuel ($C_{mc}H_{mh}O_{mo}$):

$$ER = \frac{(A/F)_{\text{stiochiometric}}}{(A/F)_{\text{actual}}} \quad (4.19)$$

Where A/F is the air fuel ratio.

Hydrogen oxidation is followed by acetylene oxidation and then char oxidation takes place to consume whatever oxygen is left as in in the following equations.



The char-oxygen reaction is fast and affected by diffusion resistance (Cho & Joseph, 1981). To Predict the number of moles of the CO (N_{CO}) and CO₂ (N_{CO_2}) formed by the reaction requires a major effort. Different correlations have been applied in the literature to estimate the ratio of number of moles of CO₂ to CO in the above reaction. As reported by Cho and Joseph (1981) the ratio of 1:1 has been used by some authors for the molar ratio of CO₂ to CO. Cho and Joseph used the correlation of the following form in their work (Arthur, 1951; Cho & Joseph, 1981):

$$N_{CO}/N_{CO_2} = F \exp(-E/RT) \quad (4.22)$$

In this work, the molar quantities of the CO₂ and CO formed from char oxidation is assumed to proceed inversely according to the inverse ratio of their heat of reaction in the form (Ratnadhariya & Channiwala, 2009; Diyoke et al., 2018b):

$$N_{CO}/N_{CO_2} = [\Delta H_R]_{CO}/[\Delta H_R]_{CO_2} \quad (4.23)$$

The heat of formation of the species is as given below:



The final moles of the product species of the oxidation zone (N_j) is estimated by implementing a mass balance of the constituents under the assumption that all the unreacted

constituents from the pyrolysis zone contribute to the final constituents in the oxidation zone (Diyoke et al., 2018b).

4.9.4 Energy Balance

Energy balance is used to account for the energy that enters and exits a thermodynamic system as a result of inflow and outflow of species including losses. It enables the determination of unknown thermodynamic properties of a system. To carry out an energy balance on the downdraft gasifier, each section of the reactor is treated separately. The temperature in the reactor evolves according to the heat released by the reactions.

4.9.4.1. Energy balance of the pyrolysis zone

The energy flows for the pyrolysis zone of the reactor is depicted in Figure 4.3. One primary heat inflow and two outflows are involved. The heat inflow, represented by Q_i is the enthalpy transferred into the pyrolysis zone of the reactor from the stoichiometric combustion of wood. This heat serves two purposes, first a small part of it is used to supply the energy required for drying (Q_{dry}) while the remaining part is used to supply the energy required for the actual pyrolysis process. The energy for drying can also be supplied from external sources like using the recovered waste heat from flue gases, heat developed during air compression in compressors, solar power or excess wind electricity.

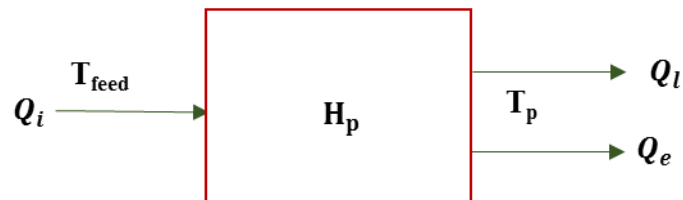


Figure 4.3 Energy input/output for a pyrolysis process

The two energy outflows are the heat loss (Q_l) and the energy (Q_e), associated with the exiting pyrolysis product species. The energy consumed by the pyrolysis process only is then the sum of the energy used for drying and pyrolysis minus any losses as represented by En_{py} as follows:

$$En_{py} = Q_i - Q_{loss} \quad (\text{Jkg}^{-1}) \quad (4.25)$$

Biomass Fuel enter the pyrolysis zone at a temperature (T_{feed}) and produce the volatile products at a pyrolysis temperature, T_p . For a steady state reacting process involving no work (W_x) and heat interactions (Q), energy balance of the pyrolysis zone (PZ) is given as (Flagan, 1988):

$$\frac{dU}{dt} = Q_i - \sum_{j,out} n_j h_j + Q_{loss} = 0 \quad (4.26)$$

Where $h(i, j) = u + pv$ and $n(i, j)$ represents the molar specific enthalpy, and molar flow rate of species entering and exiting the PZ, respectively. Q_i is approximated as the sum of heat of formation ($\dot{h}_{f,B}$) of biomass including that used to dry away moisture and it is calculated using the following relation (Daugaard & Brown, 2003):

$$Q_i = \dot{h}_{f,B} + \sum_1 \Delta h_i + Q_{dry} \quad (\text{Jkg}^{-1}) \quad (4.27)$$

The term $\dot{h}_{f,B}$, represents the enthalpy of combustion of the biomass (Jkg^{-1}). The second term refers to the sensible enthalpy of the biomass fuel entering the pyrolysis reactor. In this work, the sensible enthalpy is taken as zero since the biomass is assumed to have entered at the reference temperature. On the basis of one mole of biomass fuel ($C_{mc}H_{mc}O_{mo}$), the heat of formation of the biomass ($\dot{h}_{f,B}$) is the difference between the molar specific enthalpies of the products and reactants assuming the biomass fuel reacted stoichiometrically in air (Flagan, 1988) as in the following equation.

$$\dot{h}_{f,B} = mc \times \dot{h}_{f,CO_2}(T_0) + 0.5 \times mh \times \dot{h}_{f,H_2O}(T_0) - (x\dot{h}_{f,O_2}(T_0)) - HV \times Mm_B \quad (4.28)$$

Where x is the stoichiometric amount of air per kmol of wood required for the combustion of the biomass given as $(mc + 0.5mh - 0.25mo)$, the superscript (\cdot) represents evaluation with respect to the chemical reference state (Flagan, 1988). Heating value (HV) as used in the equation denote heat release as a result of combustion. It can be either the higher heating value (HHV) or the lower heating value (LHV). The LHV relates to the heat of reaction when the latent heat of condensation of water is present as vapour. The HHV, corresponds to the case when the water is recovered (Flagan, 1988). In the gasification process, the temperatures attained is sufficiently high such that any water formed exist only as vapour. Thus the lower heating value (LHV) is used in the heat of

formation estimation. The HHV in MJ/Kg is calculated by the empirical correlation by Seyler based on ultimate analysis (Seylor, 1938) as cited in Channiwala and Parikh (2002). The terms C, H, and O, represent the percentage by weight of carbon, hydrogen, and oxygen, in the fuel.

$$\text{HHV} = 0.519C + 1.625H + 0.001O^2 - 17.87 \quad (\text{MJkg}^{-1}) \quad (4.29)$$

The heating value or mass specific enthalpy of combustion is converted to the mole specific value by multiplying by the molar mass of the biomass fuel. Based on the general steady state energy equation, the energy balance equation for the pyrolysis zone can be written as follows:

$$\dot{h}_{f,B} + Q_{\text{dry}} = \sum_{j,\text{out}} n_j [h_j(T_p) - h_j(T_o) + \Delta h_{f,j}(T_o)] + Q_{l,\text{PZ}} \quad (4.30)$$

Where $Q_{l,\text{PZ}}$ is the heat loss in the pyrolysis zone. Heat loss takes place in the gasifier due to unrealized heats of combustion because of un-combusted char, endothermic heats of reaction and losses through the walls of the gasifier vessel. Heat loss is dependent on the temperature attained in the combustion zone and by extension the pyrolysis zone. Since temperature attained in the gasifier depends on the heating value of the fuel and the equivalent ratio (Ratnadhariya & Channiwala, 2009), the heat loss in the pyrolysis zone was calculated as 12% of the product of the LHV and reciprocal of the equivalent ratio (ER). For example, at ER of 4, HHV of 21kJkg^{-1} , the heat loss in the pyrolysis zones is 13.83kJmol^{-1} , representing 11% of the heat of formation of the biomass.

4.9.4.2 Energy balance of the oxidation zone

Figure 4.4 depicts the cross section of the oxidation zone (OZ) of the reactor. Air at temperature (T_a) and the product species of the pyrolysis zone at temperature (T_p) enter as reactants to the oxidation zone and exit as products at oxidation temperature (T_{ox}).

Rapid reactions on the order of 1 milli seconds take place in gasification process, and negligible heat or work transfer takes place on the time scale of the process. Applying the first law of thermodynamics to the system results to energy balance equation for the oxidation zone as follows:

$$\sum_{j,\text{in}} n_j [h_j(T_p) - h_j(T_o) + \Delta h_{f,j}(T_o)] \quad (4.31)$$

$$= \sum_{i,\text{out}} n_i [h_i(T_{\text{ox}}) - h_i(T_o) + \Delta h_{f,i}(T_o)] + Q_{l,\text{OZ}}$$

Where T_p is pyrolysis zone temperature, T_{ox} is the oxidation zone temperature, n is the number of moles, h is enthalpy and the subscript j and i represents the respective species of the pyrolysis and oxidation zone respectively. $Q_{l,\text{OZ}}$ is the heat loss from the oxidation zone which has been estimated using $0.5 \times \text{LHV} \times \text{ER}^{-1}$ based on the experimental results of study of temperature profiles of downdraft gasifier fed with rubber wood by Jayah et al. (2003).

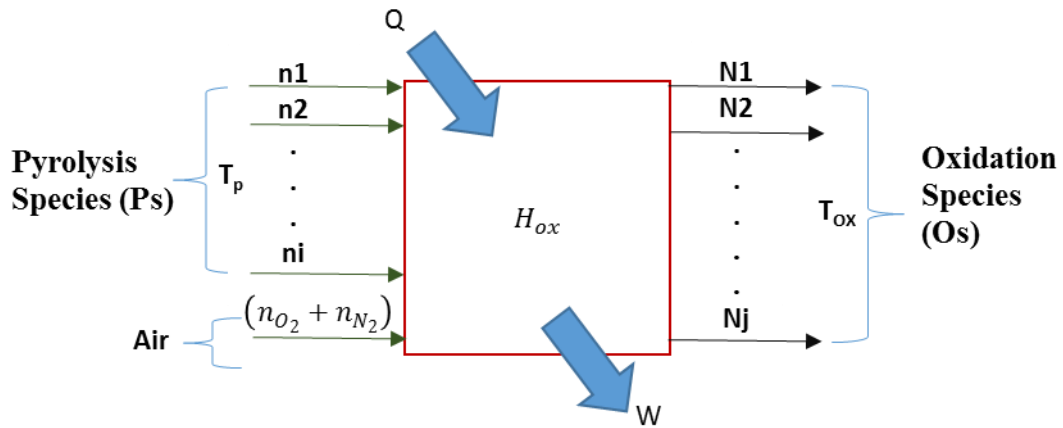


Figure 4.4 Cross-section of the oxidation zone showing species input/output

The enthalpy of formation data for each of the species has been taken from Flagan (1988) while the sensible enthalpy term is evaluated as an integral over the temperature of the specific heat at constant pressure (Flagan, 1988) given as follows:

$$h_i(T) - h_i(T_o) = \int_{T_o}^T C_{p,i}(T) dT \quad (4.32)$$

In general, the specific heat varies with temperature and since in biomass gasification and combustion applications, the range of temperature variation is large, the dependence of specific heat on temperature have to be accounted for. In the model the

specific heat is approximated as a linear function of temperature using the following (Flagan, 1988):

$$C_{p,i} \approx a_i + b_i T \quad (4.33)$$

The constants (a, b) in the expression for the various species have been taken from Flagan (1988). Thus:

$$h_i(T) - h_i(T_0) = a_i(T - T_0) + \frac{b_i}{2}(T^2 - T_0^2) \quad (4.34)$$

The specific heat of the tar has been approximated using the following expression (Gronli, 1996):

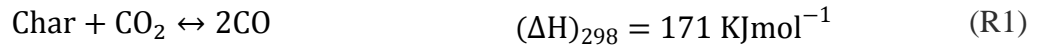
$$C_{p,Tar} = -0.10 + 4.40 \times 10^{-3}T - 1.57 \times 10^{-6}T^2 \quad (\text{kJkg}^{-1} \text{K}^{-1}) \quad (4.35)$$

The unknown temperature of the species within the pyrolysis (T_p) and oxidation zone (T_{ox}) has been estimated by solving the energy balance equations of the pyrolysis and oxidation zones through a developed Matlab computer code (Diyoke et al., 2018b).

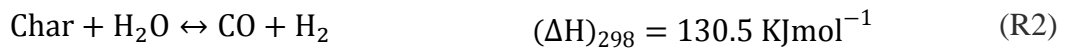
4.9.5 Reduction zone

The modelling of the reduction zone was done by assuming it is a cylindrical reactor with uniform cross sectional area. The volatiles gases and char evolved from the oxidation zone forms the initial moles of the species existing in this zone. Since the tars were assumed inert initially, they were not involved in the reactions in the gasification zone. In this zone, the char which is assumed to be elemental carbon is gasified with CO_2 , H_2 and H_2O in a complex set of heterogeneous gas-solid reactions (R1-R3) (Groeneveld & Van Swaaj, 1979):

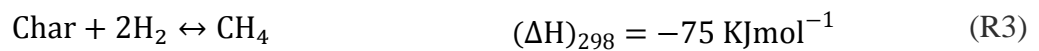
Boudouard Reaction



Water gas reaction



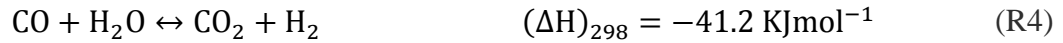
Methane formation



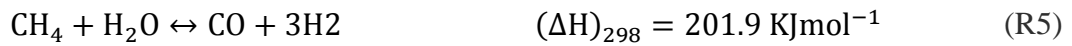
The above reactions take place instantaneously though the reaction rates are dissimilar and vary with operation conditions. The thermodynamics and kinetics of these reactions determine the rate of char conversion to gas and the resultant gas composition at any location in the gasification zone (Reed et al., 1987). Reactions R1 and R2 are first order in the CO_2 and H_2O partial pressures (P_{CO_2} and $P_{\text{H}_2\text{O}}$) respectively and both reactions proceed in parallel (Diyoke et al., 2018b). The exothermic char combustion in the oxidation zone release a tremendous amount of thermal energy and this energy plus that contained by the hot combustible gases from the zone is used to drive the two reactions (R1 & R2) since they are endothermic. As the conversion of char takes place, the temperature of the species reduces progressively, thus reducing the rate of the reactions till they are no more substantial at temperature below about 1000 K (Reed et al., 1987).

The volatile gases and products from char gasification are redistributed in the gas phase in accordance with the following homogeneous gas-gas reactions (R₄-R₆) (Giltrap et al., 2003; Gao & Li, 2008; Diyoke et al., 2018b):

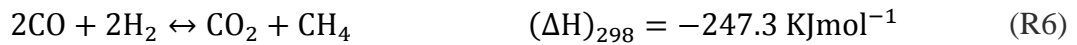
Water gas shift reaction



Methane steam Reforming



Methanation



The methane evolved by the reaction between the hydrogen and char is converted to more useful syngas components (CO , H_2) by the methane steam reforming reaction. Any char left after the reaction is deposited as carbon. The methane-steam reforming reaction and water gas shift reaction can progress in both the forward and reverse direction depending on gas composition and temperature as determined by equilibrium.

The reaction rates of the char gasification reactions are considered to have an Arrhenius type temperature dependence given by Wang and Kinoshita (1993) and to be proportional to the difference between the actual reactant/product ratio and the

corresponding equilibrium ratio (Gao & Li, 2008). The reactions (R1-R6) proceed at different rates and representing them with a general equation of the form:



The speed (r_R) of the reaction above can be expressed in Arrhenius form as:

$$r_{R,x} = R_f \times F_{f,R,x} \times \exp\left(\frac{-E_{R,x}}{RT}\right) \times \left\langle [P_A]^{n_A} \cdot [P_B]^{n_B} - \frac{[P_C]^{n_C} \cdot [P_D]^{n_D}}{K_{R,x}} \right\rangle \quad (4.37)$$

$$x = 1, 2 \dots 5$$

where R_f , $F_{f,R,x}$, E , R , P , T and K , A , E , R , P , T and K are the char reactivity factor, frequency factor for reaction, the activation energy (Jmol^{-1}), universal gas constant ($\text{JK}^{-1}\text{mol}^{-1}$), partial pressure (Pa), temperature (K) and equilibrium constant respectively for each reaction / species. The partial pressure of the char specie (P_{char}) is set as unity in the above equation since only gas molar quantities are considered for calculating the equilibrium constant of systems involving solids and liquids/gases. The subscripts R,x represents reaction number. The values for the frequency factor (F_f) and activation energy (E) for the reactions were taken from Wang and Kinoshita (1993) as cited in (Gao & Li, 2008) while F_f and E for the fifth reaction are calculated following the method described in the work of the authors (Zainal et al., 2001; Gao & Li; 2008). The R_f is a char reactivity factor that accounts for the different reactivity of various char types (Giltrap et al., 2003; Babu & Sheth, 2006). In the model R_f of 500 was used.

The equilibrium constants ($K_{R,x}$) used in the above equations is a function of temperature and standard Gibbs energy only. In the model, $K_{R,x}$ was calculated from the following equation:

$$RT[\ln(K_{R,x})] = \Delta G_i^\circ \text{ (kJkg}^{-1}\text{)} \quad (4.38)$$

The standard Gibbs free energy (ΔG_i°) and standard enthalpy (ΔH_i°) of the reactions vary with temperature at the equilibrium condition according to the following equations (Gao & Li, 2008).

$$R\Delta G_i^\circ = J_{R,x} - RT \left(\Delta a \ln T + \Delta b \frac{T}{2} + \Delta c \frac{T^2}{6} + \Delta d \frac{1}{2T^2} + I_{R,x} \right) \quad (4.39)$$

$$\Delta H_i^\circ = R \left[\frac{J_{R,x}}{R} - RT \left((\Delta a)T + \Delta b \frac{T^2}{2} + \Delta c \frac{T^3}{3} - \Delta d \frac{1}{T} \right) \right] \quad (\text{kJkg}^{-1}) \quad (4.40)$$

Where $I_{R,x}$ and $J_{R,x}$ are constants for each reaction (R,x) determined using the above two equations at standard conditions (298.15 K) respectively. The values of ΔG_i° and ΔH_i° corresponds to the values at the reference environmental state of 298.15K for each reaction whereas the values of the constants a, b, c, and d are listed in thermodynamic data tables as cited in Gao and Li (2008). The values of Δa , Δb , Δc , Δd for any reaction (Rx) is determined from the stoichiometric coefficient and the data of heat capacity a, b, c, d respectively such that for the general reaction Equation 4.36, we have:

$$\Delta a_{R,x} = n_C a_C + n_D a_D - n_A a_A - n_B a_B \quad (\text{KJkg}^{-1}) \quad (4.41)$$

Where the species (A, B, C and D) could be any of the seven species ($n_C, n_{CO_2}, n_{CO}, n_{CH_4}, n_{CH_4}, n_{H_2O}$ and n_{H_2}) entering from the oxidation zone that is present in the reaction (R, x). Similar approach and equation above is applied to determine $\Delta b_{R,x}$, $\Delta c_{R,x}$ and $\Delta d_{R,x}$ for all the reactions.

4.9.5.1 Mass and energy balance equations

The temperatures of the constituents in the reduction zone change along the gasifier height which, in turn, affect the composition of gases evolved. In order to predict the concentration and temperature profile of the volatiles along the length of the reduction zone (RZ), the length of RZ was divided into a number of elemental control volumes (dz). Then mass and energy balances are written for the species across each of the control volumes taking into account the rate of formation/consumption of the species according to the different reaction rates. For instance, the net rate of production of the four product gas species in ($\text{molm}^{-3}\text{s}^{-1}$) using the above reaction rates are (Gao & Li, 2008):

$$Rt_{CO} = 2r_{R1} + r_{R2} + r_{R5}; Rt_{H_2} = r_{R2} - 2r_{R3} + 3r_{R5} + r_{R4}; Rt_{CH_4} = r_{R3} - r_{R5}; Rt_{CO_2} = r_{R4} - r_{R1}$$

Some simplifying assumptions were made as follows (Wen et al., 1982; Giltrap et al., 2003; Gao & Li, 2008):

- The temperature of the species from the oxidation zone form the initial temperature of the reduction zone
- The elemental control volumes have uniform temperature and concentrations (Gao & Li, 2008)

- Negligible radial variation in bed and gas properties
- No heat transfer takes place between the zones
- The whole process of gasification takes place at constant atmospheric pressure
- Ideal gas conditions exist in the gasifier (Antonopoulos et al., 2012)
- Nitrogen is inert and remains in the producer gas
- Since devolatilization occurs within a very short time in the order of seconds when compared to the residence time of the biomass in the gasifier (an order of minutes to hours), it is additionally presumed that the length of the devolatilization section is negligible. The length of the reaction section is therefore equal to the length of the gasifier (Wen et al., 1982)

The mass and energy balance equations (Equations 4.42 and 4.43), are combined with the ideal gas law (Eq.19) and the pressure drop equation (Gao & Li, 2008) and solved by the Runge-Kutta method using Matlab software to obtain the concentration and temperature distribution of the six gas species along the length of the reduction zone as follows:

Mass Equation

$$\frac{dn_i}{dz} = \frac{1}{v} \left(Rt_i - n_i \frac{dV}{dz} \right) \quad (4.42)$$

Energy Equation:

$$\frac{dT}{dz} = \frac{1}{v \sum_i n_i c_i} \left(- \sum_i r_x \Delta H_x - v \frac{dP}{dz} - \sum_i Rt_i c_i T \right) \quad (4.43)$$

Where:

$$\frac{dV}{dz} = \frac{1}{\sum_i n_i c_i + R \sum_i n_i} \left(\frac{\sum_i n_i c_i \sum_i Rt_i}{\sum_i n_i} - \frac{\sum_x r_{R,x} \Delta H_x}{T} - \frac{dP}{dz} \left(\frac{v}{T} + v \frac{\sum_i n_i c_i}{P} \right) - \sum_i Rt_i c_i \right) \quad (4.44)$$

and:

$$\frac{dP}{dz} = 1183 \left(\rho_{\text{gas}} \frac{v^2}{\rho_{\text{air}}} \right) + 388.19v - 79.896 \quad (4.45)$$

Where Rt_i denote rate of production of particular product gas species (i) in ($\text{molm}^{-3}\text{s}^{-1}$), n_i represent molar density of specie of interest ($n_C, n_{\text{CO}_2}, n_{\text{CO}}, n_{\text{CH}_4}, n_{\text{H}_2\text{O}}$ and n_{H_2}) in (molm^{-3}), v denote superficial gas velocity (ms^{-1}), c_i denote, molar heat capacity of specie (i) in ($\text{Jmol}^{-1}\text{K}^{-1}$), P is partial pressure of gaseous species (i) in (Pa) , and z is axial distance in (m). Subscript i denote gaseous species of interest

4.10 Performance parameters

The following indicators are adopted to evaluate the performance of the reactor relative to variation in operating condition and fuel properties: Lower calorific value (LHV) in ($\text{JN}^{-1}\text{m}^{-3}$), carbon conversion efficiency (CCE), cold gas efficiency (CGE) and syngas yield (Yield) in ($\text{Nm}^3\text{kg}^{-1}$). The evaluation parameters are defined as follows (Basu, 2010):

$$\text{LHV}_{\text{sg}} = \sum_i \text{LHV}_i \times y_i \quad (4.46)$$

$$\text{CCE} = \frac{12Y_{\text{sg}}}{22.4C} \times \{y_{\text{CO}} + y_{\text{CO}_2} + y_{\text{CH}_4}\} \quad (4.47)$$

$$\text{CGE} = \frac{22.4Q_{\text{gas}}}{\text{HHV}_B} \times \text{LHV}_{\text{sg}} \quad (4.48)$$

$$\text{Yield} = \frac{Q_{\text{sg}}}{\dot{m}_B} \quad (4.49)$$

$$Q_{\text{sg}}(\%) = \frac{0.755 \times \dot{m}_{a,G}}{\rho_a \times y_{\text{N}_2}} \quad (4.50)$$

$$\dot{m}_{a,G} = \text{AF}_{\text{actual}} \times \dot{m}_{B,G} \quad (4.51)$$

Where Q_{sg} is flow rate of syngas (m^3s^{-1}), y is the molar ratio of the respective gases (i) at the end of the reduction zone, C is the % of carbon in dry wood and $\text{AF}_{\text{actual}}$ is actual air fuel ratio, $\dot{m}_{a,G}$ is mass flow rate of air (kgs^{-1}) in the gasifier (G), $\dot{m}_{B,G}$ is mass flow rate of wood (kgs^{-1}) in the gasifier (G), ρ_a is density of air (kgm^{-3}), HHV_B is higher heating value of biomass (Jkg^{-1}).

4.11 Model validation

The model was initially validated with the experimental data of two authors (Altafini et al., 2003; Jayah et al., 2003) to test the assumptions and operating conditions. A downdraft gasifier fed with rubber wood with ultimate and proximate analysis as shown in Table 4.33 was experimentally investigated by Jayah et al. (2003).

Table 4.3 Ultimate and proximate analysis of rubber wood (Jayah et al., 2003)

Parameter	Proximate analysis (% db.)
Volatile matter	80.1
Fixed carbon	19.2
Ash content	0.7
	Ultimate analysis (%)
C	50.6
H	6.5
N	0.2

db is dry basis.

The setup of the experimental comprises of an 80-kWth test cylindrical gasifier with a height of 1.15 and an inner reactor diameter of 0.92 m. The average chip size of the fuel feed lie in the range of 3.3–5.5 cm with moisture content ranging from 11-18 wt.%. Its chemical formula, based on a single atom of carbon, is $\text{CH}_{1.54}\text{O}_{0.63}$. The sulphur and nitrogen content of the fuel was ignored in this study. Gasifier air was supplied to the oxidation zone by means of 12 air nozzles, 6-mm in diameter, positioned 0.1-m above the throat. Three different experimental measurements from Jayah et al. (2003) for three different fuel dimensions at different flow rates of air were used to compare with the model predicted results. The comparison is as shown in Table 4.44.

It can be seen from Table 4.44 that the model predicted results largely did not show good agreement with the experimental results. While the model predicted concentration of CO and CO₂ is good to a degree, the concentration of H₂ is consistently under predicted by a large margin. Therefore, a model modification was implemented to increase the accuracy of the model prediction. Char gasification and combustion (Equation 4.24) is the most important heterogeneous reactions taking place during biomass gasification. Regarding these reactions, the char conversion has a significant influence on the overall efficiency of gasification including product gas yield.

Table 4.4 Comparison of predicted results with the experimental data (Jayah et al., 2003)

Run No	Chip size (cm)	Water content (wt. %.)	A/F	CO (%)	H ₂ (%)	CO ₂ (%)	CH ₄ (%)	N ₂ (%)	RMSE	
1	3.3	18.5	2.03	19.6	17.2	9.9	1.4	51.9	3.2	Experiment
				21.0	12.0	9.1	1.5	56.5		Model
3	4.4	16	1.96	18.4	17	10.6	1.3	52.7	4.7	Experiment
				17.8	9.7	10.5	1.7	60.3		Model
4	5.5	14.7	1.86	19.1	15.5	11.4	1.1	52.9	6.2	Experiment
				14.9	7.7	11.8	2.1	63.5		Model

To improve the quality of the product gas and the overall efficiency of gasification, it is necessary to effectively predict the ratio of (CO₂/CO) in char combustion (Diyoke et al. 2018b). In the current model, the ratio of the number of moles of the reaction products of char combustion (CO₂/CO) is estimated from the inverse ratio of their heat of reaction ($[\Delta H_R]_{CO}/[\Delta H_R]_{CO_2}$). Many different correlations have been applied by different authors to determine the ratio of the products (Arthur, 1951; Cho & Joseph, 1981). Ashman and Mullinger (2005) opined that the molar ratio of (CO₂/CO) might vary considerably for different chars, and the ratio values recommended from the literature might be specific for the chars tested in the literature (Lv et al., 2004; Diyoke et al., 2018b).

Hence, to reduce the error of the model prediction results, modification was done to the (CO₂/CO) molar ratio (N_{CO}/N_{CO₂}) by multiplying it by a coefficient (K) in the calculation process. The coefficient was determined by repetitive trial and error basis until an improved result was obtained. A value 0.05 was used as the coefficient for modifying the ratio. The result got by means of the modified model was then compared with the experimental result of Jayah et al. (2003). Table 4.55 displays the comparisons between the experimental result and the modified model. Using the root mean square error of both the modified and the unmodified model, it can be seen that the results predicted by the modified model is better compared to unmodified (Diyoke et al., 2018b)

One may argue that the procedure followed in the model modification is not satisfactory given that it is not based on any theoretical basis. However, as there are several assumptions made for the model development, here, we would like to use the evaluation results to justify our approach. Thus since the modified model gave a better result, it means that that the (CO₂/CO) ratio we initially calculated using recommended correlation from

the literature does not match the char in the current model and thus needs to be varied to match it as per Ashman and Mullinger (2005).

Table 4.5 The comparison of results from modified model with experimental data (Jayah et al., 2003)

Run No	Chip size (cm)	Water content (wt. %)	A/F	CO (%)	H ₂ (%)	CO ₂ (%)	CH ₄ (%)	N ₂ (%)	RMSE	
1	3.3	18.5	2.03	19.6	17.2	9.9	1.4	51.9	1.7	Experiment Model
				22.8	17.3	9.0	1.1	50.0		
3	4.4	16	1.96	18.4	17	10.6	1.3	52.7	2.7	Experiment Model
				23.0	17.8	8.9	1.1	49.2		
4	5.5	14.7	1.86	19.1	15.5	11.4	1.1	52.9	2.3	Experiment Model
				22.0	17.6	9.4	1.3	49.8		

A similar approach was used in the published work of Barman et al. (2012) to upgrade their equilibrium model to match experimental data. In addition, Jarunghammachote and Dutta (2007) also applied similar approach to upgrade their equilibrium model to match experimental data. The coefficient used for multiplication was obtained from the average value of the ratio of CO from the eleven experimental data and CO obtained using the model.

It can be seen from comparison between Table 4.4 & Table 4.5 that the model predicted H₂ significantly improved closer to the experimental values compared to the initial value gotten from the unmodified model. Though, the accuracy of prediction of CO₂ in the altered model is not as good as the first, the general accuracy of the prediction from the model enhanced after the alteration. It can be noted that there is a fairly close agreement between model prediction and experimental results. The difference between the model's predicted results and the experimental data may have come from the assumptions applied in simplifying the model, such as all gases are assumed ideal, constant tar yield etc. Also, the divergence could be ascribed to the prevailing reaction conditions during the experiment such as temperature, pressure and even the design of the gasifier.

An additional validity of the modified model and the accuracy of the computation results have been established by comparisons with experimental data on temperature profile of the gasifier. Figure 4.5 depicts the model and experimental temperature profile along the length of the reduction zone for 3.3m chip size at AF of 2.2 and MC of 16 wt.% (Diyoke et al. 2018b)

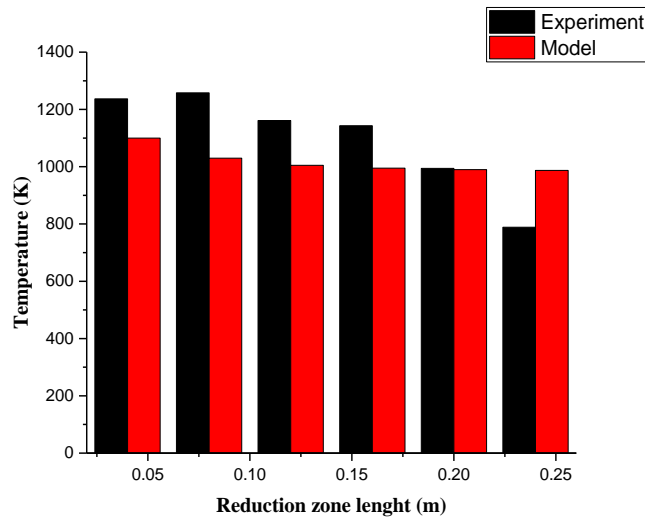


Figure 4.5 Measured and predicted temperatures along RZ (Jayah et al., 2003)

The maximum and minimum error of the model predicted temperature profile are 22% and 0.4% respectively. Notwithstanding the error, the overall trend of temperature profile from the model is satisfactorily good for engineering purposes and can be effectively deployed to access the performance of the gasifier. A number of factors could explain the cause of the difference between the experimental results and the model temperature prediction; first, the gasifier operates in the unsteady regime in practical applications because of the effect of vibrating mechanism. In addition, the various heat losses taking place in the gasifier may not have been taken into account wholly in the model (Diyoke et al., 2018b).

To test and show the applicability of the model to a different fuel feed, the modified model was applied to sawdust feedstock and the composition of syngas obtained compared to the experimental results obtained using sawdust as feedstock. The gasifier set up consists a fixed bed downdraft gasifier with an open top. It has a capacity to process approximately 12 kg of sawdust an hour. Pinus Elliotis sawdust feedstock is the biomass used. Its ultimate

analysis composition consists of 52.0%, 41.55%, 0.28%, 6.07% and 0.1% for C, O, N, H and Ash respectively (Altafini et al., 2003). The experimental measurement was carried out at AF of 1.957 and moisture content of 11% by weight at a reaction temperature of approximately 832 °C. Table 4.6 displays the comparison of the fuel gas composition predicted by the modified model and experimental results (Altafini et al., 2003)

Table 4.6 Comparison of results from modified model with experimental data (Altafini et al., 2003)

	A/F	MC	CO (%)	H ₂ %	CO ₂ %	CH ₄ %	C ₂ H ₄ (%)	C ₂ H ₆ (%)	N ₂ %	RMSE
Experiment	1.957	11	20.14	14	12.06	2.31	0.57	0.14	50.79	
Model	1.957	18.5	20.48	15.0	10.5	1.1	-	-	52.9	1.37

The values from the modified model are reasonably near to the experimental results as can be seen in Table 4.6. The concentrations of H₂ and CO predicted are greater but that of CH₄ and CO₂ are lower than the experimental figures. Another vital measurable data of gasification process is the syngas yield. In the experiment of Jayah et al.'s work, the syngas yield recorded at AF ratios of 2.03 and 2.2 was 52.7 and 57.7 m³h⁻³ respectively while the yield predicted from this model is 50.12 and 56.55m³h⁻³, further reinforcing the reasonable agreement between the model and experimental data at different operating conditions. Therefore, use can be made of the developed model to produce specific design data for a downdraft biomass reactor given the fuel composition and operating conditions. We hereunder present the performance results obtained from the developed model. Except otherwise, stated, the comparison of performance was carried out at the operating conditions of ER of 3.1 and fuel moisture content of 18.5% by weight. Rubber wood is the demonstrative feedstock used in the study at fuel consumption rate of 20 kg/hr. (Jayah et al., 2003). Its ultimate and proximate analysis is as shown in Table 4.3 (Jayah et al., 2003).

4.12. Results and Discussion

4.12.1. Temperature profile of the downdraft gasifier

The temperature reached in the oxidation zone (OZ) of the gasifier depends on the amount of air present (ER) and how dry the biomass is as revealed by its moisture content (MC). These parameters determine the heat released in the OZ and by extension the temperatures attained in the other two zones. Figure 4.6 displays the predicted temperature profiles of the three zones of the reactor at different moisture contents (Diyoke et al., 2018b)

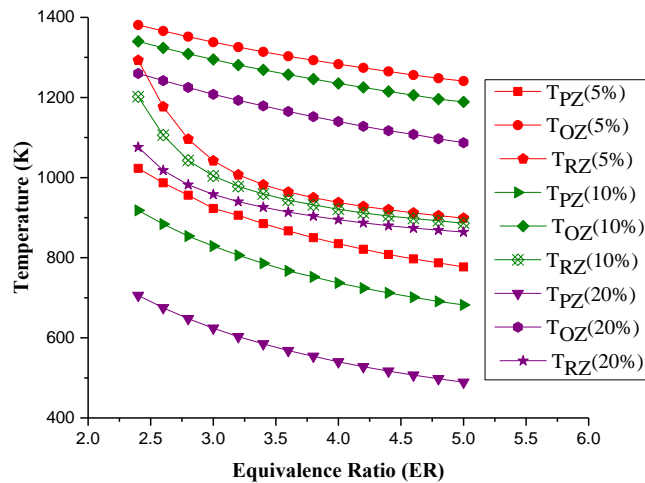


Figure 4.6 Temperature profile of the zones of pyrolysis, oxidation and reduction of the reactor using biomass with different moisture contents (5, 10 and 20 wt.%)

It can be seen that as the ER increases, the temperature reached in the three zones of the gasifier reduces, with the profiles of temperature in the pyrolysis and oxidation zones showing similar trend while that of the reduction zone is slightly dissimilar. At ER of 3.1, the highest temperature of about 1300 K is predicted for the oxidation zone for a fuel moisture content of 5 wt.%. This is because there is an air supply in the zone and an exothermic oxidation of the biomass with air happens in the zone. The evolved heat in the oxidation zone diffuses to the pyrolysis zone. In the pyrolysis zone, a temperature of approximately 917 K was attained representing about 68% of the temperature attained in

the oxidation zone whereas in the reduction zone, a temperature of about 1000 K is attained representing about 77% of the temperature attained in the oxidation zone. The rate of reduction in temperature as ER increases in the reduction zone depends on the rate of the reduction reactions, determined by their kinetics (Diyoke et al., 2018b).

For a given ER, temperature of each of the zones reduce as the moisture content increases, because additional combustion heat is lost to dry away moisture resulting to decrease in the heat supplied to both pyrolysis and reduction zones. The decrease of temperature with increase in ER is more observable in the oxidation zone, followed by the pyrolysis zone and less noticeable in the reduction zone. This is because the temperature reached in the oxidation zone depends on the heat of combustion and determines the temperature attained in the pyrolysis and reduction zones respectively. A higher value of the ER signifies a lower flow rate of air for a specific biomass feed rate which results to more incomplete combustion (less amount of CO_2 production) in oxidation zone, thus leading to decrease in the heat of combustion (Diyoke et al., 2018b).

4.12.2. Gas concentration profile

Figure 4.7 depicts the concentration of the syngas components along the height of the biomass reactor. Observe that at the inlet ($RZ \approx 0$), the temperature is at its highest possible value, and the composition of all the syngas components change very rapidly.

The molar ratio of CO and H_2 rise quickly while that of H_2O , CO_2 and CH_4 sharply reduced correspondingly. While nitrogen is inert in the reaction, its mole fractions sharply reduced due to the increase in the total number of moles of the syngas components as the char particles are transformed. Notice that the process achieved equilibrium at around $1/5^{th}$ the height of the reduction zone (RZ), very close to the oxidation zone due to the high temperature prevalent in that zone. As can be seen, the temperature in the reduction zone similarly decayed fast between the entrance and 0.15m of the reactor RZ length. The observed trend can be explained thus; a huge and rapid depletion of the heat from oxidation zone takes place at the starting point of the endothermic char gasification reaction, at the entrance. At the remaining length of the RZ length, the temperature gradient reduces to almost fixed value. This is because the rate of reaction which is temperature dependent slows down as the concentration of the char and gaseous reactants reduce since they are

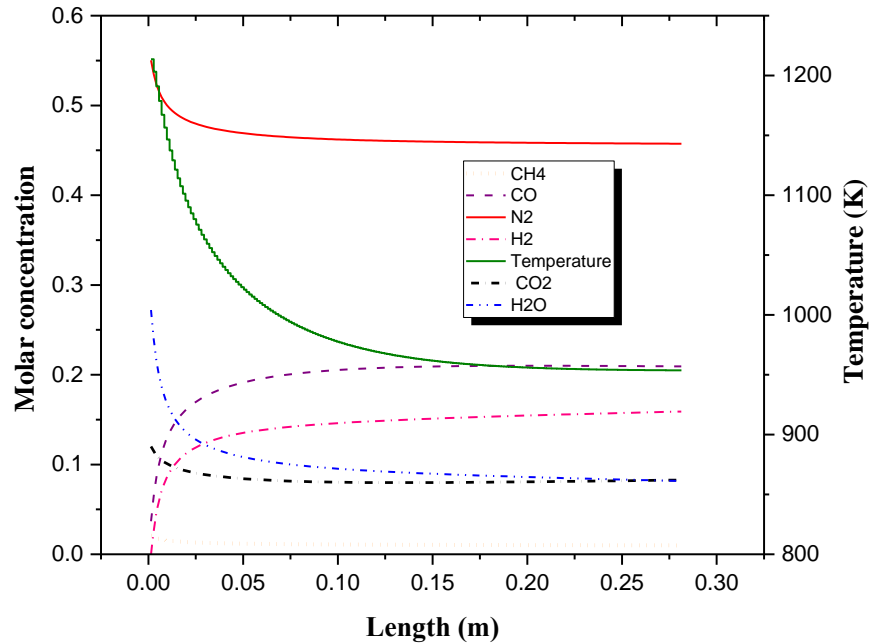


Figure 4.7 Gas concentration profile along RZ height

expended very fast in the initial reactions thus making the surface reactions inactive as more of the char surface is covered by the CO and H₂ formed (Diyoke et al., 2018b). Wang and Kinoshita (Wang and Kinoshita 1993) combined the oxidation and pyrolysis zone as one in their model and obtained similar results using kinetic model based on the mechanism of surface reactions.

The lower calorific value (LHV) of the syngas at different moisture contents are shown in Figure 4.8. As can be seen, the trend of LHV is the same as that of the syngas composition along the RZ length. At fuel moisture contents of 5, 10, 15 and 20%, the LHV of the syngas along the RZ length is seen to vary from initial values of 3.01, 2.42, 2.0 and 1.72 at the entrance (1.4 mm) to final values of 6.02, 5.52, 5.04 and 4.57 MJ/Nm^3 at the end of the RZ height. The equivalent temperature of the reduction zone is also seen to vary from initial values of 1318, 1275, 1232 and 1190 to final values of 1022, 990, 967 and 949 K respectively (Diyoke et al., 2018b).

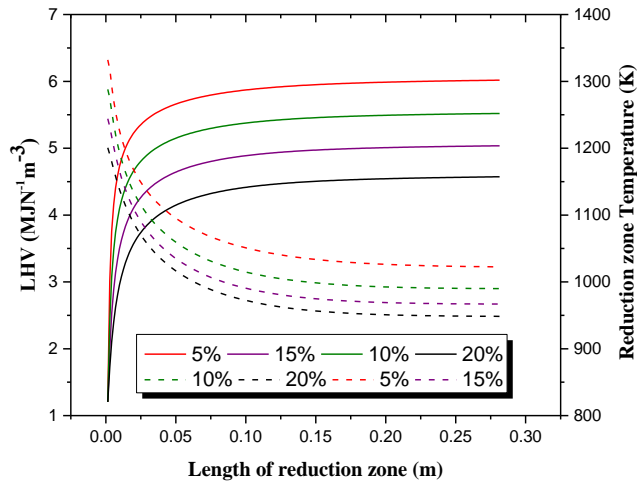


Figure 4.8 LHV profile along RZ height

The CGE along the RZ length for four moisture contents (MC) values of 5, 10, 15 and 20 wt.% respectively is depicted in Figure 4.9. Expectedly, as the MC increases, the CGE reduces. However, for each MC, the CGE increases sharply at the entrance of the reduction zone until at a height of about 0.05m when it attains an equilibrium state and remains steady

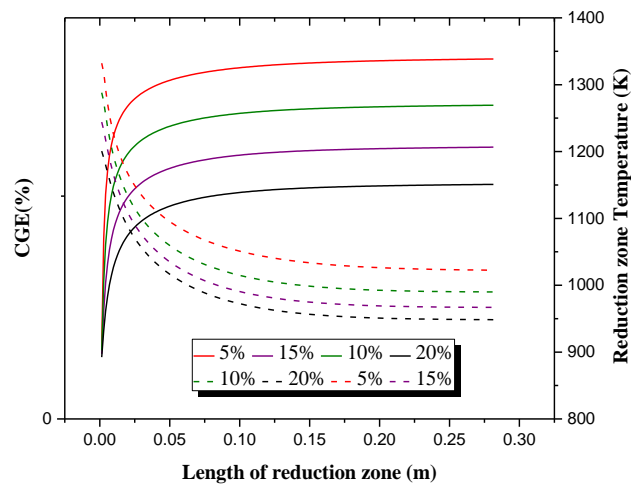


Figure 4.9 Efficiency profile along RZ height at different temperatures

The trend observed can be explained thus; the heat required by the char+CO₂ and char+H₂O gasification reactions is delivered by the oxidation of the volatiles with air. As the volatiles are spent rapidly at the RZ entrance, the conversion of the char correspondingly rises rapidly till equilibrium is achieved in the reactor at which point many of the char has been converted and the LHV and efficiency (CGE) peaks and remains steady (Diyoke et al., 2018b).

From the overall trend of the plots (Figure 4.8 and Figure 4.9), it can be evidently observed that in each case and for the same ER, rise in gasification temperature as influenced by the fuel MC improves performance. This is because the MC in the biomass determines the temperature achieved in the oxidation zone and by extension, the initial temperature in the char reduction zone. As the MC reduces, temperature reduces because energy is wasted to dry out moisture and high moisture content rubs the reduction zone of some of the energy from the oxidation zone required to drive the endothermic char gasification reactions. The consequential result is the decrease in the rate of reaction consequently leading to the decrease in the LHV and CGE observed (Diyoke et al., 2018b).

4.12.3. Influence of process parameters

4.12.3.1. Influence of air preheating

The temperature of the feed air to the gasifier plays a major role in the performance of a gasification system. Figure 4.10 displays the plot of concentrations of syngas components against feed air temperature. As can be seen, as the temperature of the feed air increases, the increase in the concentrations of H₂, and CO is seen. In contrast, the concentration of CO₂, N₂, and CH₄ in syngas, decreases as the temperature of the feed air increases.

The observed trend as depicted in the figure is so because as the temperature of the feed air increases, the enthalpy of the reaction increases, which results to an improvement in the oxidation reaction in the gasifier, and by extension, the rise in the temperature reached in the oxidation zone. The reaction rate of char gasification reactions in the reduction zone is enhanced with the increase of the oxidation zone temperature. In the endothermic Boudouard reaction(Char + CO₂ ↔ CO), the forward reaction, that is, the

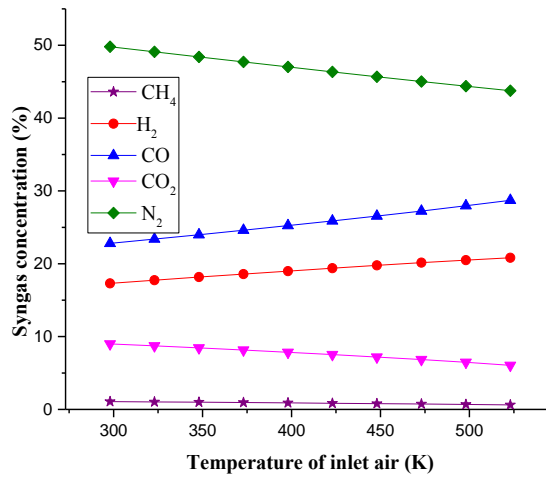


Figure 4.10 Influence of inlet air temperature on the concentration of product gas

conversion of char and CO₂ to CO depends upon the rate of reactions taking place in the reduction zone. With an increase in feed air inlet temperature from 25 to 250 °C, oxidation of the volatiles from the pyrolysis zone is improved leading to increased concentration of complete combustion products like CO₂. Thus, with the increased concentration of CO₂ in the reduction zone, more CO₂ is converted into more CO and H₂, and thereby the fraction of CO and H₂ increases. Furthermore, rise in the temperature of the reduction resulting from improvement in oxidation reaction shifts the equilibrium of the endothermic water gas reaction (R₂) towards the forward reaction; the formation of the products (CO and H₂). The methanation reaction and water gas shift reaction (R₅) are exothermic. At low feed air inlet temperature, their equilibrium are favoured towards the backward reaction; favouring the formation of the reactant (mainly H₂). Consequently, raising the temperature of the gasification process through feed air pre heating is not beneficial to the production of methane but enhances the production of syngas (CO and H₂) (Diyoke et al., 2018b).

The influence of temperature of the feed air to the gasifier on the syngas LHV, yield and CGE is presented in Figure 4.11. The LHV of the syngas increases with the increase in the temperature of the feed air, because of the rise in the amounts of (CO and H₂) produced in the reduction zone as the temperature of feed air rises.

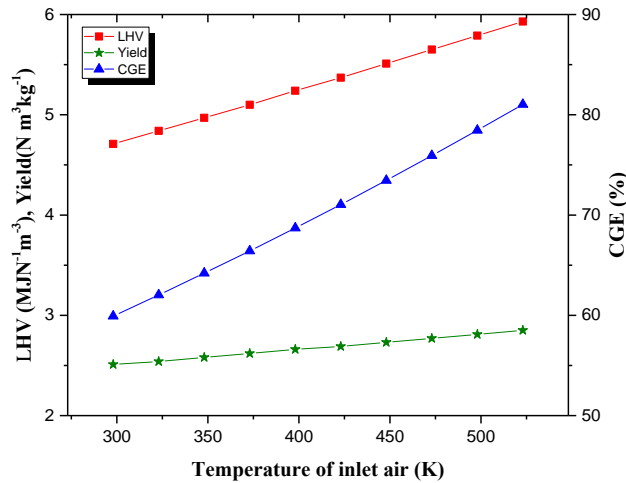


Figure 4.11 Influence of temperature of inlet air on yield, CGE, LHV

The CGE, depends on the LHV of the syngas. Since the LHV of the syngas increases with temperature of the feed air, the CGE correspondingly increases as the temperature of the feed air increases. As the feed air temperature increases from 25 to 250 °C, LHV is seen to increase from 4.7 to 5.9 MJN⁻¹m⁻³; yield from 2.5 to 2.85 Nm³kg⁻¹ and CGE from 60 to 81%. Another factor which may have caused an improvement of syngas production with increase in the temperature of feed air include steam reforming and more cracking of pyrolysis products at high temperature (Lv et al., 2004; Doherty et al., 2009; Diyoke et al., 2018b).

4.12.3.2. Effect of moisture content

Fuel moisture content influences the way a biomass gasifier is operated including the quality and composition of the syngas obtained from it. Generally, low MC feedstock is favoured because of its higher gross energy content (Reed & Das, 1988; Jayah et al., 2003). According to Dogru (2000), the maximum allowable limit of fuel MC for use in a downdraft gasifier is usually taken to be not more than 30% on wet basis. Using 38% as an upper limit, the influence of feed MC on the gasifier performance is undertaken and the result is as presented in Figure 4.12.

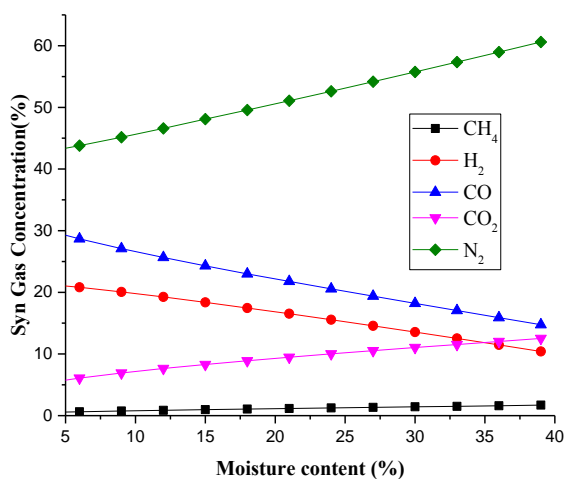


Figure 4.12 Influence of moisture content on gas composition

It is seen that, as the moisture content (MC) of the feedstock increases, an increase in the formation of CH₄ and CO₂ is observed while that for CO and H₂ reduces. For feedstock moisture content ranging from 3-30%, the percentage change in fuel gas composition (with respect to the final value) for CO, H₂, CH₄ and CO₂ is predicted as -67, -58, 66 and 54%, respectively.

This trend can be explained thus; the direct gasification of wet biomass will produce two opposing effects on gasification: (1) decrease in the oxidation zone temperature because energy lost in drying the biomass before pyrolysis and (2) auto generation of steam from moisture released from wet biomass during drying which acts as a reactant to improve the decomposition of the intermediate products (volatile and char) (Diyoke et al., 2018b).

These two opposing yet complimentary processes happen at the same time. At low moisture content, the temperature of the oxidation zone is high and almost constant, the first process becomes dominant and the comparatively high reduction zone temperature shifts the equilibrium of the endothermic water gas reaction (R₂) towards the products(CO and H₂), formation thus resulting to the evolution of more CO and H₂. As the moisture content rises, the reduction zone temperature decreases drastically and the second effect becomes dominant. The steam auto-generated from the loosed bound moisture of wet biomass react with the intermediate products (volatile and nascent char) to evolve more hydrogen. The water gas shift reaction (R₅) is exothermic. At low temperature of reduction

zone, their equilibrium is tilted towards the forward reaction; thus enhancing the production of CO. In methanation reaction, which is exothermic, CO experience additional reaction with H₂ and at high moisture content (low temperature) its equilibrium is shifted towards the formation of the products (forward reaction); thus favouring the evolution of CO₂ and CH₄ and depletion of H₂. Furthermore, at high moisture content (low reduction zone temperature), the equilibrium of the endothermic water gas reaction and the Boudouard reaction is tilted towards the backward reaction (formation of the reactants), thus resulting to the decrease in the concentration of (CO and H₂) at high moisture content. The trend observed is similar to results from previous studies (Mountouris et al., 2006; Antonopoulos et al., 2012; Diyoke et al., 2018b).

Figure 4.13 shows the effect of moisture content on gas yield, LHV, and CGE. It can be seen that the gas yield, LHV, and CGE steadily decreases with rising moisture content of the feedstock.

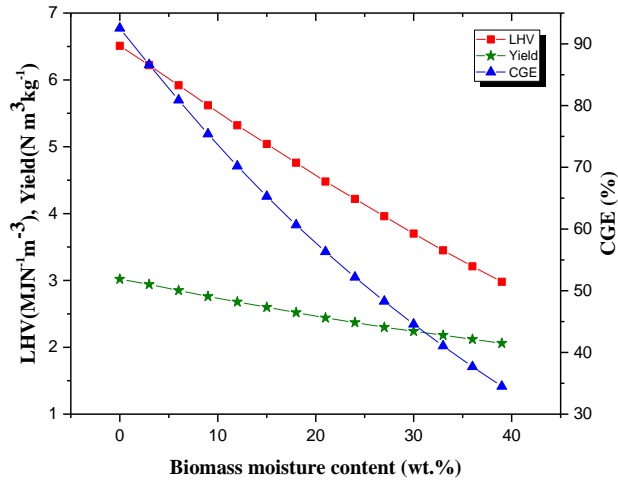


Figure 4.13 Influence of moisture content on performance indicators

This is expected given the constantly decreasing amount of H₂ and CO seen during the simulation run for variation in moisture content as in Figure 4.12. At moisture content ranging from 3-30%, the LHV varies from a high of 6.2 MJN⁻¹m⁻³ to a low of 3.7 MJN⁻¹m⁻³.

The model predicted LHV lies in the range of the expected LHV (4–6 MJN⁻¹m⁻³) for syngas produced from typical gasification of woody biomass (Zainal et al., 2002). It

can be witnessed from Figure 4.13 that for an average moisture content of 15%, the yield, LHV and CGE, are 2.5, 5.04 and 65% respectively. These values compare realistically well for the range of values reported in the literature for a downdraft biomass gasifier using wood feedstock (Reed & Das, 1988; Quaak et al., 1999).

The higher value of the performance parameters at low moisture content shows that initial drying of the fuel feed to a low moisture content value is vital to yield syngas of appropriate characteristic properties. The drying of the wet feed could be achieved through costless natural means using the sun or by artificial means by the exploitation of free or cheap waste heat recoverable from several sources (such as furnaces, or gas turbine flue gas, hot air from condenser or compressor etc.). Where free or very cheap source of heat for drying is not accessible, it is not financially prudent to try to dry out all the moisture since the gain in the value in terms of increase in LHV derivable from the syngas owing to complete removal of moisture from the feedstock will not be commensurate to the energy cost of attaining it (Diyoke et al., 2018b).

4.12.3.3. Effect of equivalence ratio

The air equivalence ratio (ER) is one of the critical variables affecting a gasifier performance. This is so since ER fixes the actual air available for oxidation and consequent formation of volatile products. The heat required to drive the two endothermic gasification reactions; $\text{char} + \text{CO}_2$ and $\text{char} + \text{H}_2\text{O}$, is provided by the oxidation of volatile products. Figure 4.14 displays the plot of composition of the product gases at ER values ranging from 2.6 to 5.2. The range of ER analysed is the range where the modelled gasifier operates well in. In other gasification related works, the performance of the gasifier has been considered in the ER range of 2–5 (Zainal et al., 2002; Jarungthammachote & Dutta, 2007; Melgar et al., 2007 and Sharma 2008).

The ER range over which a gasifier operates is determined by the gasifier produced syngas quality and the stable operation of it. The quantity of concentration of the component species of the final syngas depends principally on the chemical equilibrium between the components. The equilibrium between the component species is ultimately dependent on the reaction temperature and by extension the ER and the moisture content in the biomass. On one hand, lower ER (more feed air) will cause more combustion reaction, which leads to a deterioration of the gas quality. On the other hand, lower ER

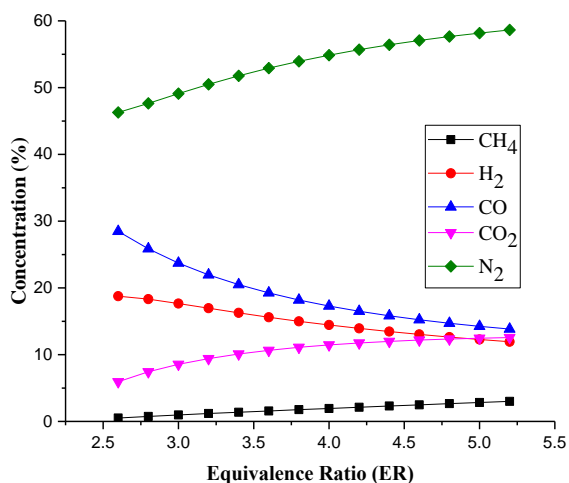


Figure 4.14 Influence of ER on the concentration of syngas

means higher temperature of gasification, which can improve the gasification and increase the quality of the syngas to a certain degree (Diyoke et al., 2018b). Therefore, the overall composition of the product gases is governed by the two factors of ER and temperature (Lv et al., 2004). As can be seen from Figure 4.14, the trend of the concentration of CO and H₂ is in direct opposite to that displayed by CH₄ and CO₂. Whereas the concentration of CO and H₂ decreases with increasing ER over the range of ER studied, the concentration of CH₄ and CO₂ increases as ER increases. As the ER increases from 3 to 5, the concentration of H₂ is seen to reduce from 17.66 to 12.28%, while that for CO₂ increases from 8.55 to 12.47%. The concentration of CO also is also seen to decrease from 23.72 to 14.25%. Additionally, the concentration of CH₄ is seen to increase from 0.97 to 2.83%. The scholars (Melgar et al., 2007; Doherty et al., 2009) in their predicted producer gas composition for wood reported similar trend of the concentration of the syngas components with the change of ER.

The observed trend is so because ER do not only influence the amount of air present in the gasifier for oxidation of the pyrolysis products but also controls the gasification temperature. The smaller the ER value is, the higher will be the air available for oxidation reactions and hence, the higher the temperature reached in the reduction zone because of improved oxidation reaction resulting from low ER value. The Boudouard reaction (R1)

and water gas reaction (R2) are endothermic and at low ER value, the temperature is high and the two reactions are favoured, so more char and CO_2 are consumed while more CO and H_2 are produced as observed in Figure 4.14 (Melgar et al., 2007; Doherty et al., 2009; Diyoke et al., 2018b). The molar ratio of H_2 is seen to reduce gradually which may imply that the rate of H_2 consumption is larger than the rate of H_2 formation in water-gas shift reaction. The increase in CH_4 with ER can be explained by the fact that the methanation reaction (R3) is exothermic, and the presence of H_2 at low ER might favour methanation reaction (Diyoke et al., 2018b). Therefore as the temperature reduces due to increasing ER, the rate of formation of CH_4 is favoured (Doherty et al., 2009; Diyoke et al., 2018b). Furthermore, the steam reforming reaction is endothermic, which means that at low ER and high temperature, the formation of the products (CO and H_2) is favoured while the consumption of the reactants (CH_4 and H_2O) is increased to maintain equilibrium. As the ER increases, the temperature reduces and the backward reaction is favoured resulting to increase in concentration of CH_4 . Even though N_2 is presumed inert in the modelling, the increase in the concentration of N_2 observed in the graph is because of general reduction in the total concentration of the syngas components as the ER increased (Diyoke et al., 2018b).

As the ER varies from 3-5, gasification parameters such as yield, LHV, CGE and CCE also varies, as shown by Figure 4.15. As it can be witnessed, the LHV decreases as the ER increases due to the fact that the production of the dominant combustible gas species (CO and H_2) is favoured more at lower ER and consequently the observable decrease in LHV. Besides, the dilution of the syngas by the air bound nitrogen and the improvement of the homogeneous and exothermic water gas shift reaction as the ER increased, may have played a role in the observed decrease in the LHV as ER increased (Gómez-Barea et al., 2005; Diyoke et al., 2018b).

The gas yield is also seen to decrease linearly as the ER increases. This trend is in complete agreement with the findings of other authors (Kurkela & Ståhlberg 1992; Gil et al., 1999; Gómez-Barea et al., 2005). High gas yield at lower ER is possibly due to the enhanced volatilization of biomass, which is more rapid at high ER (Gómez-Barea et al., 2005), i.e., at higher ER, temperature developed in the oxidization zone is more which leads to the improvement of the endothermic char gasification reactions (Diyoke et al., 2018b).

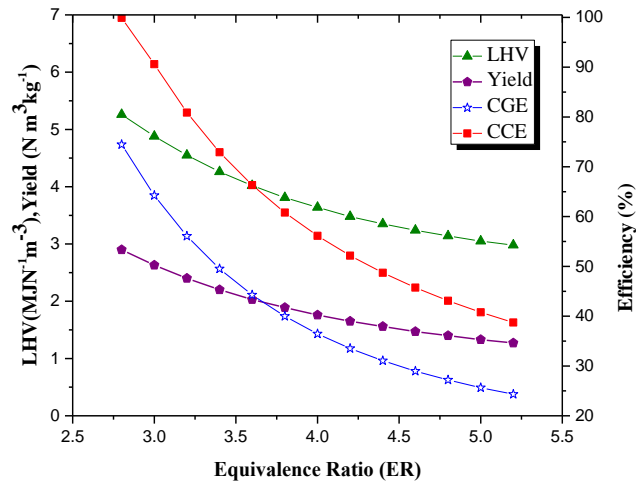


Figure 4.15 Influence of ER on CGE, Yield and CCE

Moreover, as the temperature rises, the steam reforming reactions are favoured with the resulting rise in the syngas yield. The simultaneous effect of both the decreasing trends of the yield and LHV with increasing ER has been replicated in the evolution of the CCE and CGE as can be observed in Figure 4.15. At the ER range of 3-5.2, the CGE, CCE and yield varies from 73.6-24.3%, 90.6-38.7% and 2.63-1.3Nm³kg⁻¹, respectively (Diyoke et al., 2018b).

4.13 Conclusions

A downdraft biomass gasifier model was developed in Matlab based on the first principle for process analysis of biomass gasification. Model inputs include feed rate and composition of feedstock, gasifier pressure, and temperatures of feed air. The model takes into accounts pyrolysis, oxidation, and char gasification reactions, including heat losses from the reactor.

Results obtained from the numerical simulations of rubber wood gasification using the model include the temperature distributions of the pyrolysis, oxidation and reduction zone, syngas yield and composition, carbon conversion efficiency, lower heating value and carbon conversion efficiency. The temperature and concentration profiles predicted using the model was validated against two sets of different experimental data. The simulation

results obtained with the model agree reasonably well with experimental data. In addition, parametric analysis studies were carried out using the validated model to analyse the influence of the major process parameters on syngas composition, syngas yield, carbon conversion efficiency (CCE), lower calorific value (LHV) and cold gas efficiency (CGE). The parameters analysed include: (a) equivalent ratio (ER); (b) moisture content (MC); (c) temperature of feed air to gasifier. The main conclusions drawn are as follows:

- The predicted syngas concentration at equivalent ratio of 3.1 and fuel feed moisture content of 18.5 wt.%, is about 1.1%, 17.3%, 22.8%, 9.0% and 49.8% for CH₄, H₂, CO, CO₂, and N₂ respectively. The corresponding lower calorific value, cold gas efficiency, carbon conversion efficiency and yield are 4.7 MJ/Nm³, 59.9%, 85.5% and 2.5 Nm³/kg-biomass respectively.
- As the moisture content and equivalent ratio increases, the syngas lower heat value, carbon conversion efficiency and cold gas efficiency decreases and reduction zone length smaller than 0.05m is inadequate to get maximum efficiency at a given equivalent ratio.
- The performance of the biomass gasifier in terms of yield, lower calorific value, cold gas efficiency and carbon conversion efficiency increases with feed air temperature.
- At equivalent ratio ranging from 3 to 5.2 and at MC of 18.5 wt.%, the temperatures attained in the pyrolysis, oxidation and reduction zone of the gasifier lie in the range of 654-510 K, 1221-1094 K and 964-862 K respectively.

This analysis is limited to rubber wood with an experimentally determined tar concentration as an input variable in the model. Tar yield in downdraft biomass gasification despite being negligible varies with temperature and along the gasifier axis. This no doubt will have some effects on the system performance. Thus, as a potential future research, further optimization of this model should include the prediction of tar and its effects on the performance of the gasifier

Chapter 5

Thermodynamic analysis of integrated A-CAES and BMGES system

5.1 Introduction

In this chapter, a thermodynamics analysis of the integrated adiabatic compressed air energy storage (A-CAES) and biomass gasification energy storage (BMGES) system is carried out using the first and second law analysis methodology. The exergy destruction rate, energy and exergy efficiencies of the various components and the overall integrated system is presented. The sensitivity analysis of the impact of main design variables on the performance of the system is highlighted.

Overview of thermodynamic analysis

The global energy resources are not limitless. In the recent past, an increased awareness of the unlimited nature of these energy resources and the threat posed by global warming has caused many countries to rethink their energy policies towards energy conservations and renewable based generation. In addition, there seems to be a sparked interest among the scientific community to observe the energy conversion devices closely and to develop new systems for efficient resource utilization even if it might not yet be economically reasonable. Thermodynamic analysis has proven a common and reliable optimization method among researchers.

In thermodynamic analysis, mathematical models are deployed to evaluate the thermodynamic imperfections in engineering systems and components and suggest ways through which these imperfections can be improved for efficient resource utilisation.

Thermodynamic analysis of engineering systems are often carried out using the first and/or the second law of thermodynamics by means of metrics such as energy efficiency, exergy efficiency and exergy destruction. Other method employed include pinch analysis, exergo-economics, Gibbs free energy minimization, thermo-economics and extended exergy analysis (Kreith & Raton, 2000; Bagdanavicius & Jenkins, 2014).

The first law of thermodynamics is a statement of the conservation of energy (Cengel & Boles, 2006). It deals with the *quantity* of energy and postulates that energy can neither be created nor destroyed. This law simply helps as an essential tool for the bookkeeping of energy during a process and cannot reveal whether or not and by how much it is possible to design a system for more efficient operation (Cengel & Boles, 2006). The second law, however, deals with the *quality* of energy. In specific terms, it is concerned with the energy degradation during a process, the entropy generation, and the lost opportunities to do work (Cengel & Boles, 2006); and it suggests ways for improvement.

The second law of thermodynamics has demonstrated to be a very useful and dominant tool in the optimization of complicated thermodynamic systems (Bejan et al., 1996; Cengel & Boles, 2006). The first law efficiency, makes no reference to the best possible performance, and thus it may be misleading when used alone. It is the combination of the first (energy analysis) and second laws (exergy analysis) of thermodynamics that is particularly powerful (Cengel & Boles, 2006). Exergy (also called the availability or available energy) is defined as the maximum reversible work that can be obtained from a system at a given state during its interaction with a given environment (Cengel & Boles, 2006). Exergy analysis method enables the attainment of the goal of a more efficient energy system design and use, since it can reveal the location, type, and true magnitude of wastes and losses in the system (Rosen et al., 2000).

In addition, it can reveal whether or not and by how much it is possible to design a system for more efficient operation. Therefore, in this chapter, the first law efficiency and second law efficiency metrics which depends on the concept of the first law (energy) and second law (exergy) analysis respectively, is used because it is the most popular methodology (Bejan et al., 1996; Kreith & Raton, 2000; Cengel & Boles, 2006). Numerous publications have been devoted to thermodynamic analysis through the first and second law efficiencies, entropies, exergy losses/destruction and thermo-economics. Such discussions of exergy analysis and thermal economics are covered in: Moran (1989.), Kotas (1995), Bejan et al.(1996), Kreith and Raton (2000) and Moran and Shapiro (2000). In this chapter relevant aspects are presented.

5.2. Thermodynamic analysis

All the components of the A-CAES+BMGES system (ACs, HAD, BMG, AEs, HXs, TV and DFE) are treated as steady flow energy devices and analysed using control volume approach. The assumptions used in this analysis are as follows:

- Chemical composition of the syngas is considered stable
- Tar formation is ignored
- The exergy of all fluid streams is evaluated under the reference dead state corresponding to ambient conditions of 25 °C and 1.0132 bar
- Space heating water enters HX7 at 35 °C and leaves at 55 °C (Danish Energy Agency, 2014)
- The pressure drop throughout the processes is considered negligible.
- The changes in kinetic and potential energy are neglected
- The air, syngas and exhaust gas are treated as ideal gas.
- Isentropic efficiencies of the compressor and turbine are 0.85 and 0.88 respectively (Zafirakis & Kaldellis, 2009)
- The motor (generator) efficiency of AC(AE) are 0.99 and 0.97 respectively (Zafirakis & Kaldellis, 2009)
- The recuperator has an effectiveness (ϵ) of 0.7

The analysis of control volumes and closed systems through thermodynamic analysis characteristically use, directly or indirectly, one or more of three basic laws: the conservation of energy principle, the conservation of mass principle, and the second law of thermodynamics (Kreith & Raton, 2000; Cengel & Boles, 2006). The second law may be expressed in terms of entropy or exergy (Cengel & Boles, 2006).

The first law energy balance at steady stage for a control volume is given as follows (Cengel & Boles, 2006):

$$\dot{Q}_i + \dot{W}_i + \sum \dot{m}_i h_i = \dot{Q}_e + \dot{W}_e + \sum \dot{m}_e h_e \quad (5.1)$$

The mass balance is formulated as follows;

$$\sum \dot{m}_e = \sum \dot{m}_i \quad (5.2)$$

Where \dot{m} is the mass flow rate (kg s^{-1}), \dot{Q} and \dot{W} denotes the heat and work transfer rates (W), respectively, and h denotes the specific enthalpy at the specified state (J kg^{-1}). The subscripts i and e represents ingoing and exiting flow stream, respectively.

The exergy balance for the system control volume and its components can be expressed as follows (Cengel & Boles, 2006):

$$\sum_k \left(1 - \frac{T_o}{T_j}\right) \dot{Q}_j - \dot{W}_{cv} + \sum_i \dot{m}_i \psi_i = \sum_e \dot{m}_e \psi_e - \dot{X} \quad (5.3)$$

The first and second term from the LHS represents exergy transfer accompanying heat (ψ^Q) and work respectively (ψ^W), \dot{X} is the exergy destruction of the component (W), \dot{Q}_j is the heat transfer rate in (W) through the boundary at temperature T_j (K) at location j , \dot{W}_{cv} is the work rate (W) of the control volume (cv), ψ is the flow (or specific) exergy (W), and the subscript zero indicates properties at the reference state (P_o, T_o).

The specific exergy, ψ (J kg^{-1}) is expressed as sum of physical ψ^{ph} and chemical ψ^{ch} exergy. The physical exergy is as follows:

$$\psi^{\text{ph}} = (h(T) - h(T_o)) - T_o(s(T) - s(T_o)) \quad (5.4)$$

The chemical exergy (ψ^{ch}) represents the chemical contribution to the total specific flow of exergy entering and leaving a control volume. It was calculated thus:

$$\psi^{\text{ch}} = \frac{1}{M_w} \left(\sum_k n_k \psi_o^{\text{ch}}{}_k + RT_o \sum_k n_k \ln n_k \right) \quad (5.5)$$

Where ψ_o^{ch} is the standard chemical exergy of a species in kJ per mol and n_k is molar fraction in component k . The differences of specific enthalpy ($h(T) - h(T_o)$) and entropy ($s(T) - s(T_o)$) for air, syngas and exhaust gas are expressed respectively as:

$$h(T) - h(T_o) = \int_{T_o}^T C_p dT \quad (5.6)$$

$$s(T) - s(T_o) = \int_{T_o}^T \frac{C_p}{T} dT - \frac{R}{M_w} T_o \ln \frac{P}{P_o} \quad (5.7)$$

Where R is the universal gas constant, 8.314472 in $\text{kJ}(\text{kmol K})^{-1}$; P is the pressure at the arbitrary state (bar) and M_w is molar mass (kg kmol^{-1}). The exergy rate for a flow stream is given as follows:

$$Ex = \dot{m} \psi \quad (5.8)$$

The exergy destruction rate in a component can be expressed as;

$$\dot{X} = Ex_i - Ex_e \quad (5.9)$$

5.2.1 Energy modelling of system components

The energy analyses for the A-CAES+BMGES system is carried out under the charging and discharging process as follows:

5.2.1.1 Dual fuel engine

The Control volume of DFE showing energy and fluid flows is as shown in Figure 5.1. By means of the general energy balance Eq. 5.1, the energy balance on the DFE is:

$$Q_f + Q_{a,i} = \dot{W}_{CV,DFE} + Q_{ex} + Q_{cw} + Q_{l,cr} \quad (5.10)$$

The energy supplied by the fuel (Q_f) is:

$$Q_f = \text{fuel energy input} = \dot{m}_{sg}LHV_{sg}/\rho_{sg} + \dot{m}_{df}LHV_{df} \quad (5.11)$$

Where \dot{m} is mass flow rate(kgs^{-1}), LHV_{df} is lower calorific value of diesel fuel(Jkg^{-1}), ρ is density and subscripts sg and df denote syngas and diesel fuel respectively.

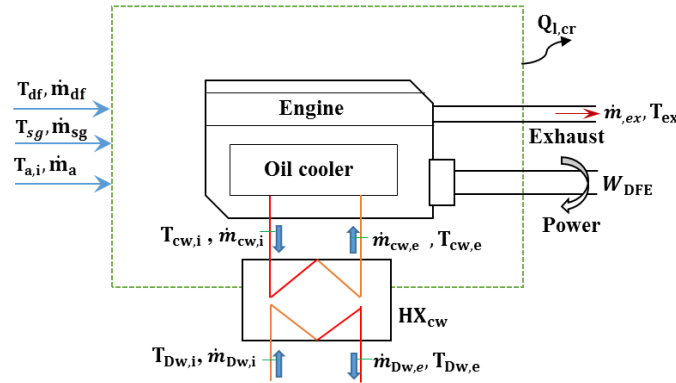


Figure 5.1 Control volume of DFE showing energy and fluid flows

The power output delivered by the engine or the brake horse power of the engine ($\dot{W}_{CV,DFE}$), is given as follows:

$$\dot{W}_{CV,DFE} = \frac{2\pi NT}{60} \quad (5.12)$$

Where N is the rotational speed of the engine (RPM) and T is the torque. The amount of heat rate, which is contained in the exhaust gas (Q_{ex}) and inlet air ($Q_{a,i}$) is given as follows:

$$Q_{ex} = \text{heat in exhaust gas} = \dot{m}_{ex} C_{p,ex} T_{ex} \quad (5.13)$$

$$Q_{a,i} = \text{heat in inlet air} = \dot{m}_{a,i} C_{p,a} T_a, \quad (5.14)$$

With the above, equation 5.10 reduces to the form as follows:

$$\begin{aligned} & (\dot{m}_{sg} LHV_{sg} / \rho_{sg} + \dot{m}_{df} LHV_{df}) \\ & = \dot{W}_{CV,DFE} + \dot{m}_{ex} C_{p,ex} T_{ex} - \dot{m}_a C_{p,a} T_{a,i} + (Q_{cw} + Q_{l,cr}) \end{aligned} \quad (5.15)$$

The heat passed to cooling water is Q_{cw} and $Q_{l,cr}$ is the heat loss due to convection and radiation. The subscripts CV, DFE, ex, a, i, cw and cr denote control volume, dual fuel engine, exhaust, air, inlet/input/in, cooling water and convection-radiation respectively. The mass flow rate of the exhaust is calculated from the mass flow rates of air ($\dot{m}_{a,theo}$) and fuel (\dot{m}_f) as follows:

$$\dot{m}_{ex} = \dot{m}_{df} + \dot{m}_{sg} + \dot{m}_{a,theo} \quad (5.16)$$

$$\dot{m}_{a,theo} = 0.5 N \eta_v V_{DFE} \rho_a / 60 \quad (5.17)$$

Where η_v , V_{DFE} , ρ_a denote volumetric efficiency, swept volume of engine (m^3) and air density (kgm^{-3}) respectively.

The power output from a dual fuel diesel engine depends on the fraction of diesel fuel in the mixture and the overall efficiency in the dual fuel mode. The overall efficiency ($\eta_{O,DF}$) in dual fuel mode lies in the range of 26–28% (Galal et al., 2002) (when using natural gas as the second fuel, whereas in the case of producer gas, the overall efficiency has been found to be about 20% (Dasappa & Sridhar, 2013). For a rated DFE power output ($P_{e,DFE}$), the required thermal power input contribution by the syngas (P_{sg}) and diesel (P_{df}) to the DFE can be determined as follows:

$$P_{th,sg} = \frac{P_{e,DF}}{\eta_{O,DF}} \times sf \quad (5.18)$$

$$P_{th,df} = \frac{P_{e,DF}}{\eta_{O,DF}} \times (1 - sf) \quad (5.19)$$

Where sf is the syngas fraction and $\eta_{O,DF}$ is the overall efficiency in dual fuel mode.

Heat Recovery from DFE for domestic application

In typical engines, 30% of the fuel energy input is contained in the jacket water and is capable of producing 90 to 99 °C hot water (Goldstein et al., 2002). In this thesis, the

CHP analysed is the supply of low pressure hot water for meeting domestic hot water, low temperature district heating applications or low grade heat process requirements. Heat is recovered from cooling water jacket of the DFE. The heat content of the cooling water is estimated based on the assumption that 30% of the fuel input is lost in the cooling water (Goldstein et al., 2002). Counter current (CC) shell-and-tube type heat exchanger is assumed (Lee et al., 2011). Based on the thermodynamic analysis using energy balances, the following equations is used to estimate the recovered thermal energy from the dual fuel engine cooling water jacket ($Q_{HX_{cw}}$).

$$Q_{HX_{cw}} = 0.3\eta_{recup}(P_{th,sg} + P_{th,df}) = \dot{m}_w C_w (T_{Dw,e} - T_{Dw,i}) \quad (5.20)$$

Where η_{recup} is the efficiency of recuperation. Subscript w and Dw denote water and district water respectively.

The area of the heat exchangers (A_{HX}), was modelled using LMTD method (Cengel, 2002). This involves applying mass-energy balances to the hot and cold fluids and a set of equations which depends on the heat exchange configuration. Thus:

$$A_{HX_{cw}} = \frac{Q_{HX_{cw}}}{U\Delta T_m} \quad (5.21)$$

Where ΔT_m is the log mean temperature difference (Cengel, 2002) which was obtained as follows:

$$\Delta T_m = \frac{(T_{h,i} - T_{c,e}) - (T_{h,e} - T_{c,i})}{\ln \left\{ \frac{(T_{h,i} - T_{c,e})}{(T_{h,e} - T_{c,i})} \right\}} \quad (5.22)$$

Where sunscripts h and c denote hot and cold respectively. In the analysis the overall heat transfer coefficient (U) value of $120 \text{ Wm}^{-2}\text{K}^{-1}$, is assumed for the recuperator (Hewitt & Pugh, 2007). Similar procedure is followed for the calculation of the area of other heat exchangers (HXs) in the subsequent sections.

5.2.1.2 Biomass Gasifier (BMG)

The biomass gasification model developed in chapter four is used to predict the properties of the syngas plus its composition and heating value. The syngas is required to supply a given thermal power input, in order for the DFE to generate the rated power output. The Biomass gasifier was sized to supply the syngas necessary to achieve this. The expected feed rate of biomass to the gasifier (G) on dry basis (db.) to achieve the required thermal power input of the syngas $P_{th,sg}$ in the DFE can be calculated as follows:

$$\dot{m}_{B,G}(d.b) = \frac{P_{th,sg}}{CGE \times LHV_B} \quad (5.23)$$

Where CGE denote cold gas efficiency of gasifier while subscript B, symbolizes biomass. The biomass (B) enters the gasifier at a given moisture content (MC). The mass flow rate of the biomass ($\dot{m}_{B,G}$) in dry basis (db) was converted to wet basis (wb) using the following equation:

$$\dot{m}_{B,G}(w.b) = \frac{\dot{m}_{B,G}(d.b)}{(1 - MC/100)} \quad (5.24)$$

The dry biomass entering the gasifier is supplied by the hot air drier (HAD). The HAD is sized such that the feed rate of dry wood chips from it matches the required feed rate of the wood chips in the biomass gasifier required to generate the rated electrical power output in the DFE. Thus, the initial feed rate of wet wood chips to the hot air biomass dryer ($\dot{m}_{B,D,i}$) at initial moisture content (MC_i) on wet basis was derived from the feed rate of wood in the biomass gasifier ($\dot{m}_{B,G}$) as follows:

$$\dot{m}_{B,D,i} = \frac{\dot{m}_{B,G}(w.b)}{(1 - MC_i/100)} \quad (5.25)$$

Where MC_i and MC_e represent the initial and final moisture content of the wet biomass entering and dry leaving the biomass dryer respectively.

5.2.1.3 Hot Air Dryer (HAD) system

The diagram of the hot air dryer is as shown in Figure 5.2.

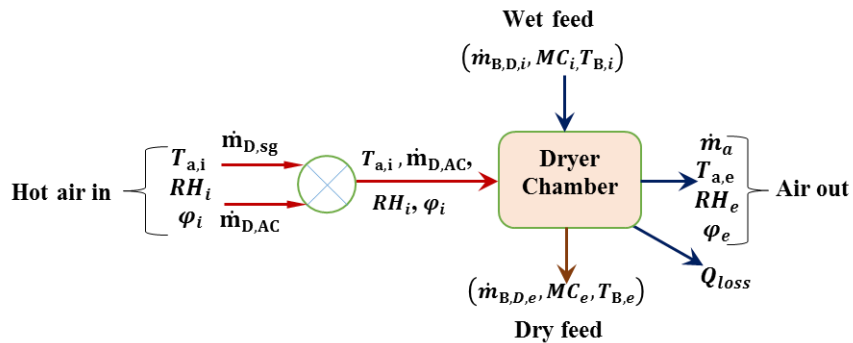


Figure 5.2 Hot air dryer system(Diyoke et al., 2018a)

In the HAD (Figure 5.2), as the wet fuel in initial state ($m_{B,i}, MC_i$) comes in direct contact with hot air, heat is transferred to the wet fuel from the hot air leading to the

vaporization of some or all the moisture in it and it is dried to a final state ($m_{B,e}$, MC_e) after some time. The heat required for drying (Q_D) was supplied by the hot air. According to the HAD, as in Figure 5.2, mass balances in the dryer (D) can be written for the dry biomass (B), air (a) and water (w) as follows:

$$\dot{m}_{B,D,i} = \dot{m}_{B,D,e} \quad (5.26)$$

$$\dot{m}_{a,D,i} = \dot{m}_{a,D,e} \quad (5.27)$$

$$\dot{m}_{a,D}(\varphi_i - \varphi_e) = \dot{m}_{w,ev} = \dot{m}_{w,i} - \dot{m}_{w,e} \quad (5.28)$$

Where RH and φ is the relative humidity and humidity ratio respectively and subscripts a, D and ev denotes air, dryer, and evaporation for specie involved respectively. The heat required for drying (Q_D) was obtained from energy balance as follows (Shottafer & Shuler, 1974; Harker et al., 2013; Luk et al., 2013):

$$Q_D = Q_{ev} + Q_s + Q_{l,D} \quad (5.29)$$

Q_{ev} is the heat required to evaporate moisture/water, $Q_{l,D}$ is heat loss from dryer structures and Q_s is sensible heat required to heat the biomass and drying structure to drying temperature.

Where:

$$Q_{ev} = \dot{m}_{w,ev} [C_{p,w}(T_{ev} - T_{ref}) + C_{p,wv}(T_{a,e} - T_{ev}) + L_{wv}] \quad (5.30)$$

$$Q_s = Q_{B,D,e} - Q_{B,D,i} \quad (5.31)$$

$$Q_{B,D,i} = [\dot{m}_{w,B,i}C_{p,w} + \dot{m}_{B,D,i}C_{p,B}](T_{B,i} - T_{ref}) \quad (5.32)$$

$$Q_{B,D,e} = [\dot{m}_{w,B,e}C_{p,w} + \dot{m}_{B,D,e}C_{p,B}](T_{B,e} - T_{ref}) \quad (5.33)$$

Where T_{ref} is the reference temperature taken as 273.15 K. Heat loss (Q_{loss}) is expressed as 5% of the heat input (Q_D). The heat input to the dryer, Q_D is supplied by the hot air as it is cooled from its initial state ($\dot{m}_a, T_{a,i}, RH_i$) to final state ($\dot{m}_a, T_{a,e}, RH_e$). The energy supplied by the hot air (HA) to the dryer is as follows:

$$Q_D = \dot{m}_{a,D}(h_{a,i} - h_{a,e}) \quad (5.34)$$

Where

$$h_a = [C_{p,a} + \varphi C_{p,wv}](T_a - T_{ref}) \quad (5.35)$$

The moisture or relative humidity ratio φ in kg per kg dry air is calculated as follows:

$$\varphi = \frac{0.62198}{(P_a - P_w)} RH \times p_{ws} \quad (5.36)$$

The water vapour saturation pressure (P_{ws}) between 0°C and 373°C was estimated using the following relation (Wagner & Prub, 2002):

$$\ln\left(\frac{P_{ws}}{P_c}\right) = \frac{T_c}{T} \times a_1\vartheta + a_2\vartheta^{1.5} + 3\vartheta^{1.5} + a_3\vartheta^3 + a_4\vartheta^{3.5} + a_5\vartheta^4 + a_6\vartheta^{7.5} \quad (5.37)$$

Where: P_c is critical pressure equal to 22.064 MPa, $\vartheta = 1 - T/T_c$, T_c is critical temperature equal to 647.096 K, $a_1 = -7.85951783$, $a_2 = 1.84408259$, $a_3 = -11.7866497$, $a_4 = 22.6807411$, $a_5 = -15.9618719$, $a_6 = 1.80122502$.

The mass flow rate of air entering the HAD ($\dot{m}_{a,D}$) is obtained as follows:

$$\dot{m}_{a,D} = \dot{m}_{D,AC} + \dot{m}_{D,sg} \quad (5.38)$$

Where $\dot{m}_{D,AC}$ and $\dot{m}_{D,sg}$ denote mass flow rate of air in (kgs^{-1}) recovered from AC1 and HX3 respectively.

In most hot air dryers, the exit temperature of the dried solid is a few degrees lower than the final temperature of the hot air (Gebreegziabher et al., 2013). In this model, the difference between $T_{a,e}$ and $T_{B,e}$ is set as 5 °C. With known $\dot{m}_{a,D}$ determined from Eq.5.38, equations 5.28 and 5.29 are solved to obtain the final humidity of air at the exit of the HAD and the temperature of the exiting air and biomass respectively. The fan electrical power required for circulation of air in the dryer can be obtained as follows:

$$P_{e,fan} = \psi \cdot \dot{Q}_{air} \quad (5.39)$$

Where ψ is the specific fan power set to $1.5 \text{ kWm}^{-3}\text{s}^{-1}$ as found by Nilsson (Nilsson, 1995).

5.2.1.4 A-CAES sub system

Air compressor (AC)

A four stage piston compressor has been assumed in this analysis to keep the outlet temperature from the compressor low and take greater advantage of the recovery of heat from the syngas from the gasifier. Higher outlet temperatures cause higher specific energy consumption, which in general is not wanted. The mass flow rate and outlet temperature from the compressor ($T_{AC,e}$) was obtained using Eq. 3.2 and Eq. 3.1 respectively in chapter three.

The heat recovered from the first stage air compressor (\dot{Q}_{AC1}) for biomass drying can be expressed as follows:

$$\dot{Q}_{AC1} = \eta_{HX} \dot{m}_{a,AC} [h_e - h_i] \quad (5.40)$$

The mass flow rate of heated air in (kgs^{-1}) recovered from AC1 for biomass drying ($\dot{m}_{D,AC}$) is obtained as follows:

$$\dot{m}_{D,AC} = \frac{\dot{Q}_{AC1}}{C_{p,a} (T_{a,i} - T_{amb})} \quad (5.41)$$

The syngas (sg) produced from the downdraft BMG modelled in chapter three is drawn from the high temperature reduction zone operating at about 815 – 1200 °C (GSTC 2018). At the exit of the gasifier, the hot syngas leaves the gasifiers at a temperature ($T_{sg,i}$) in the range of about 500 – 816 °C (Raman & Ram, 2013; GSTC, 2018). For a given heat exchanger effectiveness (η_{recup}), the air temperature leaving the first syngas cooler heat exchanger (HX2) and entering the TEST in (K) is obtained as follows:

$$T_{a,TEST,i} = \frac{\dot{m}_{a,AC} C_{p,a} T_{AC,e} + \eta_{recup} C_{min} T_{sg,i}}{\dot{m}_{a,AC} C_{p,a} + \eta_{recup} C_{min}} \quad (5.42)$$

Where C_{min} is $\min[\dot{m}_{a,AC} C_{p,a}, \dot{m}_{sg,B} C_{p,sg}]$.

The mass of the syngas is calculated from the syngas composition using the following relation (Basu, 2010):

$$\dot{m}_{sg,B} = \frac{0.755 \times \dot{m}_{a,G}}{y_{N_2}} \quad (5.43)$$

Where y_{N_2} is the molar concentration of Nitrogen in the syngas and

$$\dot{m}_{a,B} = AF \times \dot{m}_{B,G} \quad (5.44)$$

The temperature of the syngas exiting the first syngas cooler (HX2) was determined by energy balance thus:

$$T_{19} = T_{sg,G} - \frac{\dot{m}_{a,AC} C_{p,a} (T_{TEST,i} - T_{AC,e})}{\dot{m}_{sg,B} C_{p,sg}} \quad (5.45)$$

Since the temperature of the air leaving the air compressor is fairly high, all the thermal energy carried by the syngas from the gasifier is not entirely recuperated. For temperature of the syngas (T_{19}) leaving the first syngas cooler (HX2) greater than 200 °C, its heat content is further recovered and used to generate hot air at a temperature of about

80°C for biomass drying. The recovered heat from the syngas ($\dot{Q}_{sg,D}$) exiting the second syngas cooler heat exchanger (HX3) for biomass drying can be determined thus:

$$\dot{Q}_{sg,D} = \eta_{recup} \dot{m}_{sg} [h_e - h_i] \quad (5.46)$$

The mass flow rate of recuperated hot air from HX3 for biomass drying ($\dot{m}_{D,sg}$) was determined as follows:

$$\dot{m}_{D,sg} = \frac{\dot{Q}_{sg,D}}{C_{p,a}(T_{a,i} - T_{amb})} \quad (5.47)$$

Cooling the syngas before use in the DFE helps to prevent pre-ignition, to improve the volumetric efficiency of the engine at each stroke. Cooling also contributes to gas cleaning and makes it possible to avoid condensation of moisture in the gas after it is mixed with air before the engine intake. As the syngas is cooled, tars start to condense at temperatures under 350 °C (Reed & Das, 1988). Research has shown that as the syngas temperature goes below its dew point (typically 40 -50 °C), water also will condense. The condensation of water helps to remove tar particles but yields a contaminated water condensate in the process (Reed & Das, 1988). Thus, to minimise the condensation from the syngas, the temperature of the cooled syngas is limited to be above 60 °C at all times so as to use the syngas above its water dew point (40 – 60 °C) (Reed & Das, 1988).

The syngas is stored in an insulated storage tank. Heat loss in the syngas storage tank was assumed to be transferred from the side walls only. The final temperature of the syngas stored in the insulated storage tank at the beginning of the discharging operation was determined as follows:

$$T_{sg}(t) = T_{amb} + (T_{sg} - T_{amb}) e^{-UAt/\rho_{sg}V_{sg}C_{p,sg}} \quad (5.48)$$

Where U, A, t, V and ρ symbolise the overall heat transfer coefficient of the syngas storage tank (SST) in Wm^2K^{-1} , its surface area (m^2), time between storage and discharge (s), volume of syngas in the syngas store in m^3 and its density respectively in kgm^{-3} . U value for the SST was obtained using **Eq. 3.64** in Chapter Three. Table 5.1 shows the input design parameters for the A-CAES+BMGES system.

Table 5.1 Input design parameters for the system.

Parameters	Value	Ref
HAD		
Feed rate of wet wood chips, $\dot{m}_{w,BM,in}$ (kgh ⁻¹)	636.10	
Initial/final moisture content of wood feed, MC_i/MC_f (%)	50/10	
Temperature of the wood feed, $T_{BM,i}$ (°C)	22	
Temperature of the air feed, $T_{a,i}$ (°C)	80	
Relative humidity of the air feed, RH_i (%)	30	
Specific heat capacity of dry air, $C_{p,a}$ (kJkg ⁻¹ K ⁻¹)	1.006	
Specific heat of water, $C_{p,wv}$ (kJkg ⁻¹ °C ⁻¹)	4.186	(Gebreegziabher et al., 2013)
The latent heat of water vapour $LH_{w,v}$ (kJkg ⁻¹)	2.449	
Specific heat capacity of wood $C_{p,BM}$, (kJkg ⁻¹ K ⁻¹)	0.88	
Specific heat capacity of water vapour, $C_{p,wv}$ (kJkg ⁻¹ K ⁻¹)	2.01.	
DFE		
Rated power output, $P_{e,DFE}$ (MW)	0.3	
Exhaust temperature, T_{ex} (°C)	461	(Clarke, 2013)
Overall efficiency in dual fuel mode $\eta_{O,DF}$ (%)	20	(Dasappa & Sridhar, 2013)
Calorific value of Diesel, CV_{df} (MJkg ⁻¹)	45.5	(De et al., 2018)
Engine speed, N (RPM)	1000	(Clarke, 2013)
Engine capacity, V_s , (l)	91.6	(Clarke, 2013)
Volumetric efficiency, η_v (%)	80	(Reed & Das, 1988)
A-CAES		
Rated power of wind turbine P_{WT} (MW)	1	
Compressor overall Pressure ratio, $P_{r,AC}$	70	(Zhao et al., 2016)
Ratio of specific heats, γ	1.4	
Gas constant for air, R (kJkg ⁻¹ K ⁻¹)	0.287	
Round trip efficiency of TEST, RTE	0.7	
Air store temperature, T_{AS} (°C)	25	
Air store min/max operating pressure, p_{min}/p_{max} (bar)	40/70	(Zhao et al., 2016)
Charge/discharge mass flow ratio	4/3	
Expander overall Pressure ratio, $P_{r,AE}$	40	(Zhao et al., 2016)
Overall efficiency of DFE in dual fuel mode (%)	20	
Inlet pressure of AE1 turbine (bar)	40	
Charge (discharge) time (hrs.)	8(6)	

Thermal energy storage tank

A LH TES system with three different PCMs was considered in this study. A diagrammatic representation of the TEST (1-3) is shown in Figure 5.3. The thermal storage capacity of the TEST was obtained using the expression of Eq. 3.8 in chapter three. Since the number of stages of the air compressor used for thermodynamic analysis in this chapter is different from the two stages used in chapter three, the exit temperature of the air from the AC and thus the temperature of the air entering the TEST is different than in chapter three. Thus different PCMs were selected for the current analysis. Four stages is used in this current analysis so as to keep the exit temperature from the AC as low as possible to be able to fully exploit the thermal energy contained in the syngas exiting the gasifier.

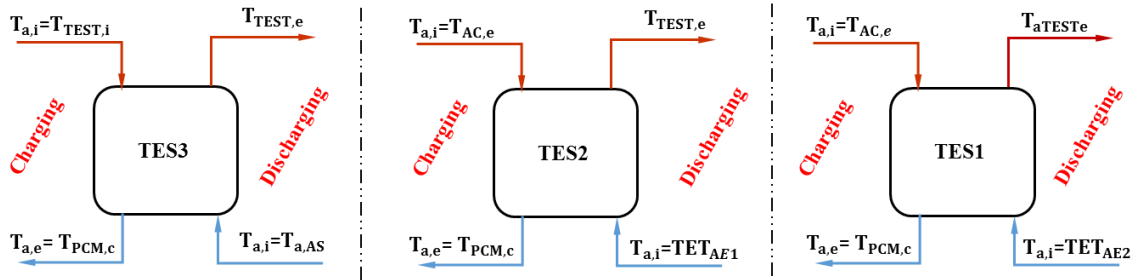


Figure 5.3 A diagrammatic representation of the TEST (1-3)

To achieve an optimal TEST, it is required that the temperature of the heat transfer fluid should match the melting point of the PCM in each TEST. Furthermore the temperature of the PCM ($T_{PCM,c}$) during discharge must always be above the temperature of the cold pressurised air entering the TEST. Thus $T_{PCM,c}$ is set as 50 °C, 75 °C and 65 °C for TEST₁, TEST₂ and TEST₃ respectively. Table 5.2 shows the thermos-physical properties and cost of the PCMs.

The mass (m) of the PCM in each TEST is calculated using Eq. 3.9 in Chapter three: The thermal energy stored in the TEST (Q_{TES}) during the charging mode was obtained using Eq. 5.49 as follows:

$$Q_{TES} = \dot{m}_{a,AC} C_{P,a} [T_{a,TEST,i} - T_{a,TEST,e}] \quad (5.49)$$

Table 5.2 Thermo physical properties of the PCMs (Pereira da Cunha & Eames, 2016).

TEST	Eutectic compounds	Mass ratio	T_m °C	L kJkg^{-1}	$C_{p,sol}$ $\text{kJkg}^{-1} \text{K}^{-1}$	$C_{p,liq}$ $\text{kJkg}^{-1} \text{K}^{-1}$	ρ_{sol} kgm^{-3}	Price £m^{-3}	£kWh^{-1}
1 & 2	$\text{KNO}_3\text{--NaNO}_2$	56/44	141	97	1.18	1.74	1994	504	9.7
3	$\text{LiNO}_3\text{--NaNO}_3$	49/51	194	262	1.35	1.72	2317	3084	19

During the discharge mode, the temperature of the air exiting the TEST ($T_{a,TEST,e}$) was obtained as follows:

$$T_{a,TEST,e} = RTE \times \frac{Q_{TES}}{\dot{m}_{a,AE}} + T_{a,i} \quad (5.50)$$

Where RTE the round is trip efficiency of the TEST and $T_{a,i}$ is the temperature of the air entering the TEST during the discharge mode.

The output power of the A-CAES system depends on the volume of air compressed during charging. The volume of the storage chamber (V_{AS}) is estimated as follows:

$$V_{AS} = \frac{\dot{m}_{a,AE} \cdot t_{ch} \cdot R_a \cdot T_{a,AS}}{(P_{max} - P_{min})} \quad (5.51)$$

The air expander (AE)

The air expander (AE) converts the hot pressurised air into mechanical energy to drive a generator. Many types of AE exist for power generation; reciprocating expander, screw expander, scroll expander, rotary vane expander, turbo-expander (Zhang et al., 2017). However, with the exception of the turbo expander, all the other AE are applied in power applications in the small capacity of not more than 10 kW with temperature up to 100 °C. Thus a turbo-expander with benefits of high efficiency, compact structure and good manufacturability, has been selected in the work presented in this thesis.

In the discharging mode of the A-CAES, the CA from the air store is discharged into the AE in two ways: The sliding pressure mode and the constant pressure operation mode. Reports in some literatures (Bullough et al., 2004; Kim & Hwang, 2006; Zhang et al., 2017) suggests the sliding operation mode in an A-CAES system can achieve higher system efficiency. The constant pressure operation mode results in a system with lower efficiency because of energy losses associated with throttling pressure from its maximum value to the inlet pressure of the AE. However, this mode is preferred for a long-term use

of the AE due to slight pressure fluctuation and stable operating conditions. Hence, the constant pressure operation mode is considered here.

The temperature of the air leaving HX(4 – 6) and entering the AE(1 – 3) in each stage respectively was obtained by energy balance as follows:

$$T_{a,AE,i} = T_{a,TEST,e} + \dot{m}_{ex}C_{P,ex}(T_{ex,i} - T_{ex,e})/\dot{m}_{a,AE}C_{P,a} \quad (5.52)$$

The outlet temperature of the DFE exhaust gas ($T_{ex,e}$) is set to the stack temperature of the selected dual fuel engine which is 120 °C to avoid condensation of air and prevent the exhaust piping from corroding (Goldstein et al., 2002). The temperature of the air exiting the AE in each AE stage ($T_{a,AE,e}$) was found as follows:

$$T_{a,AE,e} = T_{a,AE,i} \left[1 - \eta_{isen,AE} \left(1 - \beta_{AE}^{\frac{-\gamma+1}{\gamma}} \right) \right] \quad (5.53)$$

The ratio of the charge (t_{ch}) and discharge (t_{dch}) time of the AC to the AE is inversely correlated with the ratio of the charge (\dot{m}_{ch}) to discharge (\dot{m}_{dch}) mass and can be represented as (Mohammadi et al., 2017):

$$\frac{t_{ch}}{t_{dch}} = \dot{m}_{dch}/\dot{m}_{ch} \quad (5.54)$$

The generated power output by the A-CAES (P_C) and the overall power output by the system (P_T) was estimated using the following equations:

$$P_C = \sum_1^{n_{s,AE}} n_{s,AE} \times \dot{m}_{a,AE}C_{P,a}(T_{a,AE,i} - T_{a,AE,e}) \quad (5.55)$$

$$P_T = P_C + P_{DFE} \quad (5.56)$$

5.2.2 Exergy analysis

Energy analysis is not enough to analyse energy systems since it cannot reveal areas of irreversibility in the system and its components. The places of irreversibility and ways to increase the overall efficiency of the system can be examined by using exergy analysis. Equations 5.3-5.9 is applied to each component of the system, to determine the specific exergy, exergy efficiency and rate of exergy destruction in each component as follows:

5.2.2.1 Air Compressor (AC)

The exergy destruction associated with the air compressor is calculated by:

$$\dot{X}_{AC} = \dot{m}_{a,AC}\psi_i - \dot{m}_{a,AC}\psi_e + \dot{W}_{AC} \quad (5.57)$$

Where the work of the compression (\dot{W}_{AC}) is given as follows:

$$\dot{W}_{AC} = \dot{m}_{a,AC}(T_e - T_i) \quad (5.58)$$

5.2.2.2 Hot Air Dryer (HAD)

An exergy balance analogous to the energy balance for the HAD is written as follows:

$$EX_{a,D,i} - EX_{a,D,e} = EX_{B,D,e} - EX_{B,D,i} + EX_{w,D,e} - EX_{w,D,i} + EX_{ev} + EX_{l,D} + \dot{X} \quad (5.59)$$

The exergy destruction was found as follows:

$$\begin{aligned} \dot{X} = & \dot{m}_{a,D}(\psi_{a,i} - \psi_{a,e}) + \dot{m}_B(\psi_{B,i} - \psi_{B,e}) + \dot{m}_{w,B,i}\psi_w - \dot{m}_{w,B,e}\psi_{wv} + EX_{evap} \\ & - Q_{l,D} \left(1 - \frac{T_o}{T_{ave,D}} \right) \end{aligned} \quad (5.60)$$

The rate of exergy transfer due to evaporation of moisture in the dryer, EX_{ev} was estimated as follows (Inaba, 2007):

$$EX_{ev} = \dot{m}_{w,ev}L_{wv} \left(1 - \frac{T_o}{T_{ave,D}} \right) \quad (5.61)$$

Where ψ_w , and ψ_{wv} are the specific exergy transfers of water and water vapour at inlets and outlets, respectively; L_{wv} latent heat of vaporization of water (Jkg^{-1}) and T_{ave} is the average temperature of the HAD taken as the average temperature of the inlet and exit temperature of the biomass and air streams in (K) and subscript l denotes loss.

The specific total flow exergy of humid air per kg dry air was estimated as follows (Li, 1996; Dincer & Sahin, 2004):

$$\begin{aligned} \psi_a = & (C_{p,a} + \varphi C_{p,wv}) \left[T_a - T_{ref} - T_o \ln \frac{T_a}{T_o} \right] \\ & + T_o \left\{ (R_a + \varphi R_{wv}) \ln \frac{1 + 1.607\varphi_o}{1 + 1.6078\varphi} + 1.6078\varphi R_a \ln \frac{\varphi}{\varphi_o} \right\} \end{aligned} \quad (5.62)$$

where, $C_{p,wv}$ is water vapor specific heat at a constant pressure ($Jkg^{-1}K^{-1}$), R_a is the air specific gas constant ($Jkg^{-1}K^{-1}$), and the constant 1.6078 is the ratio of molar mass of air to molar mass of water vapour.

5.2.2.3 Biomass Gasifier (BMG)

The exergy balance on the biomass gasifier can be written as follows:

$$\dot{m}_B \psi_B + \dot{m}_a \psi_a = \dot{m}_{sg} \psi_{sg} + Q_{l,G} \left(1 - \frac{T_o}{T_{ave,G}} \right) + \dot{X}_{BMG} \quad (5.63)$$

Where $Q_{l,BMG}$ is the heat loss in the biomass gasifier (W) (G) and T_{ave} is the average temperature (K). The chemical exergy of biomass (ψ_B^{ch}) is calculated as follows (Szargut et al., 1998; Wang & Yang 2016):

$$\psi_B^{ch} = \beta LHV_B + W_w (\beta h_w + \psi_w^{ch}) + \psi_{ash}^{ch} W_{ash} \quad (5.64)$$

Where ψ_w^{ch} is the standard chemical exergy of the water (Jkg^{-1}), W_w is mass fraction of moisture in the biomass, W_{ash} is the mass fraction of ash in the biomass, β is the exergy coefficient of biomass for C/O ratio less than 2, which was calculated using (Ptasinski, et al., 2007):

$$\beta = \frac{1.044 + 0.0160 \left(\frac{H}{C} \right) - 0.3493 \left(\frac{O}{C} \right) \left(1 + 0.0531 \left(\frac{H}{C} \right) \right) + 0.0493 \left(\frac{N_f}{C} \right)}{1 - 0.4124(O/C)} \quad (5.65)$$

Where C, H, O, N are the mass fraction of carbon, hydrogen, oxygen and nitrogen of biomass in ultimate analysis, respectively. The physical exergy of the biomass is neglected because it enters at ambient state. The biomass gasifier operating conditions, syngas molar composition and properties are given in Table 5.3.

The specific exergy of the syngas ψ_{sg} consists of the chemical exergy and the physical exergy. The physical exergy of the syngas was calculated using the specific heat of syngas as follows:

$$\psi_{sg}^{ph} = C_{p,sg} \left(T_{sg} - T_o - T_o \frac{R}{M_{W_{sg}}} \ln \frac{T_{sg}}{T_o} \right) \quad (5.66)$$

$$C_{p,sg} = \sum_k w_k C_{p,k} \quad (5.67)$$

The specific heat of each component was obtained at the temperature of the syngas using the C_p of the syngas components in $\text{kJkg}^{-1}\text{K}^{-1}$ as shown in The chemical exergy of the syngas was calculate with Eq 5.5. The standard chemical exergy of different component

of product gas are shown in Table 5.5 Since the species in the product gas are considered ideal, their enthalpy is only a function of temperature.

Table 5.4. W_k is the mass fraction of the syngas component calculated from its molar ratio as follows:

$$w_k = \frac{y_k M_{w_k}}{\sum_k y_k M_{w_k}} \quad (5.68)$$

Where M_{w_k} is the molecular weight (kgmol^{-1}) and $C_{p,k}$ is the specific heat capacity in $\text{kJkg}^{-1}\text{K}^{-1}$ for the individual syngas components respectively.

Table 5.3 Biomass gasifier operating parameters and syngas composition.

Chemical composition of wood	$\text{CH}_{1.26}\text{O}_{0.49}$
Equivalence ratio	3.1
Biomass feeding rate, \dot{m}_B (kg h^{-1})	353.36
Gasifier operating pressure (bar)	1.013
Syngas temperature ($^{\circ}\text{C}$)	700
Syngas composition (vol. %)	
CH ₄	1.1
CO	22.8
CO ₂	9.0
H ₂	17.3
N ₂	49.8
Syngas LHV (kJNm^{-3})	5135
Density of air (syngas), kgm^{-3}	1.2041(1.0164)

The molecular weight of the syngas was calculated from the molar composition of the syngas components (k) using:

$$M_{w_{sg}} = \sum_k y_k M_{w,k} \quad (5.69)$$

The chemical exergy of the syngas was calculate with Eq 5.5. The standard chemical exergy of different component of product gas are shown in Table 5.5 Since the species in the product gas are considered ideal, their enthalpy is only a function of temperature.

Table 5.4 Constant pressure specific heat of various gases (Borgnakke & Sonntag, 2009)

$C_{P,k} = C_0 + C_1\phi + C_2\phi^2 + C_3\phi^3$				
$\phi = T_{sg}(\text{kelvin})/1000$				
k	C_0	C_1	C_2	C_3
CH_4	1.2	3.25	0.75	-0.71
H_2	13.46	4.6	-6.85	3.79
CO	1.10	-0.46	1.0	-0.454
CO_2	0.45	1.67	-1.27	0.39
N_2	1.11	-0.48	0.96	-0.42
H_2O	1.79	0.107	0.586	-0.20

Table 5.5 Standard chemical exergy of different syngas gas components (Cengel & Boles, 2006)

k^{th} Gas	$\psi_{o,k}^{\text{ch}}$ (kJ/kmol)
CH_4	831,650
H_2	236,100
CO	275,100
CO_2	19,870
N_2	720
$H_2O(l)$ ($H_2O(g)$)	900 (9500)

5.2.2.4 Dual Fuel Engine (DFE)

The rate of exergy destruction in the dual fuel engine (DFE) was obtained as follows (Canakci & Hosoz, 2006):

$$\dot{X}_d = \dot{m}_{sg,DFE}\psi_{i,sg,DFE} + \dot{m}_{df}\psi_{i,df} + \dot{m}_{a,DFE}\psi_{i,a,DFE} - \dot{m}_{ex}\psi_{ex,DFE} - \dot{W}_{CV,DFE} + \left(1 - \frac{T_o}{T_{ave,DFE}}\right)Q_{l,DFE} \quad (5.70)$$

The rate of exergy transfer accompanying heat transfer $Q_{l,DFE}$ is the sum of the heat loss and recovered heat from the system and $T_{ave,DFE}$ is the average temperature of rejection of heat to the ambient air by the DFE. In this thesis, it was assumed that heat is lost by the system at the same temperature as the engine cooling water.

The physical exergy of df, and air was computed using equation 5.4. The specific chemical exergy of diesel (ψ_{df}^{ch}) is expressed as follows (Kotas, 1995):

$$\psi_{df}^{ch} = LHV_{df} \left[1.0401 + 0.1728 \frac{H}{C} + 0.0432 \frac{O}{C} + 0.2169 \frac{S}{C} \left(1 - 2.0628 \frac{H}{C} \right) \right] \quad (5.71)$$

Where H, C, O, N and S are the mass fractions of hydrogen, carbon, oxygen, nitrogen and sulphur in the fuel. In this study, the values of 85.4, 11.68, 0.25, 0.15, 0.025 percent for diesel fuel with chemical formula of $C_{12}H_{26}$ respectively (Wang et al., 2010) has been used.

The rate of heat loss for the DFE operating at a steady state was calculated from a heat balance equation on the DFE as in Eq. 5.10. In the thesis, $Q_{l,DFE}$ is considered as the sum of $Q_{l,cr}$ and Q_{cw} .

5.2.2.5 Turbine/Air expander (AE)

The exergy destruction in the turbine was calculated as follows:

$$\dot{X}_{AE} = \dot{m}_{a,AE}\psi_i - \dot{m}_{a,AE}\psi_e - \dot{W}_{AE} \quad (5.72)$$

5.2.2.6 Heat exchangers (HXs)

The exergy destruction in the heat exchangers (HXs) was calculated as follows:

$$\dot{X}_{HX} = \dot{m}_h(\psi_{hi} - \psi_{h,e}) - \dot{m}_c(\psi_{c,e} - \psi_{c,i}) \quad (5.73)$$

5.2.2.7 Throttle Valve

The throttling process of the air exiting the cavern is assumed to be an isenthalpic process. Therefore, the following relation holds for the exergy destruction in the TV:

$$\dot{X}_{TV} = \dot{m}_{a,AE}(\psi_{a,i} - \psi_{a,e}) = \dot{m}_{a,AE}R_a T_0 \ln \frac{p_e}{p_i} \quad (5.74)$$

5.3 System performance metrics

5.3.1 Energy_efficiency

The formula used for the computation of the energy and exergy efficiency of each component in the cycle are summarized in Table 5.6.

Table 5.6 Energy and exergy efficiency of each component in the cycle

Components	Energy efficiency	Exergy efficiency
HAD	$\frac{\dot{m}w_{evap}h_{evap}}{\dot{m}_{a,D}h_{a,i}}$	$\frac{\dot{m}w_{evap}\psi_{evap}}{\dot{m}_{a,D}\psi_{a,i}}$
BMG	$\frac{\dot{m}_{sg}LHV_{sg}}{\dot{m}_a h_a + \dot{m}_B h_B + \dot{m}_B LHV_B}$	$\frac{\dot{m}_{sg}\psi_{sg}}{\dot{m}_a \psi_a + \dot{m}_B \psi_B}$
DFE	$\frac{\dot{m}_a h_a + \dot{m}_{sg} h_{sg} + \dot{m}_{df} LHV_{df}}{P_e}$	$\frac{\dot{m}_a \psi_a + \dot{m}_{sg} \psi_{sg} + \dot{m}_{df} \psi_{df}}{P_e}$
HX	$\frac{\dot{m}_c (h_{c,e} - h_{c,i})}{\dot{m}_h (h_{h,i} - h_{h,e})}$	$\frac{\dot{m}_c (\psi_{c,e} - \psi_{c,i})}{\dot{m}_h (\psi_{h,i} - \psi_{h,e})}$
AE	-	$\frac{\dot{W}_{AE}}{\dot{m}_{AC}\psi_i - \dot{m}_{AC}\psi_e}$
AC	-	$\frac{\dot{m}_{AC}\psi_e - \dot{m}_{AC}\psi_i}{\dot{W}_{AC}}$
TES	-	$\frac{\dot{m}_{a,AE}(\psi_{c,e} - \psi_{c,i})}{\dot{m}_{a,AC}(\psi_{h,i} - \psi_{h,e})}$

For the overall co-generation system, the most widely used parameter to access the efficiency of a CHP is the total system efficiency (η_T) which is the ratio of the sum of the net useful power and thermal outputs ($P_T + \dot{Q}_T$) and the total energy input as shown below (EPA) (Zhao et al., 2015; Yao et al., 2016; Mohammadi et al., 2017).

$$\eta_T = \frac{P_T + \dot{Q}_T}{\dot{Q}_{df} \times t_{dch} + (\dot{Q}_B + P_{WT}) \times t_{ch}} \times \frac{t_{dch}}{1} \quad (5.75)$$

Where \dot{Q}_B and \dot{Q}_{df} are the biomass energy input and diesel fuel energy inputs to the DFE system. The total system efficiency (TSE) is made up of the electrical efficiency (η_e) and the efficiency of heat generation (η_H) as follows:

$$\eta_E = \frac{P_T}{\dot{Q}_{df} \times t_{dch} + (\dot{Q}_B + P_{WT}) \times t_{ch}} \times \frac{t_{dch}}{1} \quad (5.76)$$

$$\eta_H = \frac{\dot{Q}_T}{\dot{Q}_{df} \times t_{dch} + (\dot{Q}_B + P_{WT}) \times t_{ch}} \times \frac{t_{dch}}{1} \quad (5.77)$$

The TSE as a metric fails to distinguish between the value of thermal output and power output (EPA) since it treats the two as additive properties with the same relative value. In truth and real life, the two forms of energy are not additive since they cannot be converted easily from one form to the other. Hence, another parameter called the electric effective efficiency (η_{ee}) is used (EPA). η_{ee} enables a direct comparison of a CHP's performance to that of other conventional power generation systems by crediting that portion of the CHP system's fuel input allocated to thermal output. Effective electric efficiency (η_{ee}) was calculated as follows:

$$\eta_{ee} = \frac{P_T \times t_{dch}}{\dot{Q}_{df} \times t_{dch} + (\dot{Q}_B + P_{WT}) \times t_{ch} - \dot{Q}_T \times t_{dch} / \eta_{cp}} \quad (5.78)$$

η_{cp} denotes the efficiency of a conventional plant that if not would be used to produce the useful thermal energy output, if the proposed A-CAES+BMGES CHP system does not exist. In the analysis, the conventional plant was assumed as a biomass-fired boiler with efficiency of about 0.75 (EPA). Typical values of η_{cp} for natural gas fired boilers and coal fired boiler are 0.75-0.85 and 0.83-0.86 respectively (Odeh et al., 2015).

Another parameter for gauging the performance of a CHP system is the primary energy savings ratio (PESR). In the thesis, it was calculated on the basis of the European directive as follows (Frangopoulos, 2012):

$$PESR = 1 - \frac{1}{\frac{\eta_E}{\eta_{rE}} - \eta_{HT} / \eta_{rH}} \quad (5.79)$$

Where η_{rE} is the efficiency reference value for separate electricity production and η_{rH} is the reference efficiency value for separate heat production. In the model, values of 44.2% and 85% for diesel generators for the production of electricity and hot water was used for

η_{rE} and η_{rH} respectively (Odeh et al., 2015). Moreover, the round trip efficiency or electrical efficiency of the A-CAES component alone could be calculated using the following equation:

$$RTE_{A-CAES} = \frac{P_C}{P_{WT}} \quad (5.80)$$

5.3.2 Exergy_efficiency_and_exergy_destruction

The total exergy efficiency (η_{ex}) of the whole system can be written analogous to the total system efficiency as follows:

$$\eta_{ex} = \frac{P_T + Ex_h}{Ex_{df} \times t_{dch} + (Ex_B + P_{WT}) \times t_{ch}} \times \frac{t_{dch}}{1} \quad (5.81)$$

Where Ex_h represent the exergy of recovered district water. The whole exergy destruction rate of the system is the summation of the exergy destruction rates of each unit operating block of the system as follows:

$$\dot{X}_T = \sum \dot{X}_{subsystems} \quad (5.82)$$

Moreover, the exergy destruction proportion (\dot{X}_{dp}) is the ratio of exergy destruction of each unit operation to the total exergy destruction of the system:

$$\dot{X}_p = \dot{X}_{subsystems} / \dot{X}_T \quad (5.83)$$

The depletion number is also selected to assess the efficiency of fuel consumption [33]. It defined as follows:

$$\dot{D}_{ex} = \dot{X}_T / Ex_f + P_{WT} \quad (5.84)$$

Where the subscript f denotes fuel.

5.4. Results and discussion

5.4.1 Overall performance results

The thermodynamic analysis of the proposed A-CAES+BMGES has been analysed by means of exergy and energy analysis using a developed Matlab simulation programme. Thermodynamic state variables such as temperature, pressure, mass flow rate enthalpy and entropy of the various state points of the A-CAES+BMGES system are required to

calculate the performance of the system. These have been calculated using relevant correlations in the published literature as contained in Appendix A1.1.

Table 5.7 lists the values of the thermodynamic state variables determined for each state of the system. By means of the calculated thermodynamic variables as contained in Table 5.7, and the equations developed in the forgoing section, the system performance parameters have been calculated. Inferences drawn from the results of the calculation shows that under design conditions and for a charging duration of 8 hours daily at a capacity factor of 0.85, the hot air dryer can process 789.34 tonne of dry wood per year on dry basis at an efficiency of about 55.3% from an initial wet biomass feed rate of 636.10 kg h^{-1} on wet basis. To achieve the output of 789.34 tonne of dry wood per year, the HAD needs 190.4 kW of thermal energy. This energy is delivered from recovered thermal energy from AC_1 (173.3 kW) and syngas (53.97 kW). To deliver an electric output of 0.3 MWe in the DFE using a mixture of syngas and diesel fuel at a mixture ratio of 80:20% respectively, fuel consumption of 855.06 and 25.18 kg h^{-1} is required for syngas and diesel respectively. In order to supply the syngas at the rate (855.06 kg h^{-1}) required by the DFE, it is found that the biomass gasifier will need biomass and air feed rates of 353.36 and 617.65 kg h^{-1} respectively in order for the DFE to deliver the rated 300 kW_e in the dual fuel mode.

Table 5.7 Properties of each stream in the system

Stream number.	Fluid type	Temperature (K)	Pressure (bar)	mass flow rate (kgs^{-1})	Enthalpy (kJkg^{-1})	Entropy (kJkg^{-1})	Specific exergy (kJkg^{-1})
1	Air	298.1	1.01	1.98	299.00	5.71	0.00
2	Air	422.5	2.93	1.98	432.15	5.88	90.88
3	Air	298.2	1.01	1.98	299.00	5.71	0.00
4	Air	422.5	8.48	1.98	432.15	5.57	90.88
5	Air	298.2	1.01	1.98	299.00	5.71	0.00
6	Air	422.5	24.52	1.98	432.15	5.27	90.88
7	Air	298.2	1.01	1.98	299.00	5.71	0.00
8	Air	422.5	70.93	1.98	432.15	4.96	90.88
9	Air	480.5	70.93	1.98	496.36	5.16	104.82
10	Air	298.2	70.93	1.98	299.00	4.49	363.54
11	Air	298.2	1.01	3.14	299.00	5.71	0.00
12	Air	353.0	1.01	3.14	361.17	6.00	4.61

Stream number.	Fluid type	Temperature (K)	Pressure (bar)	mass flow rate (kgs ⁻¹)	Enthalpy (kJkg ⁻¹)	Entropy (kJkg ⁻¹)	Specific exergy (kJkg ⁻¹)
13	Air	298.2	1.01	0.98	299.00	5.71	0.00
14	Air	353.0	1.01	0.98	361.17	6.00	4.61
15	Air	353.0	1.01	4.12	361.17	6.00	4.61
16	Wood	293.0	1.01	0.18	362.19	0.00	0.06
17	Air	306.3	1.01	4.12	322.95	6.03	2.41
18	wood	301.3	1.01	0.09	372.48	0.00	0.02
19	Syngas	973.0	1.01	0.26	1253.45	8.86	4537.42
20	Syngas	628.1	1.01	0.26	809.19	8.30	138.90
21	Syngas	397.2	1.01	0.26	511.62	7.70	17.41
22	Syngas	397.2	1.01	0.26	511.62	7.70	17.41
23	Syngas	345.3	1.01	0.24	444.85	7.52	4541.77
24	Diesel	298.2	1.01	0.01	566.48	10.82	45634.10
25	Air	298.2	1.01	0.74	299.00	5.71	0.00
26	Air	298.2	40.00	1.98	299.00	4.66	314.53
27	Air	404.8	40.00	2.64	412.79	5.06	15.64
28	Air	447.3	40.00	2.64	459.42	5.21	28.62
29	Air	330.7	11.70	2.64	333.26	5.14	210.97
30	Air	386.7	11.70	2.64	393.22	5.35	11.13
31	Air	432.1	11.70	2.64	442.71	5.51	23.64
32	Air	319.5	3.42	2.64	321.42	5.45	104.82
33	Air	381.9	3.42	2.64	388.03	5.69	10.04
34	Air	427.3	3.42	2.64	437.44	5.85	22.14
35	Air	315.9	1.00	2.64	317.68	5.79	0.51
36	Exhaust	734.0	1.01	0.33	794.14	5.50	173.85
37	Exhaust	393.0	1.01	0.33	400.01	4.45	12.62
38	Exhaust	734.0	1.01	0.33	794.14	5.50	173.85
39	Exhaust	393.0	1.01	0.33	400.01	4.45	12.62
40	Exhaust	734.0	1.01	0.33	794.14	5.50	173.85
41	Exhaust	414.8	1.01	0.33	423.69	4.52	18.41
42	Exhaust	400.3	1.01	0.98	407.88	4.47	14.45
43	Water	308.0	1.01	3.76	146.07	0.50	0.67
44	Water	328.0	1.01	3.76	229.65	0.74	5.86
45	Water	363.1	1.01	2.51	376.97	1.15	25.99
46	Water	333.2	1.01	2.51	251.18	0.81	7.99

Table 5.8 shows the summary of the thermodynamic performance of the overall integrated A-CAES+BMGES system. The thermal capacity of the thermal energy storage tanks, TES₁, TES₂ and TES₃ is estimated as 0.17, 0.15 and 0.31 MW respectively. It can be noticed that, the thermal capacity of TES₁ and TES₂ is roughly about half that of TES₃.

This is made possible by higher temperature difference in TEST₃ due to it having the highest and lowest temperature of HTF entering and leaving it, during the charging and discharging modes respectively when compared with TEST₁ and TEST₂.

The overall power output by the A-CAES+BMGES system is 2.19 MWh_{year}⁻¹ comprising of roughly 74.5% contribution from the A-CAES and the outstanding 25.5% from the DFE.

It is interesting to observe that the round trip efficiency of the A-CAES component alone is about 88.6%. This means that about 88.6% of the excess wind electricity used during the charging mode is produced in the A-CAES during the discharging mode. The high efficiency of electricity storage of the A-CAES component at 88.6% suggests that the proposed A-CAES+BMGES system is efficient and effective at storing excess wind electricity.

Table 5.8 Technical performance results for the integrated system

Parameter, Symbol (unit)	Value
Air compressor power input, P_{AC} (MW)	0.99
Thermal storage capacity of TEST, $Q_{Th,TEST}$ (MJ _s ⁻¹):	
TES ₁	0.17
TES ₂	0.15
TES ₃	0.31
Total electricity output, P_T (MW _e)	1.16
System electrical efficiency, SEE (%)	30.0
Total system efficiency, TSE (%)	38.1
System exergy efficiency, (%)	28.5
Air storage (AS) size, V_{AS} (m ³)	1549
Heat Recovery:	
Heat recovered from compressed air, RH_{AC} (MW _{th})	0.17
Heat recovered from syngas, RH_{sg} (MW _{th})	0.05
Total Heat recovered during charging, $RH_{t,ch}$ (MW _{th})	0.23
Total heat recovered discharging, $RH_{t,dch}$ (MW _{th})	0.32
Heat required by Dryer, (kW _{th})	0.20

At a look at the power output of 0.89 MW from the A-CAES alone in relation to the excess wind electricity of 1MW supplied to the air compressors during charging mode,

it might seem that the performance is unrealistic but this advantage is attributable to two key factors which we have to be mindful of:

- The syngas exiting the gasifier has a temperature of about 700 °C and its thermal energy is used to preheat the air exiting the compressor after compression which is about 149 °C before storage in the thermal energy storage tank (TEST)
- During heat recovery, the exhaust gas from the dual fuel engine (DFE) has a temperature of 461 °C and its thermal energy is again used solely to increase the temperature of the compressed air exiting the TESTs further before expansion in the turbine stages.

From thermodynamic stand point, the performance of the thermal energy storage cycles depends on the average temperature at which heat is supplied/retrieved during charging/discharging respectively. In addition, the performance of air expander depends on the turbine inlet temperature of each stage. Thus the above two factors contribute to improve the round trip efficiency of the A-CAES component of the overall system to roughly 89%. The improvement in the A-CAES performance also led to the overall improvement in the system electrical efficiency (η_e) and total system efficiency (TSE). This unique feature of the system demonstrates its hybrid nature. It is typical with the McIntosh D-CAES plant in Alabama where more electricity is discharged than is necessary for charging (Budt et al., 2016). i.e., In order to produce 1 kWh of electrical energy output, 0.69 kWh of electrical energy input is supplied to drive the compressor and 1.17 kWh of thermal energy from fuel combustion is input to heat up the air prior to expansion Budt et al., 2016). Thus, it is not unrealistic to find that more electricity can be discharged than is necessary for charging, in the system proposed in this thesis due to the added syngas and exhaust gas energy during the charging and discharging phases respectively.

If the syngas and DFE exhaust thermal energy is ignored, the electrical efficiency of the A-CAES becomes 57.54% which is comparable to the reported values in the literature (Elmegaard & Markussen, 2011; Budt et al., 2016).

One of the benefits of the configuration analysed in this thesis is that the system has dual streams of energy output (i.e. electricity and heat). The total recovered heat from the system for low temperature domestic water/district heating application is about 586.38

$\text{MWh}_{\text{th}}\text{year}^{-1}$ representing only about 21% of the total input fuel energy. This heat is recovered from the DFE cooling system jacket water.

The calculated total system efficiency and exergy efficiency of the system is about 38% and 29% respectively. Additionally, the effective electrical efficiency, electrical efficiency and the primary energy savings ratio (PESR) are found to be 33, 30 and -29% respectively. The primary energy savings ratio with negative value indicates that the CHP is less efficient than having separate heat production. The total exergy efficiency is lower than the total system and effective electrical efficiencies because there are significant losses in the system which are not accounted for in the energy analysis but are accounted for in the exergy analysis.

The A-CAES+BMGES system analysed in this thesis is not a standalone energy storage technology but a hybrid one with dual streams of energy output. Therefore a direct comparison of its efficiency with an A-CAES system can be deceptive. Nevertheless, the values of the system electrical efficiency of 30%, effective electrical efficiency of 33% and TSE of 29% computed are fairly moderate values in comparison with data found in the published literature for both A-CAES and similar hybrid systems. For example, in the work of Garrison and Webber (2011), an overall efficiency of 46% was reported for a hybrid solar-CAES system. A hybrid A-CAES and flywheel energy storage system (FESS) was reported by Zhao et al. (2014) to have a round trip efficiency (RTE) ranging from 70-74%. The round trip efficiency of about 88.6% computed for the A-CAES component alone in the present study is higher which confers some advantage to it. In another related study, Liu and Wang (2016) found RTEs that ranges between 53.9% and 67.0% for an A-CAES. Karallas and Tzouganatos (2014) reported percentage electrical efficiencies varying from 24.8 – 62.1 for an A-CAES system of different configuration (i.e. different stages with and without air preheating).

In their study of a tri-generative compressed air storage (T-CAES) compatible for a small to medium size distributed generation civil application. Facci et al. (2015) reported system electrical efficiencies of 30% which is the same with the result of the current study. They went further to report that the electrical efficiency could lie in the range of 20 to 40% depending on the operating storage pressure (10–100 bar) (Minutillo et al., 2015).

In an experimental study of compressed air energy storage system with thermal energy storage, Wang et al. (2016) estimated an average round trip efficiency of 22.6% for the system with water as thermal energy storage working medium. As can be observed, there is a wide variation in the reported efficiencies of CAES in the literature. The reason for this could be attributed to the fact that different configurations, operating parameters and conditions are applied by the various scholars in their analysis. Such parameters include (a) the average storage pressure, (b) the compressors and turbines efficiencies, (c) the number of stages of AEs and ACs (Diyoke et al., 2018a). Thus it can be concluded from the efficiency comparisons that the total system efficiency of the integrated system is less than the efficiency of a standalone A-CAES system but comparable to the efficiency of similar hybrid configurations. Moreover, the RTE of the A-CAES component of the system is higher than that of a conventional A-CAES system

It is thought-provoking to examine the exergy efficiency, exergy destruction rates (kW) and exergy destruction proportion (%) of the integrated A-CAES+BMG system components as shown in Table 5.9.

Observe that the biomass gasifier (BMG) and the dual fuel engine (DFE) accounts for more exergy destruction rates than in the other components. These two components represent roughly 98% of the total exergy destruction of the entire system.

Even though, the exergy efficiency of the gasifier is about 61.4%, it nonetheless accounted for the greatest exergy destruction rate of about 94.4%. This is on account of the fact that the chemical reactions and partial oxidations taking place in biomass gasifier are largely exothermic and irreversible combustion processes with associated high heat losses (Li et al., 2016). The high heat losses and irreversibility result to large fraction of exergy destruction. Analogous to the gasifier, the high exergy destruction rate in the DFE can be described by irreversible combustion processes, heat losses across high temperature difference and friction. Additionally, slow and poor combustion flame speed in the DFE that results from the incomplete combustion features of the syngas can lead to a fairly higher exergy loss through exhaust gas.

The exergy efficiency of the various components as depicted in table 5.9 is close to values reported for the components in similar plant configurations. Mohammadi et al. (2017) reported exergy efficiencies of 0.89, 0.90, 0.94, and 0.57 for AC1, AC2, AE and

HX. In another study by Bang-Møller et al. (2011) exergy efficiencies for BMG, AC, AE and HX was reported as 0.87, 0.79, 0.95, and 0.33-0.90 respectively. For a HAD, Dincer and Sahin (2004) reported an exergy efficiency of about 7% at temperature of drying air of 70 °C which is comparable to the value of about 5.8% we reported at drying air temperature of 80 °C since increasing drying air temperature reduces the exergy efficiency. It is pertinent to state that the exergy efficiency of any of the components could still vary out of the ranges indicated above depending on the process configuration, temperature involved and targeted output.

Table 5.9 Thermodynamic performance results for the components of the system

Components	Exergy destruction, \dot{X} (kW)	Exergy destruction ratio, \dot{X}_p	Exergy efficiency, $\eta_{ex}(\%)$
BMG	27476.78	94.37	61.38
DFE	1052.01	3.61	21.47
HAD	7.70	0.03	5.76
AC	107.22	0.37	89.17
AC1	26.80		89.17
AC2	26.80		89.17
AC3	26.80		89.17
AC4	26.80		89.17
AE	141.34	0.49	86.12
AE1	48.48		86.10
AE2	47.99		88.81
AE3	44.87		86.47
HX			
1	26.67	0.09	34.79
2	11.75	0.04	83.56
3	27.04	0.09	14.08
4	16.55	0.05	62.40
5	19.66	0.07	62.67
6	20.73	0.07	60.63
7	25.62	0.09	43.27
TES3	37.39	0.13	52.47
TES2	8.42	0.03	74.78
TES1	11.45	0.04	68.18

Components	Exergy destruction, \dot{X} (kW)	Exergy destruction ratio, \dot{X}_p	Exergy efficiency, η_{ex} (%)
TV	126.3	0.43	86.8

Reduction in energy availability can be revealed by rate of exergy destruction (Ozturk & Dincer, 2013); however, it cannot show the energy and exergy utilization efficiency of the A-CAES+BMGES system.

The exergy efficiencies of the system components are key for identifying locations of high exergy losses. It can be observed from Table 5.9 that the highest exergy efficiencies of 89.17, 86.8 and 86.12 take place in the AC, throttle valve (TV) and AE, respectively, whereas the lowest exergy efficiencies of 5.76, 14.08 and 21.47% take place in the HAD, HX3, and DFE respectively. High exergy efficiencies in the AE and AC is because they are optimized off the shelf components with negligible room for performance improvements.

The high exergy efficiency of the second syngas cooler heat exchanger (HX2) is because of low temperature difference between the streams at the cold end of the heat exchanger and the two streams having heat capacity rates ($\dot{m}C_p$) that is unequal. This indicates a potential for improving the heat exchanger network. On the other hand, the third syngas cooler (HX3) low exergy efficiency could be due to the high temperature difference between the streams at the cold end of the heat exchanger and the exergy destruction accompanying the syngas of fairly high temperature leaving the heat exchanger. In practice, the low exergy efficiency of HX3 is deceptive, as also the preheating of the air for use in biomass drying in the HAD could be seen as a useful product.

The thermal energy storage tanks has exergy efficiencies of 52.47, 74.78 and 68.18% for TES1 TES2 and TES3 respectively. TES3 has the lowest exergy efficiency because it has the lowest cold fluid inlet temperature. TES2 has the highest cold fluid inlet temperature leading to the highest exergy efficiency obtained. These TES units perform a substantial role in the storage and retrieval of the thermal energy developed during the compression process of the A-CAES.

5.4.2 Sensitivity analysis results

The A-CAES+BMGES system presented in this chapter was modelled with different operating variables and assumptions. These parameter values and assumptions are subject to variations. Thus a sensitivity analysis (SA), is carried out to investigate these potential variations and their impacts on conclusions to be drawn from the modelled A-CAES+BMGES. In carrying out the sensitivity analysis, a realistic range of each of the major parameters in the model which realistically reflects its likely range is used. The results of such sensitivity is presented in the following sections:

5.4.2.1. Impact of TES round trip efficiency of the A-CAES

The influence of the RTE of the TEST system of the A-CAES on the performance of the system is presented in Figure 5.4. According to the figure, as the RTE increases, the total power output (P_T), the exergy, energy and the effective electrical efficiency of the system increase; dissimilarly, the exergy destruction decreases. For an increase in RTE from 0.7 to 0.95, the TSE and exergy efficiency increases by about 2 and 3% respectively while for a reduction of RTE from 0.7 to 0.4, the TSE and Exergy efficiency reduces by roughly 3 and 4%, respectively. The trend can be explained thus; as the RTE increases, it leads to an increase in the heat recovered from the TEST by the CA.

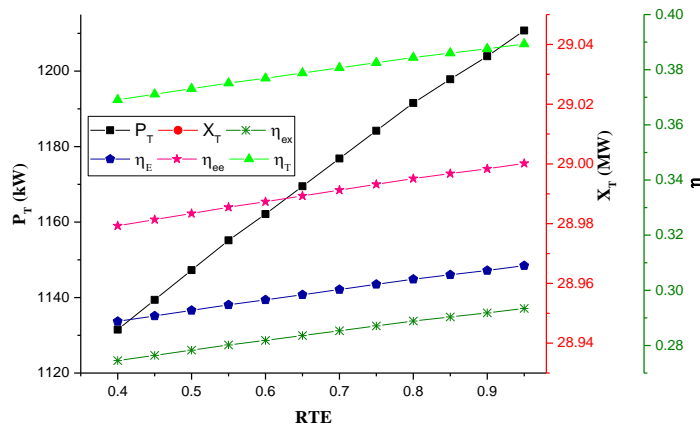


Figure 5.4 Impact of change in RTE on system performance

This consequently results to the increase in the turbine inlet temperature (TIT) of the AE stages and therefore the total generated power. Consequently, the efficiency which is a function of power out increases as well. The exergy destruction decreases with increasing RTE because at high efficiency associated with high RTE, less losses occur in the system.

5.4.2.2. Impact of syngas temperature

The impact of temperature of the syngas (T_{sg}) from the biomass gasifier on the performance of the system is presented in Figure 5.5. Notice that as T_{sg} of the BMG increases, the total power output and thus the exergy (energy) efficiency and the effective efficiency of the system increase. This is because the increase in the syngas temperature leads to a corresponding increase in the average temperature at which heat is stored and retrieved in the TES during the charging and discharging modes respectively. This results to the rise in the TIT of the AE stages and hence the whole performance of the system.

The thermal energy for heating the high-pressure compressed air entering the TEST and some of the heat supplied to the HAD for biomass drying come from the thermal energy content of the syngas exiting the biomass gasifier.

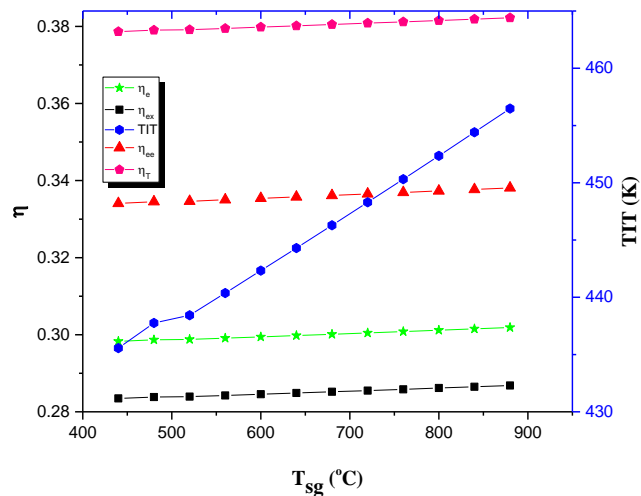


Figure 5.5 Impact of gasifier syngas temperature on the system performance

Therefore, when the syngas temperature increase, the upsurge in the TIT indicates the rise in the sensible heat of the syngas consumed for preheating the compressed air leaving the AC. For a constant syngas and compressor exit temperature, the thermal energy stored by the TES system and hence the TIT depends mainly on the effectiveness of the compression heat exchanger and the RTE of the TEST. Hence, the heat exchanger and TEST are vital equipment to improve the system performance.

5.4.2.3. Influence of the dual fuel engine exhaust temperature

The influence of the dual fuel engine (DFE) exhaust gas temperature (T_{ex}) on the system performance is shown in Figure 5.6.

In dual fuel mode, the exhaust gas temperature (EGT) is typically greater than that of the diesel only mode at the same load (Sombatwong et al., 2013; Diyoke et al., 2014). The EGT of dual fuel compression ignition (CI) engine can fluctuate considerably depending on its load. It can range from a value of about 300 °C at idle to a value of 600°C at full load (Beith, 2011).

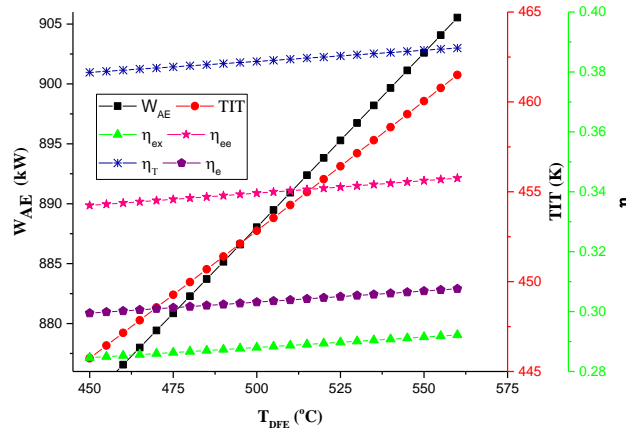


Figure 5.6 Impact of DFE exhaust temperature (T_{ex} , DFE) on the system performance

The allowed final stack temperature determines the extent of the heat content of the exhaust gas that can be recuperated. With 120 °C as the final stack temperature, raising the temperature of the DFE exhaust gas from its base value of 461°C up to 560 °C results to roughly 30% rise in temperature difference obtainable and consequently, accessible energy

for recovery (Diyoke et al., 2018a). The degree of utilisation of the thermal energy obtainable in the higher exhaust gas temperature (EGT) depends on the features of the system. In the range of EGT of 460 – 560°C, it is seen that increase in EGT improves the performance of the system. The TSE, exergy efficiency, electrical efficiency, effective electrical efficiency and TIT increases by approximately 2, 2.4, 2.5, 2.5 and 3.4 % respectively from their base values to 39%, 29.2%, 31%, 35% and 461.5K respectively. The increase is owing to rise in recoverable thermal energy at high EGT which results to rise in TIT observed and therefore power output.

5.4.2.4. Influence of heat exchangers' effectiveness

The impact of the heat exchangers effectiveness (ϵ) on the system performance is depicted in Figure 5.7. As can be seen, as the effectiveness increases, a corresponding increase in the energy, exergy, electrical and effective efficiency of the system is obtained. The impact of heat exchanger effectiveness is more prominent in the total system efficiency compared to the other efficiency indicators. The impact of heat exchanger effectiveness is seen to have negligible impact on the exergy efficiency. As the heat exchanger effectiveness increases from 0.7 to 0.95, the TSE increases by about 8% from 0.38 to 0.41, while the effective electrical efficiency and exergy efficiency increases by about 5 and 1% from 0.34 to 0.34 and 0.285 to 0.288 respectively

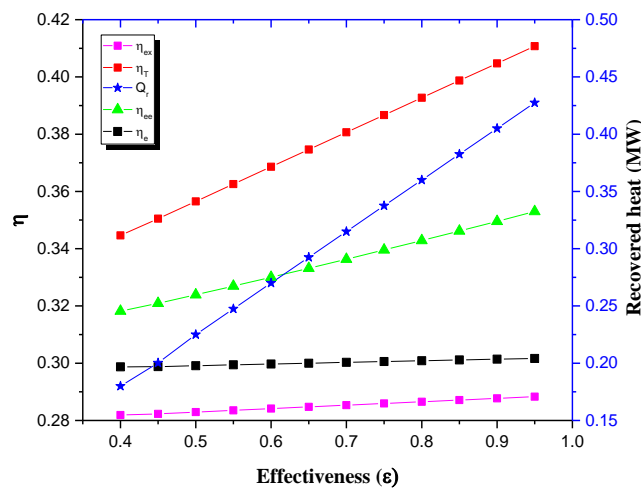


Figure 5.7 Impact of heat exchanger effectiveness on the system performance

The increase in efficiency with increasing effectiveness is due to increase in the quantity of recovered heat from the cooling water jacket with increasing effectiveness as shown in the figure.

5.4.2.5. Influence of DFE syngas fraction

The fraction of syngas used to substitute diesel in the DFE called the syngas fraction (sf) affects the performance of the DFE and hence the overall system. For the rated 300 kW_e in the DFE, the thermal energy input by the syngas (sg) and diesel fuel (df) in different syngas fraction is depicted in Figure 5.8. As can be observed from the figure, the syngas thermal power input (P_{sg}) is inversely related with the diesel fuel thermal power input (P_{df}).

At the lowest sf, the diesel fuel thermal power input is highest. However, as the sf increases, the quantity of syngas in the fuel mixture rises whereas that for diesel drops to maintain the power output constant. It can be seen from the figure that the energy exergy, and effective electrical efficiencies reduces with rising syngas fraction. This is because of the lower calorific value of the syngas when compared to that of diesel, which consequently results to overall lower calorific value of the fuel mixture at higher sf fraction.

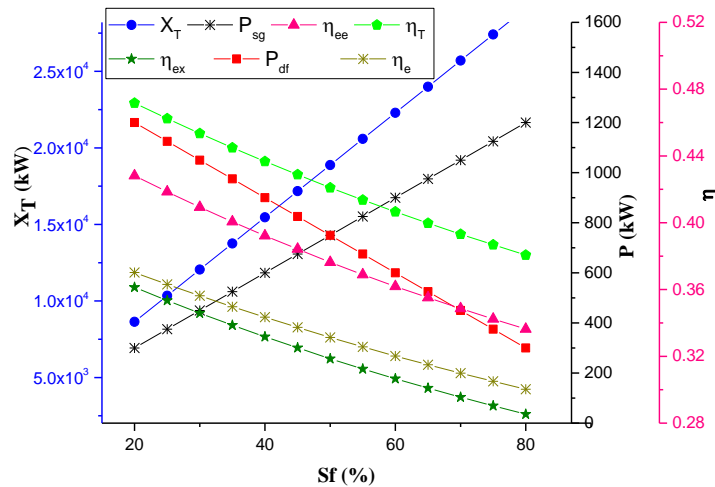


Figure 5.8 Impact of DFE syngas fraction on the system performance

The lower calorific value of the fuel mixture thus leads to reduced efficiency of conversion of fuel to electricity in the dual fuel mode. In turn, the reduced efficiency results

to increased syngas consumption at high sf fraction than that at high diesel fuel fraction (Sombatwong et al., 2013). It can be seen that the relative influence of the variation of sf on the system performance is substantial.

As the syngas fraction reduces from 80 to 20%, the total system efficiency increases from 0.38 to 0.47. Also, electrical efficiency, the effective electrical efficiency and system exergy efficiency are seen to increase from 0.30 to 0.37, 0.34 to 0.43, and from 0.29 to 0.36 respectively. In contrast, the total exergy destruction of the system reduces by about 240% with decrease in sf from 80-20%. This could be explained as due to the reduced exergy efficiency observed. Also, the decrease in losses in the DFE resulting from less syngas thermal energy supply to the DFE to keep the power output constant may contribute to the observed reduction in exergy destruction with decreasing syngas fraction (Sombatwong et al., 2013).

5.4.2.6. Impact of minimum operating pressure of the air store

The air exiting the AS is throttled down to the minimum operating pressure of the air store (AS) prior to entering the air expander (AE). The influence of the minimum pressure of the AS on the performance of the system is shown in Figure 5.9

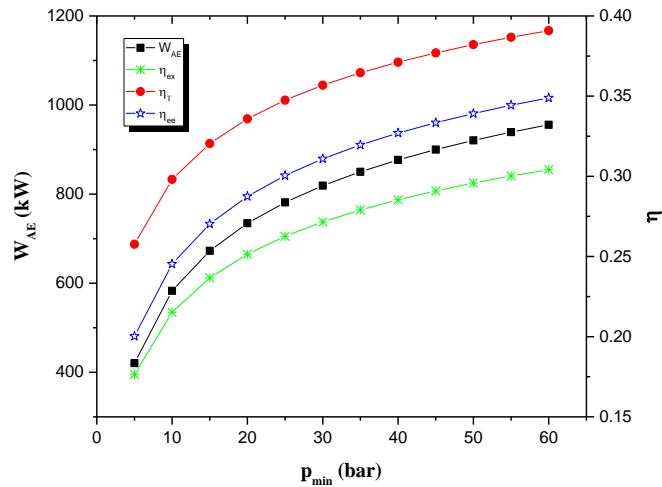


Figure 5.9 Impact of air store minimum pressure on the system performance

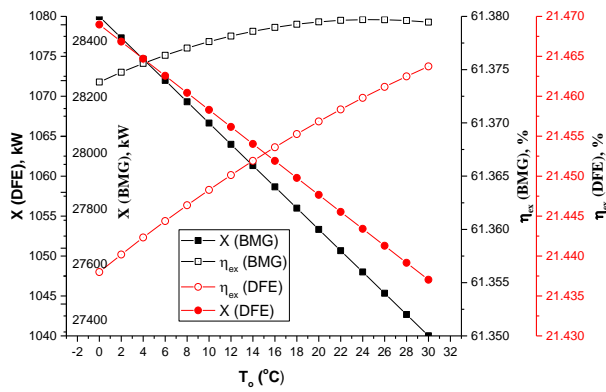
According to this figure, it can be observed that as the minimum pressure of the air store increases from 40 to 60 bar, the air expander power output increase from 876.8 to

955.8 kW. The reason for this increase is because of the increase in the overall pressure ratio of the air expander and a consequent increase in work output. In addition, the, exergy efficiency, TSE, electrical efficiency and the effective electrical efficiency of the system is seen to increase from 0.29 to 0.30, 0.38 to 0.40, .30 to 0.32 and from 0.33 to 0.36 respectively. In contrast, the heating output remains constant since pressure ratio of AE does not affect heat recovery in the DFE.

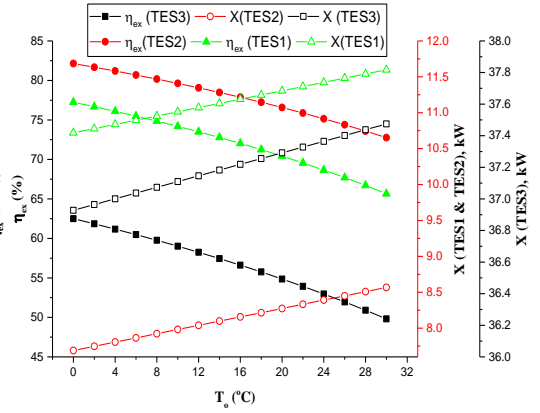
5.4.2.7: Impact of reference temperature

Figure 5.10 (a- e) shows the the exergy destruction rate of some main componenets of the system as the reference enviromental temperature (T_o) varies from 0 to 30 °C. It is seen from Figure 5.10 (a-e) that the rate of exergy destruction in all the unit operations of the system increase with increase in the reference temperature except in HX2, BMG and DFE where the exergy destruction rate reduces with T_o . In contrast, the exergy efficiency of the componenets are inversely correlated with their corresponding exergy desruction rates. From Figure 5.10 (a), observe that the exergy destruction of the BMG and the DFE varies from 28429.2 to 27286.3 and from 1078.9 to 1047.0 kW respectively as T_o caries from 0 to 30 °C. Their corresponding exergy effeiciency varies negligibly from 61.3 to 61.4 and from 21.4 to 21.5% over the same range of T_o . Referring to Figure 5.10 (b), the exergy destruction rate of the thermal energy storage tanks (TES 1-3) increase from 10.7 to 11.5, 7.7 to 8.6 and from 36.9 to 37.5 kW for TES1, TES2 and TES3 respectively. On the other hand, their exergy efficiency reduces from 77.2 to 65.7, 82.1 to 72.8 and from 62.5 to 49.8% respectively. In addition, with reference to Figure 5.10 (c), it is seen that the exergy desctruction rates of HX2 decrease with increasing T_o while that for HX3 increase with increasing T_o . The reason for reduction of exergy destruction rate in HX2 could be due to the low temperature of the cold fluid, which is almost at ambient. As T_o vary over the range analysed, the exergy destruction rate of HX2 changes significantly (about 70%) in comparison with other HXs. Thus more care should be applied in the selection and design of this component.

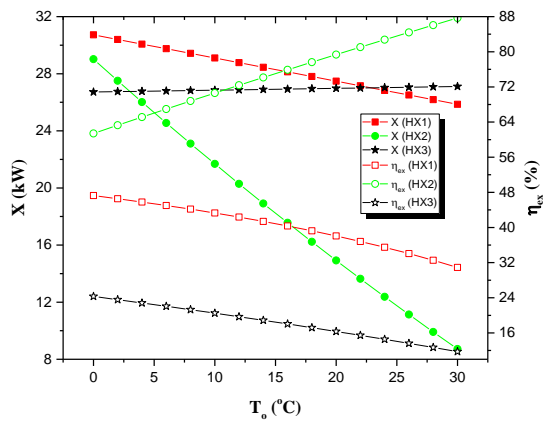
Referring to Figure 5.10 (e),It can be seen that the exergy destruction rate of the AC and AE increases from 98.1 to 107.2 and 132.1 to 143.2 kW respectively as T_o increases from 0 to 30 °C which gives rise to lower exergy efficiency at high T_o .



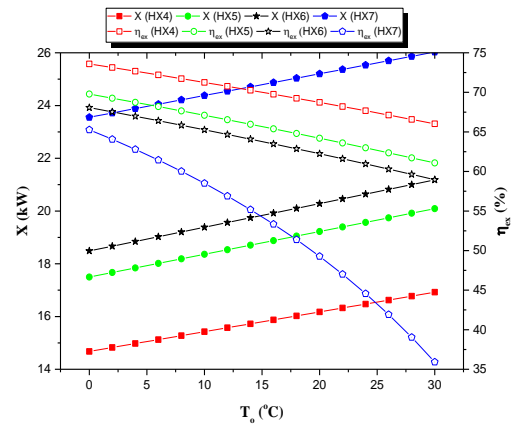
(a)



(b)



(c)



(d)

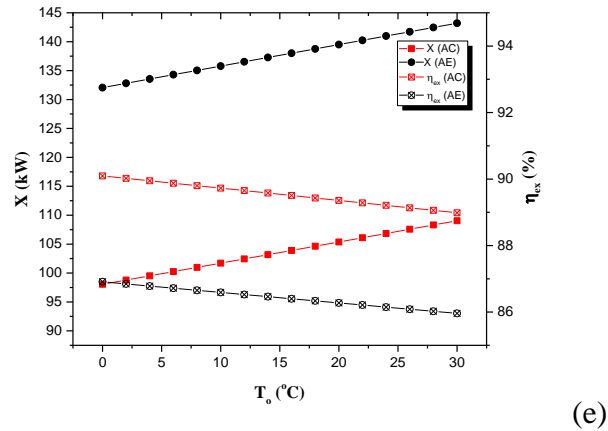


Figure 5.10 Impact of reference temperature on Exergy destruction and exergy efficiency

5.5 Conclusions

A new hybrid renewable energy power generation system utilising excess wind electricity and biomass energy has been proposed and developed in this chapter. Thermodynamic investigation of the system and its unit operations was carried out in order to determine the performance of the overall system and the magnitude of the losses and efficiency of each component. Sensitivity analysis of the influence of variation of key system parameters on the overall performance of the system was investigated. The following conclusion is drawn:

- The integrated system has been demonstrated to use both wind and biomass gasification resources to generate dispatchable power and hot water for domestic use
- The system requires an excess wind turbine electrical capacity of 1 MW, about 353.36 kg/h of biomass on wet basis and 25.18 kg hr^{-1} of diesel fuel to deliver total power output of $2.19 \text{ MWh year}^{-1}$
- The total energy and exergy efficiency of the system is about 38% and 29% respectively. The electrical and effective electrical efficiency, are 30 and 34% respectively.

- The exergy destruction of the hybrid system components is highest in the biomass gasifier followed by the DFE and the AE in that order. The least exergy destruction occurs in the HAD.
- The exergy efficiency of the sub-system components are calculated as 61.38, 21.47, 5.76, 89.17 and 86.12% for the BMG, DFE, HAD, AC and AE, respectively. In addition, the exergy efficiency of the thermal energy storage tanks is determined as 52.47, 74.78 and 68.18% for TES1, TES2 and TES3 respectively.
- Reduction in the syngas fraction by about 10% increases the biomass consumption by over 12.5%, increases the exergy destruction by about 11.8% and reduces the overall energy and exergy efficiency by 2 and 3.6%, respectively.
- Although, the system has a benefit of outputting dual stream of energy (heat for domestic use and electricity) with efficiency comparable to that of a standalone A-CAES, based on EU criterion for a system to qualify as a high efficient cogeneration system, the system cannot be used as a CHP plant since its primary energy saving ratio is not more than 10%.
- The total system efficiency of the integrated system is also found to be less than the efficiency of a standalone A-CAES system but comparable to the efficiency of similar hybrid configurations. Moreover, the RTE of the A-CAES component of the system is higher than that of a conventional A-CAES system

Chapter 6

Economic Analysis of the Integrated System

6.1 Introduction

Investment in any new power plant or machinery is driven largely by economic benefits and so investment in the proposed and analysed A-CAES+BMGES system will depend not only on its thermodynamic performance, but also on its economic performance. In this chapter, the economic analysis of the A-CAES+BMGES system for electricity generation is implemented to determine the economic performance of the system and the potential profitability of developing such a facility for supplying electricity and low temperature hot water for domestic applications in the UK Humber region by an investor, given the customer's demand for heat and electricity.

An economic analysis technique based on Cost of Electricity (COE) and Net Present Value method, is presented to enable a preliminary assessment of the likelihood of the cogeneration system being attractive for meeting customer energy needs.

In order to carry out a realistic evaluation of the cogeneration plant, a sensitivity analysis is implemented to carry out the impact of the technical factors discussed in the

previous chapter and major cost components on the economic performance of the system. The energy demand data use are presented at the end of the section. The economic modelling had been done with a simulation program written in Matlab computer code.

6.2 Economic modelling

A comprehensive economic analysis comprises of the following three steps (Kreith & Raton, 2000):

- Estimation of the requisite total capital investment for the system under consideration.
- Determination of the economic, financial, operating, and market-associated factors for the detailed cost calculation.
- Calculation of the costs of all produced outputs by the system.

These steps are now discussed in turn.

6.2.1 Component cost estimation

The total investment cost of component (x) is made up two cost factors (Kreith & Raton, 2000):

- Final installed cost or direct capital cost (c_x): The purchased equipment costs (c_x) and other costs (c_o) associated with equipment installation, piping, instrumentation, controls, electrical equipment
- Indirect costs (c_x^i): cost of materials, land, civil structural and architectural work, and service facilities

The total capital cost (c_x^T) is the sum of the final installed cost (c_x) and indirect costs (c_x^i) as follows:

$$c_x^T = c_x + c_o + c_x^i \quad (6.1)$$

The indirect costs (c_x^i) are costs that do not become a constant part of the equipment life but are a requirement for the organised completion of the project. Such costs include costs associated with engineering, supervision, and construction, contingencies (Kreith & Raton, 2000). The component other costs (c_o) are costs related with equipment installation,

pipng, instrumentation, controls, electrical equipment, supervision, and contingencies.(Diyoke et al., 2018a). These costs, and other expenses that cannot be estimated directly are considered as a fraction (z) of the purchased equipment costs. Thus:

$$c_o + c_x^i = zc_x^d \quad (6.2)$$

The purchased equipment costs can be estimated by means of quotations from experienced professional cost estimators and vendors'. It can also be estimated using extensive cost databases, or estimation harts (Kreith & Raton, 2000).

It is crucial that, the estimated cost of the purchased equipment be adjusted for size (using scaling exponents) and for time (using cost indices or inflation rates) (Kreith & Raton, 2000). The various estimating methods include: reverse engineering methods, cost curve methods, factored estimation method and step count method (Towler & Sinnott, 2013).

The cost correlation used for estimating purchased equipment cost for heat exchangers (HXs) is as follows (Towler & Sinnott, 2013; Diyoke et al., 2018a):

$$c_{HX} = (2800 + 54A_{HX}^{1.2}) \times cf_{\$-\pounds} \times (1 + e)^{CY-BY} \quad (\pounds) \quad (6.3)$$

Where $cf_{\$-\pounds}$ is conversion factor for dolar to pounds; BY is base year and CY is currency year. Cost escalation factor (e) also called inflation rate, is used in the model to account for the increase in cost of components and services over time (Diyoke et al., 2018a). Obviously, these cost factors are all subjected to strong uncertainties; consequently, in the present study all item costs were escalated from their base year to 2017 currency year using inflation rate (e) (Diyoke et al., 2018a).

The capital cost of the A-CAES sub system of the A-CAES+BMGES is made up of cost of air compressors, thermal energy storage tank, air expanders and air store as follows:

$$c_{CAES} = c_{AC} + c_{TEST} + c_{AE} + c_{AS} \quad (\pounds) \quad (6.4)$$

The Capital cost of the thermal energy storage tanks (c_{TEST}) in \pounds comprises the capital cost of the cylindrical steel tanks, the PCM filling it and insulation used as follows (Nithyanandam & Pitchumani, 2014):

$$c_{TEST} = (V_{steel-TEST})\rho_{steel} \times c_{steel} + M_{PCM} \times c_{PCM} + A_{insu} \times c_{insu} \quad (6.5)$$

The method and equation deployed to estimate the dimensions of the TEST (H_{TEST} , D_{TEST}) and the corresponding mass of PCM (M_{PCM}) to fill it has been set out in chapter three. Using the dimensions of the TEST, the volume of steel with thickness (x) used in fabricating the TEST is estimated using the following relation:

$$V_{\text{steel-TEST}} = \pi H_{\text{TEST}} \rho_{\text{steel}} [(R_{\text{TEST}} + x)^2 - R_{\text{TEST}}^2] \quad (\text{m}^3) \quad (6.6)$$

A thickness of insulation of 0.038m and steel density of 7900 kgm^{-3} was used (Nithyanandam & Pitchumani, 2014). The cost of stainless steel (c_{steel}) is obtained as £3.18 per kg from Kelly and Kearney (2006).

The capital cost of air expanders (c_{AE}) and air compressors (c_{AC}) in (£) is estimated from their rated capacities using their specific capital costs as in the following equations (Zafirakis & Kaldellis, 2009) :

$$c_{AC} = (400 \times cf_{\text{€-£}}) W_{AC} \times (1 + e)^{CY-BY} \quad (\text{£}) \quad (6.7)$$

$$c_{AE} = (400 \times cf_{\text{€-£}}) W_{AE} \times (1 + e)^{CY-BY} \quad (\text{£}) \quad (6.8)$$

The Capital cost of the air storage vessel (c_{AS}) is calculated from the volume of the air store (V_{AS}) as follows:

$$c_{AS} = V_{AS} \rho_{\text{steel}} \times c_{\text{steel}} \quad (\text{£}) \quad (6.9)$$

The capital cost of the biomass gasification power generation system (c_{BGPS}) is made up of the cost of gasifier and feed stock handling system (c_G), the power generation/interconnection system (c_{DFE}), the cost of the hot air dryer (c_{HAD}) and the cost of syngas cleaning system (c_{CS}):

$$c_{BGPS} = c_G + c_{DFE} + c_{HAD} + c_{CS} \quad (\text{£}) \quad (6.10)$$

According to the international energy agency (IEA) (IEA, 2007), the specific capital cost of biomass gasifier attached with an internal combustion engine electric generator set ($c_G + c_{DFE}$) for electricity generation and CHP lie in the range of 3000 to 4000 ($\text{\$kW}_e^{-1}$) in year 2007. Over the years, the cost of biomass gasification power system has declined due to technology learning and increased interest in the technology of biomass gasification. Hence, the lower $c_G + c_{DFE}$ value of $3000 \text{ \$kW}_e^{-1}$ was selected for use in the model and then increased by 5% for contingencies and BOP.

The capital cost of HAD (c_{HAD}) and the syngas cleaning system (c_{cs}) consisting of cyclone and scrubber was estimated by means of the factored estimation method using the “six-tenths rule” (Towler & Sinnott, 2013) . In this method, the capital cost (c_A) of any given plant with capacity (\dot{m}_A) is obtained from a known or reference plant with capacity (\dot{m}_{ref}) and cost (c_{ref}) using the following equation (Towler & Sinnott, 2013):

$$c_A = cf_{\$_{-\pounds}} \times \left(\frac{\dot{m}_A}{\dot{m}_{ref}} \right)^\phi \times c_{ref} \times (1 + e)^{CY-BY} \quad (\pounds) \quad (6.11)$$

Where ϕ is a scaling factor. The scaling factor method requires no design information other than the production rate. The reference cost factors used in the computation is contained in Table 6.1. The scaling factor (ϕ) varies from 0.8 to 0.4 depending on the type of process equipment involved. In the thesis, an average scaling factor (ϕ) value of 0.6 across the whole chemical industry has been used (Towler & Sinnott, 2013).

Finally, capital cost of the hot water tank (c_{HWT}) for storing domestic hot water recovered from the DFE jacket water was estimated as follows

$$c_{HWT} = v_{HWT} \times c_{sc} \times (1 + e)^{CY-BY} \quad (\pounds) \quad (6.12)$$

Where c_{sc} is the cost per unit volume of storage tank ($\pounds m^{-3}$) and v_{HWT} is the volume of the hot water tank (m^3) estimated from the total daily hot water production from the DFE as follows:

$$V_{HWT} = \frac{\dot{m}_w \times t_{dch}}{\rho_w} \times SF \quad (6.13)$$

Where \dot{m}_w is the mass flow rate of hot domestic water recovered in the DFE cooling jacket water (kgs^{-1}) and SF is safety factor of 1.2 adopted to accommodate error of under sizing of the hot water storage tank (HWT). The cost per unit volume of storage tank (c_{sc}) vary widely depending on its volume, quality and its capabilities. In the thesis, a modest low cost value of 925 ($\pounds m^{-3}$) has been used (BEIS, 2016).

Table 6.1 Reference costs of equipment with their maximum size

Unit	Reference capacity	Reference cost (\$)	Currency year	Reference
HAD	500 kg/h	19,891	2010	(Gebreegziabher et al., 2013)

Cyclone	9 m ³ gas/s	1.36 × 10 ⁶	2002	(Rafati et al., 2017)
Scrubber	9 m ³ gas/s	4.56 × 10 ⁶	2002	(Rafati et al., 2017)

6.2.2 Economic evaluation methodology

Numerous economic measures or approaches exist for performing economic analysis of electricity generation /cogeneration systems. Commonly used approaches comprise the simple payback period, internal rate of return method, net present value (NPV) and cost of electricity (COE) (Ujam & Diyoke, 2013) method. The NPV and COE method was applied in this research work to evaluate the proposed integrated system economic performance,

The COE is the minimum price at which energy must be sold for an energy project to break even. It involves calculating all the costs over the useful lifetime of the plant: initial investment, operating and maintenance (O&M), cost of fuel and cost of capital. To estimate the COE, first an estimate of the total life cycle cost (TLCC) for the A-CAES+BMGES system is carried out as follows (Short et al., 1995; Diyoke et al., 2018a):

$$TLCC = [TIC - Tax \times (c_D)_{PV} + (1 - Tax) \times \{(c_{O\&M})_{PV} + (c_{En})_{PV}\}] \quad (\text{£}) \quad (6.14)$$

The total investment cost (£) of the A-CAES+BMGES system (TIC) is the sum of the total capital Cost (c_x^T) of the various unit operations that constitute the system as follows:

$$TIC = \sum_i c_x + c_o + c_x^i \quad (\text{£}) \quad (6.15)$$

All component cost (c_x) estimated above are final installed costs, which include the balance of plant (BOP) costs (such as electrical connections, piping, insulation instrumentation and controls. To reiterate, the remaining direct costs (c_o) and indirect costs (c_x^i) such as costs related to engineering, supervision, and construction, and contingencies cannot be estimated directly. In the thesis, they are calculated as 5% of the purchased equipment costs. i. e ($c_o + c_x^i = 0.5c_x$).

Different variants of the expression for calculating TLCC above can be obtained depending on the nature of investment. For a non-profit organisation, governmental sector, or the owner-occupant residential sector, tax rate (T) is set equal to zero in equation 6.14.

For a private investor, income taxes are an applicable cost and equation 6.14 applies. If the investor is a utility investing for profit, the before-tax revenues needed to cover the after-tax costs may be wanted. Thus, this can easily be obtained by dividing equation 6.14 by the value of $(1 - T)$ (Short et al., 1995).

The annual cost of operation and maintenance costs ($c_{O\&M}$) denote the costs incurred in operating and maintaining the plant annually throughout its useful life (Diyoke et al., 2014). It comprises of the fixed (FC) and variable (VC) O&M cost thus:

$$c_{O\&M} = FC \times \text{yr.} + VC \times \text{kWh}_{\text{yr.}} \quad (\pounds) \quad (6.16)$$

Variable operating costs (VC) are linearly related to the quantity of kilowatt-hours of electricity generated and are referred to as incremental costs. VC can be expressed in \pounds per kWh. Fixed operating costs (FC) are fundamentally not dependent of the quantity of kilowatt-hours of electricity produced. It can be expressed in \pounds per year or \pounds per hours. However, it is sometimes very difficult to accurately separate the VC and FC as some cost items can have both, fixed and variable components.

The operation and maintenance cost ($c_{O\&M}$) can also be expressed as a fraction of the total investment cost (TIC) (Diyoke et al., 2014; IEA, 2015). In the thesis, the O&M cost ($c_{O\&M}$) is projected as 5% of the TIC (IEA, 2015).

The A-CAES+BMGES system have three fuel inputs: excess wind electricity, biomass and diesel fuel.

The total yearly cost of fuel ($c_{En,i}$) is estimated as the sum of the cost of biomass ($c_{w,B}$), diesel (c_{df}) and excess wind energy cost ($c_{r,e}$) used by the A-CAES+BMGES system as in the following equation:

$$c_{En,i} = \text{hrs}_{\text{yr}} \times \{(\dot{Q}_{df} \times c_{df} + \dot{m}_B \times c_{w,B}) + W_{WT} \times c_{r,e}\} \quad (\pounds) \quad (6.17)$$

Where \dot{Q}_{df} is the volume flow rate of the diesel fuel fed to the DFE (m^3s^{-1}).

The cost of wet biomass feed ($c_{w,B}$) in \pounds at any moisture content (MC) for industry was estimated from a line fitted from data obtained from the report ‘‘AEBIOM-wood fuels handbook’’ (Francescato et al., 2009) as follows:

$$c_{w,B} = -0.0129\text{MC}^2 - 0.0673\text{MC} + 83.925 \quad (\pounds) \quad (6.18)$$

The COE was estimated using the following equation (Short et al., 1995):

$$\text{COE} = \frac{\text{TLCC}}{\text{AEO}} \times \text{UCRF} \quad (6.19)$$

Where AEO is the annual energy output and UCRF is the ultimate capital recovery factor (UCRF) calculated as follows:

$$\text{UCRF} = \frac{d_r(1 + d_r)^n}{(1 + d_r)^n - 1} \quad (6.20)$$

Economic measures of investment projects can be expressed in the “constant” dollars or “current” dollars. Current dollar analysis report incomes in the year in which it is received/incurred without adjustment to inflation. In other words, it reports the actual cash flows observed in the marketplace whereas in “constant or real dollar” analysis, cash flows are adjusted for inflation (e). In other words, “constant dollar” cash flows represent the income that would have been required if the cost was paid in the base year. In the thesis, the constant dollar analysis is used. It pertinent to state that it does not matter which analysis method is used. What is required is to remains consistent throughout the study and to state the analysis method used and once that is done, one analysis method can be converted to the other and vice versa.

Cash flows stated in current dollars in year m (CF_m) can be converted to constant dollar cash flows in any year n (CF_n) by removing the effect of inflation (e) as follows(Short et al., 1995):

$$CF_n = \frac{CF_m}{(1 + e)^{m-n}} \quad (6.21)$$

The above formula applies when the rate of inflation (e) during the m-n year is assumed to be constant. In current dollar analysis, the nominal discount rate (r) is used, whereas in a constant dollar analysis, the use of a real discount rate (d_r) is required. The real discount (d_r) rate is estimated from the nominal discount rate (r) by means of the following equation (Short et al., 1995):

$$d_r = [(1 + r)/(1 + e)] - 1 \quad (6.22)$$

In addition, in the constant dollar analysis, it is compulsory to convert cash flows for depreciation from current to constant dollars using the inflation rate (e). Accordingly,

the transformation from current depreciation (D) to constant depreciation (D_r) was realized as follows (Short et al., 1995):

$$D_r(n) = D(n) \times (1 - e)^n \quad (6.23)$$

The straight-line method has been applied to calculate the current annual depreciation (D) because it is widely used and is simple to calculate.

The formula for calculating annual depreciation (D) using the straight line method is as shown below:

$$D = \frac{TIC - SV}{n} \quad (6.24)$$

Salvage value (SV), also called residual value or scrap value is the probable selling price of A-CAES+BMGES system at the end of its useful life of n years.

Sometimes, the annual revenues (AR) that must be realised in each of the n-years of the investment duration to recover all costs, including taxes is required by investors for planning and decision making. This can be obtained by annualising the TLCC as follows;

$$AR = TLCC \times UCRF \quad (6.25)$$

To compute the TLCC, the present value (PV) of the operation and maintenance cost ($c_{O\&M}$), fuel energy cost (c_{En}) and depreciation (c_D) is required. These are obtained by multiplying the respective energy cost, with the present value factor (PVF) as follows:

$$PV(i) = \sum_{n=1}^n \frac{i_n}{(1 + d_r)^n} \quad \dots i = \{c_{O\&M}, c_D, c_{En}\} \quad (6.26)$$

The net present value (NPV) which represents the present value of all the expenditures and incomes over the duration of the useful life of the A-CAES+BMGES system was assessed by means of the following equation (Short et al., 1995; Diyoke et al., 2014; Diyoke et al., 2018a):

$$NPV = -TIC + \sum_1^n \frac{(1 - Tax) \times (R - c_{O\&M} - c_{En,i}) + Tax \times (D_d)}{(1 + d_r)^n} \quad (6.27)$$

Where R is the income made by selling heat (R_h) and electricity (R_e) produced by the A-CAES+BMGES system. R was projected using the following expressions:

$$R = R_e + R_h \quad (6.28)$$

$$R_e = \text{Days}_{\text{yr}} \times \left[\sum_1^{t_{\text{dch}}} \text{ed}_{\text{hr}} \times c_{\text{ect}} + \sum_1^{t_{\text{dch}}} \text{ee}_{\text{hr}} \times c_{\text{est}} - \sum_1^{t_{\text{dch}}} \text{de}_{\text{hr}} \times c_{\text{ebt}} \right] \quad (6.29)$$

$$R_h = \text{Days}_{\text{yr}} \times \left[\sum_1^{t_{\text{dch}}} \text{hd}_{\text{hr}} \times h_{\text{hct}} + \sum_1^{t_{\text{dch}}} \text{eh}_{\text{hr}} \times c_{\text{hst}} - \sum_1^{t_{\text{dch}}} \text{dh}_{\text{hr}} \times c_{\text{hbt}} \right] \quad (6.30)$$

6.2.3 Electricity/heat buy and sell tariffs

The buying/selling price of wind turbine excess electricity/generated electricity by the system has an influence in the economic performance of the system. During the charging mode, the excess wind electricity price ($c_{r,e}$) was taken to be £42 per MWh, the average UK off-peak spot price in 2017 (Ofgem, 2017). During discharging (selling), the electricity consumer tariff/price (c_{ect}) is presumed to be £0.14 per kWh, the national mean price per kWh for electricity in the UK (The Eco Experts, 2017). The electricity buy back tariff (c_{ebt}) and the electricity sell back tariff (c_{est}) was presumed as £43 per MWh, the mean wholesale electricity price in the UK by year 2017 (Business Electricity Prices, 2017). Table 6.2 shows the characteristic values for the key cost parameters of the A-CAES+BMGES system. All results have been reported in the 2017 constant dollar year.

Table 6.2 Main cost parameters of the integrated system.

Parameter, symbol (unit)	value	Ref
Diesel fuel cost, c_{df} (£litre ⁻¹)	1.15	(E4tech, 2010)
Inflation rate, e (%)	3	
rejected wind electricity cost, $c_{r,e}$ (£kWh ⁻¹)	0.042	
Electricity consumer tariff, c_{ect} (£kWh ⁻¹)	0.14	
Electricity sell to grid tariff, c_{est} (£kWh ⁻¹)	0.042	
Electricity buy back tariff, c_{ebt} (£kWh ⁻¹)	0.042	
Heat consumer tariff, c_{hct} (£kWh ⁻¹)	0.10	(DECC, 2015a)
Heat sell back tariff, c_{hst} (£kWh ⁻¹)	0.10	(DECC, 2015a)
Heat buy back tariff, c_{hbt} (£)	0.10	(DECC, 2015a)

Insulation cost, c_{ins} ($\text{\$m}^{-2}$)	235	(Kelly & Kearney, 2006)
Nominal Discount rate, d (%)	10	(IEA, 2015)
Charging time (Discharging time) (h)	8(6)	
Annual operating days	310	
Economic life, n yrs.	20	
Tax rate, T (%)	34	(Short et al., 1995)

6.3 Demand profiles

To simulate the A-CAES+BMGES system's economic performance for the presumed 1600 households in the Humber region, UK, the profiles of heat and electricity demand for the households in the Humber region was generated as shown in Figure 6.1. The profile of the electricity demand was gotten from the data of half-hourly daily mean electrical energy consumption in kWh for the period 01/05/2011 to 31/05/2012 for 5554 homes from the UK Northern power grid region (Wardle & Davison, 2012).

The data was manipulated to give mean hourly data based on the daily average electricity use of 4115 kWh per household obtained from a DECC report (DECC, 2015b). The heat demand profiles were gotten from a real hourly average data for a 100 home community housing development in the UK, gotten from a published research work by Wood (Wood & Rowley, 2011). The data was manipulated to give electricity to heat ratio equal to the national average for UK social housing of 0.28 (Wood & Rowley, 2011; Diyoke et al., 2018a).

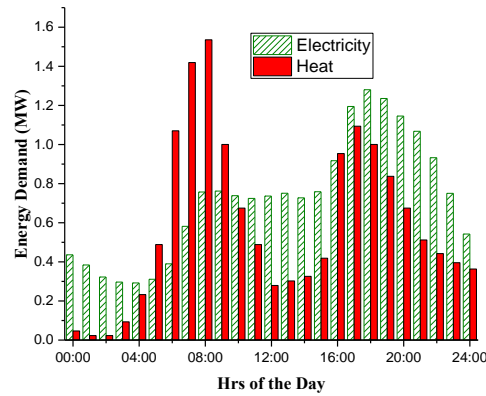


Figure 6.1 Daily hourly electrical and thermal demand profiles for North Humberstone
(Diyoke et al., 2018a)

6.4 Results

Table 6.3 shows the important economic results for the system. In the table, the TIC of the A-CAES+BMGES system is estimated as £2,370,665 representing a minimum A-CAES+BMGES system specific cost of about £2,025. The estimated COE and TLCC for the system is £0.19 per kWh and £4,417,167 respectively.

The total CAPEX value for thermal energy storage in the A-CAES+BMGES is estimated as £72.82 per kWh comprising of £26.49 per kWh for TES₁, £27.29 per kWh for TES₂ and £19.14 per kWh TES₃ respectively. The estimated cost of TES values is within the range of £8.70-43.59 per kWh (€10-50 per kWh) reported as costs of latent heat storage systems based on PCMs (IRENA 2013). It can be observed that the specific cost of TES₁ and TES₂ (£kWh⁻¹) are more than that of TES₃ by over 40%. This is because, more heat is stored in TEST₃ owing to higher HTF temperature entering it when compared with TEST₁ and TEST₂.

Table 6.3 Economic performance results for the integrated system

Parameter, (unit)	Value
TIC, (£)	2,370,665
NPV, (£)	-2,132,960
TLCC, (£)	4,417,167

COE, (£kWh^{-1})	0.19
Specific investment cost, A-CAES+BMGES(£kW_e^{-1})	2,025
Specific cost, TEST (£kWth^{-1}):	
TES ₁	26.49
TES ₂	27.29
TES ₃	19.04
Shares of Components in TIC (£):	
C _{AC}	365,904.00
C _{AE}	321,818.26
C _{HAD}	19,554.26
C _{BMG+DFE}	680,400.00
C _{TES}	114,383.21
C _{HX}	45,642.21
C _{AS}	613,052.80
C _{CS}	149,650.46
C _{HWT}	60,259.79

In addition, the cold PCM temperature in TEST₂ is higher than in TEST₃ since the temperature of the compressed air from the air store entering TEST₃ is at ambient. In TEST₁ and TEST₂, the cold temperature of the PCMs is set by the minimum TET from the AEs which is higher than ambient temperature.

It is fascinating to assess the shares of cost of the different components of the A-CAES+BMGES system in the TIC as in Table 6.3. The CAES has the highest share of all the components of the system. It accounted for about 59.69% of the TIC consisting of 15.43% for AC, 13.58% for AE, 4.82% for TES and 25.86% for AS. The Biomass gasifier with cleaning system and the DFE has the second highest share of 35.01% with the syngas cleaning system contributing 6.3% .The recuperator accounted for 1.93%.

The NPV for the A-CAES+BMGES system is found to be negative with a value of £2,132,960 indicating the non-profitability of the system in the analysed location. The detailed cost of the various components of the system is contained in Table A2.1 of Appendix 2

6.5 Sensitivity analysis

6.5.1. Impact of cost factors

The economic performance of the A-CAES+BMGES system depends on a number of cost and technical factors. Cost factors include but not limited to the following: the total investment cost (TIC), the discount rate (d), the fuel price, the O&M cost ($c_{O\&M}$), inflation rate (e), and cost of excess electricity (sold and bought). The technical factors have been discussed in chapter five. In this section, their effect on the economic performance of the system will be analysed.

In the cost factors sensitivity, the base case value of each cost factor inputted into the COE calculation is adjusted by multiplying it by a base line cost component multiplier (BCCM) that ranges from a lowest value of 0.3 to maximum value of 1.5 in accord with IEA methodology for energy plants (IEA, 2015). Then a sensitivity plot (SP) of COE for the variation of the base cost factors is illustrated. The greater the slope of the COE plot is with respect to the relative change in the base case cost factor, the greater the effect on the COE and vice versa.

Figure 6.2 displays the results of sensitivity of all the cost factors for the COE.

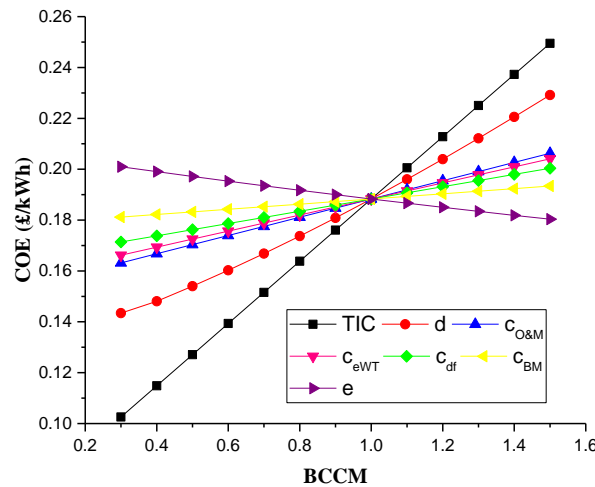


Figure 6.2 Impact of economic factors on COE

It can be seen that among the cost factors, the total investment cost (TIC) has the steepest slope of the cost factors and thus has the highest effect on the COE. This is because TIC remains the main principal element of the system's cost. If the TIC rises from its base line value by a BCCM of 1.3 (30% increase) while all other variables are held constant, the

COE increases to 0.23£kWh^{-1} . This signifies a percentage increase in the COE of about 20%.

Conversely, if the cost factor is reduced at a BCCM of 0.7 (30% reduction), the COE reduces by approximately 20% to $\text{£}0.152$ per kWh which is outside the range of current UK national average price for electricity which is $\text{£}0.141$ per kWh (The Eco Experts, 2017). This moderately high percentage change in COE with variation in the TIC highlights the substantial sensitivity of the COE to variation in the TIC.

After the TIC, the discount rate (d) has the next highest influence on the COE. The COE is seen to increase as the discount rate increases. This is because the discount rate determines the costs of capital. The greater the discount rate, the greater the cost of capital and vice versa. In other words, the rise in COE with increasing discount rate is caused by decreases in present value cost with rising discount rate. As the BCCM varies from a low value of 0.3 ($d=3\%$) to a high value of 1.5 ($d=15\%$), the COE for the discount rate is seen to vary from a low value of about $\text{£}0.14$ per kWh to a high value of about $\text{£}0.23$ per kWh representing about 21.7% increase in COE from the base value.

The other cost parameters do not affect the COE considerably in comparison to the TIC and discount rate. Cost of O&M ($c_{O\&M}$) and excess wind electricity (c_{eWT}) has third and fourth utmost influence on the COE sensitivity. As the BCCM increases from 1 (base value) to 1.5, it is observed that the COE increasing by roughly 9.5% and 8.4% for Cost of O&M ($c_{O\&M}$) and excess wind electricity (c_{eWT}) respectively.

The COE has a minimum sensitivity to the cost of biomass (c_{BM}), which sees only about 2.7% increase in COE as the BCCM is increased from base value of 1 to 1.5.

The inflation rate (e) has the second minimal impact on the COE followed by the cost of diesel (c_{df}). It can be seen from the figure that the inflation rate (e) is in an inverse relationship with the COE. That is, as the inflation rate increases, the COE decreases and vice versa. As the BCCM increases from base value of 1 to 1.5, the COE rises by roughly 6.4% with respect to the cost of diesel fuel (c_{df}).

The corresponding total life cycle cost (TLCC) for the A-CAES+BMGES system under the range of the cost factors accessed in the COE sensitivity above is shown in Figure 6.3. It is seen that the sensitivity of the cost factors to the TLCC also approximately follows

the same order as that in the COE with TIC having the maximum effect on TLCC and the cost of biomass impacting it the least.

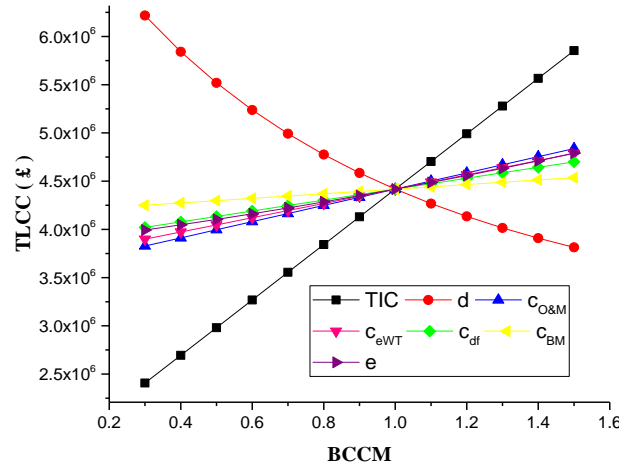


Figure 6.3 Impact of economic factors on TLCC

One would have anticipated the cost of biomass to impact the system COE more since it is one of the fuel used by the system. But, since the system takes advantage of cheap waste heat to dry cheap wet biomass, the cost of biomass apparently does not impact on the COE considerably.

Following similar procedure adopted for the COE sensitivity, the effect of varying the cost factors (TIC, C_{BM} , C_{eWT} , C_{df} , $C_{O\&M}$, C_{BM}) including the selling price for electricity and heat (e_{tariff} , h_{tariff}) on the NPV was investigated.

The NPV is essential because it reveals to the investor what dollar value a project brings while, taking into account the money that has to be spent to realize the project. It is in fact a pointer to how profitable or not the proposed system would be when implemented.

As the BCCM varies from a small value of 0.4 to maximum value of 1.5, the NPV of the system is seen to remain negative. This signifies that the A-CAES+BMGES system is not profitable for electricity and domestic hot water production in the analysed location. Nevertheless, if 70% of TIC is offset for example by means of a subsidy to the investor by the government as one of the ways to encourage RE uptake in the energy mix, the system

become profitable with a positive NPV value of £137,387.2 and COE of £0.10 per kWh at the baseline discount rate.

6.5.2 Impact of technical factors

6.5.2.1 Syngas fraction of the dual fuel engine

As already found from chapter 5, the syngas fraction (sf) of the dual fuel engine (DFE) determines the overall efficiency of electricity production from the DFE and hence influences the economic performance of the whole system. The sf is varied from 20% to 80% as in Figure 6.4.

From the Figure 6.4, it can be observed that, the COE is minimum at the highest sf of 80% and as the sf of the DFE decreases, the diesel fraction (DF) increases to maintain the power output constant. The rise in the diesel fuel consumption results to a corresponding rise in diesel cost (c_{df}). Consequently the effect of rise in diesel fuel cost (c_{df}) at small sf leads to a high COE of about £0.26 per kWh for the system at sf of 20%.

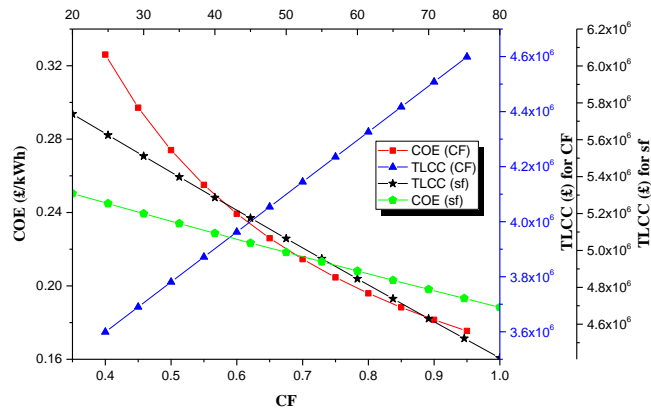


Figure 6.4 Impact of variation of sf and CF on COE and TLCC

This represents a COE increase of about 33% from the base value. It can be seen that, the relative impact of the variation of sf on the COE is substantial for the system. The equivalent TLCC for the system is also depicted in Figure 6.4. Similar to the COE, the TLCC is at its lowest value when the sf is maximum due to the reduced cost of fuel resulting

from less diesel in the fuel mixture. As the sf drops, the diesel fuel consumption and thus the cost of diesel (c_{df}) increase with a resultant increase of the TLCC of the system.

6.5.2.2 Capacity factor

The capacity factor (CF) of the A-CAES+BMGES system also influences the COE. Similar to the sf , the CF is also inversely proportional to the COE, with lower CFs leading to higher COEs and vice versa. This can be observed from Figure 6.4. An increase in the CF of the system leads to the increase in the number of operating hours of the system thus leading to the increase in energy produced by the system. In contrast, as the CF reduces, the annual operating hours of the system reduces resulting in less power generation by the system and hence, increase of the COE of the A-CAES+BMGES system. It can be inferred from Figure 6.4 that the CF has a fairly strong effect on the performance of the integrated system. As the CF increases from 0.85 to 0.95, the COE reduces from £0.1883 to 0.1754 per kWh representing a reduction of approximately 7%. Dissimilarly, as the CF reduces from 0.85 to 0.75, the COE increases by about 9% to £0.2046 per kWh. In the range of CF from 0.4-0.95, the COE is seen to vary from a maximum value of £0.326 per kWh to the lowermost value of £0.175 per kWh.

The corresponding TLCC for the system is seen to display a direct relationship with CF because of the rise in the total operating hours and therefore cost of O&M that results from increasing CF. The TLCC is seen to vary from a lowest value of roughly £3.04 million at CF of 0.4 to the highest value of approximately £4.60 million at CF of 0.95.

6.5.2.3 Round trip efficiency

The round trip efficiency (RTE) of the thermal energy storage system of the A-CAES sub system is another parameter that influences the COE of the system. A-CAES system with a less efficient thermal energy storage (TES) system will produce less electricity than a more efficient storage system. The influence of the RTE of the A-CAES TES system on the COE of the A-CAES+BMGES system is shown in Figure 6.5 over the range of 40 to 95%.

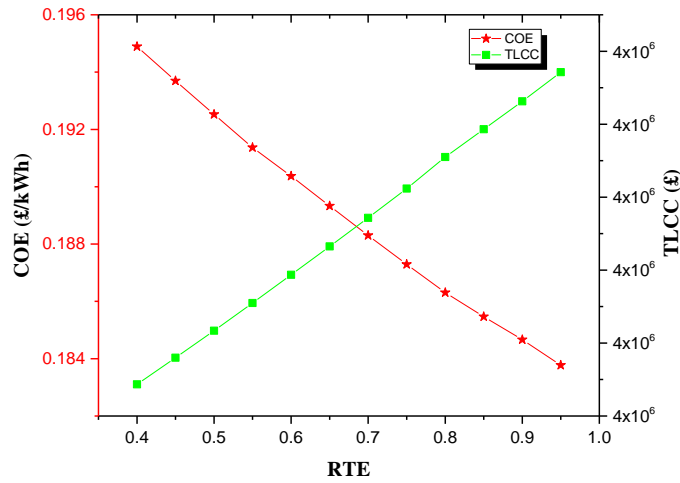


Figure 6.5 Impact of RTE of A-CAEs TEST on COE

It can be observed from Figure 6.5 that the COE for the system is inversely correlated with the RTE. This can be explained thus; as the RTE of the A-CAES TES rises, the power outputted by the A-CAES (P_C) and thus the overall system increases as already depicted in chapter five, resulting to the rise in the total system efficiency (TSE). The improved efficiency and output power of the A-CAES+BMGES at higher RTE consequently results to a reduced COE as in Figure 6.5. As the RTE reduces from the base value of 70 to 40%, the COE is seen to increase by about 4.1% to £0.1973 per kWh.

However as the RTE increases from the base value to 95%, a 2.8% reduction in COE to £0.18 per kWh is seen.

Dissimilar to the COE, the TLCC of the system is seen to be directly correlated with the RTE with higher values of the RTE leading to higher TLCC and vice versa. Over the RTE range of 0.4 to 0.95, the TLCC is seen to vary from a maximum value of £4.44 million to a minimum value of £4.39 million respectively.

6.5.2.4 DFE exhaust gas temperature

The sensitivity of the exhaust gas temperature (EGT) of the DFE to the COE of the A-CAES+BMGES system is shown in Figure 6.6. As the EGT is varied from the starting temperature of the DFE exhaust gas temperature of 361°C (634 K) up to 541 °C (814 K), it is seen that increase in EGT improves the economic performance of the system. The COE

is seen to reduce from £0.1918 to 0.1855 per kWh respectively. The reduction in the COE observed is due to increase in available heat for recovery at high EGT which leads to increase in turbine inlet temperature (TIT) of each stage and thus the TSE as can be seen in Figure 6.6.

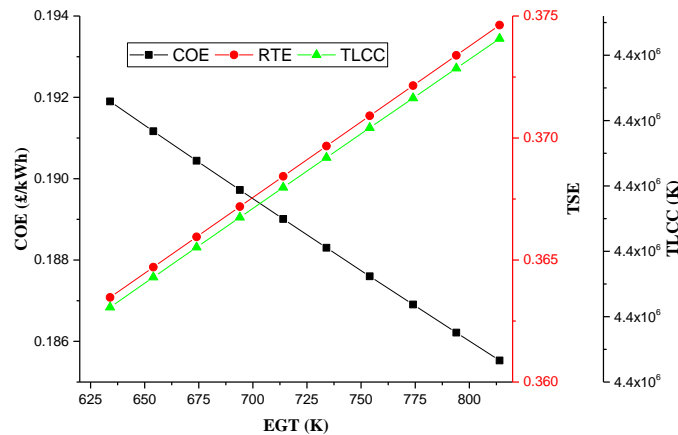


Figure 6.6 Impact of EGT on COE and TLCC

Again, dissimilar to the COE, the TLCC of the system increases with increasing EGT due to increase in capital and cost of O&M resulting from increase in heat exchanger duty as a result of higher EGT.

6.5.2.5 Biomass gasifier syngas temperature

The sensitivity of the temperature of syngas (SGT) exiting the gasifier during the charging mode on the COE of the system is depicted in Figure 6.7.

As predictable, the COE of the system fluctuates inversely with the SGT. As the SGT decreases from the base case value of 973K to 773K, the COE is seen to increase from £0.1883 to 0.1890 per kWh respectively. However, as the SGT increases from the base case value to 1073K, the COE reduces to £0.1879 per kWh. The tendency can be described by the rise in the TSE with SGT. With increase in SGT from the base value to 1073K, the higher TSE reveals the benefit of reheating on efficiency. TES efficiency rises with air re-

heating since the increased turbine inlet temperature (TIT) in the AE stages leads to increased power outputs and hence TSE as can be seen in Figure 6.7 (Diyoke et al., 2018a).

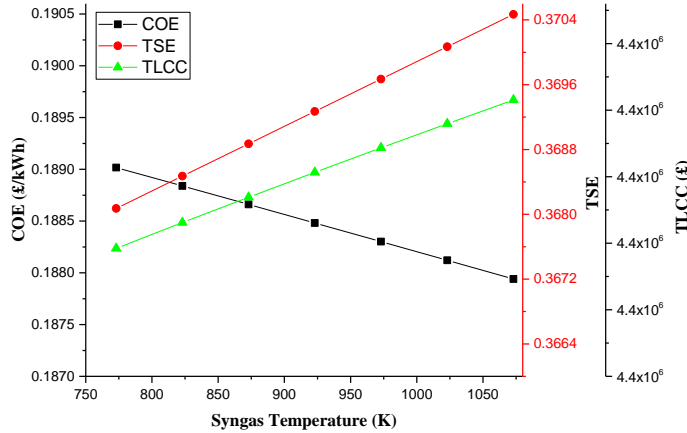


Figure 6.7 Impact of syngas temperature on COE

6.5.2.6 Number of households

The number of households (NOHs) in the study location influences the size of the A-CAES+BMGES system and hence the COE of the system. Figure 6.8 shows the impact of variation of the NOHs in the study location while keeping the other factors of the system constant. As can be seen from the Figure 6.8, the NOHs only affects the NPV of the system. As the NOHs increases, the NPV of the system increases and vice versa. The reason for this trend is because, as the NOHs increases, there is a high tendency for the energy demand of the consumers to be greater than all the power generated by the system. Thus all the power generated by the system will be sold to the consumers at the high consumer tariff of £0.14 per kWh leading to increase in revenue and hence an increase in NPV. However, as the NOHs reduces, there is a high tendency for the system to generate more power than is required by the consumers. Thus the fraction of the power output by the system that is sold back to the grid at a cheaper sell back to the grid tariff of £0.042 per kWh increases leading to the reduction in revenue and thus the NPV of the system reduces. The COE and TLCC of the system does not change with variation in NOHs because, the NOHs variation does not impact on the capacity, output or operating hours of the system, rather NOHs only affects the revenue derived from sale of electricity/heat produced by the system. Thus, for

good economic performance, it is paramount to size the system such that the power it produces at any point in time matches closely to the electricity demand.

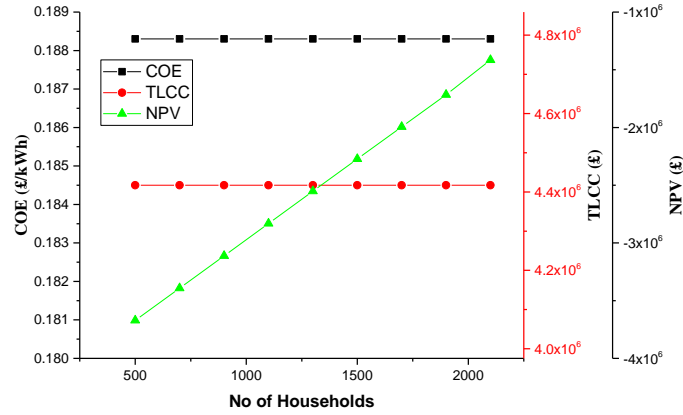


Figure 6.8 Impact of NOHs on COE and NPV

Figure 6.9 shows the percentage variation of the NPV of the system to the variation of the sensitivity factors examined above from their minimum and maximum values. It can be seen clearly that the most significant factors swaying the NPV of the A-CAES+BMGES are TIC, cost of O&M, excess wind electricity cost, electricity tariff, and cost of diesel fuel

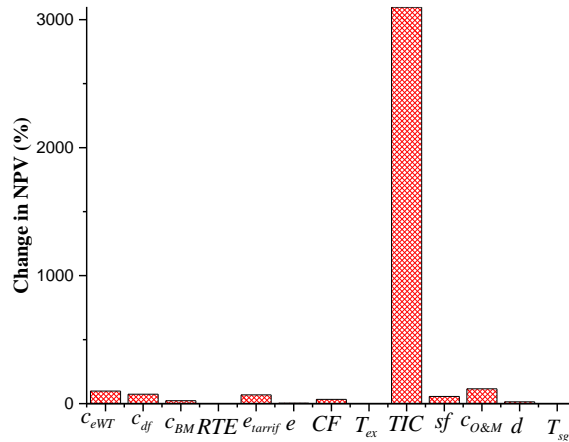


Figure 6.9 Variation of NPV with sensitivity cost parameters

6.6 Limitations of the study

The result of this study must not be considered as descriptive of the whole UK or the world in any way. Heat and electricity demand plus energy prices hinge on a variety of different supply and demand conditions, including the geopolitical location, local climate, the national energy mix, network costs and taxation. Henceforth, the case study using Hull has to only be seen as an illustration of the applicability of the methodology. The methodology can be scaled up to any capacity and used for any locality or nation while factoring in labour costs, fuels and electricity prices. Furthermore, it must be noted that the details of the hybrid system's cost and economics are valid elsewhere. The main differences between the systems would be making sure they meet the standards of the local regulators in the region of interest.

6.7 Conclusions and recommendations

The main conclusions drawn from the result of the economic analysis of the system are summarized as follows:

- The COE of the system which is estimated as £0.19 per kWh is more than the range of the mean electricity tariff for a medium user home in the UK (2,500 to 5,000 kWh a year), including taxes which is £0.152 per kWh.
- Results of the sensitivity analysis of the economic and technical parameters of the system revealed that increasing the EGT, RTE of A-CAES TEST and SGT reduces the COE of the system. In addition, it is determined that lowering the total investment cost or the discount rate will have considerable reduction effect on the COE of the system. Since the A-CAES is connected with biomass gasifier and dual fuel engine, any change in the parameter of one or the other, will result to a variation in the economic performance of the A-CAES+BMGES system. The economic results of the system and the sensitivity (Figs. 6.2–6.9) provide investors with clear guides to the economic performance of the hybrid systems for distributed cogeneration.
- The NPV of the system is found to be negative even with modest total investment cost reduction by a factor of 0.35 thus suggesting that the A-CAES+BMGES

system is not economically viable for commercial distributed electricity and domestic hot water production in the analysed location.

- Nevertheless, if 70% of total investment cost is offset for by means of a subsidy to the investor by the government as one of the ways to encourage RE uptake in the energy mix, the system become profitable with a positive NPV value of £137,387.2 and COE of £0.10 per kWh at the baseline real discount rate of 10%.

The economic performance of the system may further be improved in the future by:

- Reducing biomass gasification power generation system and A-CAES plant cost, which can be achieved through efficiency improvements as well as commercialisation
- Increase in the sale tariff received for power exported to the grid by private commercial generators
- Granting high subsidy to investment in hybrid biomass and wind generation systems
- Reductions in operations and maintenance cost, fuel cost and other balance of plant costs. These have a moderately small effect on the overall economic performance of the system, but of course should not be ignored as part of overall cost reductions.

It has to be noted that, the results reported above for the system are without allowance for renewable energy certificates, feed-in tariffs or other government subsidies. The anticipated decrease in the cost of A-CAES and biomass gasification power generation system due to commercialisation, standardisation, lower cost of capital and technology learning in the future will most certainly result to improvement in the economy of the A-CAES+BMGES system.

Chapter 7

Conclusions and further research

The global energy demand continues to increase. This coupled with depleting nature of fossil fuels and the growing global warming problem, resulting mainly from greenhouse gas (GHG) emissions from fossil fuel combustion, has stimulated increasing global attention towards the use of renewable energy (RE) sources for meeting global energy needs.

Wind power as one of the most promising renewable power sources has attracted particular attention over the last years.

Despite the growing global status of wind as one of the most reliable renewable energy source, its random and fluctuating characteristic makes it difficult to match demand with supply thus creating limitations for wind based power.

Wind power combined with energy storage (ES) has been identified as a major solution to smoothen out the variations and make wind based power more competitive.

Consequently, wind based power energy storage technologies has continued to arouse more and more interest on daily basis. Among many energy storage technologies, adiabatic compressed air energy storage technology (A-CAES) has been recognized as a viable option. Up until recently, most of the research papers relating to the wind-energy storage system have focused on the standalone energy storage systems.

However, hybrid energy storage system (HESS) involving renewable energy system and cited close to energy demand in the so called distribution generation mode has been accepted as an important trend since these systems has the capacity to deliver high cycle life, energy duration, and power capacity in a single system that may not be achievable in any of the units making up the hybrid system.

In this thesis, the thermodynamic performance of a novel hybrid adiabatic compressed-air energy storage (A-CAES) and biomass gasification energy storage (BMGES) system is investigated in detail. The system is based on electricity/heat demand data of 1600 households in Hull Humber region supplied electricity and heat by a hybrid system consisting of 1000 MW excess wind electricity powered adiabatic compressed air energy storage system, a biomass gasification power generation system made up of 353.36 $kg h^{-1}$ wood biomass gasifier, a hot air dryer and a 0.3 kWe rated dual fuel engine with overall electrical efficiency of 0.2 at a syngas fraction (fraction of diesel fuel mass flow rate replaced by syngas).of 0.8. A developed Matlab computer code is used for the simulations.

In addition, sensitivity analysis of process parameters effecting the performance of the system are analysed and results are presented. Moreover, economic analysis of the adiabatic compressed-air and biomass gasification energy storage (A-CAES+BMGES) system is carried out and reported in order to understand the economic performance and feasibility of the integrated system for an investor given the customers demand for heat

and electricity. The customer is considered to be about 1600 homes in the hull Humber region who require electricity and low/medium temperature hot water for domestic use.

The integrated model of the A-CAES+BMGES system is made up of many components, but the thermal energy storage tank of the A-CAES, the biomass gasifier, hot air dryer, dual fuel engine, heat exchangers and electricity/heat demand data are the key components. First, a Matlab model of each of the main component parts of the system are developed separately with some innovations and then combined together with an economic model to form the integrated system.

The general objective of the thesis was to develop an integrated model that has the capacity to provide a thermo economic performance of the integrated A-CAES and downdraft biomass gasification energy storage system (A-CAES+BMES) considered, including their energy and exergy efficiencies, fuel consumption, and cost per unit of electrical power produced. In the light of the above the specific objectives set out in the chapter one of this thesis were achieved as follows:

- A novel integrated adiabatic compressed air and biomass gasification energy storage systems (ACAES+BMGES) was proposed
- A detailed mathematical model suitable for analyzing the thermal performance of the TES unit as a separate component and as an fundamental part of the A-CAES system was developed and modelled
- A model of downdraft biomass gasifier as a stand-alone component and as an integral part of the integrated system was developed and presented.
- A thermodynamic model of the integrated A-CAES+BMGES system was developed and its analysis carried out using energy and exergy analyses
- An economic model to assess the feasibility of the A-CAES+BMGES was developed and its analysis carried out using net present value and cost of electricity as metrics for performance assessment.

Having achieved the general aim and objectives as detailed above, therefore, the research project is considered successful. The benefits derivable from the proposed and analysed A-CAES+BMGES in this thesis include but not limited to the following:

- A comprehensive model through which the thermodynamic and economic performance evaluation of the proposed A-CAES+BMGES can be carried out was developed and presented.
- The implementation of the developed model will increase the penetration of renewable energy distributed generation technologies especially wind and biomass generation technologies at the local community level and also help to avoid grid instability resulting from the intermittent nature of renewable energy sources
- The proposed system when implemented will also enable communities/customers to use their own renewable energy generation by shifting excess generation to meet their demand load later
- It empowers utility/private investors to access beforehand the economic performance of the proposed system on paper. It also endows them to create new business models, with cost effective energy prices that is in sync with customers' expectations and preferences

This chapter gives a summary of the key findings from analysis of the model results including the thermal energy storage tank model of the adiabatic compressed air energy storage (chapter three), the biomass gasification model (chapter four), the thermodynamic analysis model (chapter five) and the economic model (chapter six). First, the key outcomes of the research work are provided. The potential areas for possible research in the future are identified and discussed concisely and finally an outlook is given.

7.1 Main findings

In Chapter 3, two different charging modes of a thermal energy storage tank system employing multiple phase change material (PCM) system for the adiabatic compressed air energy storage (A-CAES) process was simulated to compare their performance and select the best mode for application in the overall system model. The modes are mod1 with higher mass flow rate (\dot{m}) and low temperature (T) and mod2 with higher temperature and low mass flow rate. First a mathematical formulation of the energy interactions in the heat transfer fluid and the phase change materials filling the latent heat thermal energy storage

tank of the A-CAES process is presented. The resulting equations were discretized using implicit finite difference technique and modelled in Matlab using matrix inversion technique. The developed model was then validated with experimental data, in terms of the temperature profile of the heat transfer fluid during the charging mode. The comparison results show that model predictions are in fairly good agreement with the experimental data. The two mode of charging of the thermal energy storage tank (referred to as mod1 and mod2 hereafter) was compared using the developed model. Performance indicators such as charging rate, discharging rate, charging efficiency, discharging efficiency, Charging and discharging exergy efficiency, and overall exergy and energy efficiency of charging/discharging process were adopted to evaluate the thermal performance of the phase change TEST in the two modes. Mod2 with higher temperature and lower mass flow rate was found to perform better than mod1 with higher mass flow rate and lower temperature in both the charging and discharging cycle. The round trip efficiency (RTE) of mod1 varied from 0.87 to 0.77 with an average of 0.76 while that for mod2 varied from 0.97 to 0.79 with an average of 0.78. In addition, the net energy efficiency for the charging process in the two modes lies in the range of 0.976 to 0.967 in mod1 and 0.983 to 0.978 in mod2 respectively over a charging time of six hours. Their corresponding exergy efficiency is estimated to lie in the range of 0.696 to 0.533 in mod1 and 0.743 to 0.610 in mod2 representing a percentage exergy efficiency variation of 7.2% for mod1 and 3.5% for mod2. Moreover, the overall exergy efficiency varied from a maximum value of 0.48 and 0.55 to minimum value of 0.33 and 0.44 in mod1 and mod2 respectively. This translates to average efficiencies of 0.45 and 0.51 in mod1 and mod2 respectively. Results of parametric analysis on the influence of number of multiple systems on the performance of the system shows in accordance with previous findings from other researchers that the 3 –PCM arrangement are able to store and discharge more energy than 2 PCM arrangement.

In chapter 4, a simplified downdraft biomass gasifier model based on non-kinetic multi step stoichiometric equilibrium approach for the analysis of biomass gasification process is presented. The model was developed in Matlab and results obtained from it were validated using experimental data, in terms of the syngas concentration, temperature attained in the reduction zone and syngas yield. The results of comparison show that the predictions by the model are in good agreement with the experimental measurements. The

novelty in the work is that the earlier model developed by Gao and Li. was extended to make it more robust and versatile. This is achieved by overcoming the inability of their model to predict gas concentrations at the pyrolysis and oxidation zones and the omission of H₂ and tar in the assumed pyrolysis gas. Unlike the method previously adopted in the estimation of pyrolysis product species that ignores tar, tar in the composition of syngas was considered in this work using previously determined experimental tar measurements. Predictions that can be made with the model include the temperature distribution at the pyrolysis, oxidation and reduction zones, syngas yield and composition, carbon conversion efficiency, lower calorific value and cold gas efficiency. Using rubber wood as a feed material at ambient conditions the model predicted syngas concentration at equivalent ratio of 3.1 and fuel feed moisture content of 18.5%, is about 1.1%, 17.3%, 22.8%, 9.0% and 49.8% for CH₄, H₂, CO, CO₂, and N₂ respectively. The corresponding lower calorific value, cold gas efficiency, carbon conversion efficiency and syngas yield were 4.7 MJ/Nm³, 59.9%, 85.5% and 2.5 Nm³/kg-biomass respectively. The temperatures in the pyrolysis, oxidation and reduction zone of the gasifier were found to lie between 654-510 K, 1221-1094 K and 964-862K respectively at equivalent ratio ranging from 3 to 5.2 and fuel moisture content of 18.5 wt.%. Other findings in agreement with findings of other researchers include:

- Biomass moisture content has a strong critical effect on the gasifier performance and should be kept as low as possible.
- Gasification air preheating is attractive if it can be achieved at no extra cost, otherwise, the energy cost for air preheating may not be compensated by the efficiency improvement benefit derivable from air preheating

In Chapter 5, the methodology for the technical analysis of the overall adiabatic compressed air and biomass gasification energy storage system for the production of dual stream of energy output is presented. The performance of the system was measured using the first (energy efficiency) and second law (exergy) efficiency as metrics. The key conclusion that can be drawn from the application of the technical model of the A-CAES+BMGES systems is that adiabatic compressed air energy storage (A-CAES) and biomass gasification energy storage (BMGES) technologies are ideally matched and when

integrated together are technically viable and have the potential to achieve fairly good efficiencies at small scale comparable to that of a standalone A-CAES system and other similar hybrid configurations. In addition, the system has the capacity to be cited close to areas of power and heat demand with an extra capacity to produce a significant amount of low temperature hot water for domestic use. These benefits make the system attractive in comparison to a traditional biomass combustion based systems that are only efficient at large scale. High efficiency at small scale is vital since the scale of the system is limited by biomass supply logistics and the maximum power demand of the particular study area or community housing cluster. Besides, the system is intended for use in distributed generation which requires small capacities. The configuration of the A-CAES+BMGES system would need to be co-located with the electrical and heating demands due to the technological challenges related with transferring thermal energy over large distances.

The total system efficiency and exergy efficiency was found to be about 38% and 29% respectively. Additionally, the electrical efficiency and effective electrical efficiency are found to be 30 and 33 percent respectively which are fairly moderate values in comparison with data found in the published literature for both A-CAES and similar hybrid systems. The electrical efficiency of the A-CAES component of the system is found to be about 88.6% which is far better than that of a standalone A-CAES found to be about 57.54%. This is made possible by the increase in the turbine inlet temperature as a result of heat recovered from the syngas and the DFE exhaust during the charging and discharging processes respectively.

Parametric analysis studies were also carried out to analyse the impact of main system variables on the overall performance of the integrated system. The effects of varying heat exchanger effectiveness, dual fuel engine exhaust temperature, and syngas temperature, minimum pressure of air cavern, round trip efficiency of thermal energy storage tank and no of households were explored and the results are presented. The results obtained are summarized thus according to the variables studied:

- The round trip efficiency (RTE) of the A-CAES has a direct linear relationship with the performance of the system. As RTE increases from 0.7 to 0.95, the total system efficiency and exergy efficiency increases by about 2 and 3% respectively

while for a reduction of RTE from 0.7 to 0.4, the total system efficiency and exergy efficiency reduces by roughly 3 and 4%, respectively.

- The TSE, exergy efficiency, electrical efficiency, effective electrical efficiency and TIT increases by approximately 2, 2.4, 2.5, 2.5 and 3.4% respectively as the exhaust gas temperature increases from 460 – 560°C.
- As the heat exchanger effectiveness increases from 0.7 to 0.95, the total system efficiency increases from 0.38 to 0.41, while the effective electrical efficiency and exergy efficiency increases 0.34 to 0.34 and 0.285 to 0.288 respectively.
- The syngas fraction (sf) has an inverse relationship with the performance of the system. As sf reduces from 80 to 20%, the total system efficiency increases from 0.38 to 0.47. Also, electrical efficiency, the effective electrical efficiency and system exergy efficiency increase from 0.30 to 0.37, 0.34 to 0.43, and from 0.29 to 0.36 respectively
- As the minimum pressure of the air store increases from 40 to 60 bar, the, exergy efficiency, total system efficiency, electrical efficiency and the effective electrical efficiency of the system increase from 0.29 to 0.30, 0.38 to 0.40, 0.30 to 0.32 and from 0.33 to 0.36 respectively.

In Chapter 6 is contained the economic feasibility of the overall adiabatic compressed air and biomass gasification energy storage system. First, total investment and operational costs of the individual components of the different parts of the overall system were estimated and aggregated together to arrive at the total investment cost (TIC) of the whole system. Then economic indicators such as net present value (NPV) and cost of electricity (COE) were used as metrics to access the performance of the system through a developed economic model in Matlab software. The result obtained shows that the proposed and analysed system in the thesis is not currently economically viable for commercial power and heat production in the Humber region UK. The adiabatic compressed air energy storage system and biomass gasification power generation system capital costs and discount rates must fall radically if the system is ever to become profitable and competitive with traditional fossil fuel power generation systems. For the system to fulfil its potential and make any noteworthy contribution in the UK power mix as an economically viable method to deal with the intermittency associated with wind power

generation, it is found that the government must provide financial incentive covering about 70% of the total investment cost of the system for its deployment. With the 70% incentive being provided, the power produced by the A-CAES+BMGES system becomes economically commercially feasible with a positive NPV value of £137,387.2 and COE of £0.10 per kWh at the baseline real discount rate of 10%. This compares well with the average cost of electricity for a medium user home in the UK (2,500 to 5,000 kWh a year), including taxes which is £0.15 per kWh. In addition, financial incentives should be provided to the UK farmers to grow energy crops to stimulate a drop in biomass prices as a way of improving the economic fortunes of the system. Other major findings include:

- Tariff for electricity produced and excess wind electricity used by the system is of critical importance with respect to plant economic performance.
- Increase in the sale tariff received for power exported to the grid by private commercial generators increases the economic performance of the system
- Granting high subsidy to investment in hybrid biomass and wind generation systems will help to improve the economic performance of the system further
- For a given capacity of the system, number of households (NOHs) has substantial impact on economic performance of the system. It is therefore desirable to operate at optimum NOHs. The only way to achieve this is to match the capacity of the system to correspond with the demand of the study area.

Even though the cost of electricity of the integrated system is higher than the prevailing tariffs in the market, there are many cost externalities that were not factored in. These include fuel cost volatility, carbon costs, local levies and bills. Furthermore, renewable energy certificates, feed-in tariffs or other government subsidies which are all available in the UK, were not factored in this economic analysis.

It is expected that future costs related with carbon emissions, the ongoing reduction in costs of wind and biomass gasification technologies, and the advancement of A-CAES systems through research will all help a system such as A-CAES+BMGES to become an attractive addition to the electricity market.

7.2 Further research

The current study is the foundation of a much more comprehensive thermodynamic and economic analysis of this hybrid renewable energy storage system's technical performance and viability. As a future research, real time data will be integrated including wind speed data for the specific area along with wind turbine power profiles, local biomass resource availability, real time electricity pricing, and local daily electricity/heat demand.

It is obvious that optimization of the system will be required so as to define the mode of operation for profit maximization. Optimization parameters such as time interval of energy generation, system total capacity versus fraction coming from the dual fuel engine, and the thermal energy storage and retrieval duration will all need to be considered in order to determine the most profitable design. In addition for the system and all the components modelled, the improvement of model validation could be done using more experimental results. We present potential specific future research for each major component as follows:

7.2.1 Downdraft biomass gasifier model

- The present study used rubber wood as feed stock with an experimentally determined tar composition as an input variable in the model. Tar yield in downdraft biomass gasification despite being negligible varies with temperature and of course will have effects on the system performance. Further refinement of this model should include the prediction of tar and its effects on the performance of the gasifier.
- Also, the exhaust temperature of the dual fuel engine was assumed as that recommended by the manufacturers. However, the exhaust temperature depends on so many factors such as nature of the feedstock, equivalence ratio, engine load and engine speed. As a future work, the performance of the dual fuel engine coupled with present gasification system could be studied including a study of the exhaust temperature and emissions flow/characteristics of the engine for the analysed rubber wood and other feeds.
- In addition, the model of the gasifier is not optimized yet and can be improved. A major tool to achieve this is a comprehensive physical and mathematical modelling of the behavior of the different particle sizes on their way down the gasifier. In

addition improvement in the model validation could be carried out using more experimental measurements

7.2.2 Thermal energy storage model

The thermal energy storage costs is still very high. In addition, its exergy and round trip efficiency is still below the level expected ($>85\%$). Thus a future research work could involve developing novel thermal energy storage methods like combination of molten salts and carbon nano particles to meet the technical and cost targets ($<£11.5$ per kWh_{th}). In addition, optimization studies could be carried out to improve system design and component integration.

Thermal conductivity of PCMs plays a critical role in the charging and discharging characteristics of a thermal energy storage system. A future research could also involve increasing the energy density and thermal conductivity of PCMs to make charging and discharging more efficient.

7.2.3 Overall system model

The predictive capability of the overall system models could be improved through accuracy and improved complexity by using fewer assumptions in the model for example using manufacturer compressor and turbine maps to account for off design performance of the compressor and turbines. In addition, full system optimisation studies and exergo-economic analysis of the system could be carried out to optimize the performance and cost of the system.

In the analysed model, the dual fuel engine exhaust temperature was used to preheat the air exiting the air store before expansion in the turbine. Another alternative configuration of the system is to make it a tri-generation system by using the dual fuel engine exhaust to drive a LiBr-H₂O absorption system to generate cooling duty. This alternative approach should be researched in the UK context and compared with the analysed system to know which of the two configurations would have better performance.

7.2.4 Economic model

The costs of the component parts of the system were estimated using approximate methods. A more reliable and detailed economic estimate for the system could be achieved by obtaining the actual cost data of the various components through quotes from the suppliers. In addition, the actual operation and maintenance costs could be estimated using actual cost of labour in the UK. These costs will then help in developing a comprehensive engineering economic model with minimal level of uncertainty.

7.3 Outlook

The potential for biomass and wind energy in UK is extraordinary and yet its contribution to date has been below expectation. Hybrid energy storage technologies like biomass gasification and adiabatic compressed air energy storage as analysed in this thesis is an enabling technology for wider modern biomass use and mitigation of the variability nature of wind. It offers the opportunity of storage of excess electricity and later conversion to electricity and low grade heat for domestic/industrial use. The technologies suffer from a variety of both technical and economic limitations which can hinder its commercial deployment.

- The cost of the biomass gasification system including the syngas cleaning system is still very high
- The syngas quality is a key parameter to economically run the dual fuel engine for a longer duration. Syngas from downdraft gasifiers contain high amounts of ash and dust particles because the syngas passes the oxidation zone, where it collects small ash particles. The impurities in the producer gas clog the engine valves and gas filters thus shortening the operating life of the engine.
- The cost of storage of compressed air in A-CAES is still very high and prohibitive and ranges from £741-965 per kW (\$960-1250 per kW) for underground storage and £1505-1659 per kW (\$1950-2150 per kW) for above ground storage. Moreover, though underground storage is relatively cheaper, it is however dependent on the availability of specific geological conditions at site.

- Also the cost of the thermal energy storage process of A-CAES is still very high above the levels expected to make the technology competitive

It is anticipated that in years to come, costs related with CO₂ emissions, the ongoing decrease in costs of biomass gasification and adiabatic compressed air energy storage technologies, and the advancement of biomass gasification power generation system and A-CAES systems efficiencies through research will benefit the A-CAES+BMGES system to become an attractive addition to the distributed generation electricity market.

Although, many sources of funds exists to support the research and development of a novel system to pilot or demonstration phase. But, till the system has been proven many thousands of hours of operation, commercialisation is not likely, however the cost of accomplishing this level of operation can often hinder utilization so that many promising novel developments are abandoned. Support should therefore be provided for the installation and monitoring of a number of practical systems of the A-CAES+BMGES system in different regions or housing clusters in the UK which will enable a better evaluation and demonstration of the feasibility, viability and reliability of the system. This appears to be the rational approach towards the path to commercialisation.

Appendix 1.

Correlations used in estimating fluid properties

1.1 Water vapour saturation pressure

The water vapour saturation pressure (P_{ws}) between 0°C and 373°C was estimated using the following relation (Wagner & Prub, 2002):

$$\ln\left(\frac{P_{ws}}{P_c}\right) = \frac{T_c}{T} \times a_1\vartheta + a_2\vartheta^{1.5} + 3\vartheta^{1.5} + a_3\vartheta^3 + a_4\vartheta^{3.5} + a_5\vartheta^4 + a_6\vartheta^{7.5} \quad (1)$$

Where: P_c is critical pressure equal to 22.064 MPa, $\vartheta = 1 - T/T_c$, T_c is critical temperature equal to 647.096 K, $a_1 = -7.85951783$, $a_2 = 1.84408259$, $a_3 = -11.7866497$, $a_4 = 22.6807411$, $a_5 = -15.9618719$, $a_6 = 1.80122502$.

1.2 Enthalpy of water

Enthalpy of water (kJ/kgK) is obtained with (Popiel & Wojtkowiak, 1998):

$$h_{s,w}(T, P) = a + bT + cT^2 + dT^3 + eT^4 + fT^5 \quad (2)$$

Where

$$a = -2.844699 \times 10^{-2}, b = -4.211925, c = -1.017034 \times 10^{-3}, d = 1.311054 \times 10^{-5}, e = -6.756469 \times 10^{-8}, f = 1.724481 \times 10^{-10}$$

If $P < P_{ws}$

$$h_w(T, P) = h_{s,w}(T, P) \quad (3)$$

If $P > P_{ws}$

$$h_w(T, P) = h_{s,w}(T, P) \times (1 + k_h * (P - P_{ws})) \quad (4)$$

Where $k_h = d_1 + d_2T^{-1} + d_3T^{-2}$

And $d_1 = -5.832449 \times 10^{-5}$, $d_2 = 0.0235696$, $d_3 = 5.384306 \times 10^{-3}$

1.3 Constant pressure specific heat for water

Constant specific heat for water in (kJ/kgK) is obtained with (Popiel & Wojtkowiak, 1998):

$$C_{p,w}(T) = a + bT + cT^{1.5} + dT^2 + eT^{2.5} \quad (5)$$

Where T is in °C and $a = 4.2174356$, $b = -0.0056181625$, $c = 0.0012992528$, $d = -0.00011535353$, $e = 4.14964 \times 10^{-6}$

1.4 Entropy of water

The specific entropy of water in (kJ/kgK) at temperature T in degree Celsius is give as (Liley, 1998):

$$s_f = a + bT + cT^2 + dT^3 \quad (6)$$

Where the constants are as given in table A1.1

Table A1.1 Constants for entropy of water calculation

T-range (°C)	a	b	c	d
0 – 40	-0.00047	0.015326	-2.81×10^{-5}	5.83333×10^{-8}
40 – 220	-0.00943	0.014917	-2.22847×10^{-5}	-2.86497×10^{-9}
220 – 350	-0.89251	0.025714	-6.50631×10^{-5}	8.47220×10^{-8}

1.5 Constant specific heat for air

The constant specific heat for air in J/kg is as follows:

$$C_{p,a} = 0.9992 \times 10^3 + 1.4319 \times 10^{-1}T + 1.1010 \times 10^{-4}T^2 - 6.7851 \times 10^{-8}T^3 \quad (7)$$

Where T is in °C

1.6 Enthalpy of air

$$h_a = C_p T \quad (8)$$

Appendix 2.

Detailed components investment cost

Table A2.1 Cost of major component of the integrated system

Components	cost symbol	component investment Cost
Biomass gasifier with internal engine	$C_{BMG+DFE}$	£680,400.00
Syngas cleaning system (cyclone+Scrubber)	C_{CS}	£149,650.46
Air compressor (4-stages)	C_{AC}	£365,904.00
Air expander (3 stages)	C_{AE}	£321,818.26
Phase change material for TEST1	C_{PCM1}	£6,600.19
Phase change material for TEST2	C_{PCM2}	£5,883.92
Phase change material for TEST3	C_{PCM3}	£26,091.81
Insulation for TEST1	C_{insu1}	£2,335.24
Insulation for TEST2	C_{insu2}	£2,128.18
Insulation for TEST3	C_{insu3}	£1,717.03
Steel for TEST1	C_{steel1}	£26,285.89
Steel for TEST1	C_{steel2}	£23,964.94
Steel for TEST1	C_{steel3}	£19,376.00
Above ground compressed air storage tank	C_{AS}	£613,052.80
Hot air dryer	C_{HAD}	£19,554.26
Heat exchanger 1	C_{HX1}	£22,691.60
Heat exchanger 2	C_{HX2}	£2,742.36
Heat exchanger 3	C_{HX3}	£2,636.70
Heat exchanger 4	$HX4$	£3,250.14
Heat exchanger 5	C_{HX5}	£3,367.46
Heat exchanger 6	C_{HX6}	£3,239.99
Heat exchanger 7	C_{HX7}	£7,713.96
Hot water storage tank	C_{HWT}	£60,259.79
Total investment cost	TIC	£2,370,664.99

!

References

- Adebiyi, G. A. (1991) A second-law study on packed bed energy storage systems utilising phase change materials, 113 (1991) 146–156. *ASME Journal of Solar Energy Engineering*, 113 146-156.
- Adine, H. A. & El Qarnia, H. (2009) Numerical analysis of the thermal behaviour of a shell-and-tube heat storage unit using phase change materials. *Applied Mathematical Modelling*, 33(4), 2132-2144.
- Agrawal, P., Nourai, A., Markel, L., Fioravanti, R., Gordon, P., Tong, N. & Huff, G., (2011) Characterization and assessment of novel bulk storage technologies: A study for the DOE energy storage systems program (SANDIA REPORT SAND2011-3700). Available online: <https://prod.sandia.gov/techlib-noauth/access-control.cgi/2011/113700.pdf> [Accessed 28/10/2018].
- Agyenim, F., Hewitt, N., Eames, P. & Smyth, M. (2010) A review of materials, heat transfer and phase change problem formulation for latent heat thermal energy storage systems (LHTESS). *Renewable and Sustainable Energy Reviews*, 14(2), 615-628.
- Ahrenfeldt, J., Thomsen, T. P., Henriksen, U. & Clausen, L. R. (2013) Biomass gasification cogeneration – A review of state of the art technology and near future perspectives. *Applied Thermal Engineering*, 50(2), 1407-1417.
- Aldoss, T. K. & Rahman, M. M. (2014) Comparison between the single-PCM and multi-PCM thermal energy storage design. *Energy Conversion and Management*, 83 79-87.
- Altafini, C. R., Wander, P. R. & Barreto, R. M. (2003) Prediction of the working parameters of a wood waste gasifier through an equilibrium model. *Energy Conversion and Management*, 44(17), 2763-2777.
- Amundson, N. R. & Arri, L. E. (1978) Char gasification in a counter current reactor. *American Institute of Chemical Engineers Journal*, 24 87-101.
- Aneke, M. & Wang, M. (2016) Energy storage technologies and real life applications – A state of the art review. *Applied Energy*, 179 350-377.
- Antonopoulos, I., Karagiannidis, A., Gkouletsos, A. & Perkoulidis, G. (2012) Modelling of a downdraft gasifier fed by agricultural residues. *Waste Management*, 32(4), 710-718.

- Arabkoohsar, A., Machado, L., Farzaneh-Gord, M. & Koury, R. N. N. (2015) Thermo-economic analysis and sizing of a PV plant equipped with a compressed air energy storage system. *Renewable Energy*, 83 491-509.
- Arthur, J. R. (1951) Reactions between carbon and oxygen. *Transactions of the Faraday Society*, 47 164-178.
- Ashman, P. J. & Mullinger, P. J. (2005) Research issues in combustion and gasification of lignite. *Fuel*, 84(10), 1195-1205.
- Babu, B. V. & Sheth, P. N. (2006) Modeling and simulation of reduction zone of downdraft biomass gasifier: Effect of char reactivity factor. *Energy Conversion and Management*, 47(15–16), 2602-2611.
- Bagdanavicius, A. & Jenkins, N. (2014) Exergy and exergoeconomic analysis of a Compressed Air Energy Storage combined with a district energy system. *Energy Conversion and Management*, 77 432-440.
- Bang-Møller, C., Rokni, M. & Elmegaard, B. (2011) Exergy analysis and optimization of a biomass gasification, solid oxide fuel cell and micro gas turbine hybrid system. *Energy*, 36(8), 4740-4752.
- Bannach, N. (2014) Phase Change: Cooling and solidification of metal. Available online: <https://uk.comsol.com/blogs/phase-change-cooling-solidification-metal/> [Accessed 28/10/2018].
- Baños, R., Manzano-Agugliaro, F., Montoya, F. G., Gil, C., Alcayde, A. & Gómez, J. (2011) Optimization methods applied to renewable and sustainable energy: A review. *Renewable and Sustainable Energy Reviews*, 15(4), 1753-1766.
- Barbour, E., Mingnard, D., Ding, Y. & Li, Y. (2015) Adiabatic Compressed air Energy storage with packed bed thermal energy storage. *Applied Energy*, 155 804-815.
- Barman, N. S., Ghosh, S. & De, S. (2012) Gasification of biomass in a fixed bed downdraft gasifier – A realistic model including tar. *Bioresource Technology*, 107 505-511.
- Baruah, D. & Baruah, D. C. (2014) Modeling of biomass gasification: A review. *Renewable and Sustainable Energy Reviews*, 39 806-815.
- Basu, P. (2006) *Combustion and gasification in fluidized beds*. USA: Taylor & Francis Group/CRC Press.
- Basu, P. (2010) *Biomass gasification and pyrolysis: Practical design and theory*. Burlington, USA: Elsevier Inc.

Beek, J. (1962) Design of packed catalytic reactors. *Advances in Chemical Engineering*, 3 203-271.

BEIS (2016) Evidence gathering: Thermal energy storage (TES) technologies. Available online:

https://assets.publishing.service.gov.uk/government/uploads/system/uploads/attachment_data/file/545249/DELTA_EE_DECC_TES_Final__1_.pdf [Accessed 28/10/2018].

Beith, R. (ed) (2011) *Small and micro combined heat and power (CHP) systems: Advanced design, performance, materials and applications*. UK: Woodhead Publishing.

Bejan, A., Tsatsaronis, G. & Moran, M. (1996) *Thermal design and optimization*. New York: John Wiley & Sons.

Bellan, S., Alam, T. E., González-Aguilar, J., Romero, M., Rahman, M. M., Goswami, D. Y. & Stefanakos, E. K. (2015) Numerical and experimental studies on heat transfer characteristics of thermal energy storage system packed with molten salt PCM capsules. *Applied Thermal Engineering*, 90 970-979.

Benmansour, A., Hamdan, M. A. & Bengueuddach, A. (2006) Experimental and numerical investigation of solid particles thermal energy storage unit. *Applied Thermal Engineering*, 26(5-6), 513-518.

Berends R & Brem. G. (2002) Two-stage gasification of biomass for the production of syngas with application to high-pressure chemical processes. Available online: <http://infohouse.p2ric.org/ref/35/34062.pdf> [Accessed 01/05/2017].

Blasi, C. D. (2000) Dynamic behaviour of stratified downdraft gasifiers. *Chemical Engineering Science*, 55(15), 2931-2944.

Borgnakke, C. & Sonntag, R. E. (2009) *Fundamentals of thermodynamics*, 7th edition. USA: John Wiley & Sons, Inc.

Bridgwater, A. V. (1995) The technical and economic feasibility of biomass gasification for power generation. *Fuel*, 74(5), 631-653.

Budt, M., Wolf, D., Span, R. & Yan, J. (2016) A review on compressed air energy storage: Basic principles, past milestones and recent developments. *Applied Energy*, 170 250-268.

Buffa, F., Kemble, S., Manfrida, G. & Milazzo, A. (2013) Exergy and exergoeconomic model of a ground-based CAES plant for peak-load energy production. *Energies*, 6 1050-1067.

Bullough, C., Gatzen, C., Jakiel, C., Koller, M., Nowi, A. & Zunft, S. (2004) Advanced adiabatic compressed air energy storage for the integration of wind energy. European Wind Energy Conference (EWEC 2004) London UK, 22-25 November 2004.

Business Electricity Prices (2017). A Guide to wholesale electricity pricing. Available online: <https://www.businesselectricityprices.org.uk/retail-versus-wholesale-prices/> [Accessed 01/5/2017].

Buttsworth, D. R., (2001). A Finite difference routine for the solution of transient one dimensional heat conduction problems with curvature and varying thermal properties. Available online: <https://core.ac.uk/download/pdf/11034604.pdf>. [Accessed 01/05/2018].

Caliano, M., Bianco, N., Graditi, G. & Mongibello, L. (2017) Design optimization and sensitivity analysis of a biomass-fired combined cooling, heating and power system with thermal energy storage systems. *Energy Conversion and Management*, 149 631-645.

Canakci, M. & Hosoz, M. (2006) Energy and exergy analyses of a diesel engine fuelled with various biodiesels. *Energy Sources, Part B: Economics, Planning, and Policy*, 1(4), 379-394.

Cengel, Y. A. & Boles, M. A. (2006) *Thermodynamics: An engineering approach*, 5th edition. New York: McGraw-Hill, Inc.

Cengel, Y. A. (2002) *Heat transfer: A practical approach*, 2nd edition. New York: Higher Education.

Centeno, F., Mahkamov, K., Silva Lora, E. E. & Andrade, R. V. (2012) Theoretical and experimental investigations of a downdraft biomass gasifier-spark ignition engine power system. *Renewable Energy*, 37 97-108.

Channiwala, S. A. & Parikh, P. P. (2002) A unified correlation for estimating HHV of solid, liquid and gaseous fuels. *Fuel*, 81(8), 1051-1063.

Chen, H., Cong, T. N., Yang, W., Tan, C., Li, Y. & Ding, Y. (2009) Progress in electrical energy storage system: A critical review. *Progress in Natural Science*, 19(3), 291-312.

Chen, W., Annamalai, K., Ansley, R. J. & Mirik, M. (2012) Updraft fixed bed gasification of mesquite and juniper wood samples. *Energy*, 41 454-461.

Chiu, J. N. W. & Martin, V. (2013) Multistage latent heat cold thermal energy storage design analysis. *Applied Energy*, 112 1438-1445.

Cho, Y. S. & Joseph, B. (1981) Heterogeneous model for moving-bed coal gasification reactors. *Industrial & Engineering Chemistry Process Design and Development*, 20(2), 314-318.

Clarke. (2013) Diesel engine generator set: Model specifications. Available online: http://www.clarkegen.com/Libraries/PDF_Files/BROCHURE_500_KW_MTU_STATIO NARY_STANDBY.sflb.ashx [Accessed 05/07/2017].

Copeland, R. J., (1983) Benefits from energy storage technologies (SERI REPORT SERI/TP-252-2107). Available online: <https://www.nrel.gov/docs/legosti/old/2107.pdf> [Accessed 05/01/2018].

Corfee, K., Stevens, G. & Goffri, S. (2014) Distributed generation resource assessment for long-term planning study. Available online: http://www.pacificorp.com/content/dam/pacificorp/doc/Energy_Sources/Integrated_Resource_Plan/2015IRP/2015IRPStudy/Navigant_Distributed-Generation-Resource-Study_06-09-2014.pdf [Accessed 01/01/2018].

Costa, M., Buddhi, D. & Oliva, A. (1998) Numerical simulation of a latent heat thermal energy storage system with enhanced heat conduction. *Energy Conversion and Management*, 39(3–4), 319-330.

Daniel, W. (2011) Methods for design and application of adiabatic compressed air energy storage based on dynamic modelling. Doctoral thesis. Available online: https://www.researchgate.net/publication/304335005_Methods_for_Design_and_Application_of_Adiabatic_Compressed_Air_Energy_Storage_Based_on_Dynamic_Modeling 1-175. [Accessed 28/10/2018].

Danish Energy Agency, (2014) Guidelines for low-temperature district heating. Available online: https://www.danskfjernvarme.dk/~media/danskfjernvarme/gronenergi/projekter/eudp-lavtemperatur%20fjv/guidelines%20for%20ldh-final_rev1.pdf [Accessed 28/10/2018].

Dasappa, S. & Sridhar, H. V. (2013) Performance of a diesel engine in a dual fuel mode using producer gas for electricity power generation. *International Journal of Sustainable Energy*, 32(3), 153-168.

Daugaard, D. E. & Brown, R. C. (2003) Enthalpy for pyrolysis for several types of biomass. *Energy & Fuels*, 17 934-939.

de Gracia, A. & Cabeza, L. F. (2015) Phase change materials and thermal energy storage for buildings. *Energy and Buildings*, 103 414-419

de Gracia, A. & Cabeza, L. F. (2017) Numerical simulation of a PCM packed bed system: A review. *Renewable and Sustainable Energy Reviews*, 69 1055-1063

De, S., Bandyopadhyay, S., Assadi, M. & Mukherjee, D. A. (eds) (2018) *Sustainable energy technology and policies: A transformational journey*, volume 2. USA: Springer.

DECC, (2015a), Assessment of the costs, performance, and characteristics of heat UK networks (DECC REPORT URN 15D/022). Available online: https://assets.publishing.service.gov.uk/government/uploads/system/uploads/attachment_data/file/424254/heat_networks.pdf [Accessed 28/10/2018].

DECC, (2015b) Domestic energy consumption in the UK between 1970 and 2014 (DECC REPORT URN 5D/377). Available online: <https://www.gov.uk/government/publications/energy-consumption-in-the-uk-archive> [Accessed 05/05/2016].

Denholm, P. (2006) Improving the technical, environmental and social performance of wind energy systems using biomass-based energy storage. *Renewable Energy*, 31(9), 1355-1370.

Denholm, P. & Kulcinski, G. L. (2004) Life cycle energy requirements and greenhouse gas emissions from large scale energy storage systems. *Energy Conversion and Management*, 45(13-14), 2153-2172.

Dincer, I. & Sahin, A. Z. (2004) A new model for thermodynamic analysis of a drying process. *International Journal of Heat and Mass Transfer*, 47(4), 645-652.

Dincer, I. (2002) Thermal energy storage systems as a key technology in energy conservation. *International Journal of Energy Research*, 26 567-588.

Dincer, I. & Rosen, A. M. (2011) *Thermal energy storage systems and applications*, 2nd edition. UK: John Wiley & Sons, Ltd.

Diyoke, C., Idogwu, S. & Ngwaka, U. C. (2014) An Economic assessment of biomass gasification for rural electrification in Nigeria. *International Journal of Renewable Energy Technology Research*, 3 1-17.

Diyoke, C., Aneke, M., Wang, M. & Wu, C. (2018a) Techno-economic analysis of wind power integrated with both compressed air energy storage (CAES) and biomass gasification energy storage (BGES) for power generation. *Royal Society of Chemistry Advances*, 8 22004-22022.

Diyoke, C., Gao, N., Aneke, M., Wang, M. & Wu, C. (2018b) Modelling of down-draft gasification of biomass – An integrated pyrolysis, combustion and reduction process. *Applied Thermal Engineering*, 142 444-456.

Dogru, M. (2000) Fixed bed gasification of biomass. PhD thesis. University of Newcastle, UK.

Dogru, M., Howarth, C. R., Akay, G., Keskinler, B. & Malik, A. A. (2002) Gasification of hazelnut shells in a downdraft gasifier. *Energy*, 27(5), 415-427.

- Doherty, W., Reynolds, A. & Kennedy, D. (2009) The effect of air preheating in a biomass CFB gasifier using ASPEN Plus simulation. *Biomass and Bioenergy*, 33(9), 1158-1167.
- Dominković, D. F., Ćosić, B., Bačelić Medić, Z. & Duić, N. (2015) A hybrid optimization model of biomass trigeneration system combined with pit thermal energy storage. *Energy Conversion and Management*, 104 90-99.
- E4tech, (2010), Biomass prices in the heat and electricity sectors in the UK. Available online: http://www.e4tech.com/wp-content/uploads/2016/01/100201Biomass_prices.pdf. [Accessed 01/02/2018].
- Edwards, J., Bindra, H. & Sabharwall, P. (2016) Exergy analysis of thermal energy storage options with nuclear power plants. *Annals of Nuclear Energy*, 96 104-111.
- Elfeky, K. E., Ahmed, N. & Wang, Q. (2018) Numerical comparison between single PCM and multi-stage PCM based high temperature thermal energy storage for CSP tower plants. *Applied Thermal Engineering*, 139 609-622.
- Elmegaard, B. & Markussen, W. B. (2011) Efficiency of compressed air energy storage. 24th International Conference on Efficiency, Cost, Optimization, Simulation and Environmental Impact of Energy Systems, ECOS 2011. Available online: http://orbit.dtu.dk/files/6324034/prod21323243995265.ecos2011_paper%5B1%5D.pdf [Accessed 28/10/2018].
- EPA (2018) Efficiency metrics for CHP systems: Total system and effective electric efficiencies. Available online: https://www.arb.ca.gov/cc/ccei/presentations/chpefficiencymetrics_epa.pdf [Accessed 01/09/2018].
- EPRI, (2008), Compressed air energy storage-scoping study for California (EPRI REPORT CEC-500-2008-069). Available online: <http://www.energy.ca.gov/2008publications/CEC-500-2008-069/CEC-500-2008-069.PDF> [Accessed 28/10/2018].
- Esen, M., Durmuş, A. & Durmuş, A. (1998) Geometric design of solar-aided latent heat store depending on various parameters and phase change materials. *Solar Energy*, 62(1), 19-28.
- ETI. (2012) Distributed generation; London. Available online: <https://www.eti.co.uk/news/eti-announces-distributed-energy-studies> [Accessed 01/01/2016].
- Evans, A., Strezov, V. & Evans, T. J. (2012) Assessment of utility energy storage options for increased renewable energy penetration. *Renewable and Sustainable Energy Reviews*, 16(6), 4141-4147.

- Eyer, J. and Corey, G., (2010) Energy storage for the electricity grid: Benefits and market potential assessment guide - A study for the DOE Energy Storage Systems Program (SANDIA REPORT SAND2010-0815). Available online: <https://www.sandia.gov/ess-ssl/publications/SAND2010-0815.pdf> [Accessed 28/10/2018].
- Facci, A. L., Sánchez, D., Jannelli, E. & Ubertini, S. (2015) Trigenerative micro compressed air energy storage: Concept and thermodynamic assessment. *Applied Energy*, 158 243-254.
- Fang, M. & Chen, G. (2007) Effects of different multiple PCMs on the performance of a latent thermal energy storage system. *Applied Thermal Engineering*, 27(5–6), 994-1000.
- FAO, (1986), *Wood gas as engine fuel*. Available online: <http://www.fao.org/3/a-t0512e.pdf> [Accessed 02/08/2018].
- Farid, M. M. & Kanzawa, A. (1989) Thermal performance of a heat storage module using PCM's with different melting temperatures: Mathematical modeling. *Transactions of the ASME*, 111 152-157.
- Felix Regin, A., Solanki, S. C. & Saini, J. S. (2009) An analysis of a packed bed latent heat thermal energy storage system using PCM capsules: Numerical investigation. *Renewable Energy*, 34(7), 1765-1773.
- Ferruzza, D. (2015) Techno-economic performance evaluation of a multi-layered single tank storage for solar tower power plant. MSc Thesis. The KTH School of Industrial Engineering and Management. Available online: <http://kth.diva-portal.org/smash/get/diva2:848371/FULLTEXT01.pdf> [Accessed 01/07/2018].
- Fertig, E. & Apt, J. (2011) Economics of compressed air energy storage to integrate wind power: A case study in ERCOT. *Energy Policy*, 39(5), 2330-2342.
- Flagan, R. C. (1988) Combustion fundamentals. Available online: <https://authors.library.caltech.edu/25069/4/AirPollution88-Ch2.pdf> [Accessed 01/08/2018].
- Foley, A. & Díaz Lobera, I. (2013) Impacts of compressed air energy storage plant on an electricity market with a large renewable energy portfolio. *Energy*, 57 85-94.
- Francescato, V., Antonini, E. & Bergomi, L. Z. (2009) *Wood fuels handbook*. Italy: AIEL- Interlian Agroforestry Association.
- Frangopoulos, C. A. (2012) A method to determine the power to heat ratio, the cogenerated electricity and the primary energy savings of cogeneration systems after the European Directive. *Energy*, 45(1), 52-61.

- Freund, S., Schainker, R. & Moreau, R. (2012) Commercial concepts for adiabatic compressed air energy storage. 7th International Renewable Energy Storage Conference.
- Galal, M. G., Abdel Aal, M. M. & El Kady, M. A. (2002) A comparative study between diesel and dual-fuel engines: performance and emissions. *Combustion Science and Technology*, 174 241-256.
- Gao, N. & Li, A. (2008) Modeling and simulation of combined pyrolysis and reduction zone for a downdraft biomass gasifier. *Energy Conversion and Management*, 49(12), 3483-3490.
- Garrison, J. B. & Webber, M. E. (2011) An integrated energy storage scheme for a dispatchable solar and wind powered energy system. *Journal of Renewable and Sustainable Energy*, 3 043101-043112.
- Gebreegziabher, T., Oyedun, A. O. & Hui, C. W. (2013) Optimum biomass drying for combustion – A modeling approach. *Energy*, 53 67-73.
- Ghoshdastidar, P. S. (1998) *Computer simulation of flow and heat transfer*. New Delhi: Tata McGraw Hill.
- Gil, J., Corella, J., Aznar, M. P. & Caballero, M. A. (1999) Biomass gasification in atmospheric and bubbling fluidized bed: Effect of the type of gasifying agent on the product distribution. *Biomass and Bioenergy*, 17(5), 389-403.
- Giltrap, D. L., McKibbin, R. & Barnes, G. R. G. (2003) A steady state model of gas-char reactions in a downdraft biomass gasifier. *Solar Energy*, 74(1), 85-91.
- Gómez-Barea, A., Arjona, R. & Ollero, P. (2005) Pilot-plant gasification of olive stone: a Technical assessment. *Energy & Fuels*, 19 598-560.
- Goldstein, L., Hedman, B., Knowles, D., Freedman, S. I., Woods, R. and Schweizer, T., (2002) Gas-fired distributed energy resource technology characterizations. Available online: <https://www.nrel.gov/docs/fy04osti/34783.pdf> [Accessed 28/10/2018].
- Gong, Z. X. & Mujumdar, A. S. (1996) Enhancement of energy charge-discharge rates in composite slabs of different phase change materials. *International Journal of Heat and Mass Transfer*, 39 725-733.
- Gong, Z. & Mujumdar, A. S. (1997a) Finite-element analysis of cyclic heat transfer in a shell-and-tube latent heat energy storage exchanger. *Applied Thermal Engineering*, 17(6), 583-591.
- Gong, Z. & Mujumdar, A. S. (1997b) Thermodynamic optimization of the thermal process in energy storage using multi-phase change materials. *Applied Thermal Engineering*, 17(2), 1067-1083.

- Gong, Z. & Mujumdar, A. S. (1996) Cyclic heat transfer in a novel storage unit of multiple phase change materials. *Applied Thermal Engineering*, 16(10), 807-815.
- Grazzini, G. & Milazzo, A. (2012) A Thermodynamic analysis of multistage adiabatic CAES. *Proceedings of the Institute of Electrical and Electronics Engineers*, 100(2), 461-472.
- Grazzini, G. & Milazzo, A. (2008) Thermodynamic analysis of CAES/TES systems for renewable energy plants. *Renewable Energy*, 33(9), 1998-2006.
- Groeneveld, M. J. & Van Swaaj, W. P. M. (1979) Gasification of solid waste - Potential and application of co-current moving bed gasifiers. *Applied Energy*, 165-178.
- Gronli, M. G. (1996) A theoretical and experimental study of the thermal degradation of biomass. PhD thesis. Norwegian University of Science and Technology, Norway.
- GSTC (2018) Gasifiers for biomass. Available online: <http://www.globalsyngas.org/applications/gasifiers-for-biomass/> [Accessed 01/02/2018].
- GWEC (2018) Global status of wind power. Available online: <http://gwec.net/global-figures/wind-energy-global-status/> [Accessed 25/10/2018].
- Harker, J. H., Backhurst, J. R. & Richardson, J. F. (2013) *Coulson and Richardson's chemical engineering volume 2*, 5th edition. Butterworth-Heinemann.
- Hartmann, N., Vöhringer, O., Kruck, C. & Eltrop, L. (2012) Simulation and analysis of different adiabatic compressed air energy storage plant configurations. *Applied Energy*, 93 541-548.
- Hasnain, S. M. (1998) Review on sustainable thermal energy storage technologies, part I: Heat storage materials and techniques. *Energy Conversion and Management*, 39(11), 1127-1138.
- Hewitt, G., F. & Pugh, S. J. (2007) Approximate design and costing methods for heat exchangers. *Heat Transfer Engineering*, 28(2), 76-86.
- Hu, H. & Argyropoulos, S. A. (1996) Mathematical modelling of solidification and melting: a review. *Modelling and Simulation in Materials Science and Engineering*, 4 371-396.
- IEA, (2015) Projected Costs of generating electricity. Available online: <https://www.oecd-nea.org/ndd/pubs/2015/7057-proj-costs-electricity-2015.pdf> [Accessed 25/10/2018].

- IEA, (2007) Biomass for power generation and CHP. Available online: <https://www.iea.org/publications/freepublications/publication/essentials3.pdf> [Accessed 25/10/2018].
- Inaba, H. (2007) Heat and mass transfer analysis of fluidized bed grain drying. *Memoirs of the Faculty of Engineering, Okayama University, Japan*, 41 52-62.
- Incropera, F. P. & DeWitt, D. P. (1996) *Fundamentals of heat and mass transfer*, 4th edition. New York: John Wiley & Sons.
- Indrawati, S. M. (2015) Energy and sustainable development: What's next?. Available online: <http://www.worldbank.org/en/news/speech/2015/06/10/energy-and-sustainable-development-whats-next> [Accessed 25/10/2018].
- IRENA (2013) Thermal energy storage: Technology brief. Available online: <http://stage-ste.eu/documents/TES%201%20IRENA-ETSAP%20Tech%20Brief%20E17%20Thermal%20Energy%20Storage.pdf> [Accessed 25/10/2018].
- Ismail, K. A. R., Alves, C. L. F. & Modesto, M. S. (2001) Numerical and experimental study on the solidification of PCM around a vertical axially finned isothermal cylinder. *Applied Thermal Engineering*, 21(1), 53-77.
- Ismail, K. A. R. & Henríquez, J. R. (2002) Numerical and experimental study of spherical capsules packed bed latent heat storage system. *Applied Thermal Engineering*, 22(15), 1705-1716.
- Ismail, K. A. R. & Stuginsky Jr, R. (1999) A parametric study on possible fixed bed models for pcm and sensible heat storage. *Applied Thermal Engineering*, 19(7), 757-788.
- Jarunghammachote, S. & Dutta, A. (2007) Thermodynamic equilibrium model and second law analysis of a downdraft waste gasifier. *Energy*, 32(9), 1660-1669.
- Jayah, T. H., Aye, L., Fuller, R. J. & Stewart, D. F. (2003) Computer simulation of a downdraft wood gasifier for tea drying. *Biomass and Bioenergy*, 25(4), 459-469.
- Jeffreson, C. P. (1972) Prediction of breakthrough curves in packed beds: I. Applicability of single parameter models. *American Institute of Chemical Engineers*, 18(2), 409-416.
- Jubeh, N. M. & Najjar, Y. S. H. (2012) Power augmentation with CAES (compressed air energy storage) by air injection or supercharging makes environment greener. *Energy*, 38(1), 228-235.
- Kaldellis, J. K. (2008) Integrated electrification solution for autonomous electrical networks on the basis of RES and energy storage configurations. *Energy Conversion and Management*, 49(12), 3708-3720

- Karellas, S. & Tzouganatos, N. (2014) Comparison of the performance of compressed-air and hydrogen energy storage systems: Karpathos island case study. *Renewable and Sustainable Energy Reviews*, 29 865-882.
- Karthikeyan, S. & Velraj, R. (2012) Numerical investigation of packed bed storage unit filled with PCM encapsulated spherical containers – A comparison between various mathematical models. *International Journal of Thermal Sciences*, 60 153-160.
- Kaushal, P., Abedi, J. & Mahinpey, N. (2010) A comprehensive mathematical model for biomass gasification in a bubbling fluidized bed reactor. *Fuel*, 89(12), 3650-3661.
- Kelly, B. and Kearney, D., (2006) Thermal storage commercial plant design study for a 2-tank indirect molten salt system (NREL REPORT NREL/SR-550-40166). Available online: <https://www.nrel.gov/docs/fy06osti/40166.pdf> [Accessed 28/10/2018].
- Kenisarin, M. M. (2010) High-temperature phase change materials for thermal energy storage. *Renewable and Sustainable Energy Reviews*, 14(3), 955-970.
- Kim, T. S. & Hwang, S. H. (2006) Part load performance analysis of recuperated gas turbines considering engine configuration and operation strategy. *Energy*, 31(2-3), 260-277.
- Kim, Y. M., Kim, S. J. & Favrat, D. (2012) Potential and evolution of compressed air energy storage: Energy and exergy analyses. *Entropy*, 14 1521.
- Klerk, A. (2003) Voidage variation in packed beds at small column to particle diameter ratio. *American Institute of Chemical Engineers Journal*, 49 2022-2029.
- Kotas, T. J. (1995) *The exergy method of thermal plant analysis*. Florida: Krieger Publishing Company.
- Kousksou, T., Bruel, P., Jamil, A., El Rhafiki, T. & Zeraouli, Y. (2014) Energy storage: Applications and challenges. *Solar Energy Materials and Solar Cells*, 120, Part A 59-80.
- Kreith, F. & Raton, B. (eds) (2000) *The CRC Handbook of thermal engineering*. Boca Raton: CRC Press LLC
- Kuravi, S., Trahan, J., Goswami, D. Y., Rahman, M. M. & Stefanakos, E. K. (2013) Thermal energy storage technologies and systems for concentrating solar power plants. *Progress in Energy and Combustion Science*, 39(4), 285-319.
- Kurkela, E. & Ståhlberg, P. (1992) Air gasification of peat, wood and brown coal in a pressurized fluidized-bed reactor. I. Carbon conversion, gas yields and tar formation. *Fuel Processing Technology*, 31 1-21.

- Lee, J. J., Kang, D. W. & Kim, T. S. (2011) Development of a gas turbine performance analysis program and its application. *Energy*, 36(8), 5274-5285.
- Leung, D. Y. C., Caramanna, G. & Maroto-Valer, M. M. (2014) An overview of current status of carbon dioxide capture and storage technologies. *Renewable and sustainable energy reviews*, 39 426-443.
- Li, H., Zhang, X., Liu, L., Zeng, R. & Zhang, G. (2016) Exergy and environmental assessments of a novel trigeneration system taking biomass and solar energy as co-feeds. *Applied Thermal Engineering*, 104 697-706.
- Li, K. W. (1996) *Applied thermodynamics: Availability method and energy conversion*. Washington DC: Taylor & Francis Ltd.
- Li, M., Jin, B., Ma, Z. & Yuan, F. (2018) Experimental and numerical study on the performance of a new high-temperature packed-bed thermal energy storage system with macroencapsulation of molten salt phase change material. *Applied Energy*, 221 1-15.
- Li, P. Y., Loth, E., Simon, T. W., Van de Ven, James D. & Crane, S. E. (2011) Compressed Air Energy Storage for Offshore Wind Turbines. International Fluid Power Exhibition (IFPE), Las Vegas, NV.
- Liley, P. E. (1998) Accurate simple equations for liquid water properties. *International Journal of Mechanical Engineering Education*, 27(4), 317.-323.
- Liu, J. & Wang, J. (2016) A comparative research of two adiabatic compressed air energy storage systems. *Energy Conversion and Management*, 108 566-578.
- Liu, Z., Wang, Z. & Ma, C. (2006) An experimental study on heat transfer characteristics of heat pipe heat exchanger with latent heat storage. Part I: Charging only and discharging only modes. *Energy Conversion and Management*, 47(7-8), 5944-966.
- Loh, P. C., Zhang, L. & Gao, F. (2013) Compact integrated energy systems for distributed generation. *Institute of Electrical and Electronics Engineers Transactions on Industrial Electronics*, 60(4), 1492-1502.
- Luk, H. T., Lam, T. Y. G., Oyedun, A. O., Gebreegziabher, T. & Hui, C. W. (2013) Drying of biomass for power generation: A case study on power generation from empty fruit bunch. *Energy*, 63 205-215.
- Luo, X., Wang, J., Dooner, M. & Clarke, J. (2015) Overview of current development in electrical energy storage technologies and the application potential in power system operation. *Applied Energy*, 137 511-536.
- Luo, X., Wang, J., Krupke, C., Wang, Y., Sheng, Y., Li, J., Xu, Y., Wang, D., Miao, S. & Chen, H. (2016) Modelling study, efficiency analysis and optimisation of large-scale

adiabatic compressed air energy storage systems with low-temperature thermal storage. *Applied Energy*, 162 589-600.

Lv, P. M., Xiong, Z. H., Chang, J., Wu, C. Z., Chen, Y. & Zhu, J. X. (2004) An experimental study on biomass air–steam gasification in a fluidized bed. *Bioresource Technology*, 95(1), 95-101.

Mason, J. E. & Archer, C. L. (2012) Baseload electricity from wind via compressed air energy storage (CAES). *Renewable and Sustainable Energy Reviews*, 16(2), 1099-1109.

Melgar, A., Pérez, J. F., Laget, H. & Horillo, A. (2007) Thermochemical equilibrium modelling of a gasifying process. *Energy Conversion and Management*, 48(1), 59-67.

Mendoza, D. P. (2014) Optimum community energy storage for end user applications. PhD thesis. University of Nottingham.

Merrick, D. (1983) Mathematical models of the thermal decomposition of coal: 1. The evolution of volatile matter. *Fuel*, 62(5), 534-539.

Mertens, N., Alobaid, F., Frigge, L. & Epple, B. (2014) Dynamic simulation of integrated rock-bed thermochemical storage for concentrated solar power. *Solar Energy*, 110 830-842.

Michels, H. & Pitz-Paal, R. (2007) Cascaded latent heat storage for parabolic trough solar power plants. *Solar Energy*, 81(6), 829-837.

Minutillo, M., Lubrano Lavadera, A. & Jannelli, E. (2015) Assessment of design and operating parameters for a small compressed air energy storage system integrated with a stand-alone renewable power plant. *Journal of Energy Storage*, 4 135-144.

Mohammadi, A., Ahmadi, M. H., Bidi, M., Joda, F., Valero, A. & Uson, S. (2017) Exergy analysis of a combined cooling, heating and power system integrated with wind turbine and compressed air energy storage system. *Energy Conversion and Management*, 131 69-78.

Moran, M. J. (1989) *Availability analysis: A guide to efficient energy use*. New York: ASME Press.

Moran, M. J. & Shapiro, H. N. (2000) *Fundamentals of engineering thermodynamics*. New York: John Wiley & Sons.

Morf, P., Hasler, P. & Nussbaumer, T. (2002) Mechanisms and kinetics of homogeneous secondary reactions of tar from continuous pyrolysis of wood chips. *Fuel*, 81(7), 843-853.

Morris, C. G. & Cleveland, C. J. (eds) (2013) *Handbook of Energy*. Elsevier Science.

- Morvay, Z. K. & Gvozdenac, D. D. (2008) Part III: Fundamentals for analysis and calculation of energy and environmental performance. Applied Industrial Energy and Environmental Management. John Wiley & Sons, Ltd.
- Mott, R. A. & Spooner, C. E. (1940) The calorific value of carbon in coal. *Fuel*, 19 242-251.
- Mountouris, A., Voutsas, E. & Tassios, D. (2006) Solid waste plasma gasification: Equilibrium model development and exergy analysis. *Energy Conversion and Management*, 47(13–14), 1723-1737.
- Nallusamy, N., Sampath, S. & Velraj, R. (2007) Experimental investigation on a combined sensible and latent heat storage system integrated with constant/varying (solar) heat sources. *Renewable Energy*, 32(7), 1206-1227.
- Ngo, S. I., Nguyen, T. D. B., Lim, Y., Song, B., Lee, U., Choi, Y. & Song, J. (2011) Performance evaluation for dual circulating fluidized-bed steam gasifier of biomass using quasi-equilibrium three-stage gasification model. *Applied Energy*, 88(12), 5208-5220.
- Nilsson, L. J. (1995) Air-handling energy efficiency and design practices. *Energy and Buildings*, 22(1), 1-13.
- Nithyanandam, K. & Pitchumani, R. (2014) Cost and performance analysis of concentrating solar power systems with integrated latent thermal energy storage. *Energy*, 64 793-810.
- Nithyanandam, K., Pitchumani, R. & Mathur, A. (2012) Analysis of a latent thermocline energy storage system for concentrating solar power plants. ASME 6th International Conference on Energy Sustainability, Parts A and B. San Diego, California, USA, July 23–26, 2012.
- Odeh, N., Harmsen, R., Minett, S., Edwards, P., Perez-Lopez, A. and Hu, J., (2015) Review of the reference values for high efficiency cogeneration (EC REPORT ENER/C3/2013-424/SI2.682977). Available online: https://ec.europa.eu/energy/sites/ener/files/documents/review_of_reference_values_final_report.pdf [Accessed 28/10/2018].
- Ofgem (2017) Electricity prices: Day-ahead baseload contracts – monthly average (GB). Available online: <https://www.ofgem.gov.uk/data-portal/electricity-prices-day-ahead-baseload-contracts-monthly-average-gb> [Accessed 25/10/2018].
- Oró, E., Chiu, J., Martin, V. & Cabeza, L. F. (2013) Comparative study of different numerical models of packed bed thermal energy storage systems. *Applied Thermal Engineering*, 50(1), 384-392.

- Ortega-Fernández, I., Zavattoni, S. A., Rodríguez-Aseguinolaza, J., D'Aguanno, B. & Barbato, M. C. (2017) Analysis of an integrated packed bed thermal energy storage system for heat recovery in compressed air energy storage technology. *Applied Energy*, 205 280-293.
- Öztürk, H. H. (2005) Experimental evaluation of energy and exergy efficiency of a seasonal latent heat storage system for greenhouse heating. *Energy Conversion and Management*, 46(9–10), 1523-1542.
- Ozturk, M. & Dincer, I. (2013) Thermodynamic assessment of an integrated solar power tower and coal gasification system for multi-generation purposes. *Energy Conversion and Management*, 76 1061-1072.
- Pantaleo, A. M., Camporeale, S. M., Sorrentino, A., Miliozzi, A., Shah, N. & Markides, C. N. (2017) Solar/biomass hybrid cycles with thermal storage and bottoming ORC: System integration and economic analysis. *Energy Procedia*, 129 724-731.
- Panwar, N. L., Kothari, R. & Tyagi, V. V. (2012) Thermo chemical conversion of biomass – Eco friendly energy routes. *Renewable and Sustainable Energy Reviews*, 16(4), 1801-1816.
- Parikh, J., Ghosal, G. & Channiwala, S. (2002) A critical review on biomass pyrolysis: 12th European Conference and Technical. Exhibition on Biomass for Energy, Amsterdam, Netherlands: *Industry and Climate Protection*, 2002, 889-892.
- Peng, H., Dong, H. & Ling, X. (2014) Thermal investigation of PCM-based high temperature thermal energy storage in packed bed. *Energy Conversion and Management*, 81 420-427.
- Peng, H., Li, R., Ling, X. & Dong, H. (2015) Modeling on heat storage performance of compressed air in a packed bed system. *Applied Energy*, 160 1-9.
- Pereira da Cunha, J. & Eames, P. (2016) Thermal energy storage for low and medium temperature applications using phase change materials – A review. *Applied Energy*, 177 227-238.
- Pielichowska, K. & Pielichowski, K. (2014) Phase change materials for thermal energy storage. *Progress in Materials Science*, 65 67-123.
- Popiel, C. O. & Wojtkowiak, J. (1998) Simple formulas for thermophysical properties of liquid water for heat transfer calculations (from 0°C to 150°C). *Heat Transfer Engineering*, 19(3), 87-101.
- Ptasinski, K. J., Prins, M. J. & Pierik, A. (2007) Exergetic evaluation of biomass gasification. *Energy*, 32(4), 568-574.

- Puig-Arnabat, M., Bruno, J. C. & Coronas, A. (2010) Review and analysis of biomass gasification models. *Renewable and Sustainable Energy Reviews*, 14(9), 2841-2851.
- Quaak, P., Knoef, H. and Stassen, H., (1999) Energy from biomass: A review of combustion and gasification technologies (WTP 422). Available online: <http://documents.worldbank.org/curated/en/936651468740985551/Energy-from-biomass-a-review-of-combustion-and-gasification-technologies>. [Accessed 01/02/2017].
- Raam Dheep, G. & Sreekumar, A. (2014) Influence of nanomaterials on properties of latent heat solar thermal energy storage materials – A review. *Energy Conversion and Management*, 83 133-148.
- Radmanesh, R., Chaouki, J. & Guy, C. (2006) Biomass gasification in a bubbling fluidized bed reactor: experiments and modeling. *American Institute of Chemical Engineers (AIChE) Journal*, 52(12), 4258-4272.
- Rady, M. (2009) Thermal performance of packed bed thermal energy storage units using multiple granular phase change composites. *Applied Energy*, 86(12), 2704-2720.
- Rafati, M., Wang, L., Dayton, D. C., Schimmel, K., Kabadi, V. & Shahbazi, A. (2017) Techno-economic analysis of production of Fischer-Tropsch liquids via biomass gasification: The effects of Fischer-Tropsch catalysts and natural gas co-feeding. *Energy Conversion and Management*, 133 153-166.
- Raman, P. & Ram, N. K. (2013) Design improvements and performance testing of a biomass gasifier based electric power generation system. *Biomass and Bioenergy*, 56 555-571.
- Rath, J. & Staudinger, G. (2001) Cracking reactions of tar from pyrolysis of spruce wood. *Fuel*, 80(10), 1379-1389.
- Ratnadhariya, J. K. & Channiwala, S. A. (2010) Experimental studies on molar distribution of CO/CO₂ and CO/H₂ along the length of downdraft wood gasifier. *Energy Conversion and Management*, 51(3) 452-458.
- Ratnadhariya, J. K. & Channiwala, S. A. (2009) Three zone equilibrium and kinetic free modeling of biomass gasifier – a novel approach. *Renewable Energy*, 34(4), 1050-1058.
- Reed, T. B., Levie, B. and Graboski, M. S., (1987), Fundamentals, development and Scaleup of the air-oxygen stratified downdraft gasifier. Available online: <https://www.nrel.gov/docs/legosti/old/2571.pdf> [Accessed 28/10/2018].
- Reed, T. B. & Das, A. (1988) *Handbook of biomass downdraft gasifier engine systems*. USA: Solar Energy Research Institute. Available online: <https://www.nrel.gov/docs/legosti/old/3022.pdf> [Accessed 28/10/18].

- Rezaei, M., Anisur, M. R., Mahfuz, M. H., Kibria, M. A., Saidur, R. & Metselaar, I. H. S. C. (2013) Performance and cost analysis of phase change materials with different melting temperatures in heating systems. *Energy*, 53 173-178.
- Rosen, M. A., Dincer, I. & Pedinelli, N. (2000) Thermodynamic performance of Ice thermal energy storage systems. *Journal of Energy Resources Technology*, 122(4), 205-211.
- Sadaka, S. (n.d.) Gasification, producer gas and syngas. Division of Agriculture research and extension, University of Arkansas System. Available online : <https://www.uaex.edu/publications/PDF/FSA-1051.pdf> [Accessed 28/10/18].
- Sadaka, S. S., Ghaly, A. E. & Sabbah, M. A. (2002) Two phase biomass air-steam gasification model for fluidized bed reactors: Part I—model development. *Biomass and Bioenergy*, 22(6), 439-462.
- Salvini, C. (2015) Techno-economic analysis of small size second generation CAES system. *Energy Procedia*, 82 782-788.
- Salvini, C., Mariotti, P. & Giovannelli, A. (2017) Compression and air storage systems for small size CAES plants: Design and off-design analysis. *Energy Procedia*, 107 369-376.
- Sarker, S. & Nielsen, H. K. (2015) Preliminary fixed-bed downdraft gasification of birch woodchips. *International Journal of Environmental Science and Technology*, 12 2119-2126.
- Sattler, J., Hoffschmidt, B., Günther, M. & Joemann, M.(n.d.) Advanced CSP teaching materials: Chapter 9, thermal energy storage. Aachen University of Applied Sciences, Germany, unpublished
- Schumann, T. E. W. (1929) Heat transfer: a liquid flowing through a porous prism. *Journal of the Franklin Institute*, 208 405-416.
- Seylor, A. C. (1938) Petrology and the classification of coal. *Proceedings of the South Wales Institute of Engineer*, 53(4), 254-327.
- Shafizadeh, F. & Chin, P. S. (1977) Thermal deterioration of wood, Chemical Aspects. *American Chemical Society Symposium Series*, 43 57-81.
- Sharma, A., Tyagi, V. V., Chen, C. R. & Buddhi, D. (2009) Review on thermal energy storage with phase change materials and applications. *Renewable and Sustainable Energy Reviews*, 13(2), 318-345.
- Sharma, A. K. (2011) Modeling and simulation of a downdraft biomass gasifier 1. Model development and validation. *Energy Conversion and Management*, 52(2), 1386-1396.

- Sharma, A. K. (2009) Experimental study on 75kWth downdraft (biomass) gasifier system. *Renewable Energy*, 34(7), 1726-1733.
- Sharma, A. K. (2008) Equilibrium and kinetic modeling of char reduction reactions in a downdraft biomass gasifier: A comparison. *Solar Energy*, 82(10), 918-928.
- Sheth, P. N. & Babu, B. V. (2009) Experimental studies on producer gas generation from wood waste in a downdraft biomass gasifier. *Bioresource Technology*, 100(12), 3127-3133.
- Short, W., Packey, D. J. & Holt, T. (1995) A Manual for the economic evaluation of energy efficiency and renewable energy technologies. National Renewable Energy Laboratory (NREL). Available online: <https://www.nrel.gov/docs/legosti/old/5173.pdf> [Accessed 25/10/2018].
- Shottafer, J. E. and Shuler, C. E., (1974) Estimating heat consumption in kiln drying lumber. Life Sciences and Agriculture Experiment Station Technical Bulletin 73. Available online: https://digitalcommons.library.umaine.edu/cgi/viewcontent.cgi?article=1124&context=ae_s_techbulletin [Accessed 25/10/2018].
- Sikarwar, V. S., Zhao, M., Clough, P., Yao, J., Zhong, X., Memon, M. Z., Shah, N., Anthony, E. J. & Fennell, P. S. (2016) An overview of advances in biomass gasification. *Energy and Environmental Science*, 9 2927-3304.
- Singh, A. & Baredar, P. (2016) Techno-economic assessment of a solar PV, fuel cell, and biomass gasifier hybrid energy system. *Energy Reports*, 2 254-260.
- Singh, S., Singh, M. & Kaushik, S. C. (2016) Feasibility study of an islanded microgrid in rural area consisting of PV, wind, biomass and battery energy storage system. *Energy Conversion and Management*, 128 178-190.
- Sombatwong, P., Thaiyasuit, P. & Pianthong, K. (2013) Effect of pilot fuel quantity on the performance and emission of a dual producer gas–diesel engine. *Energy Procedia*, 34 218-227.
- Srinivas, T. & Reddy, B. V. (2014) Hybrid solar–biomass power plant without energy storage. *Case Studies in Thermal Engineering*, 2 75-81.
- Storm, C., Ruediger, H. & Spliethoff, K. R. G. (1999) Co-pyrolysis of coal/biomass and coal/sewage sludge mixtures. *Journal of Engineering for Gas Turbines and Power*, 121 55-63.
- Strbac, G., Ramsay, C. and Pudjianto, D., (2007) Integration of distributed generation into the UK power system. Available online: <https://www.ofgem.gov.uk/ofgem-publications/55759/dgseeewpdgvaluepaper30.pdf> [Accessed 25/10/2018].

Succar, S. and Williams, R. H., (2008), Compressed air energy storage: Theory, resources, and applications for wind power. Energy Systems Analysis Group, Princeton University.

Szargut, J., Morris, D. R. & Steward, F. R. (1998) *Energy analysis of thermal, chemical, and metallurgical processes*. Hemisphere Publishing Corporation.

Taylor, S. M. (1981) Mathematical modelling of heat transfer in packed beds with two phase flow. MSc Thesis. Texas Tech University.

Tessier, M. J., Floros, M. C., Bouzidi, L. & Narine, S. S. (2016) Exergy analysis of an adiabatic compressed air energy storage system using a cascade of phase change materials. *Energy*, 106 528-534.

The Eco Experts (2017) Cost of electricity per kWh. Available online: <https://www.theecoexperts.co.uk/kwh-electricity-prices> [Accessed 02/05/2018].

Thring, M. W. (ed) (1962) *The science of flames and furnaces*, 2nd edition. Chapman & Hall.

Tinaut, F. V., Melgar, A., Pérez, J. F. & Horrillo, A. (2008) Effect of biomass particle size and air superficial velocity on the gasification process in a downdraft fixed bed gasifier. An experimental and modelling study. *Fuel Processing Technology*, 89(11), 1076-1089.

Tola, V., Meloni, V., Spadaccini, F. & Cau, G. (2017) Performance assessment of Adiabatic Compressed Air Energy Storage (A-CAES) power plants integrated with packed-bed thermocline storage systems. *Energy Conversion and Management*, 151 343-356.

Towler, G. & Sinnott, R. (2013) *Chemical engineering design*, 2nd Edition. Boston: Butterworth-Heinemann.

Toyama, S., Aragaki, T. & Murase, K. (1983) Simulation of a multi-effect solar distillator. *Desalination*, 45 101-108.

Toyama, S., Aragaki, T., Salah, H. M., Murase, K. & Sando, M. (1987) Simulation of a multi-effect solar still and the static characteristics. *Journal of Chemical Engineering of Japan*, 20(5), 473-478.

Ujam, A. J. & Diyoke, C. (2013) Economic viability of coal based power generation for Nigeria. *American Journal of Engineering Research*, 2(11), 14-24.

ULB, (2010) Energy storage technologies for wind power integration. Available online: <http://en.escn.com.cn/download/show/125.aspx> [Accessed 03/10/2016].

- Wagner, W. & Prub, A. (2002) The IAPWS formulation 1995 for the thermodynamic properties of ordinary water substance for general and scientific use. *Journal of Physical and Chemical Reference Data*, 31(2), 387-535.
- Wakao, N. & Kaguei, S. (1982) *Heat and mass transfer in packed beds*. New York: Gordon and Braech.
- Wakao, N. & Kagei, S. (1983) *Heat and mass transfer in packed beds*, 2nd edition. Amsterdam, Netherlands: Gordon and Breach.
- Wang, J. & Yang, Y. (2016) Energy, exergy and environmental analysis of a hybrid combined cooling heating and power system utilizing biomass and solar energy. *Energy Conversion and Management*, 124 566-577.
- Wang, S., Zhang, X., Yang, L., Zhou, Y. & Wang, J. (2016) Experimental study of compressed air energy storage system with thermal energy storage. *Energy*, 103 182-191.
- Wang, Y. & Kinoshita, C. M. (1993) Kinetic model of biomass gasification. *Solar Energy*, 51(1), 19-25.
- Wang, Y., Huang, Y., Roskilly, A. P., Ding, Y. & Hewitt, N. (2010) Trigeneration running with raw jatropha oil. *Fuel Processing Technology*, 91(3), 348-353.
- Wardle, R. and Davison, P., (2012), Initial load and generation profiles from CLNR monitoring trials. Available online: http://www.networkrevolution.co.uk/wp-content/uploads/2014/02/DEI_CLNR_DC1XX_LoadProfilesSDRC_Dec2012_Version_1_1.pdf [Accessed 25/10/2018].
- Wei, J., Kawaguchi, Y., Hirano, S. & Takeuchi, H. (2005) Study on a PCM heat storage system for rapid heat supply. *Applied Thermal Engineering*, 25(17-18), 2903-2920.
- Wen, C. Y., Chen, H. and Onozaki, M., (1982) User's manual for computer simulation and design of the moving bed coal gasifier. Available online: <https://www.osti.gov/servlets/purl/6422177> [Accessed 28/10/2018].
- Wichert, B. (1997) PV-diesel hybrid energy systems for remote area power generation — A review of current practice and future developments. *Renewable and Sustainable Energy Reviews*, 1(3), 209-228.
- Wolf, D. & Budt, M. (2014) LTA-CAES – A low-temperature approach to Adiabatic Compressed Air Energy Storage. *Applied Energy*, 125 158-164.
- Wood, S. R. & Rowley, P. N. (2011) A techno-economic analysis of small-scale, biomass-fuelled combined heat and power for community housing. *Biomass and Bioenergy*, 35(9), 3849-3858.

- World Energy Council (2016) World energy resources: *Resources 2016 summary*. Available online: <https://www.worldenergy.org/wp-content/uploads/2016/10/World-Energy-Resources-Full-report-2016.10.03.pdf>. [Accessed 01/05/2018].
- Wu, M., Xu, C. & He, Y. (2014) Dynamic thermal performance analysis of a molten-salt packed-bed thermal energy storage system using PCM capsules. *Applied Energy*, 121 184-195.
- Wurzenberger, J. C., Wallner, S. & Raupenstrauch, H. (2002) Thermal conversion of biomass: comprehensive reactor and particle modeling. *American Institute of Chemical Engineer Journal*, 48(10), 2398-2411.
- Xia, L., Zhang, P. & Wang, R. Z. (2010) Numerical heat transfer analysis of the packed bed latent heat storage system based on an effective packed bed model. *Energy*, 35(5), 2022-2032.
- Xu, B., Li, P. & Chan, C. (2015) Application of phase change materials for thermal energy storage in concentrated solar thermal power plants: A review to recent developments. *Applied Energy*, 160 286-307.
- Yang, Z., Wang, Z., Ran, P., Li, Z. & Ni, W. (2014) Thermodynamic analysis of a hybrid thermal-compressed air energy storage system for the integration of wind power. *Applied Thermal Engineering*, 66(1-2), 519-527.
- Yao, E., Wang, H., Wang, L., Xi, G. & Maréchal, F. (2016) Thermo-economic optimization of a combined cooling, heating and power system based on small-scale compressed air energy storage. *Energy Conversion and Management*, 118 377-386.
- Zafirakis, D. & Kaldellis, J. K. (2009) Economic evaluation of the dual mode CAES solution for increased wind energy contribution in autonomous island networks. *Energy Policy*, 37(5), 1958-1969.
- Zainal, Z. A., Ali, R., Lean, C. H. & Seetharamu, K. N. (2001) Prediction of performance of a downdraft gasifier using equilibrium modeling for different biomass materials. *Energy Conversion and Management*, 42(12), 1499-1515.
- Zainal, Z. A., Rifau, A., Quadir, G. A. & Seetharamu, K. N. (2002) Experimental investigation of a downdraft biomass gasifier. *Biomass and Bioenergy*, 23(4), 283-289.
- Zalba, B., Marín, J. M., Cabeza, L. F. & Mehling, H. (2003) Review on thermal energy storage with phase change: materials, heat transfer analysis and applications. *Applied Thermal Engineering*, 23(3), 251-283.
- Zanganeh, G., Pedretti, A., Zavattoni, S., Barbato, M. & Steinfeld, A. (2012) Packed-bed thermal storage for concentrated solar power – Pilot-scale demonstration and industrial-scale design. *Solar Energy*, 86(10), 3084-3098.

Zhang, X., Chen, H., Xu, Y., Li, W., He, F., Guo, H. & Huang, Y. (2017) Distributed generation with energy storage systems: A case study. *Applied Energy*, 204 1251-1263.

Zhang, Y., Yang, K., Li, X. & Xu, J. (2013) The thermodynamic effect of thermal energy storage on compressed air energy storage system. *Renewable Energy*, 50 227-235.

Zhao, P., Dai, Y. & Wang, J. (2015) Performance assessment and optimization of a combined heat and power system based on compressed air energy storage system and humid air turbine cycle. *Energy Conversion and Management*, 103 562-572.

Zhao, P., Dai, Y. & Wang, J. (2014) Design and thermodynamic analysis of a hybrid energy storage system based on A-CAES (adiabatic compressed air energy storage) and FESS (flywheel energy storage system) for wind power application. *Energy*, 70 674-684.

Zhao, P., Gao, L., Wang, J. & Dai, Y. (2016) Energy efficiency analysis and off-design analysis of two different discharge modes for compressed air energy storage system using axial turbines. *Renewable Energy*, 85 1164-1177.